Neutron stars as laboratories for fundamental physics: from dense QCD to dark matter

Dake Zhou

A dissertation
submitted in partial fulfillment of the
requirements for the degree of

Doctor of Philosophy

University of Washington

2021

Reading Committee:

Sanjay Reddy, Chair

Larry McLerran

Laurence Yaffe

Program Authorized to Offer Degree:
Physics

University of Washington

Abstract

Neutron stars as laboratories for fundamental physics:
from dense QCD to dark matter

Dake Zhou

Chair of the Supervisory Committee:
Professor Sanjay Reddy
Department of Physics

This dissertation explores the subatomic world with observations of neutron stars. Neutron stars are exotic and mysterious objects and are placed under the spotlight with current and planned investigations. In the coming decades, multimessenger (electromagnetic, neutrino, gravitational wave and cosmic ray) observations are expected to reveal the physical processes that underlie extreme astrophysical phenomena involving neutron stars such as compact star mergers and core-collapse supernovae. These observations could provide new insights about particle and nuclear physics under extreme conditions and physics beyond the standard model. Open questions concerning *ab initio* nuclear theory, dense quantum chromodynamics matter and the nature of dark matter are summarized. Following a brief review of neutron stars, the prospect of constraining neutron matter equation of state with future gravitational wave detections is examined. The rest of the thesis focuses on potential neutron star observables and constraints of a few emerging dark matter models. It is shown that dark baryons lighter than ~ 1.2 GeV are incompatible with observed massive pulsars. A scenario where effects of self-interacting dark matter may be detected via gravitational waves from binary neutron star mergers is studied. Finally, the closing chapter investigates impacts and potential observable signatures of a novel superfluid phase of matter arising from neutrino-portal scalars carrying lepton numbers in newly-born neutron stars.

TABLE OF CONTENTS

LIST OF FIGURES

LIST OF TABLES

ACKNOWLEDGMENTS

I would like to express deep gratitude towards my advisor Sanjay Reddy for his patient guidance and enlightening insights into broad aspects of neutron stars. I wish to thank my collaborators Michael Forbes, David McKeen, and Ann Nelson, from whom I learned a great deal. I am very grateful to members of the Institute for Nuclear Theory and the particle theory group at the University of Washington, particularly Steve Ellis, David Kaplan, Andreas Karch, Larry McLerran, and Larry Yaffe, for discussing a wide range of topics in physics.

DEDICATION

To my grandparents

GLOSSARY

BBN Big Bang nucleosynthesis.

BCS Bardeen-Cooper-Schrieffer.

BEC Bose-Einstein condensate.

CMB cosmic microwave background.

ChPT, χPT chiral perturbation theory.

BNS binary neutron star.

CDM cold dark matter.

CLDM compressible liquid-drop model.

DM dark matter.

EFT effective field theory.

EOS equation of state.

GW gravitational wave.

LIGO laser interferometer gravitational wave observatory.

NICER Neutron Star Interior Composition Explorer.

NS neutron star.

PCA principle component analysis.

PNS proto-netron star.

pN post-Newtonian.

QCD quantum chromodynamics.

QMC quantum Monte Carlo.

SIDM self-interacting dark matter.

SM Standard Model.

SN supernova.

SNR signal-to-noise ratio.

TF Thomas-Fermi.

TOV Tolman–Oppenheimer–Volkoff.

vev vacuum expectation value.

WIMP weakly interacting massive particle.

Chapter 1

INTRODUCTION

Despite the huge success of the Standard Model (SM) of particle physics, there are a number of outstanding questions the standard model fails to address. High on the list is the nature of dark matter (DM). Since stumbling upon the "missing mass" through its gravitational effects nearly a century ago [212, 280, 396], we have gathered abundant evidence of dark matter in numerous astrophysical and cosmological settings. While some may be explained by modified theories of gravity [260, 44] or elusive astrophysical objects known as primordial black holes [181, 394], the consensus is that particles beyond the SM constitute at least a fraction of DM.

A population of stable, non-relativistic, collisionless particles, known as cold dark matter (CDM), has been considered the conventional DM candidate since the 1980s. It received its reputation because (i) the standard ΛCDM[1] cosmology, in which CDM plays a central role, successfully explains a wide range of observations including the cosmic microwave background (CMB), abundances of light nuclei and large scale cosmic structures [13]; and (ii) it is well-motivated from model building perspectives. CDM fits the description of massive weakly interacting particles (WIMP), which are natural predictions of many then-promising extensions to the standard model, most notably lightest neutralinos from a variety of supersymmetric theories [162, 129].

Fruitless direct searches for WIMP in colliders and nuclear recoil experiments have stimulated interests in alternative possibilities in recent years. On the one hand, a large number of DM models are proposed. Some of them are equally well-motivated [377, 382, 195, 121]; On the other, phenomena beyond the Standard Model (BSM) have since surfaced in various ter-

[1] Λ denotes dark energy.

restrial experiments in the leptonic [15][14][10], nucleonic [224][169] and mesonic [194, 339, 1] sectors spanning a wide energy range $\sim$ eV-GeV. These deviations seem to hint at a broad and colorful landscape of dark matter rich in particle contents and phenomenology. This line of inquiry appears to be supported by recent developments in cosmology and galactic astrophysics. In particular, discrepancies between observations and results of CDM N-body simulations on small-scale structures [215, 268, 344] strongly suggest that at least part of dark matter may experience stronger-than-expected interactions [269][365].

Where the standard model prevails, predictability may still be limited. This issue is especially conspicuous in quantum chromodynamics (QCD). Since forces between nucleons are residue effects of the strong interaction among constituent quarks and gluons, one would expect a first-principle (re-)construction of nuclear theory from QCD. An *ab initio* approach to nuclear forces, however, has not been fully achieved. To be clear, the problem runs deeper than the infeasible computing power required for solving quantum many-body systems that is plaguing broad areas of science. We have yet to write down a systematically improvable Hamiltonian appropriate for nuclear phenomena with full confidence. Currently at very low energies ($E \lesssim 100$ MeV) an effective description called *pionless effective field theory (EFT)* works well [283]. Its cousin theory known as *chiral EFT (χEFT)* that is appropriate for higher energies [380, 381], however, appears to be non-renormalizable thus requires justifications for its validity and utility.

Moreover, understanding the QCD vacuum at finite temperature, as is realized in the early universe, and at finite baryon chemical potential, as is relevant in the interior of neutron stars, is another challenging frontier. While the finite temperature axis of the QCD phase diagram is relatively better-studied thanks to powerful numerical frameworks and direct experimental probes, little is known about cold and dense QCD matter. As degenerate nuclear matter gets compressed to higher densities, quarks are liberated from nucleons and eventually form a degenerate quark matter. Where and how exactly this transition occurs, what intermediate states there are (if any), remain unclear despite decades of work.

Neutron stars (NSs) could help address these questions. Born in the aftermath of core-

collapse supernovae, NSs are among the most exotic and extreme environments in the observed universe. With masses around solar masses $M \sim M_\odot \simeq 10^{30}$ kg but radii only of order $R \sim 10$ km, neutron stars are compact objects ($GM/Rc^2 \sim 1$) of extremely high densities ($\rho \sim M/R^3 \sim 10^{15}$ g/cm^3). The corresponding baryon number density $n_B \sim 2 - 10 n_0$ is around a few times the typical density encountered in nuclei $n_0 = 0.16$ fm^{-3} known as the saturation density, suggesting the presence of exotic states of matter in the neutron star interior. All four known interactions, strong, weak, electromagnetic and gravity, play important roles in determining the stellar composition, structure, evolution and response to external disturbances.

The diversity displayed among NSs is also intriguing. Neutron stars are known for the ferocious and spectacular explosions associated with their births, when the core temperature can reach around tens of MeV or 10^{12} K; Old neutron stars, on the contrary, are fairly cold and only feebly emit electromagnetic waves as they dim out and get outshined by the rest of the sky. Further, a small fraction of neutron stars known as magnetars possesses strong surface magnetic fields north of 10^{10} T that are not seen anywhere else in the universe (for a recent review on magnetars see [214]). These extreme physical conditions found in neutron stars make them unique and ideal laboratories to test the SM and to search for what lies beyond.

Admittedly, resorting to compact stars to study fundamental physics is not a new proposal [356, 358, 301, 130, 300]. What makes this avenue particularly promising and exciting right now and in the coming decades is the advent of multimessenger astrophysics. Preluded by the detection of supernova neutrinos from SN1987a [63, 193], the era of multimessenger astronomy was formally ushered in by the detection of gravitational waves (GWs) from the binary neutron star (BNS) merger GW170817. The observation of GW170817 has already contributed to efforts in understanding the cosmic history [3, 93, 271, 342] as well as dense matter encountered in the NS interior [4, 5].

This is only the beginning. With improvements to the laser interferometer gravitational wave observatory (LIGO) gradually roll out and commissions of future generation earth- and

space-based gravitational wave detectors expected in the coming decades [247][247], a growing number of events are anticipated to be observed with refined accuracy. It is estimated that as many as ~ 10 BNS mergers per year could be detected by the global LIGO-VIRGO-KAGRA network starting this year (2021) and may reach ~ 100 per year in 2025 when LIGO-India comes online [7]. Prospects of observing continuous GW backgrounds [9, 230, 160], post-merger ring-down phases in BNS systems [305, 57, 56, 134, 37], GW memory effects from core-collapse supernovae [366, 79, 133, 218, 270, 241], mergers of supermassive black holes and white dwarfs [361, 275, 334, 267], etc., will further inject excitement and energy into this field. When coupled with steady theoretical advancements and rapid increases in computational power, these observations can provide unprecedented details of extreme environments and once-secluded corners of the universe, which will be instrumental in advancing our exploration towards the unknown.

The dissertation is structured as follows: In chapter 2, a family of χEFT-based nuclear equations of state is constructed, and the prospect of constraining dense neutron matter properties using future gravitational wave detections is examined; Chapter 3 focuses on neutron star constraints on a class of dark matter known as dark baryons that directly couple to nucleons; Chapter 4 raises the possibility for observing and constraining self-interacting dark matter with gravitational waves from compact binary mergers; In the last chapter, a new phase of matter in proto-neutron stars arising from condensations of dark lepton scalars coupling to neutrinos is studied.

The rest of this chapter will expand on the aforementioned conundrums in QCD and mysteries surrounding dark matter. This introduction ends with a brief overview of neutron stars to provide readers with background information on astrophysics and multimessenger observations. Unless otherwise stated, the "mostly minus" metric $||\eta_{\mu\nu}|| = \mathrm{diag}\,(1, -1, -1, -1)$ and natural units in which $G = \hbar = k_B = c = 1$ are assumed in what follows.

1.1 Dense matter and QCD

At its core QCD is a non-abelian gauge theory (Yang-Mills theory [389]) based on the Lie group $SU(3)$. Quarks live in the fundamental representation of $SU(3)$ and the gluon fields $A^\mu = A^\mu_a T^a$ transform in the adjoint representation. Here, T^a with $a = r, g, b$ are generators of the gauge group, and their commutation relation $[T^a, T^b] = if^{abc}T^c$ defines the Lie algebra $su(3)$. The structure constant f^{abc} is totally anti-symmetric for Lie algebras. The QCD Lagrangian is

$$\mathcal{L}_{QCD} = -\frac{1}{2g_s^2}\text{tr } G^{\mu\nu}G_{\mu\nu} + \bar{q}(i\not{D} - m)q, \tag{1.1}$$

where $G_{\mu\nu} = \partial_\mu A_\nu - \partial_\nu A_\mu - i[A_\mu, A_\nu]$ is Lie algebra valued gluon field strength tensor and $D_\mu = \partial_\mu - iA_\mu$ is the covariant derivative. The Feynman slash notation $\not{\mathcal{O}} \equiv \mathcal{O}_\mu\gamma^\mu$ and normalization convention $\text{tr}\left(T^aT^b\right) = \frac{1}{2}\,\delta^{ab}$ are assumed.

Before quantizing the theory, the first sign of challenge already emerges at the level of Lagrangian. The gauge field kinetic term $G^{\mu\nu}_a G^a_{\mu\nu}$ contains cubic and quartic couplings among gluon fields. Contrary to the electrically neutral photon in QED, the gluon fields carry color charges thus themselves participate in the strong interaction, making QCD a non-linear theory.

Asymptotic freedom [171, 295] renders perturbation theory of very limited applicability in regard to low energy phenomena. The beta function at 1-loop for QCD-like theories described by $SU(N_c)$ gauge groups coupled with N_f flavors of quarks is

$$\beta(g_s) = \frac{\mathrm{d}}{\mathrm{d}\log\mu}g_s = -\frac{g_s^3}{16\pi^2}\left(\frac{11}{3}N_c - \frac{2}{3}N_f\right). \tag{1.2}$$

Specialize to QCD where $N_f = 6$ and $N_c = 3$, the beta function is negative. The coupling $\alpha_s = g_s^2/4\pi$ runs with energy scale μ as

$$\alpha_s(\mu) = \frac{2\pi}{7}\frac{1}{\log\frac{\mu}{\Lambda_{\text{QCD}}}}. \tag{1.3}$$

Above, Λ_{QCD} is the location of the Landau pole, suggesting perturbative treatments break down below the scale $\Lambda_{\text{QCD}} \sim 300$ MeV.

Indeed, the strong interaction becomes so strong at low energies such that quarks and gluons are *confined* into color singlet states. Therefore, quarks and anti-quarks, which carry fractional electric charges, are not present below $\Lambda_{\rm QCD}$, and are only found within mesons and baryons.

The fact that hadrons are the only relevant degrees of freedom at low energies hints at alternative *effective* descriptions built solely in terms of hadrons. In QCD, the relatively large energy gap of order ~ 600 MeV between pions ($m_\pi \sim 130$ MeV) and the lightest vector mesons ($m_\rho \sim 770$ MeV) provides a natural separation of scales thus admits an effective field theory approach. This gap is the consequence of *spontaneous chiral symmetry breaking*.

Chiral symmetry is exact for massless fermions. In the real world, the up u and down d quark masses $m_{u,d} \sim \mathcal{O}(\text{MeV})$ are negligible compared to $\Lambda_{\rm QCD}$. In the massless u and d limit, chiral eigenstates $q_{L,R} = P_{L,R} q$ obtained by applying projection operators $P_L = \frac{1-\gamma^5}{2}$ and $P_R = \frac{1+\gamma^5}{2}$ do not mix under the equations of motion. The Lagrangian is invariant under separate $SU(2)$ transformations on flavor doublets $\psi_{L,R} = (u_{L,R}, d_{L,R})^T$:

$$\psi_L \to g_L \psi_L,\ \psi_R \to g_R \psi_R,\ \text{where } g_L \in SU(2)_L,\ g_R \in SU(2)_R. \tag{1.4}$$

In fact, the full symmetry group is larger: $U(2)_L \times U(2)_R = SU(2)_L \times SU(2)_R \times U(1)_V \times U(1)_A$. The abelian vector symmetry $U(1)_V$, under which $\psi \to e^{i\theta}\psi$, persists even for massive quarks. It corresponds to baryon (fermion) number conservation. On the other hand, the axial symmetry $U(1)_A$ associated with axial rotations $\psi \to e^{i\theta\gamma^5}\psi$ is anomalous [45, 11], i.e., lost upon quantization. The symmetry $SU(2)_L \times SU(2)_R$ is called chiral because left- and right-handed fields transform differently under its actions.

Below $\sim \Lambda_{\rm QCD}$, $SU(2)_L \times SU(2)_R$ is spontaneously broken by a finite vacuum expectation value (vev) of the quark bilinear operator in the ground state

$$\langle \bar{u} u \rangle = \langle \bar{d} d \rangle = v^3 \sim \Lambda_{\rm QCD}^3 \tag{1.5}$$

known as chiral condensate. While the detailed condensation mechanism is not well-understood, lattice simulations have confirmed this picture [97, 159, 131, 144, 143, 132].

That the condensate is proportional to identity in the flavor space (up and down quark bilinears develop the same vev) implies a residue $SU(2)$ flavor symmetry, under which both left-handed and right-handed fields rotate the same way in the $(u, d)^T$ space. Specifically, $SU(2)_L \times SU(2)_R \to SU(2)_{\text{isospin}}$, where the unbroken $SU(2)_{\text{isospin}}$ is the diagonal subgroup. Here *isospin* shares the same meaning as in nuclear physics since quark contents of neutrons (udd) and protons (uud) are related to each other via $u \leftrightarrow d$.

One consequence of the spontaneous broken chiral symmetry is the emergence of massless particles as dictated by the Goldstone theorem [165, 164]. These particles are pions. Each of the three pions π^0, $\pi^\pm$ corresponds to a broken generator. They clearly form a triplet under the unbroken $SU(2)_{\text{isospin}}$ and can be packed into an $SU(2)$-valued object

$$U(x) = \exp\left(2i\frac{\pi^a(x)\tau_a}{f_\pi}\right) = \exp\left[\frac{i}{f_\pi}\begin{pmatrix}\pi^0(x) & \sqrt{2}\pi^-(x)\\ \sqrt{2}\pi^+(x) & -\pi^0(x)\end{pmatrix}\right], \tag{1.6}$$

where τ_a are generators of $SU(2)$, $\pi^0 = \pi^3$, $\pi^\pm = (\pi_1 \pm \pi_2)/\sqrt{2}$, and $f_\pi \approx 92$ MeV [354] is the pion decay constant. Under the full (anomaly-free) symmetry group $SU(2)_L \times SU(2)_R \times U(1)_V$, the Goldstone modes transform as

$$U(x) \to g_L U(x) g_R^\dagger \tag{1.7}$$

For infinitesimal transformations $g_{L,R} = \exp\left(i\theta^a_{L,R}\tau_a\right) \approx 1 + i\theta^a_{L,R}\tau_a$,

$$\pi^a \to \pi^a + \frac{f_\pi}{2}(\theta^a_L - \theta^a_R) - \frac{f^{abc}_{su(2)}}{2}(\theta^a_L + \theta^a_R)\pi^c. \tag{1.8}$$

Hence except for the diagonal isospin subgroup (in which $\theta_L = \theta_R$) chiral symmetry is realized nonlinearly under which pions shift at leading order. In other words, there are infinitely many parameterizations for the pions that differ from each other only by a non-linear transformation of the type that appeared in eq. 1.8. When used to describe physical processes, these equivalent parameterizations shall all yield the same predictions for given observables.

With a compact representation of pions at hand, it would seem reasonable to assume that it is possible to construct an effective description of pion dynamics in terms of U. Consistency

is the only guidance: in order for predictions of the effective description to be consistent with QCD, the effective theory should respect all the symmetries the underlying theory exhibits. Bearing this in mind, one may proceed to write down the most general effective Lagrangian involving U that respects the chiral symmetry. Since $UU^\dagger = 1$, non-trivial operators must contain derivatives:

$$\mathcal{L}_{\pi\pi} = \frac{f_\pi^2}{4}\mathrm{tr}\left[(\partial^\mu U)(\partial_\mu U)^\dagger\right] + L_1\mathrm{tr}\left[(\partial^\mu U)(\partial_\mu U)^\dagger\right]^2 + L_2\mathrm{tr}\left[(\partial^\mu U)(\partial^\nu U)^\dagger\right]\mathrm{tr}\left[(\partial_\mu U)(\partial_\nu U)^\dagger\right] + L_3\mathrm{tr}\left\{\left[(\partial^\mu U)(\partial_\mu U)^\dagger\right]^2\right\} + \ldots, \quad (1.9)$$

where the trace is over the flavor space. The coefficient of the leading term guarantees the canonical normalization for scalar fields:

$$\frac{f_\pi^2}{4}\mathrm{tr}\left[(\partial^\mu U)(\partial_\mu U)^\dagger\right] = \frac{1}{2}(\partial_\mu\pi^0)(\partial^\mu\pi^0)+(\partial_\mu\pi^+)(\partial^\mu\pi^-)^\dagger+\frac{1}{f_\pi^2}\left[\frac{1}{3}\pi^0\pi^0(\partial_\mu\pi^+)(\partial^\mu\pi^-)^\dagger+\ldots\right]+\ldots \quad (1.10)$$

Results in the square bracket give the leading pion scattering amplitudes. One may perform similar expansions for sub-leading terms in eq. 1.9 to calculate observables such as pion scattering amplitudes to higher accuracy. Although infinitely many terms are contained in eq. 1.9, they can be ordered according to the number of derivatives each contains, allowing an estimation of truncation errors in powers of (E_π/f_π). Observables such as S-matrices can be calculated up to any given order and the effective description is predictive. The unknown coefficients $L_{1,2,3,\ldots}$ (dubbed *low energy constants (LECs)*) may be determined by fitting to experimental data such as pion scattering phase shifts.

To summarize, without worrying about the details of quark and gluon dynamics in QCD we arrived at a phenomenological Lagrangian describing pions following symmetry principles alone. This procedure was pioneered by Callan, Coleman, Wess and Zumino (CCWZ) [100, 84]. The price is that the unknown LECs need to be obtained from experiments. The *chiral Lagrangian* eq. 1.9 [156] is an example of nonlinear sigma models which arise naturally from studying spontaneous symmetry breaking [84, 375].

1.1.1 chiral effective field theory

Manifested throughout the CCWZ approach to chiral Lagrangian is the essence of *effective field theory* (EFT). The procedure of constructing an EFT may be summarized as the following:

1. Identify the separation between high energy ("hard") and low energy ("soft") scales;
2. Identify the relevant degrees of freedom around the soft scale;
3. Write down all the operators consistent with symmetries and symmetry breaking patterns (if any);
4. Organize the terms according to their importance to form a systematic expansion;
5. Calculate observables using the low energy effective theory just as with any other renormalizable perturbative theories up to appropriate order for the desired accuracy[2].

The chiral effective field theory (chEFT, χEFT) describing low energy nuclear physics is exactly constructed in this manner. In this scenario, the nucleon and pion momenta Q and pion mass m_π are clearly the soft scale. The hard scale is often chosen to be $\Lambda_\chi \sim m_\rho \simeq 770$ MeV since ρ mesons show up as resonances in pion scatterings and they are the lightest non-Goldstone excitations in the spectrum. A perturbative expansion in terms of $(Q/\Lambda_\chi)^\nu$ and $(m_\pi/\Lambda_\chi)^\nu$ therefore allows an order-by-order arrangement in ν (sometimes called *chiral dimension*) for operators allowed by chiral symmetries. The power counting scheme ensures up to any given order only a finite number of terms from the infinite-many possibilities are required. Schematically, the Lagrangian for χEFT is built upon the chiral Lagrangian and takes the form

$$\mathcal{L}_\chi = \mathcal{L}_{\pi\pi} + \mathcal{L}_{N\pi} + \mathcal{L}_{NN} + \dots \tag{1.11}$$

[2]Loop integrals arising from this truncated series can be regulated by the renormalization of LECs up to the order under consideration. A valid EFT would make predictions that are independent of the underlying regularization and renormalization schemes.

where the ellipsis stands for three-, four-,... and higher n-body interactions.

As it turns out, however, incorporating nucleons introduces complications. Let us start with the simplest term $\mathcal{L}_{\pi N}$. The leading order term for 2-body pion-nucleon ($\Psi = (p, n)^T$) coupling is [155]

$$\mathcal{L}^{(1)}_{N\pi} = \bar{\Psi}(i\not{D} - m_N + \frac{g_A}{2}\gamma^5\gamma^\mu u_\mu)\Psi, \tag{1.12}$$

where m_N denotes nucleon mass, g_A the nucleon axial coupling. The chiral connection Γ_μ in the covariant derivative $D_\mu = \partial_\mu + \Gamma_\mu$ and the axial-vector u_μ are defined as

$$\begin{aligned} \Gamma_\mu &= \frac{1}{2}(\xi^\dagger\partial_\mu\xi + \xi\partial_\mu\xi^\dagger), \\ u_\mu &= i(\xi^\dagger\partial_\mu\xi - \xi\partial_\mu\xi^\dagger), \end{aligned} \tag{1.13}$$

respectively, with $\xi = U^{1/2}$ an equivalent parameterization of pions [100, 84]. The inclusion of relativistic baryons creates another hard scale $E_N \sim m_N$ which is the result when Ψ is acted upon by ∂^0. Note that the nucleon mass $m_N \sim 1$ GeV is at least comparable to Λ_χ. If not treated properly the enhancement m_N/Q would destroy power counting of pion loops using the naive dimensional regularization [54, 55, 155]. The heavy baryon formalism developed by Jenkins and Monahar [202] based on Georgi's work [158] in heavy quark physics is a straightforward solution. It assumes baryons are nearly static and is essentially an expansion in Q/m_N.

Employing non-relativistic kinematics, however, does not solve all the issues in the few-nucleon ($n > 1$) sector. Unlike the dynamics of pions, which is restricted to derivative couplings as required by chiral symmetry, interactions involving baryons are not constrained by symmetries and may contain derivative-less terms. As a result, interactions among nucleons do not vanish at zero momentum or in the chiral limit. In fact, the NN scattering length $a_0 \sim -20$ fm is rather long, suggesting non-perturbative effects dominate few nucleon interactions at low energies. This is expected from nuclear physics since nucleons may form nuclei which are bound states.

Weinberg first attempted at this problem [379] and traced non-perturbative effects to infrared enhancements of order $\sim m_N/Q$ stemming from reducible diagrams containing purely

nucleonic intermediate states [380]. He realized that the EFT is still predictive provided that the nucleon mass is counted as a separate hard scale:

$$m_N \sim \Lambda_\chi^2/Q \gg \Lambda_\chi.$$

In this updated version of EFT the old-fashioned perturbation theory is invoked to isolate and exclude infrared-enhanced contributions, resulting in "chiral potentials" obtained by summing irreducible graphs only. Non-perturbative resummation is then carried out by supplying this truncated potential up to desired order to the Lipperman-Schwinger equation when calculating observables [379, 380, 381].

The resulting power counting scheme, named after Weinberg, is

$$\nu = -2 + 2N - 2C + 2L + \sum_i \Delta_i, \text{ with } \Delta_i = (d_i + \frac{n_i}{2} - 2), \tag{1.14}$$

where N denotes the number of nucleons, C the number of separately connected pieces, L the number of loops; d_i is the number of derivatives or pion mass insertions and n_i the number of nucleon fields involved in vertex i. The sum is over all the vertices in the diagram under consideration.

The hierarchy of few-nucleon potentials resulting from Weinberg's prescription is demonstrated in fig. 1.1. A nice feature is that many-body interactions arise naturally from the power counting eq. 1.14 and are put on equal footings with 2-body forces. The leading order (LO, $\nu = 0$) consists of contributions from one-pion-exchange (OPE) and a derivative-less contact term. They lead to s-wave intermediate- and short-range 2-body nuclear forces. At the next leading order (NLO, $\nu = 2$), three body terms appear but they all cancel out [381]. Non-vanishing three-body interactions emerge at the next-to-next-leading order (NNLO, $\nu = 3$), and they are known to be important even in light nuclei such as ^{4}He.

The remaining issue concerns the renormalizability of χEFT. While it is true that in a regular EFT such as eq. 1.9 contact interactions are sufficient to renormalize the EFT order by order, here the non-perturbative resummation through the Lippman-Schwinger equation generates additional short-distance singularities that contact LECs at the order

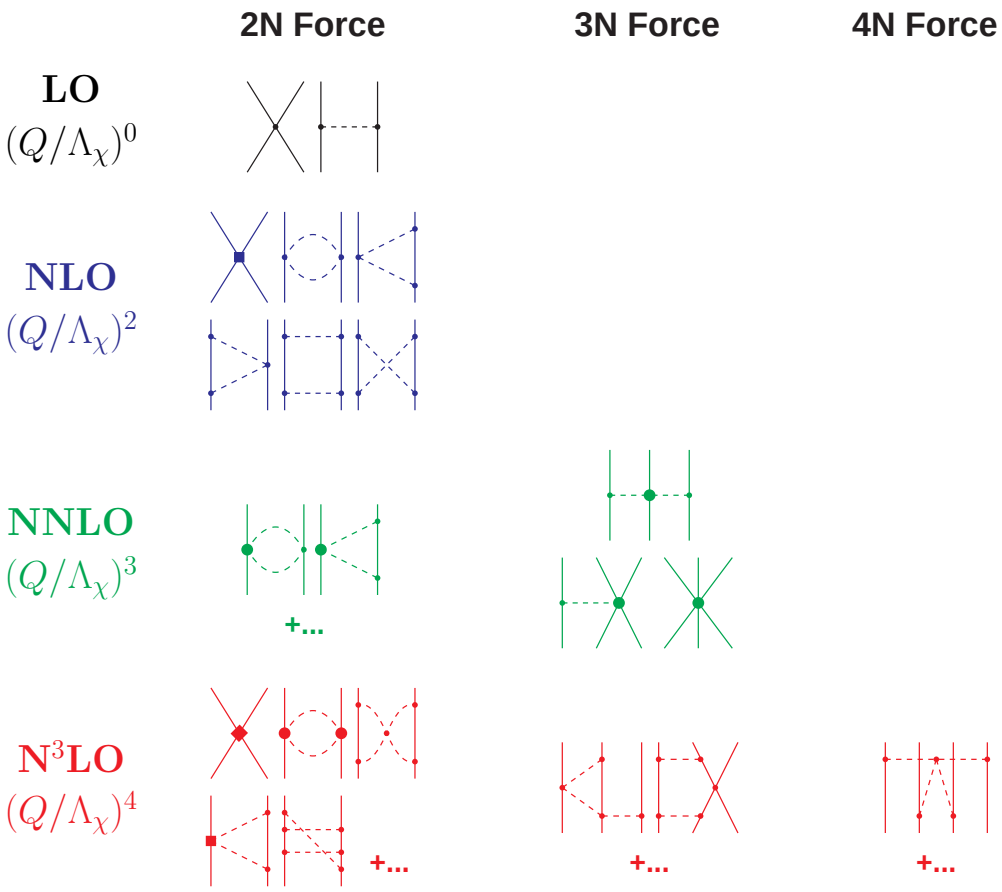

Figure 1.1: Systematic organization of nuclear forces by the Weinberg power counting scheme eq. 1.14. Solid lines represent nucleons and dashed lines pions. Small dots, large solid dots, solid squares, and solid diamonds denote vertices $\Delta = 0, 1, 2$, and 4 respectively. Figure taken from [246]

one is working cannot compensate. This issue necessitates a finite ultraviolet (UV) cutoff Λ in the EFT and was first identified in the 2-nucleon $^1S_0$ channel at LO [206]. It has a simpler explanation attributed to renormalizing attractive singular potentials in coordinate space Schrodinger equations [40]. In practice, if the cutoff is chosen too low, the applicable

energy range of EFT is greatly restricted, while if it is too high, observables are found to be quite sensitive to chosen values of the cutoff Λ, indicating the predictions might not be reliable.

One notable alternative approach due to Kaplan, Savage and Wise [207, 208] took insights from *pionless EFT* consisting of explicit nucleonic degrees of freedom only [283]. Partially motivated by unitary Fermi gas as suggested by the large NN scattering length, the theory reproduces effective range expansion for NN scatterings. The inverse scattering length $1/a \sim Q$ is treated as an explicit soft scale. The KSW power counting scheme ensures that physical *observables* instead of chiral potentials are expanded consistently to achieve order-by-order renormalization. However, the extension to include perturbative pions fails to converge in spin-triplet channels at NNLO even for small momenta $Q \sim m_\pi$ [137]. To date, whether χEFT is truly renormalizable hence gives valid predictions remains an open question despite tremendous efforts [137, 41, 293, 64, 290, 277, 42, 369].

In practice, Weinberg's χEFT with explicit UV cutoffs in loop integrals around $\Lambda \sim 400 - 600$ MeV and LECs determined from NN scattering data and light nuclei structure [3] has been applied to a range of topics in nuclear physics. In particular, χEFT-based many-body calculations have produced valuable insights into dense neutron matter relevant for neutron stars, as shall be discussed in chapter 2.

1.1.2 QCD phase diagram

Color confinement and the spontaneous breaking of chiral symmetry suggest the QCD ground state shall have non-trivial dependencies on the temperature T and baryon chemical potential μ_B. The QCD phase diagram fig. 1.2 nicely summarizes the various possible states of QCD matter. Sadly, though, the labeling of a large landmass particularly towards finite μ_B is mainly based on conjectures.

The gross structures are clear: at low temperatures and baryon chemical potentials,

[3] if were not for the non-perturbative nature of nuclear forces the LECs could have been obtained from analytically matching the EFT to QCD at Λ_χ.

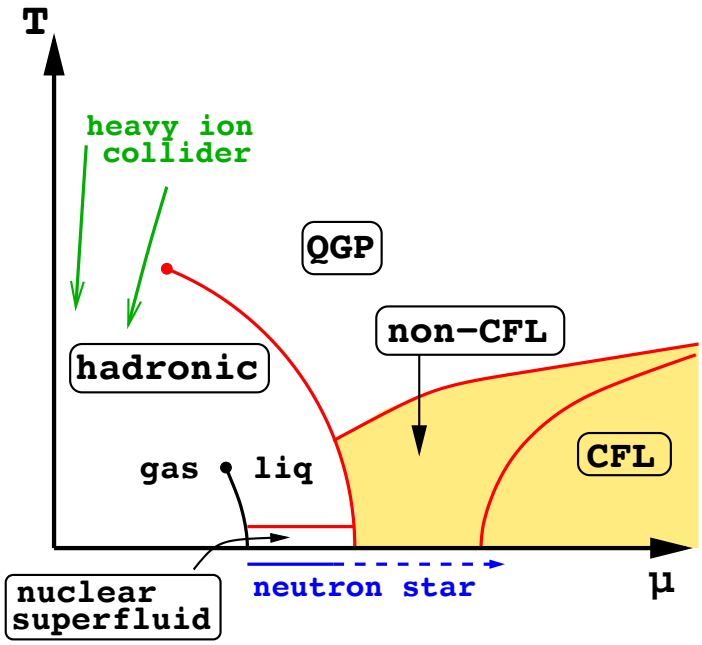

Figure 1.2: The conjectured QCD phase diagram. Figure taken from [21].

hadron gas is the QCD ground state. With increasing T or μ_B, quarks and gluons would eventually deconfine. At $\mu_B = 0$ and asymptotic temperatures, *quark-gluon plasma (QGP)* is the result. We know our universe was briefly in this phase around 13.8 billion years ago. QGP is also produced as small droplets in the heavy-ion collision experiment. The smashing of high Lorentz factor ($\gamma \gtrsim 100$) ions (typically Au or Pb) briefly creates a high temperature environment in which quarks and anti-quarks are produced in pairs in abundance. Densities of quarks and anti-quarks may reach $\sim n_0$, but the net baryon number density $n_B = (n_q - n_{\bar{q}})/3$ is much lower. Although asymptotic freedom suggests perturbation theory should work fine at large T, QGP remains an inherently non-perturbative system owning to static magnetic interactions arising from small-angle quark-quark scatterings mediated by low energy gluons [38].

Near zero temperature and sufficiently large μ_B, the QCD vacuum is characterized by a degenerate quark matter phase. The only place such conditions might be realized is in the

interior of massive neutron stars, where μ_B could reach ~ 2 GeV at the center. Hence in the following discussions on cold and dense QCD we will ignore the heavy c, t, b quarks and focus on the light u, d, s flavors only. At asymptotic baryon chemical potentials all the u, d, s quarks can be treated as massless and weakly interacting. Under these circumstances, the ground state is a color superconductor known as the *color-flavor-locked (CFL)* phase. We will discuss this in detail below.

The tricky part is understanding the phases at intermediate energy scales and figuring out the properties and locations of boundaries separating different phases. Ideally, to study the QCD phase diagram one shall evaluate the grand canonical partition function with Euclidean path integrals

$$\begin{aligned}\mathcal{Z}(T,\mu_B) = \text{tr } e^{-(H-\mu_B N_B)/T} &= \int [\mathcal{D}A][\mathcal{D}\bar{q}][\mathcal{D}q] \\ &\times \exp\left\{\int_0^{1/T} \mathrm{d}\tau \int \mathrm{d}^3x \left[\mathcal{L}_{\text{YM}} + \bar{q}(-\gamma^0\partial_\tau + i\gamma^i\partial_i + i\gamma^\mu A_\mu - m + \frac{1}{3}\mu_B\gamma^0)q\right]\right\} \quad (1.15)\end{aligned}$$

While the non-linear nature of non-Abelian gauge theories precludes a closed-form result, lattice gauge theory [383, 216] provides a powerful non-perturbative probe into QCD. The finite lattice spacing a serves as a UV cutoff, and the finite volume ensures a tractable theory. Lattice gauge theory made explicit use of the fact that gauge fields are connections that define parallel transports

$$U = \mathcal{P}\exp\left[i\int_{\mathcal{C}} A_\mu(x)\mathrm{d}x^\mu\right], \quad (1.16)$$

along arbitrary curves $\mathcal{C}$. Above, $\mathcal{P}$ is the path-ordering operator [it is necessary because of the non-Abelian nature of $SU(N_c)$] and U is known as the Wilson line. From this one may obtain gauge-invariant quantities know as the Wilson loops (holonomies) by taking the integral over closed loops

$$W = \text{tr } \mathcal{P}\exp\left[i\oint_{\mathcal{C}} A_\mu(x)\mathrm{d}x^\mu\right]. \quad (1.17)$$

Discretization onto Euclidean hypercubic lattice is straightforward and the resulting Wilson lines are link fields connecting neighboring lattice sites. The discretized Wilson loop is

obtained by contracting (oriented) links on all four sides of little boxes, leading to plaquettes $W_\Box$. The Yang-Mills action can now be put on lattice since

$$S_{\text{Wilson}} = -\frac{1}{g_s^2}\sum_{\Box}(W_\Box + W_\Box^\dagger) = -\frac{1}{2g_s^2}\int \mathrm{d}^4x\ \mathrm{tr}G^{\mu\nu}G_{\mu\nu} + \mathcal{O}\big(a^5\big)\,. \tag{1.18}$$

After integrating out fermions [4] the grand partition function eq. 1.15 takes the form:

$$\mathcal{Z}(T,\mu_B) = \int [\mathcal{D}U] e^{-S_{\text{wilson}}} \det\left[D(\mu_B) + m\right]. \tag{1.19}$$

The Wilson Dirac operator $D(\mu_B)$ satisfies γ^5-Hemiticity in the absence of μ_B: $D(0) = \gamma^5 D(0)^\dagger \gamma^5$, such that eigenvalues of $D(0)$ come in Hermitian conjugate pairs. Specifically, for any eigenfunction ψ with $D(0)\psi = d_i\psi$, there exists an independent eigenfunction $\gamma^5\psi^*$ with eigenvalue

$$D(0)\gamma^5\psi^* = \gamma^5\gamma^5 D(0)\gamma^5\psi^* = \gamma^5 D(0)^\dagger\psi^* = \gamma^5[D(0)\psi]^\dagger = d_i^*\gamma^5\psi^*.$$

The fermion determinant is therefore real and positive:

$$\det\left[D(0)+m\right] = \prod_i (d_i + m)(d_i^* + m) > 0.$$

This enables a probabilistic interpretation of $e^{-S_{\text{wilson}}}\det\left(D(0)\right)$, hence Monte Carlo integration methods can be used to evaluate $\mathcal{Z}(T,\mu_B = 0)$ with the appropriate choice of integral measure on link variables U (Haar measure) .

Lattice QCD is indeed successful in calculating properties of finite temperature QCD at zero (sometimes small values of) μ_B. Following decades of analytical efforts [85, 170, 176, 177, 199, 376], lattice simulations directly confirm chiral symmetry restoration around $T_c \simeq 150 - 200$ MeV, above which the hadronic gas transitions into QGP. It is also demonstrated that the transition is a smooth cross-over without abrupt changes in the internal energy [97, 159, 131, 144, 143, 132].

---

[4] Putting light fermions on the lattice can be challenging in practice due to the *fermion doubling* problem. Various solutions are available, for a review see [205].

On the finite baryon chemical potential frontier, however, lattice QCD suffers from the fermionic *sign problem* that renders numerical evaluations of eq. 1.19 impossible. At finite μ_B, the Dirac operator does not satisfy the γ^5-Hemiticity but instead $\gamma^5 D(\mu_B)\gamma^5 = D^\dagger(-\mu_B^*)$. Therefore the determinant is no longer real and positive unless μ_B is purely imaginary. Despite tremendous efforts no reliable lattice calculations at interestingly high μ_B have been completed so far.

Perturbative calculations, however, work great for highly degenerate quark matter phases. In contrast to scenarios in the high-temperature QGP, Landau damping and Deybe screening regulate long-wavelength magnetic interactions in the presence of Fermi surfaces [343]. Interesting phenomena arise in this scenario. Cooper instability suggests the Fermi surface is unstable against arbitrarily weak attractive interactions [102]. It is straightforward to show that one-gluon exchange gives rise to attractive interactions in the color anti-symmetric channel ($3 \otimes 3 = \bar{3}_A \oplus 6_S$). Consequently, quarks with opposite momenta near their Fermi surfaces form color-bearing Cooper pairs, leading to color superconductivity.

The fact that quarks carry both color and flavor indices indicates a large number of possible pairing schemes. In the BCS description of superconductivity [34] spin-singlet Cooper pairs are energetically favored. Therefore by Pauli's principle quarks of different flavors (with the same helicity) condense into Cooper pairs. As noted earlier, at asymptotic densities u, d, s flavors effectively have the same mass (massless) and they shall all participate in the pairing. In the resulting CFL *color-flavor locked (CFL)* phase where

$$\langle q_\alpha^i q_\beta^j \rangle \sim \epsilon^{ijA}\epsilon_{\alpha\beta A} = (\delta_\alpha^i \delta_\beta^j - \delta_\beta^i \delta_\alpha^j),$$

the condensate is invariant under a diagonal rotation in the combined flavor and color space, hence the name "locked". Let $SU(3)_C$ denote the color gauge group, the symmetry breaking pattern in the CFL superconducting phase is

$$SU(3)_C \times SU(3)_L \times SU(3)_R \times U(1)_V \to SU(3)_{C+L+R} + Z_2.$$

Therefore, even at asymptotic μ_B the (3-flavor) chiral symmetry remains broken by the

quark-quark condensate. Additionally, the $U(1)_V$ associated with baryon number conservation is also broken, giving rise to a baryon number superfluid.

Although the theoretical case for the CFL phase is solid, it is not clear whether the baryon chemical potential $\mu_B \lesssim 2$ GeV inside neutron stars is sufficient to support such a state. At these lower densities perturbative calculations become less reliable, and the strange quark mass starts to disturb the CFL paring. One possible outcome is the *2-flavor color superconducting (2SC)* phase involving u and d alone. There the 2-flavor chiral symmetry $SU(2)_L \times SU(2)_R$ remains unbroken. Moreover, non-BCS pairings are likely scenarios as well due to electromagnetism and the Weak interaction. Various models have been developed to study this regime. The predictions however are model-dependent and speculative. Eventually baryons consisting of 3 valence quarks take over at sufficiently low μ_B as expected. It remains unclear at what values of μ_B this transition occurs, and if the transition is of first order or not [328, 94]. Or perhaps the quark matter phase does not show up in the neutron star interior at all.

Finally, cousin theories of QCD are also examined to aid in deciphering the QCD phase diagram. These include QCD-like theories in the large N_c limit [257], and gauge-gravity duality [95].

1.2 Dark matter

In 1933, Zwicky attempted to estimate the total mass of the Coma cluster using the Virial theorem [396]. For matter bounded by Newtonian gravitational potentials (fall off as r^{-1}), Virial theorem relates the (time) averaged total kinetic energy $\langle K \rangle$ to the mean total potential energy $\langle V \rangle$ as $2\langle K \rangle + \langle V \rangle = 0$. Assuming galaxies are uniformly distributed within radius R,

$$M_{\text{tot}} \sim R\langle v^2 \rangle.$$

Much to his surprise, the mean velocity of component galaxies inferred from direct measurements of the line of sight velocities suggests the luminosity of the Coma cluster would be at

least a hundred times larger than what is observed if all the inferred mass from the Viral theorem are in the form of luminous matter. Zwicky further noted that modeling uncertainties would only induce corrections of a factor of ~ 10 at the most [397]. The failure to reconcile this discrepancy between luminous mass and gravitational mass led him to the conclusion that the Coma cluster contains "dark matter".

Zwicky was indeed correct. Modern observation and analysis confirmed that dark matter accounts for more than 90% of the mass in the Coma cluster [259]. At the time, however, his reasoning was not quite convincing. For one thing, what if most of the baryonic mass is not in the form of luminous stars? Subsequent works ruled out this possibility. If the missing baryonic matter is in the form of ionized gas, their X-ray emissions would have been observed [108, 187]. Even neutral hydrogen gases can be spotted by 21-cm observations. Further, analysis of stellar evolution suggests that the population of invisible cold dwarf stars is inadequate to explain all the missing mass [187]. Another possibility is that the Coma cluster is not in Virial equilibrium. While this possibility might be difficult to rule out for a particular cluster, as evidence accumulates in similar environments it becomes apparent that this argument cannot apply to all the clusters.

Further evidence is found in measurements of stellar motions in nearby spiral galaxies. In Newtonian dynamics the orbital velocity of stars in the outskirt of a galaxy is determined by enclosed masses $M(r)$ as

$$v(r) \sim \sqrt{M(r)/r}.$$

Since the enclosed visible mass approaches a constant, one would expect $v(r)$ to decrease as $v(r) \sim 1/\sqrt{r}$ towards the edge of the visible galactic disk. It turns out, however, $v(r)$ roughly stays constant near the edge and does not bend over even at distances a few times the size of the visible disk, suggesting additional matter components with $M(r) \sim r$ that dominate galactic masses. Current measurements of galactic rotation velocities are inferred from both optical emissions from luminous stars and the 21 cm radio line from neutral hydrogen gases that extend further out than the visible stellar disk. Flat rotation curves have been observed in a handful of galaxies (see fig. 1.3) [324][325][313, 314][31][281].

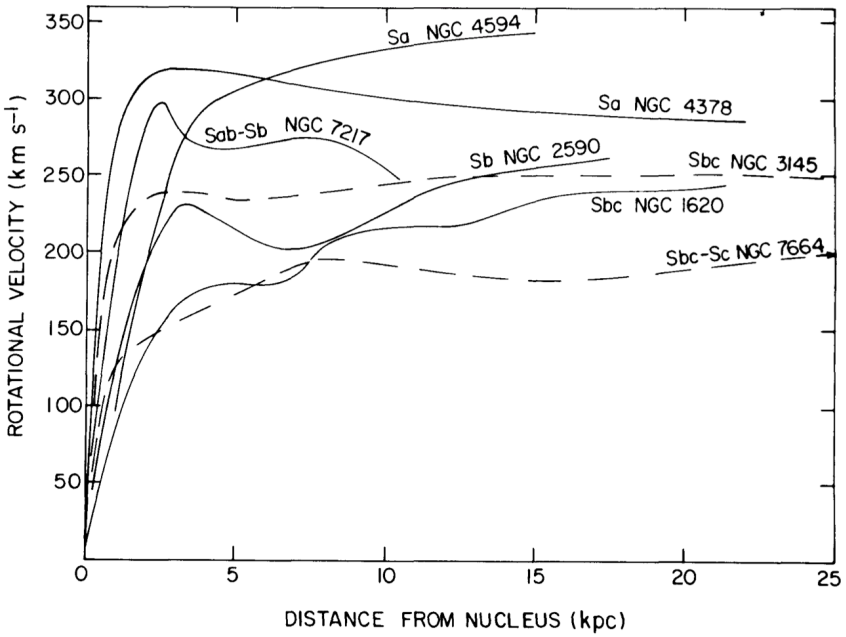

Figure 1.3: Galaxy rotation curves. Figure taken from [324].

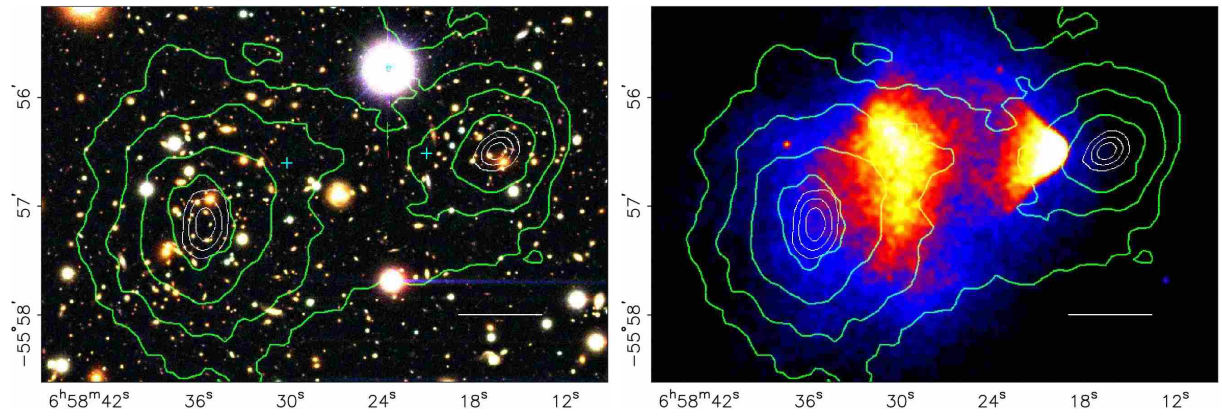

Figure 1.4: The Bullet Cluster. The left panel shows luminous stars observed in the visible band and the right panel shows the hot gases as reveled bt X-ray observations. The green contours show the total mass distribution inferred from gravitational lensing. The white contours are the 1-, 2- and 3-σ error bars on the locations of the centers of mass of the component galaxies. It is evident that the peaks of the mass distribution are not aligned with regions with hot gases. Figure taken from [98].

The Bullet Cluster is another attestation of dark matter. It is the aftermath of a collision between two clusters of galaxies. Luminous stars are mostly unaffected by the collision and maintain their initial trajectories. They become the leading edges in the remnant. On the contrary, intergalactic gases, which accounts for the majority of baryonic contents, are slowed down as they are heated and ionized due to electromagnetic interactions. Their distributions are recognizable from X-ray emissions and clearly lag behind the stars. However, observations (see fig. 1.4) suggest that the bulk part of mass-energy in the remnant is not stored in the hot gases. Through gravitational lensing effects the respective centers of masses of the clusters are revealed to be around the region occupied by visible stars [99, 251], indicating the presence of an invisible weakly-interacting component.

Tracing backwards in time, the ubiquitous and abundant presence of dark matter on galactic scales suggests dark matter should have left observable imprints on the evolution of the universe. In fact, in the standard model of cosmology ΛCDM, cold dark matter is responsible for the formation of cosmic structures we observe and reside in today. In the early universe, clumps of dark matter seeded gravitational potentials to which baryons [5] later fell inwards.

More specifically, the early universe becomes matter (dark matter and baryons) dominated around redshift $z \sim 2700$ and temperature $\sim$ eV, when the energy density of matter (baryons and dark matter) surpasses that of radiations. Non-relativistic ("cold") dark matter particles begin to congregate due to inhomogeneities originated from inflation. As CDM particles gradually collapse into over-density regions the gravitational wells deepen. Baryons, on the contrary, are tightly coupled to photons forming a plasma. Instead of simply sinking into the bottom of gravitational potentials, due to the relativistic photons the baryon-photon plasma sustains a pressure which acts as a restoring force. This competing effect between gravity and the radiation pressure generates sound waves which manifest as oscillations between over-density and under-density regions in the plasma.

---

[5] in cosmology "baryon" refers to both nucleons and charged leptons $e^{\pm}$.

The acoustic oscillation is frozen when photons decouple from the plasma at redshift $z \sim 1100$ and temperature $T \sim 0.1$ eV [6]. Known as the *recombination* epoch, during this time the Thompson scattering can no longer keep photons and electrons in thermal equilibrium in the expanding universe thus electrons recombine with protons and ions to form atoms. Oscillation modes frozen at their peaks (over-densities) or troughs (under-densities) display the largest density and temperature perturbations and they all show up as peaks in the cosmic microwave background (CMB) power spectrum. The first peak near the angular scale $l \sim 200$ reflects the mode with the longest wavelength and corresponds to an over-density perturbation. As we go to higher multiple moments (smaller length scales), peak amplitudes are expected to decrease because photons wash out inhomogeneities on smaller scales when they diffuse out of the baryon fluid at recombination. However, the second and third acoustic peaks are comparable in size, as revealed by the Planck data [13]. This is because dark matter amplifies over-density perturbations (whose extrema correspond to odd number peaks) and does not affect under-density regions. The relative height of the second and the third peak strongly constraints the dark-matter-to-baryon ratio. Analysis of the CMB power spectrum indeed provide the best measurements of matter densities [13]

$$\Omega_c h^2 = 0.1200 \pm 0.0012, \quad \Omega_B h^2 = 0.00237 \pm 0.00015 \tag{1.20}$$

where $h = H/(100\,\mathrm{km/s/Mpc})$ is a dimensionless representation of the Hubble constant H, and Ω_c and Ω_b denote energy densities of cold dark matter and baryons over the critical density $\rho_c = 3H^2/(8\pi) \approx 1.3 \times 10^{-6}$ GeV/cm^3, respectively. Taking $h = 0.68$ [13], we see that dark matter accounts for $\Omega_c \simeq 26\%$ of energy density in the universe.

The necessity of a non-relativistic population of matter components prior to the recombination epoch for the cosmic structure formation was used to exclude (active) neutrinos as a dark matter candidate [393], and is the strongest evidence for cold dark matter (CDM). One of the most appealing CDM candidates is a class of particles known as the weakly in-

[6] the high entropy forbids appreciable populations of neutral atoms to build up at earlier times even when the temperature drops below the binding energies.

teracting massive particles (WIMPs). They arise in many extensions of the standard model whose original motivations are often unrelated to those of dark matter. Most notably, superpartners of particles in the standard model from various supersymmetric extensions to the SM were motivated by the hierarchy problem. For comprehensive reviews see [203, 252]. The lightest supersymmetric states in the resulting doubling of particle spectrum are massive ($m_\chi \gtrsim$ GeV) stable particles hence natural DM candidates. They are thermally produced in the early universe and their relic abundance as explained by a Weak-scale annihilation cross-section agrees well with the observed DM density eq. 1.20, known as the *WIMP miracle*.

In the early universe, WIMPs (denoted by χ's) are kept in equilibrium with the SM thermal bath through $\chi + \bar{\chi} \leftrightarrow X + \bar{X}$, where X may represent any relevant SM species in the bath. If the equilibrium persists to the present day, the WIMP number density is highly suppressed by the Boltzmann factor and is given by

$$n_\chi^{eq} \sim (m_\chi T)^{3/2} e^{-m_\chi/T}.$$

The key for explaining a large Ω_c today is the freeze-out process. WIMPs decouple from the thermal bath when the annihilation ($\chi + \bar{\chi} \to X + \bar{X}$) rate drops below the expansion rate of the universe (the Hubble rate) $\Gamma = n_\chi^{eq} \langle \sigma v \rangle \lesssim H$. Here $\langle \sigma v \rangle$ is the thermally averaged cross-section times velocity. Afterwards, the distribution function of WIMPs ceases to follow its value in thermal equilibrium and the subsequent evolution of DM abundance is solely the result of cosmic expansions.

To accurately account for the WIMP thermal relic density arising from freeze-out, one needs to solve the Boltzmann equation in the expanding universe

$$\dot{n}_\chi + 3Hn_\chi = -\langle \sigma v \rangle (n_\chi^2 - (n_\chi^{eq})^2).$$

Note that the larger cross-section $\langle \sigma v \rangle$ the smaller the relic density, as expected from the argument presented earlier. For a simple estimate one may assume the freeze-out temperature $T_f \sim m_\chi \gtrsim$ GeV and solve for the relic density from $\Gamma \simeq H$. Noting that the universe is still radiation dominated at such high temperatures, the present day relic density can be related

to the cross-section as

$$\Omega_c h^2 \approx 0.2 \left(\frac{T_f/m_\chi}{10}\right)\left(\frac{100}{g_*}\right)\left(\frac{3\times 10^{-26}\ \mathrm{cm}^3/\mathrm{s}}{\langle\sigma v\rangle}\right). \tag{1.21}$$

Above, g_* is the effective number of relativistic degrees of freedom at WIMP freeze-out. This estimation suggests the relic density is achieved assuming Weak scale coupling strengths $\langle\sigma v\rangle \sim G_F^2 m_\chi^2$ for $m_\chi \sim$ TeV. This miraculous agreement between predicted and observed relic density renders WIMP a renowned DM candidate.

However, as mentioned earlier, the WIMP paradigm faces several challenges as N-body simulations employing CDM reveal disagreements with observations over small scale structures. To begin with, simulation seems to over-predict dark matter densities near the center of galaxies. Observations indicate ρ_{DM} is roughly a constant but simulations generally show cusps towards galactic centers [269]. This is known as the "core-cusp" problem; furthermore, the "missing satellites problem" concerns the mismatch of the abundance of dwarf galaxies between simulation and observation: we have not observed nearly as many satellite galaxies as predicted by simulations [273, 268]. While incorporating baryonic feedback effects such as supernova explosions into simulations could alleviate these issues [168, 304], a more likely scenario is that dark matter may not be collisionless [346][365]. If dark matter particles experience sizable self-interactions their scatterings could smoothen small scale clumps and solve small scale puzzles while maintaining agreements between CDM simulations and observations on large scales.

1.3 Neutron stars

Around the time (perhaps even before [388]) Chadwick discovered neutrons in 1932, Landau put forward the possibility of very dense matter in a star forming one gigantic nucleus. The existence of neutron stars is formally predicted by Baade and Zwicky (the same Zwicky who studied the Coma cluster) [28, 29, 30] in their attempt to explain the energy source behind supernova explosions shortly afterwards. It was not until three decades later that the first confirmation of neutron stars arrived. In 1967 Piacini proposed that magnetized spinning

neutron stars could radiate radio waves [285], only a few months before the discovery of pulsar B1919+21 by Bell and Hewish [191]. Since then, over 2000 neutron stars have been observed [357, 249, 279], and we had made considerable progress towards understandings the physics of these "giant nuclei".

1.3.1 life of a neutron star

During the last stage of nuclear burning in heavy stars with $M \gtrsim 10M_\odot$, iron is made via the ignition of neon, oxygen and silicon [7] . At temperature $T \sim 10^9$ K (~ 0.1 MeV) and density $\rho \sim 10^{10}\mathrm{g/cm}^3 \equiv \rho_{10}$ the iron core is stabilized by both electron thermal and degeneracy [$\mu_e \simeq 10(Y_e\rho_{10})$MeV, where $Y_e = n_e/n_B$] pressure. Once the core temperature reaches $T \sim 10^{10}$ K, photo-dissociation $\gamma + {}^{56}_{26}\mathrm{Fe} \rightarrow 13\alpha + 4n$ rapidly depletes high energy photons thereby reduce thermal pressure. As the core starts to contract, the increased density enables rapid electron capture onto nuclei $e^- + {}^A_Z X \rightarrow {}^A_{Z-1} X + \nu_e$ and free protons $e^- + p \rightarrow n + \nu_e$ which reduces the Fermi pressure. The loss of both sources of stabilization further speeds up the contraction, triggering a self-perpetuating implosion.

The collapsing progenitor core is characterized by two decoupled components. The inner core with mass $\sim 0.5M_\odot$ collapses subsonically and homologously ($v \sim r$), whereas the outer core falls inward at supersonic speeds. Due to repulsive short range interactions between nucleons, the collapse of the inner core is halted and reversed when the central density reaches nuclear densities $n_B \sim 1 - 2n_0$. As the subsonic inner core rebounces into the infalling supersonic outer core, a rapidly expanding shock wave is generated at the interface. The shock wave loses energy at a high rate as it disintegrates nuclei (mostly iron group) along its path before stalling at a radius around $r \sim 100 - 200$ km within tens of milliseconds. How to revive the shock is the central piece of the puzzle in the supernovae explosion theory [77, 237, 78, 75]. Although the detailed mechanism is still under debate, neutrinos appear to play

[7] For progenitor stars of solar metalicity in the mass range $8 - 10M_\odot$, an Oxygen-Neon-Magnesium (O-Ne-Mg) core is the end product [278]. In the O-Ne-Mg core the instability is solely caused by electron capture. The core collapse and subsequent evolution, however, proceed almost identically as with iron cores.

a crucial role as simulations suggest they reheat matter behind the shock front [61]. The reinvigorated shock wave then plows through the outer shells (e.g., H, He) of the progenitor star and launches the ferocious explosion with peak luminosity briefly eclipsing that of the host galaxy.

Left behind the shock is a nascent neutron star (proto-neutron star) of mass $M \sim 1.4 M_\odot$, initial radius ~ 20 km, electron fraction $Y_e \sim 0.3$, entropy per baryon $s/n_B \sim 1$ and temperature $T \sim 30$ MeV in the core. In this hot and dense nuclear matter, neutrinos of all flavors and both helicities are produced in abundance. While productions through neutral current interactions (mediated by the Z boson) such as pair production $e^+ + e^- \to \nu_X + \bar{\nu}_X$ and nucleon-nucleon bremsstrahlung $N+N \to N+N+\nu_X+\bar{\nu}_X$ are viable for electron, muon and tau flavors ($X = e, \mu, \tau$), only electron (anti-)neutrinos can be produced via charge current reactions (mediated by $W^\pm$) $n + e^+ \to p + \bar{\nu}_e$ and $p + e^- \to n + \nu_e$.

Subsequent to their production, neutrinos are trapped by the PNS medium at densities $n_B \gtrsim n_0/10$ and temperature $T \gtrsim 5$ MeV. Through diffusion they are transported out of the star on the diffusion time scale $\tau_{\rm diff} \sim 15$ seconds. The μ [8] and τ flavors only participate in neutral current reactions such as scattering off nucleons

$$N + \overset{(-)}{\nu}_X \to N + \overset{(-)}{\nu}_X, \ N = n, p, \tag{1.22}$$

whereas electron (anti-)neutrinos are further trapped via

$$\nu_e + n \to e^- + p, \tag{1.23}$$

$$\bar{\nu}_e + p \to e^+ + n. \tag{1.24}$$

These suggest at sufficiently low densities and temperatures where ν_μ, μ_τ and their anti-particles decouple from the star, ν_e and $\bar{\nu}_e$ are still in equilibrium with baryons, and their decoupling can only occur at lower densities, or equivalently larger radii. Furthermore, in neutron-rich environments the rate for ν_e absorption by neutrons is larger than that of $\bar{\nu}_e$

[8] A small fraction of muons could present in PNS medium under favorable conditions therefore opens up charged current reactions for ν_τ.

onto protons. Hence the ν_e decoupling surface [9] sits outside that of $\bar{\nu}_e$. Since temperature is generally lower further from the core, the average energy of neutrinos emitted at their decoupling surfaces $\langle E_{\nu_e} \rangle \lesssim \langle E_{\bar{\nu}_e} \rangle \lesssim \langle E_{\nu_x} \rangle$. Typical values from simulations are $\langle E_{\nu_e} \rangle \sim \langle E_{\bar{\nu}_e} \rangle \simeq 5 - 10$ MeV whereas $\langle E_{\nu_x} \rangle \simeq 10 - 20$ MeV. Simulations suggest 99% of the total energy released during core-collapse

$$\Delta E \sim M^2(1/R_{NS} - 1/R_{\rm core}) \approx M^2/R_{NS} \sim 3 \times 10^{53} \text{ ergs} \sim 10^{59} \text{ MeV}$$

is carried by neutrinos. This general picture of neutrino production and transport in proto-neutron stars is in agreement with neutrinos detected from supernova SN1987a [63, 81, 193].

The trapping and diffusion of ν_e and $\bar{\nu}_e$ have significant implications for the composition and evolution of PNS. In beta equilibrium, the chemical potentials for neutrons, protons, electrons, and electron neutrinos μ_{n,p,e,ν_e} satisfy

$$\mu_n - \mu_p = \mu_e - \mu_{\nu_e}. \tag{1.25}$$

Near the center $\mu_e \sim 200 - 300$ MeV and $\mu_{\nu_e} \sim 150 - 200$ MeV [76, 80, 311]. This non-zero and large electron neutrino chemical potential corresponds to a large excess of ν_e over $\bar{\nu}_e$, a scenario not realized in other parts of the universe. The electron neutrino chemical potential decreases towards the surface and vanishes near the ν_e sphere. The radial gradient of μ_{ν_e} drives neutrino diffusion and "deleptonizes" the star by pushing the equilibrium $p + e^- \leftrightarrow n + \nu_e$ towards the right hand side. Analogous to Joule (Ohmic) heating in electric circuits, the electron neutrino current furnished by gradients of μ_{ν_e} generates heat and increases the core temperature to around $T \sim 50 - 60$ MeV [76]. Maximum heating is achieved after $\tau_{\rm diff} \sim 20$ s as μ_{ν_e} decreases substantially in the star. The electron fraction is now reduced to $Y_e \sim 0.1$ [311] and gradually decreasing as neutrinos leave and cool the star. Neutrino mean free paths in proto-neutron stars have been studied in detail [296, 307, 312].

---

[9] Neutrino sphere is only a crude notion. Since neutrino-nucleon cross-sections are sensitive to the incoming neutrino energy, the decoupling of neutrinos of different energies does not take place at the same location.

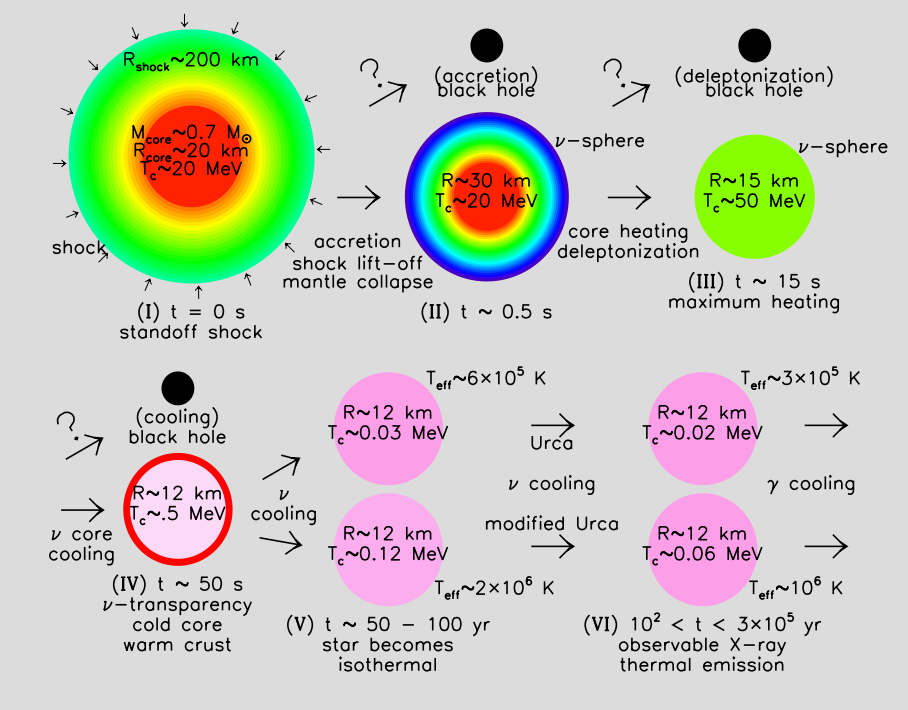

Figure 1.5: Evolution of proto-neutron stars. Figure taken from [231]

Deleptonization comes to an end once the temperature drops below $\sim$ MeV. Now the star becomes transparent to neutrinos, and the radius of PNS settles down to around $\sim$ 12 km. Nucleons near the edge of the star are now bonded into nuclei. Known as the crust, this portion of neutron stars may extend up to $\sim$ 2 km below the surface. Starting from ^{56}Fe at the surface, heavier isotopes of increasingly high n-to-p ratios such as Ni, Kr, Se gradually populate the crust as we dive into the star. At densities around $n_B \sim 10^{-3} n_0$ neutrons drip outside nuclei and form a degenerate Fermi sea. This mixed phase persists all the way to around $n_B \sim n_0/2$, where a transition to homogeneous nuclear matter occurs. Chapter 2 will further expound on neutron star crusts.

At this stage the nucleon Fermi energies are far greater than the temperature therefore thermal effects become negligible. The star is usually referred to as a cold neutron star for temperature $T \lesssim 10^9$ K.

Subsequent PNS evolution is characterized by neutrino cooling. One channel is the *(direct) URCA* processes

$$\begin{aligned} p + e^- &\to n + \nu_e, \\ n &\to p + e^- + \bar{\nu}_e. \end{aligned}$$

In neutron-rich dense nuclear medium the kinematics mandates $k_{F,e} + k_{F,p} \gtrsim k_{F,n}$, or equivalently the proton fraction $x_p = n_p/n_B \gtrsim 0.1$, for direct URCA processes to proceed. While the proton fraction may exceed 1/10 at high densities $n_B \gtrsim 5n_0$, it is below the threshold around $n_B = n_0$ assuming nucleonic degrees of freedom. Under these circumstances, participation of spectator nucleons is required to conserve energy and momentum simultaneously. The result is modified URCA processes

$$\begin{aligned} e^- + p + N &\to n + N + \nu_e, \\ n + N &\to p + N + e^- + \bar{\nu}_e. \end{aligned}$$

Modified URCA processes are significantly slower than their direct counterparts as is evident from dimensional analysis for the emissivity (energy loss per unit volume per unit time) : $\dot{\mathcal{E}}_{\text{direct}} \sim T^6$ whereas $\dot{\mathcal{E}}_{\text{modified}} \sim T^9$. Deviation from the standard picture might be indications for exotic phases inside NS [69].

Surface blackbody photon emission takes over once the temperature drops below $T \sim 10^6$ K. Without active nuclear burning, isolated neutrons gradually fade out. Most old neutron stars are believed to be too cold to be observed. As shall be seen, however, the existence of old NS puts strong limits on certain dark matter models.

1.3.2 structure

The hydrostatic equilibrium of spherically symmetric stars in general relativity was first tackled by Tolman and by Oppenheimer and Volkov independently [282, 364]. They arrived at what is now known as the *Tolman-Oppenheimer-Volkoff* equations:

$$\begin{aligned} \frac{\mathrm{d}p(r)}{\mathrm{d}r} &= -\left[p(r)+\mathcal{E}(r)\right]\left[\frac{M(r)}{r}+4\pi r^2 p(r)\right]\left[r\Big(1-\frac{2M(r)}{r}\Big)\right]^{-1}, \\ \frac{\mathrm{d}M(r)}{\mathrm{d}r} &= 4\pi r^2 \mathcal{E}(r). \end{aligned} \tag{1.26}$$

If a relation between pressure p and energy density $\mathcal{E}$ is specified, solutions to the TOV equations uniquely determine the stellar radius R (defined implicitly via $p(r=R)=0$) and mass $M=M(r=R)$ for compact stars of given central pressure p_c.

The task of determining neutron star global structure then rests on obtaining the function $p(\mathcal{E})$, or the equation of state (EOS), of dense nuclear matter [10]. As discussed earlier, this is a difficult problem with many undergoing efforts working from different angles, including potential models [17], relativistic mean-field approaches [331, 332, 373, 374], Skyrme type models [126, 323], and the most promising χEFT-based calculations [226, 317, 385]. While some justifications can be made below $n_B \sim 2n_0$, all are speculations at best in the high density region $n_B \gtrsim 2n_0$.

A crude but powerful classification of EOSs is based on their predicted pressures at given energy densities. An EOS is loosely referred to as "soft" ("stiff") if it supports low (high) pressures. Because densities inside neutron star interior span several orders of magnitude, and short-, intermediate- and long-range nuclear forces exhibit different behaviors, this nomenclature generally assigns density-dependent labels to EOSs. For example, an EOS could start as soft at low densities, then turns stiff, and so on. Typically, stronger or increasingly stronger (with increasing density) repulsive interactions result in stiffer EOS. Underlying microphysical degrees of freedom can be a crucial factor [326, 327][204, 258], too.

---

[10] In general $\rho(p,T)$, but as discussed earlier matter in neutron stars becomes highly degenerate when $T \lesssim$ MeV shortly after birth.

An important model-independent constraint on how stiff an EOS can be comes from causality: the isentropic sound speed squared C_s must be less than the speed of light (squared)

$$C_s = \left(\frac{\mathrm{d}p}{\mathrm{d}\mathcal{E}}\right)_s \leq 1. \tag{1.27}$$

Other requirements on EOS from thermodynamics along with a few popular and light-weighted EOSs are summarized in appendix B.

By varying p_c, solutions of the TOV equations for a given EOS trace a curve in the mass-radius plane. Universal to predictions of all physical EOSs (satisfy causality) is the existence of maximum mass. A heuristic way of understanding this is by turning to the Newtonian "gradients of pressure balance gravity" picture [11]. Since energy sources gravity, the higher the pressure the higher the masses an EOS can support. But the rate at which pressure can increase with energy density is bounded by causality eq. 1.27. The upshot is that gravity always wins, and all physical neutron star EOS are bound to produce neutron stars of mass $\lesssim 3M_\odot$. This line of reasoning also suggests stiffer equations of state would produce more massive stars. Therefore the observation of heavy neutron stars could rule out EOS models that are too soft. This is usually known as the maximum mass constraint. A similar connection between EOS and observables also applies to radii. The stiffer the EOS, the larger the radii it predicts.

The correspondence between compact star structure and underlying nuclear physics EOS suggests astrophysical measurements of M or R or even better M and R could provide valuable information about the microscopic properties of dense nuclear matter.

Appendix A.1 contains a collection of topics related to TOV equations. Effects of spin have been studied extensively [178, 180, 179, 351, 288, 101] and it is found that maximum mass may increase up to 30% for fastest rotating stars close to break-up; Magnetic fields encountered in magnetars may impact neutron stars structure noticeably if $B \gtrsim 10^{12}$ T [86]; Finally, tidally deformed configurations relevant for binary neutron star (BNS) mergers will

[11] the Newtonian treatment is in fact a reasonably good approximation for qualitative arguments; see appendix A.1.1.

be discussed later.

1.3.3 traditional measurements

Radio pulsars constitute the majority of neutron stars detected so far. Their reliable and periodic signals provide an accurate timing mechanism. As will be discussed below, pulsar timing has already successfully produced a handful of accurate pulsar mass measurements. Due to radio emissions, the period P is not expected to be constant, though. The *spin-down* rate $\dot{P}/P$ can be used to estimate pulsar ages. Since the energy is lost in the form of electromagnetic radiation, the pulsar spin-down rate also yields estimates for the pulsar magnetic dipole field. A few pulsars are observed to exhibit *glitches*, which are the likely result of angular momentum transfer in the crust from superfluid components to the normal phase [23, 242].

1.3.4 mass

It is well-known since Newton that stellar masses can be in principle determined from classical mechanics if the star is in binary systems (or in the same spirit, has planets). The same principle holds for pulsars in binaries as well. The radio pulse profile is affected by orbital modulations and can be used to determine the binary orbit. However, Keplerian orbital parameters inferred from Newtonian dynamics are usually degenerate. The binary orbit period $P_{\rm orb}$ and the pulsar radial orbital velocity measured from time variations of pulse arrival time specifies the combination

$$f_1(M_1, M_2) = \Omega^2 (a \sin i)^3 = \frac{(M_1 \sin i)^3}{M_1 + M_2} \tag{1.28}$$

known as the mass function (of star 1, here refers to the pulsar). Above, $\Omega_{\rm orb} = 2\pi/P_{\rm orb}$, a is the semi-major axis, i is the inclination angle ($i = \pi/2$ corresponds to an edge-on orbital plane), $M_{1,2}$ are masses of the pulsar and its companion, respectively. This only provides a lower bound on M_2 since $M_2 \geq f_1$ therefore does not resolve the binary. While the inclination

angle i or the mass ratio may be obtained independently from other measurements in very limited cases, such degeneracy cannot be lifted in most binary systems.

General relativistic effects come in handy. First off, compact binary systems emit gravitational waves. The resulting orbital decay is given by

$$\dot{P}_{\rm orb} = -\frac{192\pi}{5}(2\pi)^{5/3}(1-e^2)^{-7/2}\left(1+\frac{73}{24}e^2+\frac{37}{96}e^4\right)\frac{M_1M_2}{(M_1+M_2)^{1/3}} \tag{1.29}$$

where e denotes the eccentricity of the binary orbit. Secondly, time dilation of the pulsar signal owning to the combination of Doppler effects and gravitational redshift is

$$\gamma = e\Omega_{\rm orb}^{-1/3}\frac{(M_1+2M_2)M_2}{(M_1+M_2)^{4/3}} \tag{1.30}$$

Thirdly, the advance of periastron angle ω is given by

$$\dot{\omega} = 3\Omega_{\rm orb}^{5/3}(M_1+M_2)^{2/3}(1-e^2)^{-1}. \tag{1.31}$$

Lastly, for sufficiently large orbital inclination angle, Shapiro delay [335] also applies when radio pulses emitted by the pulsar pass near its companion before reaching Earth.

To date, pulsar timing has produced accurate mass measurements for around 40 neutron stars [233]. The most massive ones are found to be around $2M_\odot$ and are listed in table 1.1. Their existence put stringent constraints on neutron star EOS, as noted earlier. Measurements of so-called "black widow" pulsars yielded $2.74\pm0.12M_\odot$ for PSR B1757+20 [368] and $2.68\pm0.14M_\odot$ for PSR J1311-3430 [319, 318]. Instead of using relativistic post-Keplerian orbital dynamics these measurements infer the inclination angle from orbital brightness variations of the low mass ($M \lesssim 0.1M_\odot$) companion, which is bloated and strongly irradiated by the pulsar. The deduced masses, however, are prone to large unknown systematic uncertainties associated with the observed light curve, and may well be as low as $1.6-1.8M_\odot$.

1.3.5 radii

While the miniature size of neutron stars makes point particle orbital dynamics particularly accurate in extracting NS masses using pulsar timing, it poses great challenges for radii

pulsar	J1614-2230 [118]	J0348+0432 [25]	J0740+6620 [104]	J1810+1744[320]
mass ($M_\odot$)	1.97 ± 0.04	2.01 ± 0.04	$2.14^{+0.10}_{-0.09}$	2.13 ± 0.04

Table 1.1: Massive pulsars around or above $2M_\odot$ observed so far. The quoted bounds are 1-σ intervals.

measurements. One major effort focuses on extracting radii from the neutron star surface blackbody radiations. Isolated NS or NS actively undergoing transient accretion are the cleanest targets. In the latter case the binary in which the pulsar resides is often called *quiescent low-mass X-ray binary (qLMXB)*. Assuming the emission comes from a spherically symmetrical star, if the flux F and apparent effective temperature $T_{\text{eff},\infty}$ can be extracted from the observed emission spectrum (which for most cases falls in the soft X-ray band), and the NS mass M and the distance D is known, the radius can be obtained from

$$R^2 = \Big(1 - \frac{2M}{R}\Big)\frac{FD^2}{\sigma_{\text{S}} T_{\text{eff},\infty}} \tag{1.32}$$

where σ_S is the Stefan-Boltzmann constant, and the factor $1 - 2M/R$ accounts for redshifts due to gravitational potentials of the emitting NS.

However, this method suffers from a variety of unknown systematic uncertainties. Most notably, extraction of the effective temperature $T_{\text{eff},\infty}$ is shown to be sensitive to magnetic field configurations and compositions of the NS atmosphere. For example, even if assuming strong B fields are absent, inferred radii based on the same data disagrees by 50% depending on whether a Hydrogen or Helium atmosphere model is used [87, 333, 188]. The (poorly-known) ambient astrophysical environment is another source of systematic. The stellar medium could significantly affect the observed X-ray spectrum leading to large dependence of inferred radii on the modeling of interstellar absorptions. Finally, time-varying spectra are observed in a few NS, suggesting non-thermal components may be polluting the signal [172, 188]. This might even be the case for data not displaying time variations since non-axisymmetric magnetic emissions could be disguised as thermal components if the magnetic

dipole roughly aligns with the spin axis [228, 229].

A promising improvement has been proposed and is the underlying principle for analyzing data from current and planned missions such as the Neutron Star Interior Composition Explorer (NICER). Using synthetic data it was demonstrated that systematic errors are minimized if additional rotational phase data are available and fitted as a reference [266]. Usually, this information comes from modulated emission of surface hot spots [265, 266, 272, 291]. Two measurements are made so far: $R = 13.02^{+1.24}_{-1.06}$ km and $M = 1.44^{+0.15}_{-0.14} M_\odot$ for J0030+0451 [262] and $R = 13.7^{+2.6}_{-1.5}$ km for J0740+6620 [263] (mass is obtained independently from pulsar timing listed in table 1.1). While still compatible with χEFT-base predictions, these radii are on the larger side. This tension might hint at other unknown systematic errors.

Millisecond pulsars could potentially put a bound on the allowed NS radius if their mass is known. Assuming Newtonian gravity, the mass-shedding limit for a uniform density solid ball is

$$R_{\max} = \left(\frac{MP}{2\pi}\right)^{2/3} \approx 16 \text{ km} \left(\frac{M}{M_\odot}\right)^{1/3} \left(\frac{P}{1 \text{ ms}}\right)^{2/3}$$

Note that R and M are those for the un-deformed star. This estimation is shown to be accurate within 20% in fully relativistic simulations employing physical EOSs [175, 142, 234].

Finally, the newly available gravitational wave detection from binary neutron star mergers could also constrain neutron star radii, as shall be discussed below.

1.3.6 gravitational wave probes

While observations of the Hulse–Taylor binary pulsar system indirectly confirmed gravitational radiations [200, 358], it was not until GW150914 [2] that we directly detected gravitational waves for the first time. Nowadays, instead of a mere test for general relativity, observations of gravitational waves from binary neutron star mergers such as GW170817 can further assist in understanding compact star structures and composition.

propagation and detection of GWs

Analogous to wave-like solutions to the vacuum Maxwell's equation, gravitational waves are propagating perturbations of the spacetime itself as predicted by general relativity [127]. Because gravity is the weakest interaction among the four known forces, these spacetime ripples are small in size, enabling perturbative frameworks that work very well for most astrophysical applications. To demonstrate the basic principles we restrict to the leading order of the field equation $G_{\mu\nu} = 8\pi T_{\mu\nu}$. Assuming small deviations h from the Minkowski background $\eta_{\mu\nu}$, the full metric can be decomposed as

$$g_{\mu\nu} = \eta_{\mu\nu} + h_{\mu\nu}. \tag{1.33}$$

Although the 4×4 symmetric tensor $g_{\mu\nu}$ contains 10 degrees of freedom, most of them are redundancies associated with the diffeomorphism exhibited in general relativity. Metrics related to each other via arbitrary infinitesimal coordinate transformations $x^\mu \to x^\mu + \xi^\mu$ describe the same spacetime geometry. This reparameterization invariance is similar to the local gauge symmetry in Maxwell's and Yang-Mills theories.

After imposing the Lorenz gauge $\partial^\mu h_{\mu\nu} - \frac{1}{2}\partial_\nu h = 0$ where $h = h^\mu{}_\mu$ is the trace, the linearized equation takes the form

$$\Box \bar{h}_{\mu\nu} = -16\pi T_{\mu\nu}, \tag{1.34}$$

where $\bar{h}_{\mu\nu} = h_{\mu\nu} - \frac{1}{2}\eta_{\mu\nu}h$ is the trace-reversed perturbation, and $\Box = \eta_{\mu\nu}\partial^\mu\partial^\nu$ since at linear order covariant derivatives reduce to ordinary partial derivatives. Note that in terms of $\bar{h}$ the Lorenz gauge imposes $\Box\bar{h}_{\mu\nu} = 0$ and is in analogy to $\partial_\mu A^\mu = 0$ in electromagnetism.

To find the vacuum wave solutions we set the stress-energy tensor $T_{\mu\nu} = 0$. Only two independent propagating modes can be identified from the above weak-field equation. They are purely spatial and their amplitudes can be expressed in terms of traceless tensors. Align the z-axis with the direction of propagation such that $k^\mu = (\omega, 0, 0, k)$, the two polarization

modes ($h_{+,\times}$) are

$$||h_{\mu\nu}|| = \begin{pmatrix} 0 & 0 & 0 & 0 \\ 0 & h_+ & h_\times & 0 \\ 0 & h_\times & -h_+ & 0 \\ 0 & 0 & 0 & 0 \end{pmatrix} e^{ik^\mu x_\mu}. \tag{1.35}$$

Together with the Lorentz gauge (which implies $k^\mu h_{\mu\nu} = 0$) the conditions $\bar{h}_{0\mu} = \bar{h}^\mu{}_\mu = 0$ are known as the transverse-traceless gauge and indeed lead to $10-4-4 = 2$ degrees of freedom. The wave equation suggests $k^\mu k_\mu = 0$, i.e., gravitational waves travel at the speed of light hence $k = \omega$. The $h_{+,\times}$ polarizations can be visualized by considering their effects on a ring

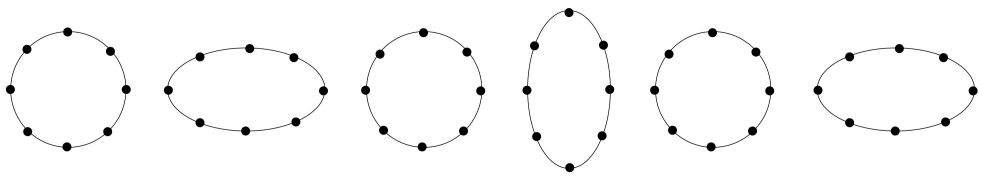

Figure 1.6: Effects of the "plus" polarization on a ring of test masses placed in the plane perpendicular to the propagation direction.

of test masses. By the equivalence principle isolated test particles simply follow geodesics in the perturbed geometry and cannot feel the effect of passing gravitational waves. Relative motions between neighboring observers characterized by geodesic deviations, however, are disturbed by GWs. For example, effects of the + mode in eq. 1.35 is shown in fig. 1.6.

Motivated by the tensorial distortion patterns, interferometers are conveniently proposed to detect gravitational waves. It essentially simplified the ring of test masses to two perpendicular arms. Assuming the arms are perpendicular to the direction of propagation, the maximum relative arm length differences encode GW amplitudes as $\frac{\Delta L}{L} = |h|/2$. Known as the *strain*, this is a tiny number for currently known sources (because gravity is weak). As shall be discussed below, for GWs expected from compact binary mergers $h \lesssim 10^{-21}$. The current LIGO detectors have arm lengths $L = 4$ km, and the planned Einstein telescope

is designed to have $L = 10$ km [299]. Future space-based observatories will be equipped with larger arm lengths, such as the astronomical size $L = 2.5 \times 10^6$ km proposed for the LISA project [22]. It indeed takes engineering miracles to detect such tiny variations. However, it is noteworthy that the ability to directly detect GW amplitudes (which fall off as $1/D$ at large distances from the source) instead of *intensities* (which fall off as $1/D^2$) may compensate for the weak signals and renders GW a powerful probe compared to traditional electromagnetic observations in certain scenarios.

GWs from compact binary systems

The presence of matter fields makes it tricky to solve even the linearized field equations. When coupled to matter the perturbed metric $h_{\mu\nu}$ would not assume the transverse-traceless form in general since $T_{\mu\nu}$ does not. One approach is to directly solve the fully nonlinear field equations numerically. Numerical relativity can now simulate GW emissions from merging relativistic binaries reasonably well but at great computational costs. On the analytical front, one may still achieve controlled calculations under further approximations. For compact binary inspirals a common assumption made is that the source moves slowly (both internally and as a whole) in addition to the weak-field approximation eq. 1.33. This is the *post-Newtonian (PN)* approximation, in which the (dimensionless) velocity v is the expansion parameter [12].

The leading order behavior in the PN expansion is obtained from Newtonian treatments of $T_{\mu\nu}$. It assumes the radiation travels faster than the component velocities of the source, and that the GW wavelength $\lambda_{\rm GW} \gg r$ is much larger than the size of the source r. Using the standard retarded Green's function method, the radiation from an isolated source can be arranged through multiple expansions in the radiation zone ($D \gg \lambda$) where D is the distance to the source.

[12]It is noteworthy that although the slow-moving assumption does not appear to be valid in compact binary mergers, predictions of the PN framework are found to be in good agreement with those from numerical relativity.

Because the monopole (energy) and dipoles of both electric and magnetic types (linear and angular momenta) are conserved, the quadruple moment Q_{ij} is the first term in the series that can radiate. The quadruple radiation formula reads

$$\bar{h}_{ij} = -\frac{2}{D}\frac{\mathrm{d}^2 Q_{ij}}{\mathrm{d}t^2}. \tag{1.36}$$

For a binary neutron star system with reduced mass $\mu = M_1 M_2/(M_1 + M_2)$ and orbital separation r in the x-y plane (orbital plane), the strain is given by

$$|h| \simeq \frac{4\mu\omega_{\rm orb}^2 r^2}{D} \approx 10^{-23}\left(\frac{\mu}{M_\odot}\right)^2\left(\frac{r}{50\ \mathrm{km}}\right)^{-1}\left(\frac{D}{100\ \mathrm{MPc}}\right)^{-1}, \tag{1.37}$$

where $\omega_{\rm orb} = \sqrt{4\mu/r^3}$ is the orbital frequency following from Keplerian analysis. As noted earlier the GW amplitude is indeed tiny.

The emitted GW carries away orbital energies, which causes orbital decay. At this order the effect was shown in eq. 1.29. It is convenient for GW data analysis to express the orbital decay in terms of the rate of change of GW frequencies. The rapid rising in GW frequency is known as the "chirp" and is given by

$$\frac{\mathrm{d}f_{\rm GW}}{\mathrm{d}t} = \frac{96}{5}\pi f_{\rm GW}^2\left(\pi\mathcal{M}\right)^{5/3}, \quad \text{with } \mathcal{M} = \frac{(M_1 M_2)^{3/5}}{(M_1+M_2)^{1/5}}. \tag{1.38}$$

assuming circular orbits[13]. Above $\mathcal{M}$ is known as the chirp mass. The chirp becomes most noticeable during late stages of the inspiral when separations between component stars are comparable to the stellar size. Existing LIGO observations of compact binary mergers can indeed measure chirp masses incredibly well (with sub-percent uncertainties) just from hearing the chirp [2, 4].

Tidal deformability and gravitational waves

While the black hole no-hair theorem suggests that GWs emitted from binary black hole systems only depend on the masses $M_{1,2}$ and spins $J_{1,2}$ [14], the wave train coming from

[13]GW has a braking effect near periapsis that diminishes eccentricity during binary evolution.

[14]BHs formed from stellar collapses are expected to be electrically neutral.

mergers involving neutron stars contains additional information about the structure of NSs. During the late stage of compact binary inspirals, finite-size effects leave discernible imprints on GW emissions when the separation between component stars becomes comparable to the size of NSs. Component neutron stars develop quadruple moments $\mathcal{Q}_{ij}$ in response to the tidal field $\mathcal{E}_{ij}$ sourced by their companions. At the leading order the response is linear $\mathcal{Q}_{ij} = -\lambda \mathcal{E}_{ij}$. The dimensionful quantity λ dubbed *tidal deformability* is often written as $\lambda = \frac{2}{3} k_2 \ R^5$ where k_2 is a dimensionless quantity known as the tidal Love number and depends on the internal structure of the object [244]. The strong sensitivity on the compact star radii through R^5 suggests that extracting λ from GW observations could constrain the neutron star size independently from EM observations.

The evolution of inspirals involving tidally deformed neutron stars is almost dissipationless and adiabatic since the viscosity is small [62]. In this limit, stellar quadruple deformations are forced harmonic oscillators driven by the tidal fields at frequency $\omega_{\rm GW} = 2\omega_{\rm orb}$. Hence these deformations add coherently to the orbital quadruple moment thereby enhancing GW emissions and accelerating the inspiral. For circular orbits the phase shift of GW due to the tidal effect is given by

$$\delta\Psi = -\frac{117}{256} v^5 \frac{M}{\mu} \ \tilde{\Lambda} \,,$$

where

$$\tilde{\Lambda} = \frac{16}{13} \frac{(M_1 + 12M_2) M_1^4 \Lambda_1 + (12M_1 + M_2) M_2^4 \Lambda_2}{(M_1 + M_2)^5} \,,$$

is the relevant measure of the tidal deformability of the BNS system [136]. Here M_i and $\Lambda_i = \lambda_i / M_i^5$ are the masses and dimensionless tidal deformabilities of component stars, $M = M_1 + M_2$ is the total mass, μ is the reduced mass, and $v = (\pi M f_{\rm GW})^{1/3}$ the orbital velocity. Although tidal effects change the phase only at the 5th order in the post-Newtonian expansion, corrections at this order from point-particle general relativistic dynamics are expected to be significantly smaller for NSs with low spins [136]. The calculation of λ and k_2 for relativistic stars was first performed in [192] and is summarized in appendix A.2.

Analysis of GW from the binary neutron star merger GW170817 already put constraints

on $\Lambda_{1.4}$ [5, 8, 114]. In chapter 2 we will construct a new family of EOS from χEFT-based pure neutron matter calculations and examine the constraining power of future LIGO detections under the LIGO designed sensitivity.

Chapter 2

CONSTRAINING THE NEUTRON-MATTER EQUATION OF STATE WITH GRAVITATIONAL WAVES [1]

We show how observations of GWs from binary neutron star (BNS) mergers over the next few years can be combined with insights from nuclear physics to obtain useful constraints on the EOS of dense matter. In particular, the neutron-matter EOS between 1 and 2 times the nuclear saturation density $n_0 \approx 0.16\,\mathrm{fm}^{-3}$ can be constrained to within 20%, given the simulated data from about 15 merger events. Using Fisher information methods, we combine observational constraints from simulated BNS merger events drawn from various population models with independent measurements of the neutron star radii expected from x-ray astronomy (the NICER observations in particular) to directly constrain nuclear physics parameters. To parameterize the nuclear EOS, we use a different approach, expanding from pure nuclear matter rather than from symmetric nuclear matter to make use of recent QMC calculations. This method eschews the need to invoke the so-called parabolic approximation to extrapolate from symmetric nuclear matter, allowing us to directly constrain the neutron-matter EOS. Using a principal component analysis, we identify the combination of parameters most tightly constrained by observational data. We discuss sensitivity to various effects such as different component masses through population-model sensitivity, phase transitions in the core EOS, and large deviations from the central parameter values.

2.1 Introduction

Recent articles that followed the discovery of GW170817 have shown that upper bounds on the dimensionless tidal deformability $\Lambda = \lambda/M^5$ of the neutron stars obtained from

[1] this chapter is based on the published work [138].

gravitational wave data analysis provide constraints on the EOS of dense matter encountered inside neutron stars [113, 359, 8]. This is a great opportunity and challenge for several reasons: neutron-rich matter, although relevant for many applications, is not easily accessible in experiments, while theoretical approaches require solving the difficult quantum many-body problem and lack a precise characterization of the underlying interactions. Observational constraints provide an anchor for nuclear theory in this uncertain regime, allowing one to extrapolate low-density and symmetric properties of nuclear matter to significantly improve constraints on neutron-rich matter at higher densities.

In this chapter we discuss how we can extract more detailed information about the properties of dense neutron-rich matter and neutron stars during the next few years with more GW detections and measurements of neutron star radii expected from x-ray astronomy, and highlight the importance of an informed parameterization of the dense matter EOS. We make the reasonable assumption that all neutron stars are described by the same EOS. Further, modern nuclear Hamiltonians based on chiral effective field theory provide a systematic momentum expansion of two- and many-body nuclear forces. This, combined with advanced computational methods to solve the nonrelativistic quantum many-body problem, now allows us to calculate the EOS of pure neutron matter up to nucleon number density $n_c \approx 2n_0$, where $n_0 = 0.16$ nucleons per fm^3 is the average nucleon density inside large nuclei (corresponding to a mass density $\rho_0 \simeq 2.7 \times 10^{14}\,\mathrm{g/cm^3}$) [360]. Interestingly, there is a convergence of different ab initio methods based on realistic microscopic Hamiltonians that account for two and three neutron forces [152, 151, 148, 147]. These calculations suggest that the functional form of the EOS of pure neutron matter in the density interval $0.5n_0$ to $2n_0$ is well determined. We use this information to parameterize the EOS and show how it helps with the analysis of multiple BNS detections and provide tighter and more useful constraints for dense matter physics. In turn, these constraints for the EOS of pure neutron in the density interval where calculations are feasible will provide new insights for nuclear physics.

Our study differs from earlier work in the following aspects:

- We incorporate insights about neutron-rich matter obtained from nuclear physics by implementing a new parameterization of the nuclear equation of state and identify parameters that can be best constrained by GW observations.

- We quantify how constraints on these parameters and on the pressure of neutron matter in the density interval n_0 to $2n_0$ will improve with the number of detections.

- Our analysis uses a numerical relativity based tidal waveform model.

- We study the effect of different population synthesis models on the accuracy with which EOS parameters can be measured with GWs and use several thousand binary neutron star source simulations to assess errors in EOS parameter measurements.

- While a nearby event like GW170817 at LIGO design sensitivity would significantly constrain the properties of neutron matter, we show that similar constraints can be obtained from about 15 events beyond 100 Mpc.

We begin with a summary of our results in section 2.2, then describe how we have parameterized the dense matter EOS in section 2.3. In section 2.4 we discuss how we obtain constraints from the gravitational waveform of simulated merger events. Finally, we discuss details of the method we use to obtain these constrains in section 2.6.

2.2 Results

Our main result is that even a handful of GW observations of BNS mergers will provide the most stringent constraints on the low-temperature equation of state of dense neutron matter in the density interval between $n_0 - 2n_0$. This is summarized in fig. 2.1, which shows how the constraints on the pressure of pure neutron matter $P_n(n_n)$ improve as a function of additional NICER or LIGO observations. We start from the errors listed in table 2.1, which, for the purposes of this analysis, we interpret as uncorrelated 1σ normal errors for the parameters. This gives the upper dotted line labeled “Nuclear”.

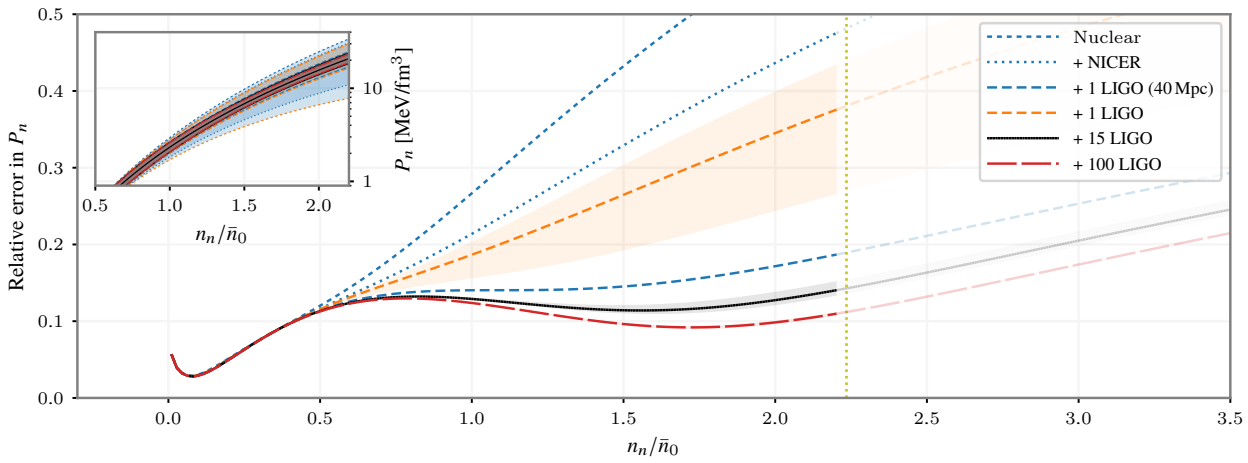

Figure 2.1: Relative constraints on the pressure of neutron matter $P_n(n_n)$ from $N_{\text{obs}} \in \{1, 15, 100\}$ simulated merger events, and expected constraints from NICER (J0437) [264] ($M = 1.44(7)M_\odot$, $\delta R/R = 0.1$). From top: Constraints from nuclear theory augmented by NICER, from a single merger event at $D = 40\,\text{Mpc}$ with LIGO sensitivity, then various N_{obs} LIGO events drawn from `SubSolarA` model that are uniformly distributed within the volume spanned by $D \in [100\,, 400\,]\text{Mpc}$. The shading shows the range of sampling errors (1σ or 68th percentile) demonstrating variation within the `SubSolarA` population model [122]. Beyond the vertical yellow line, we use the core EOS. Inset: $P_n(n_n)$ with 1σ error bands corresponding to each of the constraints.

To this, we add the following constraints:

- Constraints from a simulated binary with similar masses and distance $D \sim 40\,\text{Mpc}$ to GW170817 but at LIGO design sensitivity.

- GW observations at LIGO design sensitivity of $N_{\text{obs}} \in \{1, 15, 100\}$ distant $D \in [100\,, 400\,]\text{Mpc}$ simulated merger events from population model `SubSolarA` as described in section 2.4. To estimate the variance possible within the population model, we sample 500 different populations, each containing N_{obs}, and plot the 1σ (68th percentile) error bands as

shaded regions.

- An uncorrelated mass and radius measurement of J0437 projected to be measured at a 5% level from NASA's NICER mission – i.e. $1.44(7)M_\odot$ with a 10% measurement of R [261, 264].

This analysis demonstrates several key points: A nearby event such as GW170817 is comparable to a dozen or so events from $D \geq 100\,\mathrm{Mpc}$. The NICER constraints are comparable to a single LIGO observation from a distant population sample having low signal-to-noise ratio (SNR), however, nearby or multiple accumulated LIGO events yield significant improvement. After about $N_{\mathrm{obs}} = 15$ observations, we observe rather limited improvement from additional $N_{\mathrm{obs}} = 100$. This can also be seen in fig. 2.2, which shows how the constraints improve as a function of the number of observations.

One caveat: these constraints assume Gaussian errors and linear error propagation. A proper analysis requires a much more expensive Bayesian approach (see, e.g., Ref. [12]). To assess the nonlinear effects, we provide similar plots for comparison in appendix D.2 for the different central values listed in table 2.2.

To put these results in perspective, consider the nuclear symmetry energy S_{sym} and slope L of its density dependence:

$$S_{\mathrm{sym}} = E_{np}(n_0, 0) - E_{np}(\tfrac{n_0}{2}, \tfrac{n_0}{2}), \tag{2.1a}$$

$$L = 3n_0 \left.\frac{\partial E_{np}(n_n, 0)}{\partial n_n}\right|_{n_n = n_0} = 3\frac{P_n(n_0)}{n_0}, \tag{2.1b}$$

where $E_{np}(n_n, n_p)$ is the energy per particle of uniform nuclear matter. If the so-called parabolic approximation holds at saturation ($L_2 \approx L$ – see eq. 2.5 and the surrounding discussion), then upcoming neutron skin experiments [196, 198, 197] expect to constrain $\Delta L = 41\,\mathrm{MeV}$ with a possible reduction to $\Delta L = 15\,\mathrm{MeV}$ with a follow-up experiment. This is comparable to combined constraints from ab initio calculations [186, 184, 384, 153, 245] and astrophysical observations [286, 152, 151, 148, 147, 347, 349, 235]. From our analysis we

thus see that GW observations alone could have an impact at the $\sim 15\%$ level corresponding to $\Delta L \approx 10\,\mathrm{MeV}$.

2.3 Parameterization of the nuclear equation of state

To relate the nuclear equation of state to the structure of neutron stars, we must first characterized the equation of state (EOS) of nuclear matter. This is conveniently parameterized by the energy density $\mathcal{E}(n_B)$ as a function of the baryon number density $n_B = n_n + n_p$, which is the sum of the neutron and proton number densities. Simple approximation for this function in terms of polytropes is often a starting point for astrophysical analysis. Indeed, many families of nuclear EOS can be characterized quite well by a simple set of piecewise polytropes [306].

Our approach here, however, is to directly express $\mathcal{E}(n_B)$ in terms of nuclear physics parameters. This approach allows one to directly assess how observations translate into constraints on nuclear physics. We shall demonstrate this by providing constraints on the pressure of pure neutron matter $P_n(n_n)$, which is inaccessible from a general polytropic analysis (fig. 2.1).

It is useful to divide the neutron star interior into four regions: the outer crust, the inner crust, the outer core, and the inner core. The radial extent of the outer crust, which is composed of neutron-rich nuclei embedded in an electron gas, is only a few hundred meters and its contribution to the neutron star mass is negligible. The EOS of the outer crust is well understood and depends weakly on the composition of nuclei present. The inner crust extends from $n_B = n_{\mathrm{drip}} \simeq 2 \times 10^{-3} n_0$ to $n_B = n_{\mathrm{core}} \simeq 2n_0$, has radial thickness $\sim 2\,\mathrm{km}$, and contains a modest fraction of the mass. Here, exotic neutron-rich nuclei are embedded in a dense liquid of neutrons and electrons, as described by the CLDM in section 2.3.1. The outer core is a liquid composed primarily of neutrons and a small (few percent) admixture of protons, electrons, and muons. It extends from $n_B \sim 0.5 n_0$ to $n_B = n_c \sim 2n_0$ where the description of matter in terms of nucleons interacting with static potentials is expected to break down. The inner core extends to higher densities, and we switch here to the speed-of-

sound parameterization discussed in section 2.3.3.

On dimensional grounds one expects the dimensionless tidal deformability Λ to be related to $\int_0^R \mathcal{E} r^n \mathrm{d}r = \langle \mathcal{E} r^n \rangle$ with $n \sim 7$ for $M \sim 1.4 M_\odot$ (see the second section of chapter 4 or equivalently [276]). Although the EOS around intermediate densities dominates the seventh moment of energy distribution for massive neutron stars, the inner crust also makes a large contribution to Λ for low-mass stars (which are believed to be more common in binary neutron star systems). This contribution is shown by the dashed (purple) lines at the bottom of fig. 2.3. Thus, it is important to provide a unified description of the EOS of the inner crust and the outer core in any analysis that aims to constrain the EOS using GW observations of binary neutron stars.

2.3.1 Compressible Liquid Drop Model

The compressible liquid-drop model (CLDM) (see [174, 90]) provides a unified EOS connecting a fixed outer crust for $\rho < \rho_{\mathrm{drip}}$ (for which we use the data in Table 4 of [336]) to the inner core EOS. In the inner crust, the CLDM constructs spherical nuclei in a spherical Wigner-Seitz cell, ensuring equilibrium with surrounding neutron and lepton gases by establishing both electric and β-equilibrium. This is similar to the approach taken in [140, 392], but differs in how we define the nuclear matter EOS $\mathcal{E}_{np}(n_n, n_p)$. Instead of using $\mathcal{E}_{np}(n_n, n_p)$ obtained from specific models based on effective Hamiltonians solved in the mean-field approximation to reproduce empirical parameters like nuclear saturation properties, we use what we believe is close to a minimal phenomenological parameterization that directly encodes properties that can either be measured or calculated reliably. The advantage of our approach is that these parameters are directly connected with the unified EOS, allowing us to provide a full covariance analysis linking nuclear parameters with neutron star observables.

Although the use of a spherical Wigner-Seitz cell precludes the possibility of pasta phases [303] the errors incurred by the Wigner-Seitz approximation for different lattice structures are less then 0.5% (see e.g. [89, 90]).

Our implementation of the CLDM introduces two effective parameters: the surface ten-

sion for symmetric nuclear matter σ_0 and the parameter $C_{\rm sym} = \sigma_\delta/\sigma_0$ which characterizes the isospin dependence of the surface tension $\sigma(n_n, n_p) = \sigma_0\big(1 - C_{\rm sym}\beta_p^2 + \mathcal{O}(\beta_p^4)\big)$ [236] (see appendix C.1 for the exact form used), where $\beta_p = (n_n - n_p)/(n_n + n_p)$ is the isospin asymmetry. We fix the parameter σ_0 to smoothly match the tabulated outer crust equation of state, leaving free the single parameter σ_δ. Additionally, we include as a parameter a suppression factor $\mathcal{C}$ for the Coulomb interaction to allow for the diffusivity of the proton charge distribution (see the discussion in [348]). As will be shown in section 2.2, these parameters have negligible effects on the constructed EOS.

This approach allows for a small first-order phase transition from the region modeled by the CLDM to homogeneous nuclear matter. With our parameters, this phase transition is weak: $\delta n/n < 10\%$.

To establish β-equilibrium we include leptons modeled as a Fermi gas of electrons (and muons at sufficiently high densities) in the Thomas-Fermi (TF) approximation.

2.3.2 Homogeneous Nuclear Matter

One of the main new features of our analysis is to parameterize the nuclear-matter EOS as an expansion in the proton fraction $x_p = n_p/(n_n + n_p)$ from pure neutron matter to symmetric neutron matter. This allows us to directly translate constraints from neutron star observations to the properties of neutron-rich matter, which are poorly constrained by terrestrial experiment. As a consequence of this analysis, we find that the properties of symmetric nuclear matter will not be strongly constrained by neutron stars without a priori theoretical constraints on the form of the isospin dependence. This is somewhat expected: fitting the Seattle–Lawrence-Livermore (SeaLL1) nuclear energy density functional [72] showed that virtually any form of neutron-matter EOS can be accommodated with quartic β_p^4 terms without spoiling global fits of nuclear masses, charge radii etc.

In contrast, the common approach of expanding about symmetric nuclear matter in powers of the isospin asymmetry $\beta_p = (n_n - n_p)/(n_n + n_p)$ allows one to directly connect experimentally relevant properties of symmetric nuclear matter to properties of neutron

matter. This connection, however, is generally predicated on the so-called parabolic approximation, which is valid only if quadratic terms β_p^2 dominate over quartic β_p^4 and higher-order terms. While there is some support for this below saturation density from relativistic Dirac-Bruckner-Hartree-Fock (DBHF) calculations [238], Gogny forces [166], and other perturbative techniques (see [240] for a review), it is not well established at higher densities.

For these reasons, we start with a parameterization of pure neutron matter, then use the properties of symmetric nuclear matter to constrain the extrapolation in the proton fraction x_p.

To describe pure neutron matter we use a double polytrope for the energy per particle:

$$E_n(n_n) = \frac{\mathcal{E}_n(n_n)}{n_n} = m_N c^2 + a\left(\frac{n_n}{\bar{n}_0}\right)^{\alpha} + b\left(\frac{n_n}{\bar{n}_0}\right)^{\beta},$$
$$P_n = n_n\left[a\alpha\left(\frac{n_n}{\bar{n}_0}\right)^{\alpha} + b\beta\left(\frac{n_n}{\bar{n}_0}\right)^{\beta}\right], \tag{2.2}$$

where m_N is the nucleon mass, $\bar{n}_0 = 0.16\,\mathrm{fm}^{-3}$ is a constant (approximately the nuclear saturation density), and a, b, α, and β are four EOS parameters. This form was found to accurately fit QMC calculations of the EOS using nuclear Hamiltonians with realistic two- and three-body forces [152, 151, 148, 147], and is consistent with recent QMC results based on chiral EFT interactions [384, 153, 154, 245]. For small proton fractions $x_p = n_p/(n_n+n_p)$, we perform an expansion:

$$E_{np}(n_n, n_p) = (1-x_p)E_n(n_n) + x_p\Big(m_p + \Sigma^p(n_B)\Big) + \\ + \frac{(3\pi^2)^{2/3}}{2m^*}x_p^{5/3}n_B^{2/3} + x_p^2 f_2(n_B) + x_p^3 f_3(n_B) + \cdots \tag{2.3}$$

where m^* is the proton effective mass, and $\Sigma^p(n_B)$ describes the self-energy of the proton polaron. This function is presently poorly constrained by QMC and experimental data and all known results are consistent with a simple two-parameter quadratic expansion:

$$\Sigma^p(n_B) = \mu_p \frac{n_B}{\bar{n}_0}\frac{u_p - \frac{n_B}{\bar{n}_0}}{u_p - 1} \tag{2.4}$$

where $\mu_p = \Sigma^p(\bar{n}_0)$, and u_p sets the density where $\Sigma^p(n_B = u_p\bar{n}_0) = 0$. (We expect $\Sigma^p(n_B)$ to curve up for higher densities due to the repulsive nature of nuclear three-body interactions.)

The additional powers $f_n(n_B)$ are chosen to match the properties of nuclear matter to quadratic order in the isospin asymmetry β_p and expansion away from saturation δ_n:

$$E_{np}^{\rm sym}(n_n, n_p) = \epsilon_0 + \frac{K_0}{2}\delta_n^2 + \Big(S_2 + L_2\delta_n + \frac{K_2}{2}\delta_n^2\Big)\beta_p^2,$$
$$\beta_p = \frac{n_n - n_p}{n_B}, \qquad \delta_n = \frac{n_B - n_0}{3n_0}. \tag{2.5}$$

Fitting two even powers, β_p^0 and β_p^2, and the lack of odd powers uniquely defines the functions $f_2(n_B)$ through $f_5(n_B)$, completing our characterization of the nuclear equation of state in terms of the nuclear saturation density n_0, energy per particle ϵ_0, and incompressibility K_0; the symmetry energy S_2, slope L_2 and incompressibility K_2. Note that a term proportional to β_p^4 is allowed in eq. 2.5, but our EOS is unconstrained by this term, i.e., does not rely on the parabolic approximation eq. 2.5.

Finally the leptons are included and described as a Fermi gas in the $\beta-$equilibrated star.

2.3.3 Speed of Sound Parameterization of the Inner Core

Above densities $n_c \sim 2n_0$ the EOS is virtually unconstrained. The typical approximation at high density is in terms of a polytrope, but we choose a more physically motivated high-density EOS parameterized in terms of the square of the speed of sound: $C(\mathcal{E}) = c_s^2(\mathcal{E}) = P'(\mathcal{E}) \leq 1$ which approaches the perturbative QCD result $C(\mathcal{E}) \to 1/3$ at asymptotic densities. The combination of a soft nuclear EOS as predicted by nuclear physics at low densities, and observations of $\sim 2M_\odot$ neutron stars, suggests that $C(\mathcal{E}) > 1/3$ inside the neutron star [43, 360]. $C(\mathcal{E})$ thus exhibits at least one peak before returning to the asymptotic value. This is intriguingly similar to the behavior of $C(\mathcal{E})$ as a function of temperature at zero baryon density [20]. We thus include a simple parameterization $C(\mathcal{E})$ as a quadratic polynomial smoothly connecting to the homogeneous equation of state at a fixed transition energy density $\mathcal{E}_c$ reaching a maximum $C_{\rm max} \leq 1$ at an energy density $\mathcal{E}_{\rm max}$, then returning to $C = 1/3$ at which it remains for higher densities. This core EOS thus

introduces three parameters $\mathcal{E}_c$, $C_{\max}$, and $\mathcal{E}_{\max}$. To better understand the sensitivity of our results to the properties of the core, we include one slightly different form `Core_trans` which has a first-order phase transition with discontinuity $\mathcal{E}_{\text{trans}}$ at $\mathcal{E}_c$.

2.3.4 Parameters

Our equation of state is thus characterized by 18 parameters: σ_δ and $\mathcal{C}$, (CLDM), n_0, ϵ_0, K_0, (symmetric nuclear matter), S_2, L_2, K_2, (symmetry energy), a, α, b, β, (neutron matter) μ_p, u_p, m^*, (proton polaron), and $\mathcal{E}_c$, $\mathcal{E}_{\max}$, $C_{\max}$ (core). We explore various ranges of these parameters centered about the values listed in table 2.1, which defines our base `Central` EOS model. In addition to these central values, we repeat our analysis at a handful of different parameter values, defining the models listed in table 2.2. All the sets of EOS parameters considered can support stars beyond two solar mass (see fig. 2.4), in accordance with the two observed neutron stars with $M \sim 2M_\odot$ [117, 24].

We now discuss how these constraints are derived from gravitational wave observations.

2.4 Gravitational waveform

Gravitational waves from merging binary neutron star systems carry information about the nuclear equations of state. During late stages of inspiral tidal interactions between neutron stars can leave imprints on the GW signal that is otherwise dominated by point-mass contributions. As discussed earlier, tidal responses of neutron stars can be quantified by the dimensionless tidal deformability parameter $\Lambda = \frac{2}{3} k_2 R^5/M^5$, where the second Love number k_2 is weakly sensitive to the matter distribution inside the star [136].

The calculation of Λ and k_2 for relativistic stars has been discussed extensively in [192,

297] and is summarized in appendix A.2. Here we quote the results:

$$k_2 = \frac{8C^5}{5}(1-2C)^2\left(2(1-C)+(2C-1)y_R\right)\times \left\{4C^3\left(13-11y_R+2C^2(1+y_R)+C(-2+3y_R)\right)\right. \\ \left. +2C\left(6-3y_R+3C(5y_R-8)\right)+3(1-2C)^2\times\left(2+2C(y_R-1)-y_R\right)\ln(1-2C)\right\}^{-1}. \tag{2.6}$$

where $C = M/R$ is the compactness of the NS, and $y_R = y(R)$ is related to quadrupolar perturbed metric functions (for details see appendix A.2) and is obtained as a solution to the differential equation

$$\frac{dy(r)}{dr} = -\frac{y(r)^2}{r} - \frac{y(r)g_{rr}(r)}{r}\left[1+4\pi r^2\Big(p(r)-\mathcal{E}(r)\Big)\right] \\ -4\pi r\left[9p(r)+5\mathcal{E}(r)+\frac{\mathrm{d}\mathcal{E}}{\mathrm{d}p}\Big(p(r)+\mathcal{E}(r)\Big)\right]g_{rr}(r)+r\left[\frac{6g_{rr}(r)}{r^2}+\left(\frac{d\ln g_{tt}(r)}{dr}\right)^2\right], \tag{2.7}$$

where $g_{rr}(r)$ and $g_{tt}(r)$ are the diagonal radial and temporal components of the unperturbed spherically symmetric metric (c.f. appendix A.1).

As discussed in section 1.3.6, the strong dependence of Λ on the radius R of the neutron star allows us to extract information regarding nuclear EOS. Indeed, post-Newtonian (pN) theory is able to quantitatively describe the effect of the neutron star (NS) EOS on the signal by parameterizing the waveform in terms of M and Λ of component stars [136, 372]. Gravitational wave observations of inspiraling compact binaries involving neutron stars can therefore constrain Λ [4, 5]. However, since the constraint on Λ from a single BNS is weak for small to medium SNR events, multiple observations of such systems will be required for remote sources to reduce the statistical error in Ms and Λs in order to discern the effects of similar EOS [116, 12, 66]. Fortunately, tens-to-hundreds of binaries of this type [6] are expected to be observed over the next several years by the advanced (or "second generation") LIGO.

We consider only nonspinning neutron stars here because astrophysically their spins J are expected to be small when in a BNS system; in particular it is believed that the dimensionless spin parameter $J/M^2 \leq 0.04$ [353, 4] We plan to study the effect of spin in a future follow-up study.

The GW signal from a BNS system in a detector can be expressed as the strain

$$h(t) = A(t)e^{i\Psi(t)}\,, \tag{2.8}$$

where $A(t)$ and $\Psi(t)$ denote its amplitude and phase in the time domain. For Fisher information matrix (FIM)-based parameter estimation, we work with the Fourier transform $\tilde{h}$ of the strain above. This is constructed by adding to the point-particle part of the `TaylorF2` model at 3.5pN [73], a phase correction that is taken here to be the Fourier domain tidal waveform, with Padé fits, as prescribed in Dietrich et al. [120].

In all signal simulations the errors are all statistical and are caused by the random noise in the detector. Impacts of systematic errors, e.g., owing to erroneous waveform modeling, detector calibration, etc., will be studied elsewhere.

2.5 Population models

We employ different sets of stellar evolution model parameters of zero-age main sequence (ZAMS) binary stars each of which would lead to a binary neutron star system that merges within Hubble time. The differences among stellar evolution models can be large, resulting in appreciable variation in the component mass distribution. Since the tidal deformability parameter is sensitive to the masses, we explore six cases of mass distributions produced by population synthesis studies [122]. These are more realistic than the uniform or Gaussian distributions owing to the application of stellar evolution mechanism of binary stars including two important factors, namely, metallicity and the nature of the common envelop interaction in the binary.

Metallicity plays the most dominant role in determining the strength of stellar winds in main sequence stars. The larger the metallicity the larger the stellar winds, due to increased

scattering cross-section of the electrons. This results in increased mass loss; therefore, the remnant mass left behind at the end of main sequence phase is reduced. This decreases the total baryonic mass content of the supernova engine at the onset of the explosion. In our study, we consider two different variants of metallicities produced by [122]. In the first case, the stellar evolution model was used with metallicity abundances being the same as solar metallicity, while in the second case 1/10th of solar metallicity was used. The latter is termed to be of subsolar metallicity. Component masses are narrowly peaked for solar metallicity systems while subsolar metallicity systems produce a wider mass distribution.

The second most important effect that can change the component masses of BNS systems is the way mass transfer takes place during the common envelop phase of stellar evolution of the binary stars. The mass transfer in the common envelop stage depends on the evolutionary phase of the two stars. In one extreme case, for example, if the common envelop phase is initiated by the star in the Hertzsprung gap stage, it is likely to transfer a significant amount of orbital angular momentum to the entire binary system. This case is denoted by "submodel A" in [122]. On the other hand, depending on the nature of interaction between the core and the envelop, one possible outcome is that during each common envelop stage for Hertzsprung gap donor stars the outer envelope acquires the significant part of the orbital angular momentum and gets ejected from the system, leaving behind the cores of the two stars to inspiral. This case is denoted by "submodel B" in [122]. Furthermore, a higher metallicity in the parent star can result in greater mass loss and consequently a less massive remnant. Therefore, we employ NS populations resulting from solar metallicity stars as well as those with 10% of solar metallicity.

Additionally, we consider a population model motivated from the observed mass distribution of BNS systems in our galaxy from electromagnetic astronomical measurements [284]. In this case, we utilize the mean and variance of the higher mass component (m_1) and lower mass component (m_2) to generate an uncorrelated two-dimensional Gaussian distribution in component masses (m_1, m_2) of the BNS population model, which we refer to here as the electromagnetic observed (`EMObserved`) model.

Note that, while this population distribution is derived from a set of astronomical observations, most of the systems have a coalescence time much larger than the Hubble time. Moreover, all these BNS systems are distributed in our galaxy, whereas the expected BNS events observed with LIGO/Virgo detectors will be of extragalactic origin and likely to be distributed in different metallicity environments. These effects can cause potential biases in our analysis. However, such a bias will have a very different, independent origin as compared to the suite of particular stellar evolution population models considered above. Thus, exploring these different scenarios for the population models will project an amount of systematic bias translated into the constraints of nuclear physics parameters.

These different characteristics lead to the following six models of populations studied here:

Solar metallicity submodel A (`SolarA`) These are binary NS populations produced by solar metallicity stars of the submodel A type.

Subsolar metallicity submodel A (`SubSolarA`) These are binary NS populations produced by sub-solar metallicity stars of the submodel A type.

Solar metallicity submodel B (`SolarB`) These are binary NS populations produced by solar metallicity stars of the submodel B type.

Subsolar metallicity submodel B (`SubSolarB`) These are binary NS populations produced by sub-solar metallicity stars of the submodel B type.

Electromagnetic observed (`EMObserved`) This population mimics the BNS population observed in our galaxy. It is not limited to binaries that will merge in the Hubble time.

Uniform (`Uniform`) Uniform sampling of neutron stars with masses between $1M_{\odot}$ and $2M_{\odot}$.

Constraints on $P_n(n_n)$ for 15 LIGO observations sampled from these population distributions are shown in fig. 2.6.

2.6 Statistics and methods

Given a particular parameterization of the EOS, we compute the mass M, radius R, and tidal deformability parameter Λ of a NS with a given central density by solving the TOV equations as discussed in section 1.3.6 The signals (gravitational waveforms) from merging neutron stars is computed with the numerical relativity based frequency-domain model [120] mentioned above. From those waveforms, we compute the corresponding FIM characterizing the correlated uncertainties of the masses, M_1 and M_2, and the tidal deformabilities, Λ_1 and Λ_2 (maximizing the matched filter over the source distance, signal time, and phase at coalescence [16]), to estimate the information obtainable in a merger event at LIGO design sensitivity, as described below.

Statistical Analysis To estimate how large the noise-limited errors are of the BNS parameters $\boldsymbol{\vartheta}$, we begin by modeling the measured values after the maximum likelihood estimators (MLEs) [189]. Owing to noise, the MLE will fluctuate about the respective true values, i.e., $\hat{\boldsymbol{\vartheta}} = \boldsymbol{\vartheta} + \delta\boldsymbol{\vartheta}$, where $\delta\boldsymbol{\vartheta}$ is the random error. The extent of these fluctuations is estimated by the elements of the variance-covariance matrix, $\gamma^{ab} = \overline{\delta\vartheta^a \delta\vartheta^b}$ [189].

The matrix γ^{ab} is bounded by the signal via the Cramer-Rao inequality, which states that

$$|\gamma| \geq |\boldsymbol{\Gamma}|^{-1} \ , \tag{2.9}$$

where $\boldsymbol{\Gamma}$ is the FIM:

$$\begin{aligned} \Gamma_{ab} &= \langle \partial_a \tilde{h}(\boldsymbol{\vartheta}), \partial_b \tilde{h}(\boldsymbol{\vartheta}) \rangle \\ &\equiv 4\Re \int \mathrm{d}f \ \frac{\partial_a \tilde{h}^*(f;\boldsymbol{\vartheta}) \ \partial_b \tilde{h}(f;\boldsymbol{\vartheta})}{S_h(f)} \, . \end{aligned} \tag{2.10}$$

Above, ∂_a is the partial derivative with respect to the parameter ϑ^a and $S_h(f)$ is the one-sided noise power-spectral density (PSD) [189]. We take the latter to be the zero-detuned

high-power PSD for LIGO [338]. Therefore, $(\Delta\vartheta^a)^2 \equiv \overline{\delta\vartheta^a\,\delta\vartheta^a} = \Gamma^{-1}_{aa}$ gives the lower bound on the root mean square (RMS) error in estimating ϑ^a. The two are equal in the limit of large SNR (see, e.g., [367]). The error estimates listed here are the $\Delta\vartheta^a$ obtained from the FIM.

The FIM method is known to underestimate the error in the estimation of the masses [315]. We therefore used error estimates for total mass $M_{\rm tot}$ and mass ratio q (i.e., the ratio of the lighter mass to heavier mass) that were obtained with Bayesian methods in Ref. [316], and set them such that the 1σ error is $\Delta M_{\rm tot}/M_{\rm tot} = 2\%$ and $\Delta q = 0.28$, respectively, at a single-detector SNR of 10.

The corresponding error in Λ for individual systems is consistent with that found in the available literature [107, 227, 12]. While these studies probe how accurately Λ can be measured from GW observations, they do not explore the effect of directly including inputs from nuclear theory, which is the point of this work.

To translate these correlated uncertainties in observables Ms and Λs (assuming effects of component spins to be small for $J/M^2 \leq 0.04$) to nuclear physics parameters, the FIM generated from the waveforms described above is transformed to the space of nuclear parameters Θ via the Jacobian $\partial\theta/\partial\Theta$ such as the partial derivative $\partial M/\partial\alpha$. These are then combined with a FIM from the base nuclear uncertainties, and information about neutron star masses and radii at levels expected of NASA's NICER mission to obtain a final covariance matrix for the 18 parameters.

The Fisher method for estimating errors has limitations, one of the main being the need for a high SNR. Bayesian methods are more reliable, but computationally much more expensive. For this latter reason use Fisher methods, whose computationally efficiency allows us to reduce source selection effects on the error estimates. We are able to quickly compute the FIM for hundreds of binaries, characterizing the variance within the population models. In spite of the drawbacks, the Fisher errors quoted here make the case to invest in Bayesian methods.

Methodology For a given population synthesis model, we simulate 10 000 BNS systems and distribute them uniformly in comoving volume between a luminosity distance of 100 Mpc and 400 Mpc. The latter limit is not too far from the horizon distance ($\sim$ 450 Mpc) of the network of LIGO and Advanced Virgo detectors beyond which BNS sources will produce signals with network SNR of less than 8. Also, below 100 Mpc we expect almost an order of magnitude fewer sources than those up to a distance of 200 Mpc. This fact notwithstanding the measurement precision for a nearby source (GW170817 was at a distance of $\sim$40 Mpc) can rival that of a population of more distant sources. This is why we also present results for a GW170817-like source at LIGO design sensitivity.

Our main results are summarized in fig. 2.1, which shows how the constraints on the pressure of pure neutron matter $P_n(n_n)$ improve as a function of additional NICER or LIGO observations. We start from the errors listed in table 2.1 which, for the purposes of this analysis, we interpret as uncorrelated 1σ normal errors for the parameters.

In general, errors have been overestimated to ensure that our results are conservative. The resulting FIM – a diagonal matrix of the inverse variances σ_p^{-2} – provides our starting point. From this FIM, we use forward error propagation to determine the error in pressure, which we label "Nuclear".

The largest uncertainty comes from the form of the EOS in the core of the neutron star. Although a description in terms of homogeneous nuclear matter may persist to some depth, it is likely that there is some sort of phase transition to hyperonic or strange quark matter. The core EOS is thus largely unknown. To assess the impact of large variations in the core EOS, we compare the constraints obtained under a rather large variation of the core parameters, as well as in the presence of a strong first-order phase transition (`Core_trans`). This comparison was summarized in fig. 2.5. Here we see rather large sensitivity to a smaller $\mathcal{E}_c$ as expected: if this is small, the core transition occurs at low density, and not enough conventional nuclear matter exists to be sensitive to GW observations. As long as the core transition is above $2n_0$ or so, the constraints on P_n are relatively insensitive to the form of the core EOS unless there is a strong first-order phase transition.

2.7 Conclusion

The GW170817 event demonstrated that useful constraints on the neutron star structure can be obtained from GWs. In this article we have addressed how future observations can provide more detailed constraints on the properties of dense matter. By separating the neutron star into four distinct regions, and providing a unique nuclear physics based parameterization of the equation of state (EOS) of the crust and outer core, we have analyzed how measurements of the tidal deformability can constrain nuclear properties of dense matter. Our parameterization, which uses the same underlying EOS of neutron matter in both inner crust and outer core, allows us to estimate for the first time constraints on the EOS of pure neutron matter in the density interval where controlled calculations are becoming feasible. In the inner core, where the EOS is poorly constrained, the speed of sound is allowed to vary over a large range constrained by causality and the requirement that the EOS produce a two solar mass neutron star. We have taken the first steps to study how the large uncertainties associated with the EOS of the inner core limit our ability to constrain the EOS of neutron matter in the outer core. The results we obtain suggest that, in the absence of strong first-order transitions in the core, even a handful of detections can constrain the pressure of neutron matter in the density interval between n_0 and $2n_0$ to better than 20%.

The principal component analysis presented in fig. 2.7 suggests that future LIGO observations will provide strong constraints on the density dependence of the pure neutron matter EOS in the outer core. In particular, we find that the exponent β in the neutron matter EOS defined in eq. 2.2 will be well constrained. As expected, the nuclear physics parameters are better constrained when the outer core makes the dominant contribution to the tidal deformability. This is the case when the neutron matter EOS is stiff in the dense regions of the outer core and for low-mass neutron stars. If instead, the EOS in the outer core is soft or if a strong first-order phase transition were to occur at relatively low density, constraints on the neutron matter EOS are weaker. In these cases, the inner core has a larger impact on the tidal deformability and GW detections will provide constraints for matter encountered

in the inner core.

Although our focus here was to study the impact of the most common events that occur at large distances, we find that a single close by event similar to GW170817 at 40 Mpc at design sensitivity will provide improved constraints. However, in the absence of such a nearby event, similar constraints may be realized by a dozen or so more distant events.

One limitation of our study is the simple parameterization of the EOS of the inner core. To constrain the EOS of the inner core, a parameterization that allows for larger variability at high density will be needed. In addition, to gain more confidence in the constraints we have presented for neutron matter, it will be necessary to systematically marginalize over population models for neutron star masses and spins, and the uncertainty in the EOS of the inner core. A Bayesian approach would be better suited for this purpose, and we are in the processes of developing computer programs needed for such a study.

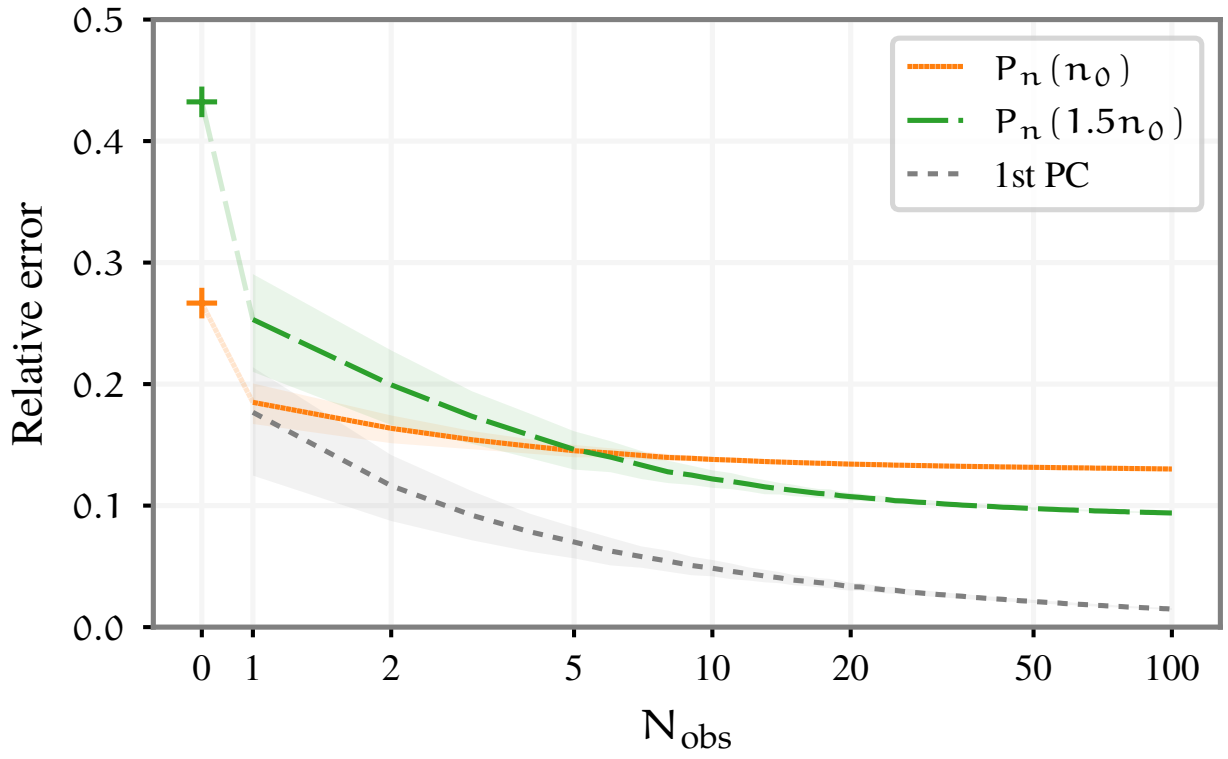

Figure 2.2: Improvement in relative constraint on the pressure of neutron matter $P_n(n_n)$ at $n_n = 1.5n_0$ and $n_n = n_0$ (related to the slope $L = 3P_n(n_0)/n_0$ of the symmetry energy) to an increasing number of simulated merger events applied to the initial nuclear constraints denoted with a plus at $N_{\rm obs} = 0$. The shading shows the range of sampling errors (1σ or 68th percentile) demonstrating variation within the `SubSolarA` population model. The lower dotted curve shows the level of the most tightly constrained principal component (1st PC).

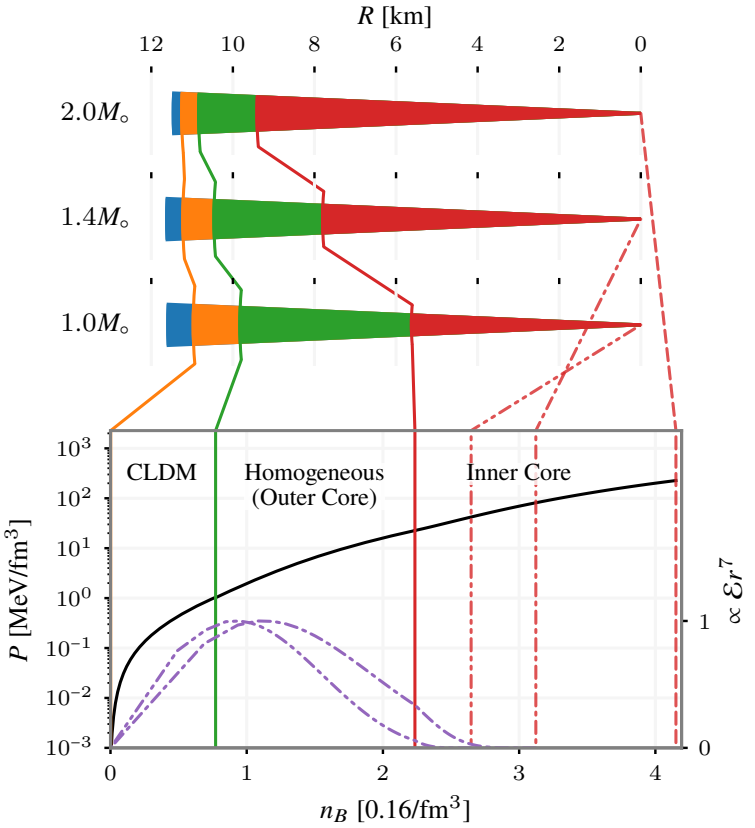

Figure 2.3: Regions of the neutron star. The upper three wedges represent a cross-section of $M = 2M_\odot$, $M = 1.4M_\odot$, and $M = 1M_\odot$ neutron stars respectively. As discussed in the text, the unified EOS smoothly connects four distinct regions from low density on the left to high density on the right. The radius of these transitions for the `Central` parameter values is shown in the top plot. These are connected to the equation of state expressed in terms of the pressure $P(n_B)$ (solid (black) line on left axis) as a function of the total baryon density in units of the saturation density $n_0 = 0.16\,\mathrm{fm}^{-3}$. From low to high density, the regions of the EOS are: a) the outer crust (very low density which is too small to see on the lower plot) that interpolates the data of [39] and [274] as tabulated in [336] (blue) with minor corrections to ensure convexity as discussed in appendix B.6; b) the inner crust modeled by the CLDM [174, 90] (orange); c) the outer core of homogeneous nuclear matter in beta-equilibrium (green); d) the inner core equation of state parameterized by a quadratic speed of sound (red). At the right, the various (red) dashed lines correspond to the core density of the respective stars. At the bottom are corresponding dashed curves (purple) proportional to $\mathcal{E}r^7$ (normalized to the maximum value on the right axis) for the two lower-mass stars. This roughly correlates with the local contribution to the dimensionless tidal deformability (see section 4.2, or equivalently the second section in [276]).

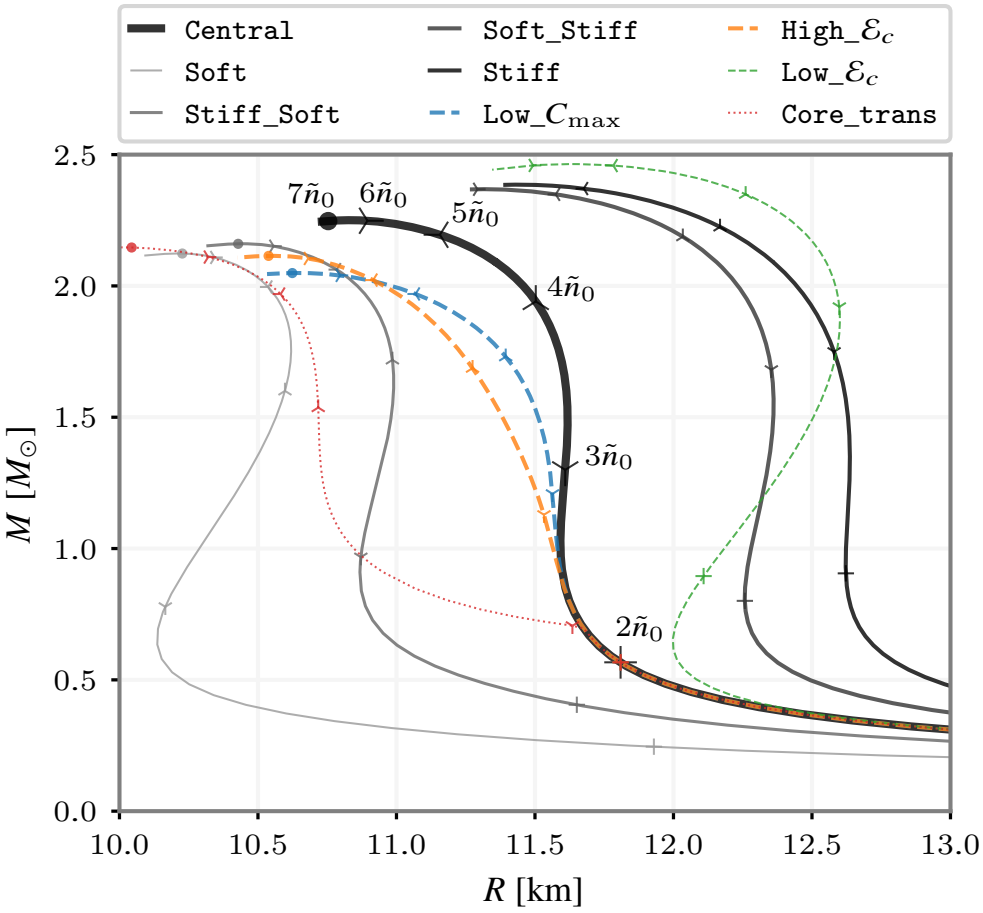

Figure 2.4: Mass-radius curves for the EOSs considered in table 2.2. The thick solid curve is our `Central` EOS along which markers annotate the stars with central densities from $2n_0$ to $7n_0$. (Corresponding markers are shown on the other curves.) Dashed curves correspond to different core parameterizations. Thin curves correspond to EOSs for which astrophysical observations would provide poor constraints for nuclear physics. These include a sharp first-order transition in the core (`Core_trans`), and soft EOSs (`Soft` and `Stiff_Soft`) which form very compact objects with low deformability. The two solar mass constraint [117, 24] on the maximum mass is satisfied for all the EOSs. The `Low_`$\mathcal{E}_c$ EOS also poorly constrains nuclear physics since the core appears close to the saturation density. As shown later in fig. 2.9, for these types of EOS, observations constrain the core parameters rather than the properties of neutron matter.

CLDM parameters:

$$\sigma_\delta = 1.38(138)\,\mathrm{MeV/fm^2}, \qquad \mathcal{C} = 0.9(1),$$

Symmetric nuclear matter and symmetry parameters:

$$n_0 = 0.16(1)\,\mathrm{fm^{-3}}, \qquad S_2 = 31(4)\,\mathrm{MeV},$$
$$e_0 = -16.0(3)\,\mathrm{MeV}, \qquad L_2 = 60(40)\,\mathrm{MeV},$$
$$K_0 = 240(40)\,\mathrm{MeV}, \qquad K_2 = 30(30)\,\mathrm{MeV},$$

Neutron matter parameters:

$$a = 13.0(3)\,\mathrm{MeV}, \qquad \alpha = 0.50(2),$$
$$b = 3.5(15)\,\mathrm{MeV}, \qquad \beta = 2.3(5),$$

Proton polaron parameters:

$$\mu_p(n_0) = -105(10)\,\mathrm{MeV}, \qquad u_p = 3.1(6), \qquad \frac{m_{\mathrm{eff}}}{m_p} = 0.8(1),$$

Inner-core parameters:

$$\mathcal{E}_c = 350(35)\,\mathrm{MeV/fm^3}, \qquad \mathcal{E}_{\max} = 0.8(4)\,\mathrm{GeV/fm^3}, \qquad C_{\max} = 0.8(2).$$

Table 2.1: Parameters defining the `Central` EOS along with their uncorrelated 1σ covariance (expressed using the si convention $3.5(15) \equiv 3.5 \pm 1.5$) used to define the "Nuclear" error estimates prior to including information from astrophysical observations. We take the values of the CLDM parameters from the fits to the APR EOS tabulated in [348] but assign large errors to encompass missing physics such as the possibility of pasta phases. Symmetric nuclear matter and symmetry parameters have errors taken from the extensive analysis [250]. Neutron matter parameters have errors estimated from QMC calculations with various three-body interactions [152, 151, 148, 147], and are consistent with recent QMC results based on chiral EFT interactions [384, 153, 154, 245]. Proton polaron parameters have errors estimated from the QMC calculations [317] and are consistent with estimates from chiral interactions [322]. The core parameters are chosen to allow for a $2M_\odot$ star at the extremes of all of our models except for the `Soft` EOS which requires a lower core transition and are given large errors to be conservative with the exception of the parameter $\mathcal{E}_c$. This is given a small error for the purposes of our statistical analysis as the dependence is highly nonlinear. Variations of this parameter are considered specifically in fig. 2.5.

	Neutron Matter				Inner Core	
EOS	a [MeV]	α	b [MeV]	β	$\mathcal{E}_c$ [MeV/fm^3]	$C_{\max}$
`Central`	13.0	0.5	3.5	2.3	350	0.8
`Soft`	12.7	0.3	2	2.1		
`Stiff`	13.3	0.7	5	2.5		
`Soft_Stiff`	12.7	0.3	5	2.5		
`Stiff_Soft`	13.3	0.7	2	2.1		
`Low_`$\mathcal{E}_c$					200	
`High_`$\mathcal{E}_c$					500	
`Low_`$C_{\max}$						0.6
					$\mathcal{E}_{\text{trans}}$ [MeV/fm^3]	
`Core_trans`					150	

Table 2.2: List of changed EOS parameters compared in this chapter. All other parameters share the same values as the `Central` EOS in the top row, which takes the central values listed in table 2.1. The first four variations – `Soft`, `Stiff`, `Soft_Stiff`, and `Stiff_Soft` – refer to the properties of the neutron-matter equation of state and whether the EOS of the outer core is softer or stiffer than `Central` at low/high density. The next three variations – `Low_`$\mathcal{E}_c$, `High_`$\mathcal{E}_c$, and `Low_`$C_{\max}$ – explore variations of the core EOS. To better understand the sensitivity of our results to the properties of the core, we include one slightly different form `Core_trans` which has a first-order phase transition with discontinuity $\mathcal{E}_{\text{trans}}$ (See fig. 2.5). All parameter sets are chosen to accommodate the 2 solar mass constraint [117, 24].

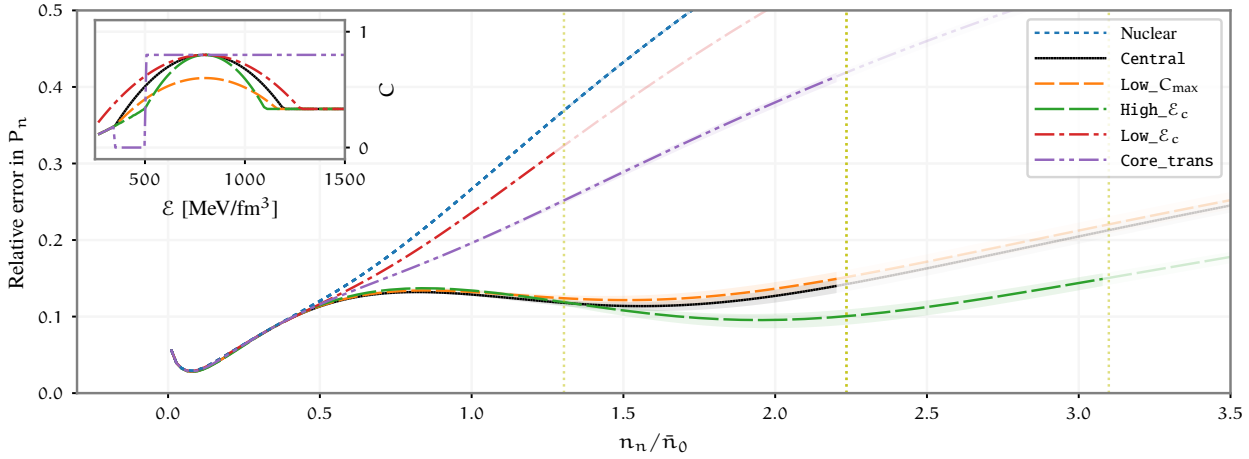

Figure 2.5: Sensitivity of the constraint on the pressure of neutron matter $P_n(n_n)$ from $N_{\rm obs} = 15$ simulated merger events drawn from the `SubSolarA` population model to variations of the core equation of state. The vertical yellow lines denote the density n_c at which the EOS reverts to the core form. Inset: form of the various core speed-of-sound functions $C(\mathcal{E}) = c_s^2$.

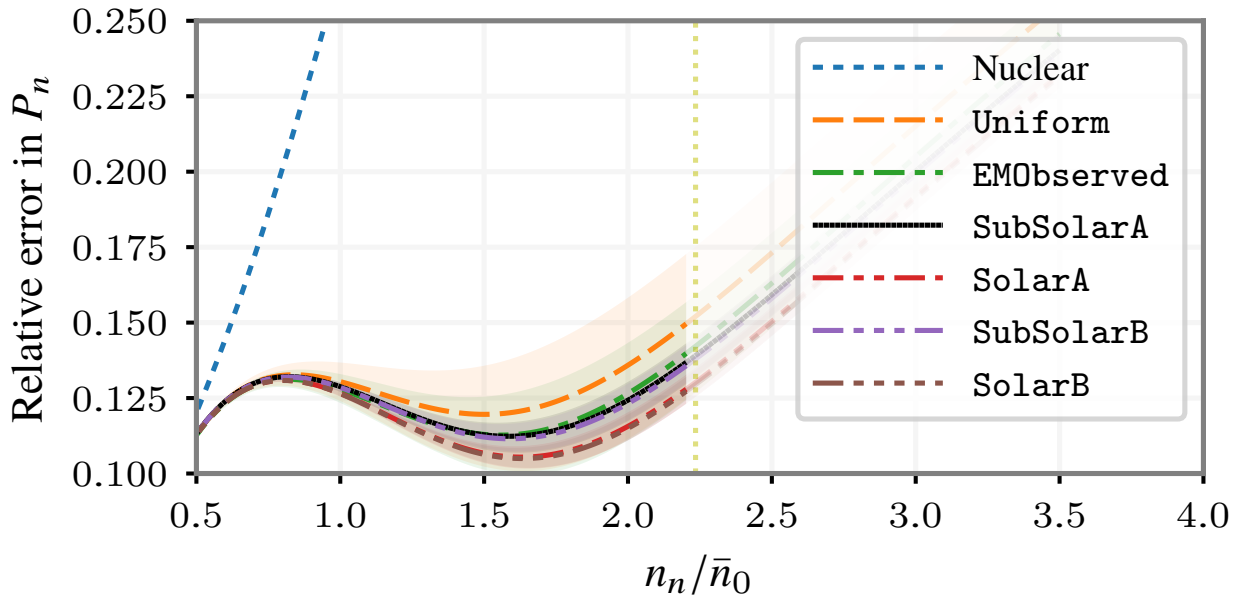

Figure 2.6: Population model sensitivity of the constraint on the pressure of neutron matter $P_n(n_n)$ from $N_{\text{obs}} = 15$ simulated merger events drawn from various different population models. The weaker constraints from the `Uniform` model result from distributing the events over larger mass objects. As shown in fig. 2.8, this provides more information about the properties of the core at the expense of information about the lower-density regions that constrain neutron matter.

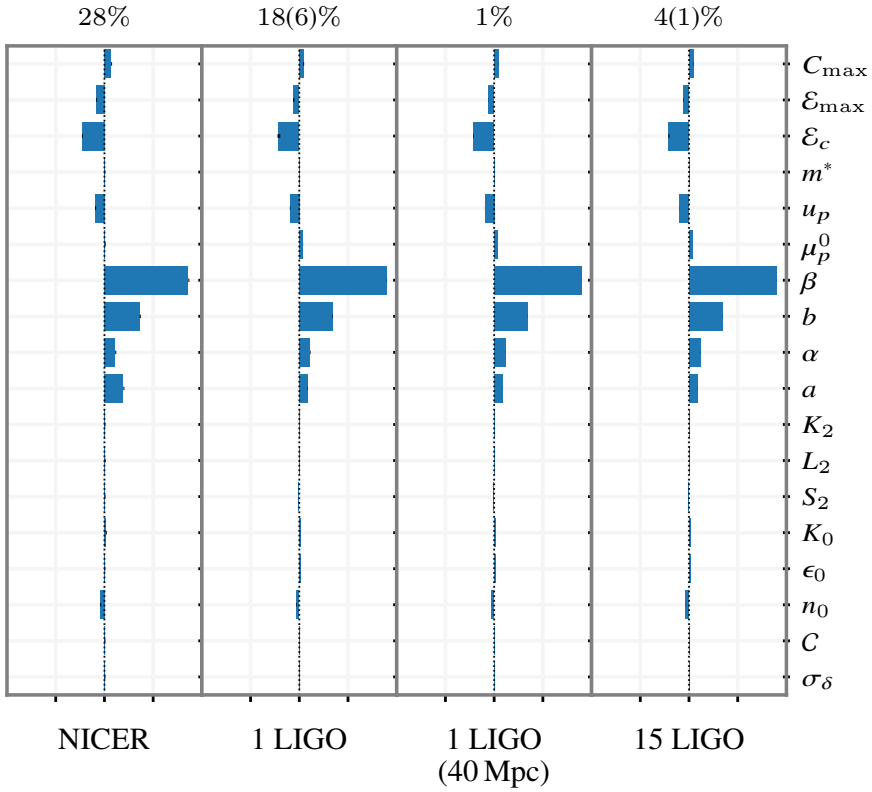

Figure 2.7: Principal component analysis of the simulated observational data in terms of the EOS parameters. Each column is a plot of the components of most significantly constrained eigenvector for the particular combination of observations listed at the bottom. These should be interpreted as follows: A linear combination of the log of the corresponding parameters is constrained to the tolerance shown at the top. The rightmost column shows the principal component analysis for $N_{\text{obs}} = 15$ simulated merger events drawn from the `SubSolarA` population model, and is the same as the leftmost column of fig. 2.9. The 1σ errors in the tolerances, shown as small black strips in middle of the component bars, are obtained by performing 200 independent samples and demonstrate variation within the population model. *(These errors are small here, but quite visible in the second principal components of fig.* 2.8*.)*

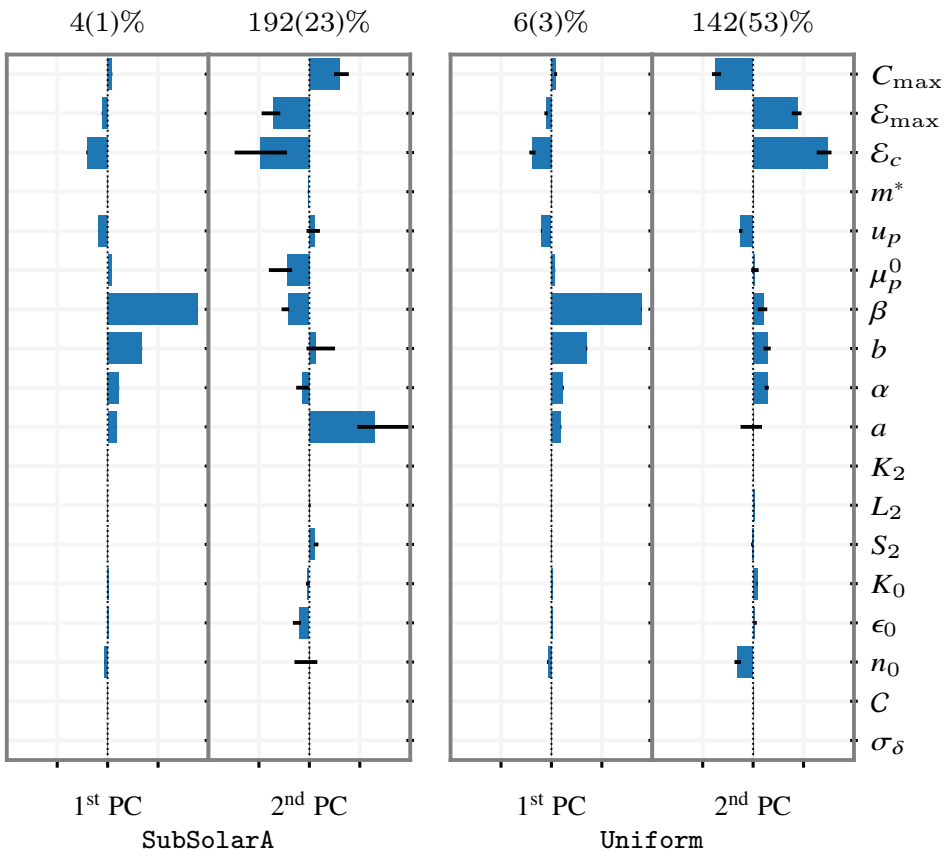

Figure 2.8: First two principal components for $N_{\rm obs} = 15$ GW observations drawn from the `SubSolarA` (left) and `Uniform` (right) population models. This demonstrates the wider distribution of masses in the `Uniform` model as compared to `SubSolarA`. The narrow distribution in `SubSolarA` leads to tighter statistical constraints on the 1st principal component, but leaves other directions in parameter space poorly explored. In contrast, the `Uniform` model distributes the 15 events over a larger range of masses, reducing the constraints on the 1st principle component, but providing more information about other directions. Even for $N_{\rm obs} = 15$ observations, the next principal component is poorly constrained at a level worse than 100%: more observations would be required to constrain this component at a useful level. Thus, neutron-star observables seem to provide tight constraints in a single direction of parameter space.

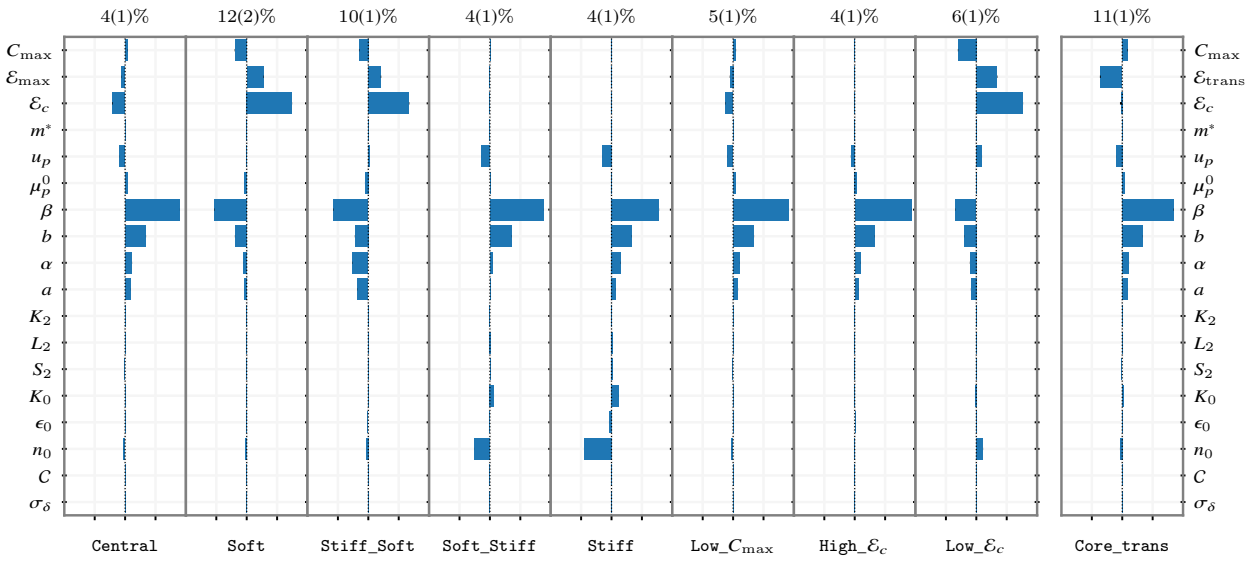

Figure 2.9: Principal component analysis of $N_{\text{obs}} = 15$ simulated merger events drawn from the `SubSolarA` population model for each of the EOS parameters listed in table 2.2. The leftmost column thus corresponds to the rightmost column of fig. 2.7. This analysis makes clear the nonlinear dependence of the problem on the EOS parameters: neutron star observations constrain either properties of the core for parameter values such as `Soft`, `Stiff_Soft`, `Low_`$\mathcal{E}_c$, or `Core_trans`, or the neutron matter EOS for more central values.

Chapter 3

NEUTRON STARS EXCLUDE LIGHT DARK BARYONS [1]

Exotic particles carrying baryon number and with mass of order the nucleon mass have been proposed for various reasons including baryogenesis, dark matter, mirror worlds, and the neutron lifetime puzzle. We show that the existence of neutron stars with mass greater than 0.7 $M_\odot$ places severe constraints on such particles, requiring them to be heavier than 1.2 GeV or to have strongly repulsive self-interactions.

3.1 Introduction

Exotic states that carry baryon number and have masses below a few GeV have been theorized in a number of contexts, such as asymmetric dark matter [337, 395, 111, 112], mirror worlds [51], neutron-antineutron oscillations [255] or in nucleon decays [109]. In general, such states are highly constrained because they can drastically alter the properties of normal baryonic matter–in particular, if too light, they can potentially render normal matter unstable. We currently understand that matter is observationally stable because the standard model (accidentally) conserves baryon number. This ensures that the proton, the lightest baryon, does not decay (up to effects caused by higher dimensional operators that violate baryon number).

Now, consider the simple case of an electrically neutral single new fermion, χ, that carries unit baryon number, and carries no other conserved charge. Assuming that its couplings to ordinary matter are not highly suppressed, because of the conservation of baryon number and electric charge, it must have a mass larger than the difference between the proton and electron masses, $m_\chi > m_p - m_e = 937.76$ MeV, in order to not destabilize the proton. In

[1] this chapter is based on the published work [256].

fact, a slightly stronger lower bound on m_χ comes from the stability of the weakly bound ^{9}Be nucleus: $m_\chi > 937.90$ MeV. If $m_\chi < m_n = 939.57$ MeV, a new neutron decay channel can open up, $n \to \chi + \ldots$, where the ellipsis includes other particles that allow the reaction to conserve (linear and angular) momentum.

It is interesting to note that if $m_\chi < m_p + m_e = 938.78$ MeV, χ is itself kept stable by the conservation of baryon number and electric charge. It could therefore be a potential candidate for the dark matter, which we know to be electrically neutral and stable. It is compelling that in such a situation that the stability of normal matter and of dark matter is ensured by the *same* symmetry: baryon number.

A potential new decay channel for the neutron has recently received attention as a solution to the 4σ discrepancy between values of the neutron lifetime measured using two different techniques, the "bottle" and "beam" methods [51, 330, 139]. The "bottle" method, which counts the number of neutrons that remain in a trap as a function of time and is therefore sensitive to the total neutron width gives $\tau_n^{\text{bottle}} = 879.6 \pm 0.6$ s [248, 329, 294, 352, 27]. The "beam" method counts the rate of protons emitted in a fixed volume by a beam of neutrons, thus measuring only the β-decay rate of the neutron, results in $\tau_n^{\text{beam}} = 888.0 \pm 2.0$ s [83, 390, 82]. These two measurements can be reconciled by postulating a new decay mode for the neutron, such as $n \to \chi + \ldots$, with a branching fraction

$$\text{Br}_{n\to\chi} = 1 - \frac{\tau_n^{\text{bottle}}}{\tau_n^{\text{beam}}} = (0.9 \pm 0.2) \times 10^{-2}. \tag{3.1}$$

However, a recent reevaluation of the prediction for the neutron lifetime from post 2002 measurements of the neutron g_A concludes that any nonstandard branching for the neutron is limited to less than 2.7×10^{-3} at 95% CL [106].

In this chapter we note that a new state that carries baryon number and has a mass close to the neutron's can drastically affect the properties of nuclear matter at densities seen in the interiors of neutron stars. In neutron stars the neutron chemical potential can be significantly larger than m_n, reaching values $\simeq 2$ GeV in the heaviest neutron stars [232]. Thus any exotic particle that carries baryon number and has a mass $\lesssim 2$ GeV will have a

large abundance if in chemical equilibrium. Because they replace neutrons, their presence will soften the equation of state of dense matter by reducing the pressure due to short-range repulsive nuclear forces and the degenerate Fermi sea, while contributing to an increase in the energy density. This will in turn reduce the maximum mass of neutron stars from those obtained using standard equations of state for nuclear matter. As we shall show below, even a modest reduction in the pressure at high density can dramatically lower the maximum mass to a value that is significantly smaller than the observed heaviest neutron stars with masses $\simeq 2\ M_\odot$ [118, 25].

The remainder of this chapter is organized as follows. In § 3.2 we describe a simple model of fermion dark matter which is charged under baryon number. In § 3.3 we show the effects of such a fermion on mass-radius relation and maximum mass of neutron stars. Possible extensions of these constraints, future work, and ways to avoid the constraints are described in the conclusions, § 3.4.

3.2 Model

We begin by considering a simple model with a single neutral Dirac fermion, χ, that carries unit baryon number. As mentioned above, $m_\chi > 937.90$ MeV so as to not destabilize ^{9}Be. The relevant terms in the effective Lagrangian involving the neutron are

$$\mathcal{L}_{\rm eff} = \bar{n}\left(i\partial\!\!\!/ - m_n\right) n + \bar{\chi}\left(i\partial\!\!\!/ - m_\chi\right)\chi - \delta\left(\bar{\chi} n + \bar{n}\chi\right), \tag{3.2}$$

where δ is a coupling determined by the underlying theory. A simple UV completion [26, 255] of this involves integrating out a scalar diquark coupled to u and d quarks as well as to d and χ, generating the four fermion operator

$$\frac{1}{\Lambda^2}\bar{\chi} udd. \tag{3.3}$$

Matching this onto the effective theory gives

$$\delta \sim \frac{0.01\ \text{GeV}^3}{\Lambda^2}. \tag{3.4}$$

In what follows, we assume that this coupling between n and χ is small, in particular $|\delta| \ll |\Delta m|$, where $\Delta m \equiv m_n - m_\chi$. This coupling leads to a mixing between n and χ and the mass terms are diagonalized by taking $n \to n + \theta\chi$, $\chi \to \chi - \theta n$, where the mixing angle is $\theta = \delta/\Delta m$.

If $m_\chi < m_n$, a new decay mode for the neutron opens up, $n \to \chi\gamma$. In addition, if $m_\chi < m_p + m_e = 938.78$ MeV, χ is stable. The new decay mode for the neutron comes from the neutron magnetic dipole moment operator, which, after the mass matrix is diagonalized contains the term

$$\mu_n \theta \bar{\chi} \sigma^{\mu\nu} n F_{\mu\nu}, \tag{3.5}$$

where $\mu_n = -1.91e/(2m_p) = -0.31$ GeV^{-1} is the neutron magnetic dipole moment. The partial width for $n \to \chi\gamma$ is

$$\Gamma_{n\to\chi\gamma} = \frac{\mu_n^2 \theta^2 m_n^3}{16\pi}\left(1 - \frac{m_\chi^2}{m_n^2}\right)^3 \simeq \frac{\mu_n^2 \theta^2 \Delta m^3}{2\pi}. \tag{3.6}$$

Given a total width of $\Gamma_n = 1/\tau_n^{\text{bottle}} = (879.6 \text{ s})^{-1}$, the branching ratio for the neutron to decay into $\chi\gamma$ is

$$\begin{aligned} \text{Br}_{n\to\chi\gamma} &= 0.01 \left(\frac{\Delta m}{1 \text{ MeV}}\right)^3 \left(\frac{\theta}{7\times 10^{-10}}\right)^2 \\ &= 0.01 \left(\frac{\Delta m}{1 \text{ MeV}}\right) \left(\frac{\delta}{7\times 10^{-13} \text{ GeV}}\right)^2. \end{aligned} \tag{3.7}$$

Thus, we see that for $m_n - m_\chi \sim 1$ MeV, a mixing angle of order 10^{-9}, or a n-χ coupling of about 10^{-12} GeV can explain the neutron lifetime anomaly.[2] This value of δ corresponds to a scale for the four fermion interaction in Eq. (3.3) of $\Lambda \sim 10^5$ GeV. We note here, however, that a very recent search for the decay $n \to \chi\gamma$ using ultracold neutrons sets a limit on this branching, for 937.90 MeV $< m_\chi <$ 938.78 MeV, of roughly 10^{-3} [355].

Although $\delta \sim 10^{-12}$ GeV is a small coupling between the neutron and χ, it can lead to the efficient conversion of neutrons into χ's in the high density environments encountered inside

[2]We note here why a model with Dirac χ where baryon number is conserved is necessary. If instead χ were Majorana with $\theta = 10^{-9}$ and $\Delta m = 1$ MeV, a $\Delta B = 2$ n-$\bar{n}$ transition amplitude of roughly $\theta^2 \Delta m \sim 10^{-21}$ GeV would arise. This is many orders of magnitude larger than the experimental upper bound of 10^{-33} GeV.

neutron stars. In addition, because of the large neutron chemical potential inside neutron stars, the conversion $n \to \chi$ can take place there even for $m_\chi > m_n$ where free neutron decays are kinematically blocked.

We investigate the effects of a χ-n coupling on neutron stars in the next section.

3.3 Neutron stars

As discussed in section 1.3.2, the structure of neutron stars is determined by the equation of state (EOS) of dense matter which specifies the relationship between pressure P and energy density $\mathcal{E}$. For a given EOS, $P(\mathcal{E})$, the Tolman-Oppenheimer-Volkoff (TOV) equations of general relativistic hydrostatic structure can be solved numerically to obtain the mass-radius curves.

Representative nuclear EOSs used in this chapter are shown as dot-dashed curves in Fig. 3.1. The curve labeled APR, calculated by Akmal, Pandharipande and Ravenhal [17] has been widely used to describe neutron stars. The curves labeled "Soft" and "Stiff" are the extreme possibilities consistent with our current understanding of uncertainties associated with the nuclear interactions up to 1.5 n_s [146, 185]. The EOS labeled "Soft" uses a nuclear EOS with a low pressure compatible with neutron matter calculations and is extrapolated to high density to ensure that produces a neutron star with mass just shy of 2 $M_\odot$. The curve labeled "Stiff" is obtained by using the largest pressure up to $1.5n_s$ compatible with neutron matter calculations, and at higher density we use the maximally stiff EOS with $P(\mathcal{E}) = P_0 + (\mathcal{E} - \mathcal{E}_0)$ where P_0 and $\mathcal{E}_0$ are the pressure and energy density predicted by the nuclear EOS at 1.5 n_s (details see appendix B.5). We believe that the "Soft" and "Stiff" EOSs bracket the extreme possibilities subject to constraints from nuclear physics and observations of the massive neutron stars with $M_{\rm NS} \simeq 2\ M_\odot$. In what follows we shall use these EOSs to demonstrate that, despite the uncertainty at supra-nuclear density, the observation of neutron stars with mass $M_{\rm NS} \simeq 2\ M_\odot$ rules out the existence of a weakly interacting dark matter candidate which carries baryon number and has a mass in the range $937.90\ \text{MeV} < m_\chi < 938.78\ \text{MeV}$. In fact, we shall find that any such weakly interacting

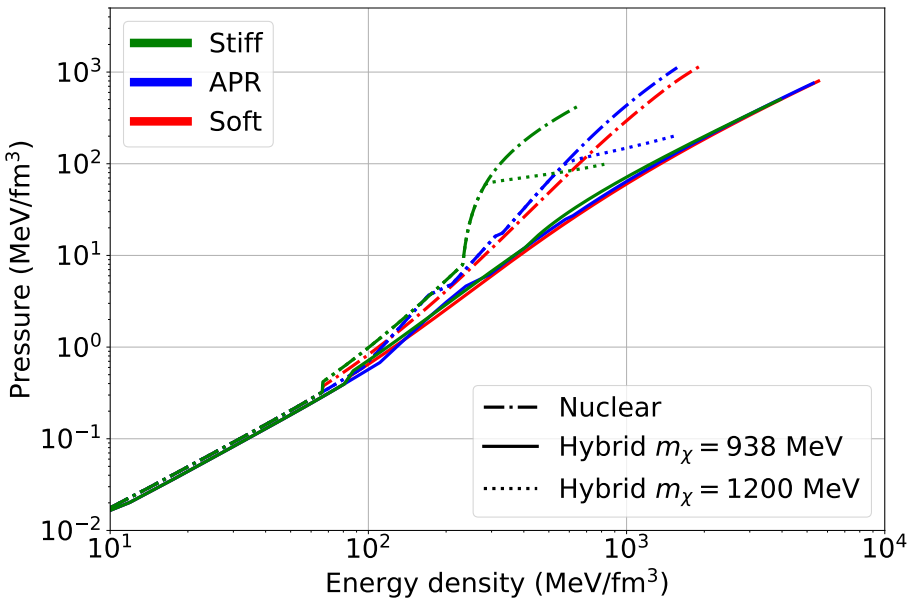

Figure 3.1: Hybrid EOSs and underlying nuclear EOSs. The standard nuclear matter EOSs are shown as dash-dotted curves. The "Stiff" EOS makes a second-order transition to a causal EOS at $n_B = 1.5\ n_s$. This is the stiffest possible EOS and predicts a maximum mass $\simeq 3.3\ M_\odot$ (Fig. 3.2). Adding a dark baryon with $m_\chi = 938$ MeV results in solid curves, which are dominated by χ's Fermi gas EOS for $\mathcal{E} \gtrsim 0.1$ MeV/fm^3. Dotted lines show hybrid EOS with $m_\chi = 1.2$ GeV. All curves are truncated at maximum central densities inside stable neutron stars.

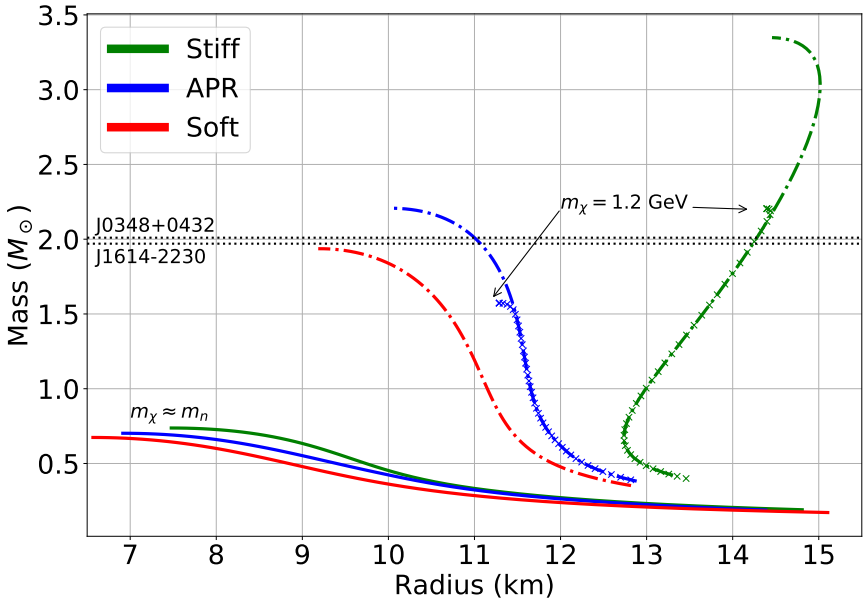

Figure 3.2: The mass-radius relationship generated using EOS in Fig. 3.1. Even for the extremely stiff EOS, the maximum mass of hybrid stars containing non-interacting dark neutrons does not exceed 0.8 $M_\odot$. The measured masses of the two most massive neutron stars J0348+0432 and J1614-2230 are also shown.

particle with mass $m_\chi \lesssim 1.2$ GeV can be robustly excluded.

In Fig. 3.2 we show the mass-radius curve for neutron stars predicted by the standard nuclear EOS as dash-dotted curves. The curves terminate at the maximum mass. For the maximally stiff EOS the speed of sound in the high density region $c_s = c$, and this construction produces the largest maximum mass of neutron stars compatible with nuclear physics.

Any exotic neutron decay channel $n \to \chi + \cdots$ which makes even a small contribution to the neutron width, of order the inverse lifetime of a neutron star, will be fast enough to ensure that χ is equilibrium inside the star. The typical age $t_{\rm NS}$ of old observed neutron

stars is $t_{\rm NS} \approx 10^6 - 10^8$ years. In a dense medium, due to strong interactions, the dispersion relation of the neutron can be written as $\omega_n(p) = \sqrt{p^2 + m_n^2} + \Sigma_r + i\Sigma_i$ where Σ_r and Σ_i are the real and imaginary parts of its self-energy. The mixing angle is suppressed at finite density and is given by

$$\tilde{\theta} = \frac{\delta}{\sqrt{\widetilde{\Delta m}^2 + \Sigma_i^2}}\,, \tag{3.8}$$

where $\widetilde{\Delta m} = \Delta m + \Sigma_r$. Since Σ_r and Σ_i are expected to be of the order of $10 - 100$ MeV at the densities attained inside neutron stars [161], it is reasonable to expect the ratio $\tilde{\theta}/\theta$ to be in the range $0.01 - 0.1$. The rate of production of $\chi's$ in the neutron star interior due to neutron decay, defined in Eq. 3.6, is suppressed by the factor $(\tilde{\theta}/\theta)^2$ but enhanced by $(\widetilde{\Delta m}/\Delta m)^3$ when $\widetilde{\Delta m} > \Delta m$. For $\widetilde{\Delta m} \approx 10$ MeV the neutron decay lifetime is $< 10^8$ yrs when $\delta > 10^{-19}$ GeV, and it is safe to assume that for the phenomenologically interesting values of $\delta \simeq 10^{-14} - 10^{-12}$ GeV, χ will come into equilibrium on a timescale $t \ll t_{\rm NS}$.[3]

Because χ carries baryon number, in equilibrium its chemical potential $\mu_\chi = \mu_B$, where μ_B is the baryon chemical potential. Given a nuclear EOS the baryon chemical potential is obtained using the thermodynamic relation $\mu_B = (P_{\rm nuc} + \mathcal{E}_{\rm nuc})/n_B$ where n_B is the baryon number density. If χ is a Dirac fermion with spin 1/2 and its interactions are weak, its Fermi momentum and energy density are given by

$$k_{{\rm F}\chi} = \sqrt{\mu_B^2 - m_\chi^2}\,, \tag{3.9}$$

$$\mathcal{E}_\chi = \frac{1}{\pi^2}\int_0^{k_{{\rm F}\chi}} dk\; k^2\sqrt{k^2 + m_\chi^2}\,, \tag{3.10}$$

respectively. The dark neutron number density $n_\chi = k_{{\rm F}\chi}^3/3\pi^2$ and its pressure $P_\chi = -\mathcal{E}_\chi + \mu_B n_\chi$. The total pressure $P_{\rm tot} = P_{\rm nuc} + P_\chi$ and energy density $\mathcal{E}_{\rm tot} = \mathcal{E}_{\rm nuc} + \mathcal{E}_\chi$ are easily obtained, and the TOV equations are solved again to determine the mass-radius relation for hybrid stars containing an admixture of χ particles. The net result is a softer EOS where the pressure is lower at a given energy density, because, as we mentioned earlier, χ replaces

[3] We delegate to future work a detailed calculation of the production rate for such small values of δ which may be interesting in other contexts.

neutrons and reduces their Fermi momentum and pressure. Results for $m_\chi = 938$ MeV are shown in Fig. 3.2 as solid curves which terminate at the maximum mass. We allow the nuclear EOS to vary from maximally stiff to soft, and also show the results for the APR EOS. The striking feature is the large reduction in the maximum mass. This reduction is quite insensitive to the nuclear EOS. Even for the maximally stiff EOS, the presence of non-interacting dark neutrons reduce the maximum mass to values well below observed neutron star masses. Thus, a dark neutron with a $m_\chi \simeq 938$ MeV and weak interactions is robustly excluded. For larger m_χ we can still obtain useful bounds as long as m_χ is smaller than the baryon chemical potential attained in the core. For $m_\chi = 1.2$ GeV we find, as expected, that the appearance of dark neutrons is delayed to supranuclear density, but as soon as they appear, they destabilize the star. This can be inferred by the behavior of the mass-radius relation labeled $m_\chi = 1.2$ GeV and denoted by points represented as crosses. For the APR EOS the maximum mass is about 1.6 $M_\odot$ and for the maximally stiff EOS it is about 2.2 $M_\odot$.

Although interactions between χ's and nucleons are necessarily weak,[4] interactions between χ's could be strong. If χ is charged under a U(1) with coupling strength g to a new gauge boson a mass m_V, repulsion between χ's modifies the EOS. In the mean-field approximation, both the pressure and energy density are increased by

$$\Delta P_\chi = \Delta \mathcal{E}_\chi = \frac{1}{2}\frac{g^2}{m_V^2} n_\chi^2 \,. \tag{3.11}$$

For strong coupling with $g \simeq 1$, and small m_V corresponding to a Compton wavelength of the gauge boson that is larger than the inter-particle distance, this interaction energy will dominate. Under these conditions, the number density of $n_\chi \approx m_V^2(\mu_B - m_\chi)/g^2$ in equilibrium will be greatly reduced, and its impact on the dense matter EOS will be negligible. For $m_\chi \simeq m_N$, we find that when $g > 1.1\,(m_V/100\text{ MeV})$ the stiff EOS predicts a maximum mass $> 2M_\odot$, while for the APR EOS we require $g > 2.4\,(m_V/100\text{ MeV})$ to accommodate this maximum mass (see appendix E). Another possibility is that dark neutrons have inter-

[4] In the model leading to the four fermion interaction of Eq. (3.3), χ-nucleon interactions come from the four fermion interaction $\bar{\chi}\chi\bar{d}d/\Lambda^2$. With $\Lambda \gtrsim 10^5$ GeV for $\delta \lesssim 10^{-12}$ GeV, this interaction is highly suppressed compared to nuclear strength interactions.

actions that mimic interactions between ordinary neutrons. In such a mirror scenario, we find that the maximum mass of neutron stars is 1.6 $M_\odot$ for the APR EOS and 2.4 $M_\odot$ for the maximally stiff EOS construction. For details see appendix E.

3.4 Conclusions

States that carry baryon number and have a mass close to the nucleons have been studied in several scenarios. The extreme environments encountered in the interiors of neutron stars can readily produce such states. However, because these new states do not in general have the same interactions that neutrons do, they can lead to radically different EOS in neutron stars. In particular, new states will reduce the maximum possible neutron star mass which is consistent with a given nuclear EOS.

Simple scenarios where the dark baryons have a mass similar to that of the nucleon and are not charged under a new force do not allow for neutron stars with mass above $\sim 0.7-0.8 M_\odot$. This bound is in stark conflict with observation. Charging such dark baryons under a new force with a very light gauge mediator will result in interactions much larger than standard nuclear interactions and can greatly suppress their presence in dense matter. This can mitigate their effects on the EOS enough to allow for neutron stars as heavy as have been observed, $\sim 2M_\odot$. However, if such a new force is similar to nuclear forces as expected in a "mirror world" set up where the dark neutron has the same self-interactions as does the visible neutron, the maximum mass is still significantly reduced and one requires a very stiff high density EOS to produce $2M_\odot$ neutron stars. Interestingly, in the case where the dark baryons are stable dark matter, with $m_\chi \simeq 938$ MeV, nuclear strength self-interactions have been implicated to explain DM small scale structure puzzles (see, e.g., [365] and references therein).

Extensions of this work can easily be shown to constrain other possible new weakly interacting particles. For instance in the "hylogenesis" baryogenesis scenario [111, 112] there are two kinds of baryon number carrying dark matter particles, called "Y" and "Φ", which also carry another conserved charge for stability, but which have an allowed reaction $n+\gamma \leftrightarrow$

$Y+\Phi$. Stability of matter places a lower bound of 937.90 MeV on m_Y+m_Φ. The existence of observed neutron stars will place a more stringent bound on $m_Y + m_\Phi$, which will be similar to the lower bound of 1.2 GeV we found on m_χ. Another type of new particle which would be constrained would be a new weak interacting neutral integer spin boson, called "ξ", with baryon number 1 and interactions with ordinary matter which are not highly suppressed. As long as lepton number is conserved, both ξ and the proton are stable. The stability of nuclei with atomic number A and charge Z against decays of type $(A, Z) \to (A-2, Z) + 2\xi$ will place a lower bound of order the nucleon mass on m_ξ. Neutron stars, however, will constrain ξ to be heavier than the minimum chemical potential for neutrons in a 2 solar mass neutron star, or else neutrons could convert to ξ particles and destabilize the star.

As noted earlier avoidance of such constraints is possible if the dark matter/dark baryon carries sufficiently repulsive self-interactions. If the self-repulsion of the new state is large enough most of the mass of the star will remain in the form of neutrons and the effect on the maximum mass will be small.

Chapter 4

DARK HALOS AROUND NEUTRON STARS AND GRAVITATIONAL WAVES [1]

We find that models of MeV-GeV dark matter (DM) in which dark matter interacts strongly can be constrained by the observation of gravitational waves from binary neutron star (BNS) mergers. Trace amounts of dark matter, either produced during the supernova or accreted later, can alter the structure of neutron stars (NS) and influence their tidal deformability. We focus on models of dark matter interacting by the exchange of light vector gauge bosons that couple to a conserved dark charge. In these models, dark matter accumulated in neutron stars can extend to large radii. Gravitational waves detected from the first observed BNS merger GW170817 place useful constraints on such not-so compact objects. Dark halos, if present, also predict a greater variability of neutron star tidal deformabilities than expected for ordinary neutron stars.

4.1 Introduction

The similar abundances of baryons and DM have led to theorizing that DM might, like ordinary matter, carry a conserved charge. It could then be produced similar to baryons by creating an asymmetry between DM and anti-DM. This type of DM is known as asymmetric dark matter (ADM). Such an asymmetry would allow for sizable self-interactions without annihilation. As noted earlier in section 1.2, while the paradigm of cold dark matter fits a broad range of data, some discrepancies at scales smaller than galaxy clusters could be addressed by a more complicated DM sector including large self-interactions [345, 243, 110, 391, 59, 292, 71, 103, 119, 365, 125]. Some recent work suggests that a strong velocity

[1] this chapter is based on the published work [276].

dependence in the interaction, such as would be the case if DM exchanges a light boson, provides the best fit to a range of galactic structures [211]. If neutron stars trap DM, the resulting DM density is much higher and relative velocity much lower than found in other places in the universe, providing a different regime to constrain dark forces. Here we will show how a dark halo surrounding NS resulting from repulsive dark forces can affect gravitational wave production in neutron star mergers.

Interesting ideas about the role of DM inside NSs have been explored and are reviewed in [210, 67, 395]. Recent work in [221, 239, 220, 60] has shown that ADM can accrete and thermalize in the NS core even when the DM-nucleon cross-section $\sigma_{\chi n}$ is significantly smaller than the current terrestrial bound. The accreted DM mass in a NS is

$$M_{\rm acc} \approx 10^{-16} \left(\frac{\rho_\chi}{\rm GeV/cm^3}\right) \left(\frac{\sigma_{\chi n}}{10^{-45}{\rm cm}^2}\right) \left(\frac{t_{NS}}{10^8 \text{ yrs}}\right) \; M_\odot \,, \tag{4.1}$$

where t_{NS} is the age of the neutron star and ρ_χ is the ambient DM density. When the DM mass in the core exceeds a critical value the DM self-gravity dominates, and in the absence of repulsive interactions bosonic DM becomes unstable and collapses to form a black hole. This black hole is then expected to devour the NS on a short timescale [163, 167, 221, 239, 220]. For MeV-GeV asymmetric bosonic DM a Bose-Einstein condensate can form earlier and hasten black hole formation. This may happen when the accreted number exceeds $N_c > 10^{36}\ (T/10^5 K)^3$ where $T \simeq 10^5 - 10^6$ K is the expected core temperature of an old NS [201]. The corresponding critical mass $M_c = N_c m_\chi \simeq 10^{-21} (m_\chi/{\rm GeV})\ M_\odot$ is small, suggesting that old neutron stars in our galaxy with ages $\simeq 10^8$ yrs should have accreted the DM mass needed to become unstable [221]. Old neutron stars such as J0437-4715 with estimated age $t_{NS} \simeq 10^9$ yrs thereby provide strong constraints on models of weakly interacting asymmetric bosonic DM [254].

Fermionic or bosonic DM with repulsive interactions can evade these constraints and form a stable hydrostatic configuration inside the NS [46]. Here we consider a simple renormalizable model of DM with self-repulsion. The repulsion arises from the exchange of a vector mediator from a spontaneously broken U(1) gauge interaction. We also couple this vector to

the Standard Model baryon number. The DM particle which we shall label χ can be either a charged scalar or a charged Dirac fermion. The model is defined by the following parameters: (i) m_χ is the mass of the charged fermion or scalar; (ii) m_ϕ is the mass of the mediator gauge boson ϕ; (iii) g_χ is the coupling strength of the gauge boson to the dark charge; and (iv) g_B, the gauge boson coupling to baryon number, is constrained by experiment and SN 1987a to be $\lesssim 10^{-10}$ [321]. As baryon number is anomalous in the standard model, there must be new physics which cancels this anomaly, see e.g. [141, 135]. Although the new physics may involve only new heavy particles, there will be an upper bound on the allowed strength of such a coupling, [123, 124], as the electroweak anomaly in baryon number will induce a coupling of the longitudinal mode of the dark photon to ordinary matter which goes inversely as the dark photon mass. For a coupling to baryons as large as 10^{-10} the dark photon must be heavier than about 10^{-4} MeV.

One objective of this chapter is to identify NS observables that can shed light on interacting DM candidates. Another is to explore the diversity of gravitational wave (GW) signals from merging NSs which may contain DM. Gravitational wave properties of compact dark stars were studied in [253, 287]. The possibility of hybrid compact objects containing DM has been discussed earlier in Ref. [239] and implications of a dark core with mass $\simeq 10\%$ of the NS mass for post-merger dynamics was explored in Ref. [128]. Here we calculate for the first time the tidal deformability of hybrid stars to address how trace amounts of DM would form a halo and influence GW emission during inspiral.

As discussed in sections 1.3.6 and 2.4 the quadrupole polarizability or tidal deformability λ of a star is defined by $Q_{ij} = -\lambda \mathcal{E}_{ij}$ where Q_{ij} is the induced quadrupole moment and $\mathcal{E}_{ij}$ is the applied tidal field. It is known that the tidal deformation of ordinary NSs with radii in the range $10 - 14$ km can produce discernible changes to the observed waveforms by accelerating inspiral and advancing the phase of the emitted GWs when the orbital radius is larger than but comparable to the radius of NS. The detection and analysis of GW emission from GW170817 suggest that the dimensionless measure of the tidal deformability $\Lambda = \lambda/M^5$ where M is the mass of the NS is small. GW170817 provides an upper bound

on tidal deformability of a canonical neutron star with mass $M = 1.4\ M_\odot$ and requires that $\Lambda_{1.4M_\odot} < 800$ [4] and the 90% confidence interval $\Lambda_{1.4M_\odot} = 190^{+390}_{-120}$ favors even smaller values [5]. Most nuclear physics based equations of state (EOS) predict $\Lambda_{1.4M_\odot}$ in this range and a large parameter space of the DM model defined earlier can be excluded if the NS contains a trace amount of DM with mass $\gtrsim 10^{-5}\ M_\odot$. This is our main result and will be discussed in detail in section 4.2. In section 4.3 we discuss the plausibility of finding trace amounts of DM inside neutron stars, and we conclude in section 4.4 by providing constraints for the DM interaction strengths for MeV-GeV scale DM.

4.2 Dark halos and their tidal deformability

As noted earlier fermionic DM and bosonic DM with repulsive interactions can form stable hydrostatic configurations since they have adequate pressure to balance gravity. In this section we shall assume that the DM mass inside the NS $M_\chi \ll M_{NS}$ where $M_{NS} \simeq 1.4 M_\odot$ is the mass of the neutron star. Since DM will represent a small perturbation of the radial distribution of baryon matter when M_χ is small, we first construct a NS composed of only nuclear matter. As discussed in section 1.3.2 this is done by choosing a nuclear EOS which specifies the relationship between pressure (p) and energy density ($\mathcal{E}$) and solving Tolman-Oppenheimer-Volkoff (TOV) equations for the hydrostatic structure[364, 282]. We adopt a widely used EOS for NS called the Akmal-Pandharipande-Ravenhall (APR) EOS [17] to determine the NS structure. Later we will explore more general parameterizations of the nuclear EOS to account for uncertainties associated with the dense matter EOS. For a chosen central energy density the solution to TOV equations determines the mass M, radius R, and radial profiles of the baryon density $n_B(r)$, the energy density $\mathcal{E}(r)$, the pressure $p(r)$, and metric functions $g_{rr}(r)$ and $g_{tt}(r)$ that define the spherically symmetric geometry. The profile of the pressure and the baryon number density inside a NS of mass $M = 1.4\ M_\odot$ are shown in Fig. 4.1.

To include DM we first note that in equilibrium the chemical potential of DM, denoted as μ_χ, should be a constant, and in the presence of neutron star's gravitational field this

requires (see appendix A.1.3)

$$\mu_\chi = \tilde{\mu}_\chi(r)\ \sqrt{g_{tt}(r)} = \text{constant}\,, \tag{4.2}$$

where $\tilde{\mu}_\chi(r)$ is the DM chemical potential in the stationary reference frame at radial coordinate r. If one neglects the back reaction of DM on the NS structure, a specification of $\tilde{\mu}_\chi(r=0)$ uniquely determines the distribution of DM inside the NS. The number density of DM n_χ is obtained by noting that $\tilde{\mu}_\chi(r) = (\partial\mathcal{E}_\chi/\partial n_\chi)$ where $\mathcal{E}_\chi$ is the DM energy density. Neglecting finite temperature effects, since thermal energies in NS are small, the energy density of DM is given by (recall $\hbar = c = 1$)

$$\mathcal{E}_\chi = \mathcal{E}_{\rm kin} + m_\chi n_\chi + \frac{g_\chi^2}{2m_\phi^2}\ n_\chi^2\,, \tag{4.3}$$

with $\mathcal{E}_{\rm kin}$ the DM kinetic energy. Here we neglect interaction between DM and baryons since we expect $g_B \ll g_\chi$. For spin $\frac{1}{2}$ dark fermions

$$\mathcal{E}_{\rm kin} = \frac{1}{\pi^2}\int_0^{k_{F\chi}}\ k^2{\rm d}k\ (\sqrt{k^2+m_\chi^2} - m_\chi)\,, \tag{4.4}$$

where the Fermi momentum $k_{F\chi} = (3\pi^2 n_\chi)^{1/3}$. For bosonic DM, the kinetic energy $\mathcal{E}_{\rm kin} \approx 0$ since bosons occupy the lowest momentum state. The pressure of DM is obtained from the thermodynamic relation $p_\chi = -\mathcal{E}_\chi + \tilde{\mu}_\chi n_\chi$ valid at zero temperature.

Repulsive interactions are necessary to stabilize bosonic DM, while for fermions the degeneracy pressure provides additional stabilization. The Compton wavelength for light mediators with m_ϕ in the eV-MeV range is much larger than the inter-particle distance, and the interaction between DM particles is enhanced since they interact with a large number of surrounding particles.

To include the back reaction of DM we adopt the following procedure. First we choose the central DM number density $n_\chi(0)$ and its corresponding local chemical potential $\tilde{\mu}_\chi(r=0)$. Using $g_{tt}(r)$ obtained from solving the TOV equations for nuclear matter NSs, by Eq. 4.2 the DM density profile is calculated in the local density approximation. The corresponding energy density and pressure contributions due to DM is obtained and used to update the

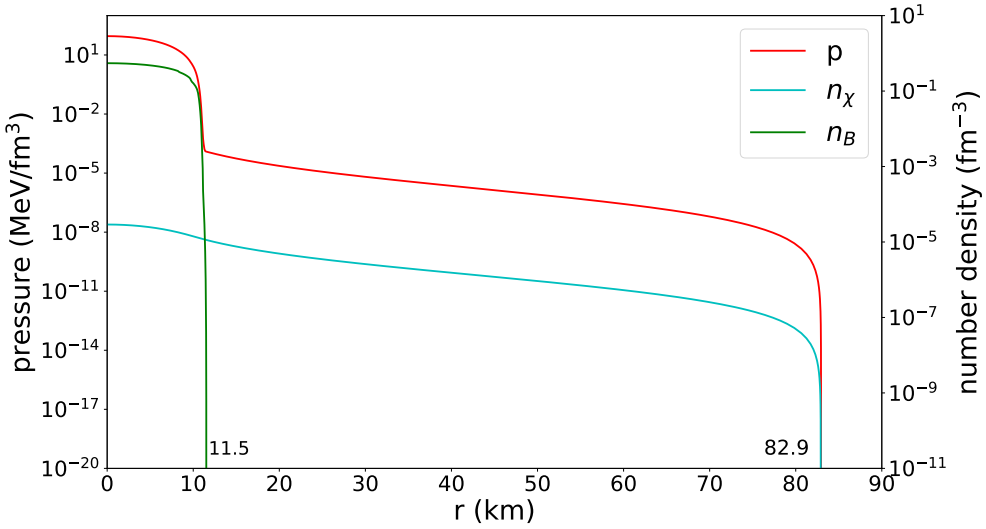

Figure 4.1: Density profile for a hybrid star with total mass $1.4M_\odot$ containing $M_\chi = 1.7 \times 10^{-4}\ M_\odot$ of DM. The presence of DM increases the tidal deformability of the NS from $\Lambda^{\rm APR}_{1.4M_\odot} = 260$ to $\Lambda_{1.4M_\odot} = 800$ for $m_\chi = 100$ MeV and $g_\chi/m_\phi = 5 \times 10^{-1}$ MeV^{-1}. The baryon density is shown in green, the total pressure shown in red, and the dark matter density is depicted by the cyan curve. The radius of dark halo increases with increasing coupling strength g_χ or decreasing DM particle mass m_χ. The baryon profile is almost independent of DM properties as long as $M_\chi \ll M_{NS}$.

EOS. The TOV equation is solved using the updated EOS and repeated iteratively for fixed central baryon number density $n_B(0)$ and $n_\chi(0)$ until convergence. We find that for total DM mass $M_\chi \lesssim 10^{-2}\ M_\odot$ effects of DM on the baryon density profile is negligible.

The extended DM halo modifies tidal interactions between merging NSs. As has been discussed in section 1.3.6, tidal interactions among component stars leave observable imprints on GW emission through the dimensionless tidal deformability $\Lambda = \frac{2}{3} k_2 R^5/M^5$. The calculation of Λ is discussed in section 2.4 and appendix A.2. We note that the functions $p(r)$ and $\mathcal{E}(r)$ appearing on the right hand side of Eq. 2.7 are uniquely specified by the hydrostatic structure of the unperturbed star and contain contributions due to baryons and DM as discussed earlier.

For reasonable ranges of DM model parameters we find large changes to Λ are possible. Results for $m_\chi = 100$ MeV and for different interaction strengths are shown in Fig. 4.2. Either strong couplings or light mediators can result in large Λ even for trace amounts of DM with total mass $M_\chi \ll M_{NS}$.

The enhancement of Λ with increasing total DM mass is remarkable. For small M_χ dark matter mostly reside inside NS (or its extent beyond the baryon surface is small) therefore the change in Λ due to DM is small. However, with increasing M_χ the dark halo extends further and the mass of dark matter at large radius increases. Since $\lambda = Q_{ij}/\mathcal{E}_{ij}$ where $Q_{ij} \propto \int \mathcal{E}(r) r^4 dr$ is the quadrupole moment induced by an external tidal $\mathcal{E}_{ij} \sim 1/r^3$, we expect λ to grow rapidly with M_χ because the halo radius R_χ increase with M_χ and the support of energy density $\mathcal{E}_\chi(r)$ extends further out. Dimensional analysis suggests that $\lambda \propto \int \mathcal{E}(r) r^7 dr$ and it is confirmed by our calculation. As the extent of the dark halo increases, $\langle \mathcal{E}_\chi r^7 \rangle$ increases rapidly and becomes the dominant contribution to λ when it exceeds the baryonic contribution $\langle \mathcal{E}_B r^7 \rangle$. This provides an explanation of the behavior seen in Figs. 4.2 and 4.3. Deformations of the halo will then dominate and greatly amplify tidal responses of the hybrid object. This is the main new finding of this study, and it provides a novel probe of the strongly interacting bosonic and fermionic light dark sectors.

Fermion dark halos are bigger and have larger Λ due to the additional contribution from

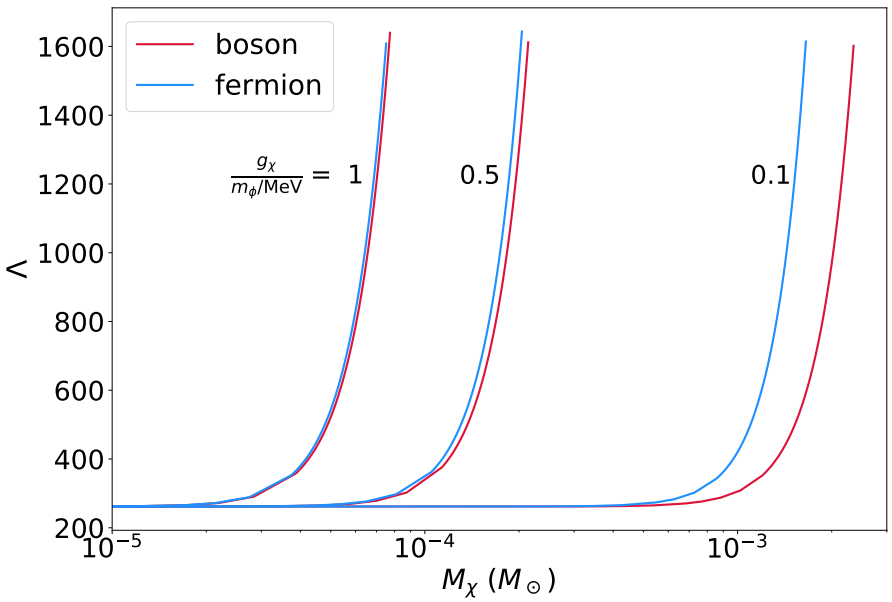

Figure 4.2: $\Lambda_{1.4M_\odot}$ increases rapidly with increasing total DM mass M_χ. For self-interacting DM with $g_\chi/m_\phi > 1$ MeV^{-1}, $M_\chi > 10^{-4}M_\odot$ will boost Λ above the upper bound ($\simeq 800$) set by GW170817.

the Fermi degeneracy pressure. For $m_\chi = 100$ MeV, the difference between fermions and bosons is modest but the difference increases rapidly with decreasing m_χ. Halos formed by fermions with $m_\chi \lesssim 30$ MeV can have large Λ even without vector-mediated self-interactions. For example, $\Lambda_{1.4M_\odot} = 800$ is reached for $m_\chi = 30$ MeV at $M_\chi = 10^{-4}M_\odot$, for $m_\chi = 10$ MeV at $M_\chi = 3 \times 10^{-6}M_\odot$, and for $m_\chi = 5$ MeV at $M_\chi = 4 \times 10^{-7}M_\odot$. However, the radii of these halos are large. At $\Lambda_{1.4M_\odot} = 800$, the halo radius $R \simeq 100$ km for $m_\chi = 30$ MeV, and $R \simeq 210$ km for $m_\chi = 10$ MeV. Since finite size effects during inspiral on waveforms are modeled without accounting for hydrodynamics, we focus on the phase when the dark halos do not overlap. For this reason we restrict our study to dark halos with radii $R \lesssim 150$ km. This will ensure that at lower frequencies detectable by LIGO the halos do not overlap.

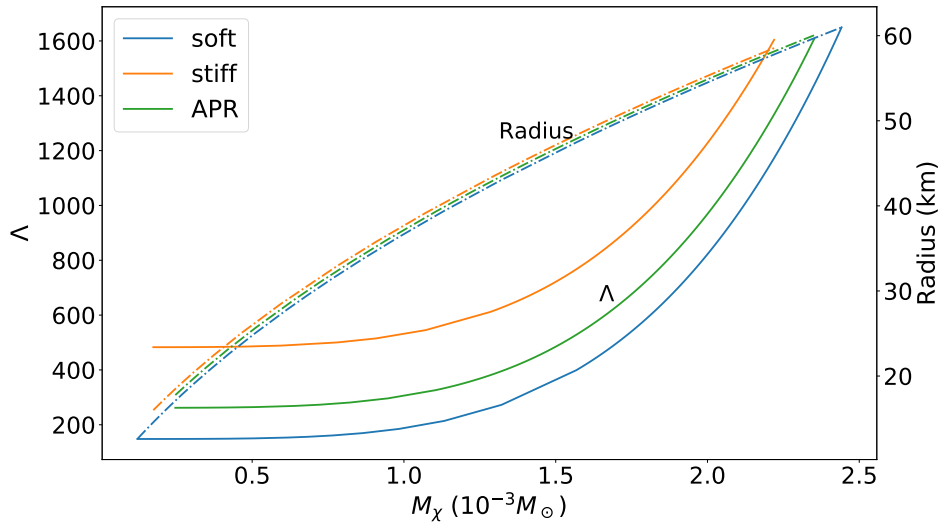

Figure 4.3: Variation of Λ (solid lines) and radius (dashed lines) of $1.4 M_\odot$ hybrid stars based on three representative realistic nuclear EOS [150] as a function of total dark matter mass M_χ. $\Lambda_{1.4 M_\odot}$ for neutron stars vary from 150 to 500. Dark matter is assumed to be bosonic with $m_\chi = 100$ MeV and $g_\chi / m_\phi = 0.1$ MeV^{-1}. The EOS labeled "soft" has a smaller pressure at a given density compared to the APR EOS and the EOS labeled "stiff" has a higher pressure. The former produces more compact neutron stars with a maximum $\simeq 2\ M_\odot$ NS, while the latter predicts a maximum mass $\simeq 2.4\ M_\odot$ and larger radii.

Many-body theories of neutron matter which employ realistic nucleon-nucleon interactions can calculate the EOS up to densities $\simeq 3 \times 10^{14}$ g/cm^3 and estimate its error rather reliably[150, 182, 360]. Using these calculations, and despite large uncertainties associated with the nuclear EOS at higher density, earlier work has shown that the radius of a $1.4\ M_\odot$ NS is in the range $10 - 13$ km [183, 150, 360]. The corresponding tidal deformability Λ is in the range $100 - 500$. To explore this range we employ a more general parameterization of neutron matter EOSs based on realistic nucleon-nucleon interactions discussed in [150] and construct equations of state that are stiffer and softer than the APR EOS discussed

earlier. A softer EOS has on average lower pressure for the densities encountered and would result in more compact neutron stars with a smaller maximum mass compared to the APR EOS. In contrast a stiffer EOS will have a larger pressure at a given density compared to the APR EOS and would result in larger NS radii and a maximum mass. The radii and tidal deformabilities of NSs with DM constructed using the three representative nuclear EOSs as a function of M_χ is shown in Fig. 4.3. A relatively small increase in the amount of DM allows one to obtain large values of Λ inaccessible to ordinary NSs.

4.3 Accumulating dark matter in a neutron star

The proto-neutron star (PNS) formed subsequent to core-collapse during a supernova is characterized by high temperature $T_{\rm PNS} \simeq 30 - 50$ MeV and density. Under these conditions reactions such as $NN \to NN\chi\bar{\chi}$ can produce a large number of dark matter pairs even when the coupling between dark matter and baryons is weak. In our simple model, the interaction between baryons and dark matter particles is mediated by a light vector boson which couples weakly to baryons with $g_B \lesssim 10^{-10}$. The upper bound on g_B is in fact obtained by requiring that the total energy radiated due to the Bremsstrahlung reaction $NN \to NN\phi$ from the PNS does not exceed $\approx 10^{53}$ ergs, to be compatible with the neutrino signal observed from SN1987 [321, 91, 92]. The supernova bound is most constraining for gauge bosons that either only couple to baryon number or when their mass is greater than about a MeV. More stringent constraints have been derived using observations of stellar evolution for lighter vector bosons couple to electrons as would be the case when they are identified with either the dark photon or the $B - L$ gauge boson. In this case observations of horizontal branch stars and red giants require that $g_B \lesssim 10^{-14}$ for $m_\phi \lesssim 1$ MeV. In what follows we assume that dark matter only couples to baryons to establish that an adequate amount of dark matter can be produced during the supernova.

Pair production through the reaction $NN \to NN\chi\bar{\chi}$ will proceed at a rate comparable to the Bremsstrahlung reaction when the mass of the DM pair is not much larger than $T_{\rm PNS}$. This implies that a non-negligible fraction of thermal energy of the PNS can be converted into

DM pairs. For $g_B = 10^{-10}$ and $m_\chi \lesssim 100$ MeV, we have estimated that the energy radiated as DM pairs is $\approx 10^{51}$ ergs and the corresponding mass of DM produced is $M_\chi = 6\times10^{-4}\ M_\odot$.

In the absence of interactions between dark matter and baryons these pairs will either escape the star when their velocities are larger than the (local) escape velocity ($\sim v_{\rm esc} = R_S/R_{\rm NS} \simeq 0.4$, where $R_S = 2M_{\rm NS}$ is the Schwarzschild radius of NS) or will annihilate away inside the star. However, the coupling to baryons creates an asymmetry between the energies of dark particles and dark antiparticles and provides a unique mechanism to trap dark charges in NSs.

For the DM model under consideration, the energy of χ and $\bar{\chi}$ in a dense background of baryons can be calculated using mean-field theory. Assuming that dark matter is attracted to baryons and the anti-dark matter is repulsed, we find that their energies are given by

$$E_\chi(p) = \sqrt{p^2 + m_\chi^2} - \frac{g_\chi g_B}{m_\phi^2}\ n_B\,,$$
$$E_{\bar{\chi}}(p) = \sqrt{p^2 + m_\chi^2} + \frac{g_\chi g_B}{m_\phi^2}\ n_B\,,$$

respectively. The energy splitting

$$\begin{aligned}\Delta E = E_{\bar{\chi}} - E_\chi &= \frac{2g_\chi g_B}{m_\phi^2}\ n_B \\ &\simeq 40\ \text{MeV}\ \frac{g_\chi g_B}{10^{-11}} \left(\frac{0.1\ \text{keV}}{m_\phi}\right)^2 \frac{n_B}{0.5\ \text{fm}^{-3}}.\end{aligned} \tag{4.5}$$

can be large. For m_ϕ in the range eV - MeV and $g_B g_\chi \simeq 10^{-16} - 10^{-10}$ this energy splitting is comparable to the gravitational binding energy of DM.

This asymmetry will preferentially expel anti-dark matter from the PNS and provide a mechanism to trap a net dark charge in NS that will not be diminished by annihilation. The gradient in the baryon density will induce a force on dark matter towards the core and expel anti-dark matter towards the surface. For example, for model parameters $m_\chi = 50$ MeV, $g_\chi = 1$, $g_B = 10^{-10}$ and $m_\phi = 1$ keV, we find that 80% of χ's produced during the supernova will remain trapped and survive annihilation while most of the $\bar{\chi}$'s will be accelerated to velocities adequate to escape the PNS.

Once trapped the cloud of DM particles will thermalize among themselves rapidly by exchanging energy and momenta through multiple $\chi\chi \to \chi\chi$ scatterings. In the born approximation the cross-section is

$$\sigma_{\chi\chi}^{\rm Born} = \frac{g_\chi^4 m_\chi^2}{4\pi m_\phi^2 (m_\phi^2 + p^2)} \approx \frac{g_\chi^4 m_\chi}{8\pi m_\phi^2 T}.$$

where $p^2 \simeq T^2 + 2m_\chi T \simeq 2m_\chi T$ is the typical momenta of χ's at temperature T, and we assume that $m_\phi^2 \ll m_\chi T$ to obtain the last equality. The corresponding mean free path λ is estimated to be

$$\begin{aligned} \lambda &= \frac{1}{n_\chi \sigma_{\chi\chi}} \simeq 10^{-12}\ \text{km} \\ &\times \frac{10^{-4} M_\odot}{M_\chi} \left(\frac{0.1}{g_\chi}\right)^4 \left(\frac{R_\chi}{10\ \text{km}}\right)^3 \left(\frac{m_\phi}{1\ \text{keV}}\right)^2 \frac{T}{30\ \text{MeV}}, \end{aligned} \tag{4.6}$$

assuming that the DM density $n_\chi = (M_\chi/m_\chi)/(4\pi R_\chi^3/3)$. The short mean free path implies that the timescale for thermalization among DM particles $\tau \approx 1/(n_\chi v \sigma_{\chi\chi})$ is much smaller than all other relevant timescales. Further, despite its weaker coupling to baryons the timescale for DM to thermalize with baryons is also very short, typically much less than a second, for reasonable values of the coupling needed to produce adequate DM. Thus, it is safe to assume that DM in neutron stars shortly after their birth will be characterized by the same low temperature $T <$ MeV of ordinary matter and any further loss of DM due to evaporation is negligible. Although a detailed study of DM production and charge separation due to interactions with baryons is warranted and will be reported elsewhere, the preceding arguments provide a natural mechanism to generate DM in neutron stars with a mass on the order of $10^{-4}\ M_\odot$.

Another possibility is to link the asymmetry in lepton number or baryon number in a supernova to the DM asymmetry. To provide an existence proof for an asymmetric production mechanism for ADM in a supernova, we constructed the following simple model. In our model, besides the DM particle χ, which carries dark charge $+1$, we also introduce a particle Φ which carries dark charge -1. We also charge χ under the global $B - L$ symmetry of the standard model. If χ is a spin 0 boson then Φ is a Dirac Fermion, although this scenario will

also work if χ is a Dirac fermion and Φ is a boson. The dark $U(1)$ will be Higgsed by a field ξ which carries dark charge 2. In addition, we introduce a "right handed" (aka "sterile") Dirac neutrino N, which can mix with the standard model neutrinos ν as in reference [59] and has no standard model gauge interactions. This mixing will also lead to productions of N particles via charged weak currents, with N and $\bar{N}$ being produced asymmetrically due to the lepton asymmetry. This asymmetry will be converted to an asymmetry in the DM due to the following interaction term:

$$\mathcal{L} \supset \lambda N \Phi \chi + g \Phi \Phi \xi + \text{h.c.} \tag{4.7}$$

These terms are allowed by all symmetries. The vacuum expectation value of ξ will split the CP even and CP odd components of Φ, leaving a Z_2 symmetry unbroken under which χ and Φ are both charged. We label the two mass eigenstates of Φ as Φ_1, Φ_2. Because ξ is not allowed by B-L number to couple to the DM particle χ, the CP even and odd components of χ are not split, and χ continues to carry an exactly conserved $U(1)_D$ global charge. Provided that $m_N > m_{\Phi_1} + m_\chi$, the decays $N \to \bar{\chi} + \Phi_1$ will transmit the asymmetry in the production of N particles to an asymmetry in the production of DM χ particles. The Φ_1 particles, which are CP eigenstates, will decay with equal branching fractions into $\bar{\chi} + \nu$ and $\chi + \bar{\nu}$. Note that a related mechanism in the early universe could lead to genesis of a DM asymmetry from the lepton number asymmetry.

The mechanisms discussed above are generic and would endow all neutron stars with similar amounts of dark matter with perhaps a small variability associated with differences between neutron star and supernova properties. This allows us to constrain the properties of DM using the upper bound on the tidal deformability obtained from GW170817 as we shall discuss in the next section. However, we note that third-generation GW detectors such as the Einstein telescope [298] capable of detecting thousands of BNS mergers within a few years motivate looking for variability in neutron star merger properties. If variability in the tidal deformability is detected in rare events it would imply that some fraction of neutron stars are able to capture large amounts of dark matter. Further, since neutron stars are not estimated

to accrete nearly enough dark matter on average to produce an observable gravitational wave signature if dark matter is distributed uniformly on galactic scales [222, 223, 219, 88, 217], discovering variability would have important implications for small scale structures in dark matter and hint at the existence of compact dark objects.

Such objects are possible in some models of self-interacting DM such as atomic dark matter which contain particles and interactions that can lead to the formation of macroscopic objects through cooling mechanisms analogous to the baryonic sector [209]. Constraints on dark compact objects such as clumps of dark matter arise from microlensing surveys. However, even the most stringent constraints derived by the EROS collaboration cannot exclude the possibility that a few percent of dark matter in the galactic halo is in the form of dark compact objects with mass $\gtrsim 10^{-5}\ M_\odot$ [363]. It is conceivable that such compact dark objects can be captured by massive stars or neutron stars, and would provide an explanation should variability in the tidal deformability be seen in future observations of merging neutron stars.

4.4 Conclusions

Motivated by the prospect that more BNS and black hole-NS merging events will give better constraints on the tidal deformability Λ, we have studied how these observations might provide insights about strongly interacting DM. We have shown that trace amounts of DM with total mass $M_\chi \gtrsim 10^{-5}\ M_\odot$ trapped in a NS, either produced during a supernova, or inherited from the progenitor star, may form a stable dark halo with radius $R \simeq 30 - 150$ km given sufficient self-repulsion. This can enhance Λ of the hybrid to a value significantly larger than expected for ordinary NSs, which despite uncertainties associated with the EOS at supra-nuclear densities, have $\Lambda_{1.4M_\odot} \lesssim 500$. Interactions between DM due to exchange of light mediators are coherent and lead to large halos even when M_χ is small. Further, we find that small variability in the amount of trapped DM can produce large variability in $\Lambda_{1.4M_\odot}$, distinguishing them from ordinary NS where the expected variability is small. These observable features are unique signatures of strongly interacting DM that can be probed

with LIGO and future GW detectors.

If trace amounts of DM were present in all neutron stars because it was produced during the supernova the constraint from GW170817 that $\Lambda_{1.4M_\odot} < 800$ already excludes a significant fraction of the DM parameter space in our model. The bounds for bosonic DM from our simple model are shown in Fig. 4.4. We have fixed $M_\chi = 10^{-4}\ M_\odot$ and varied the DM particle mass m_χ and effective coupling strength g_χ/m_ϕ to obtain the contours of $\Lambda_{1.4M_\odot}$. Bounds for different values of M_χ can also be obtained and we found the contour of $\Lambda_{1.4M_\odot} = 800$ when $M_\chi \lesssim 0.1 M_\odot$ can be approximately fitted by

$$\left(\frac{g_\chi}{m_\phi/\mathrm{MeV}}\right)_{\Lambda_{1.4M_\odot}=800} = 1.6\times 10^{-5}\left(\frac{M_\chi}{M_\odot}\right)^{-2/3}\frac{m_\chi}{\mathrm{MeV}}\,. \tag{4.8}$$

It is remarkable that models with light mediators are severely constrained. For example, a model with $m_\chi = 100$ MeV and $m_\phi = 1$ eV requires $g_\chi \lesssim 10^{-6}$. These constraints should be especially useful since recent observations of strong absorptions of the Lyman-α radiation from some of the earliest stars corresponding to the 21-centimeter transition of atomic hydrogen around redshift $Z \sim 20$ [68] appears to favor light DM in the MeV-GeV mass range and whose interactions (with baryons) are due to the exchange of much lighter mediators [35].

Similar bounds can be obtained for fermions as shown in fig. 4.5. For heavy fermions, where the contribution due to the Fermi degeneracy pressure is small, contours of Λ are very similar to those obtained for bosons. As already noted it is interesting that for light dark fermions with $m_\chi \lesssim 30$ MeV, $\Lambda_{1.4M_\odot}$ can be larger than 800 even in the absence of strong interactions or light mediators. This is clearly seen in the behavior of contours for small values of m_χ when they plunge to smaller values of the effective coupling strength g_χ/m_ϕ. In all cases we have used the APR EOS to describe the underlying NS. We also set $g_B = 0$ in which case the effective Fermi coupling $(g_\chi/m_\phi)^2$ alone determines the interaction strength.

As noted earlier, simulations of large scale structure performed with collisionless DM is unable to account for features on small scales. In particular, simulations predict an excess

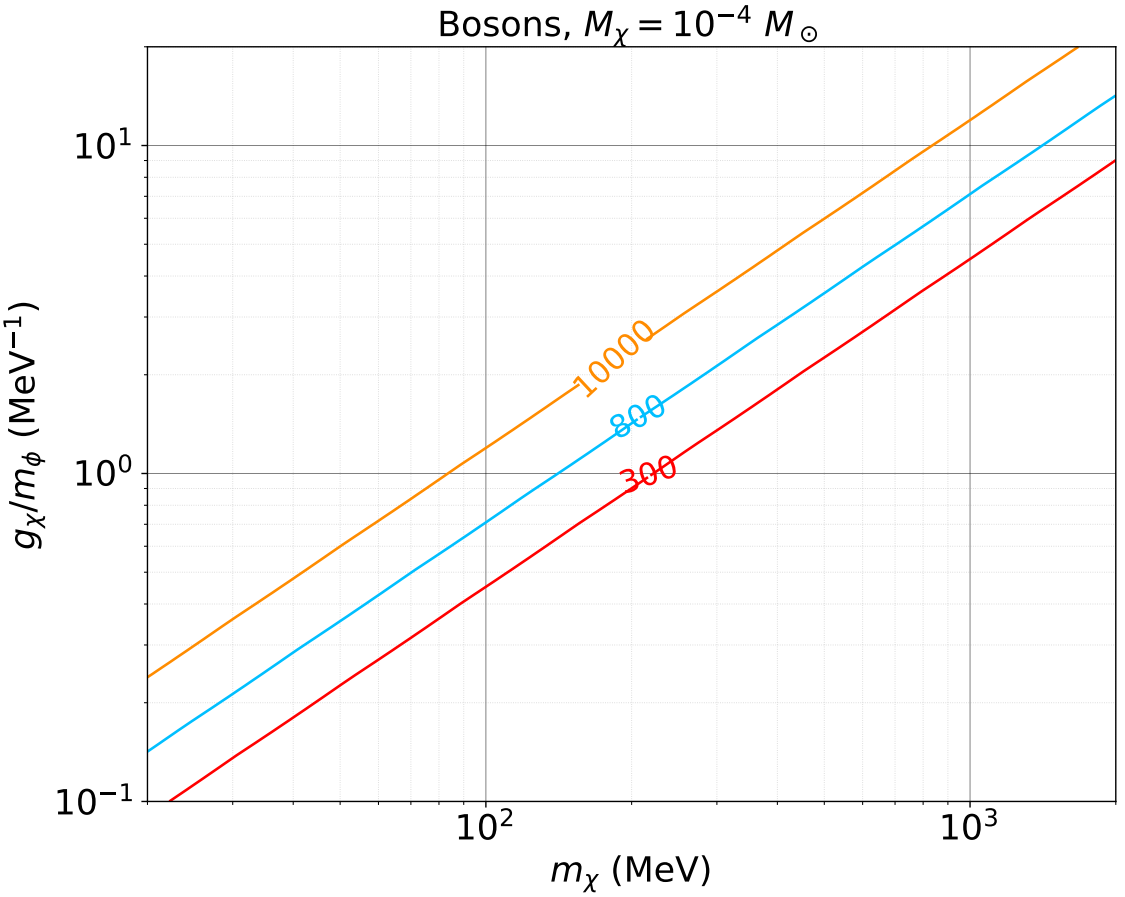

Figure 4.4: Contours of dimensionless tidal deformability for 1.4 $M_\odot$ hybrid stars containing 10^{-4} $M_\odot$ of bosonic DM. The parameter space to the left of the red contour labeled 800 is disfavored by the first detection of gravitational waves (GW170817) from merging neutron stars.

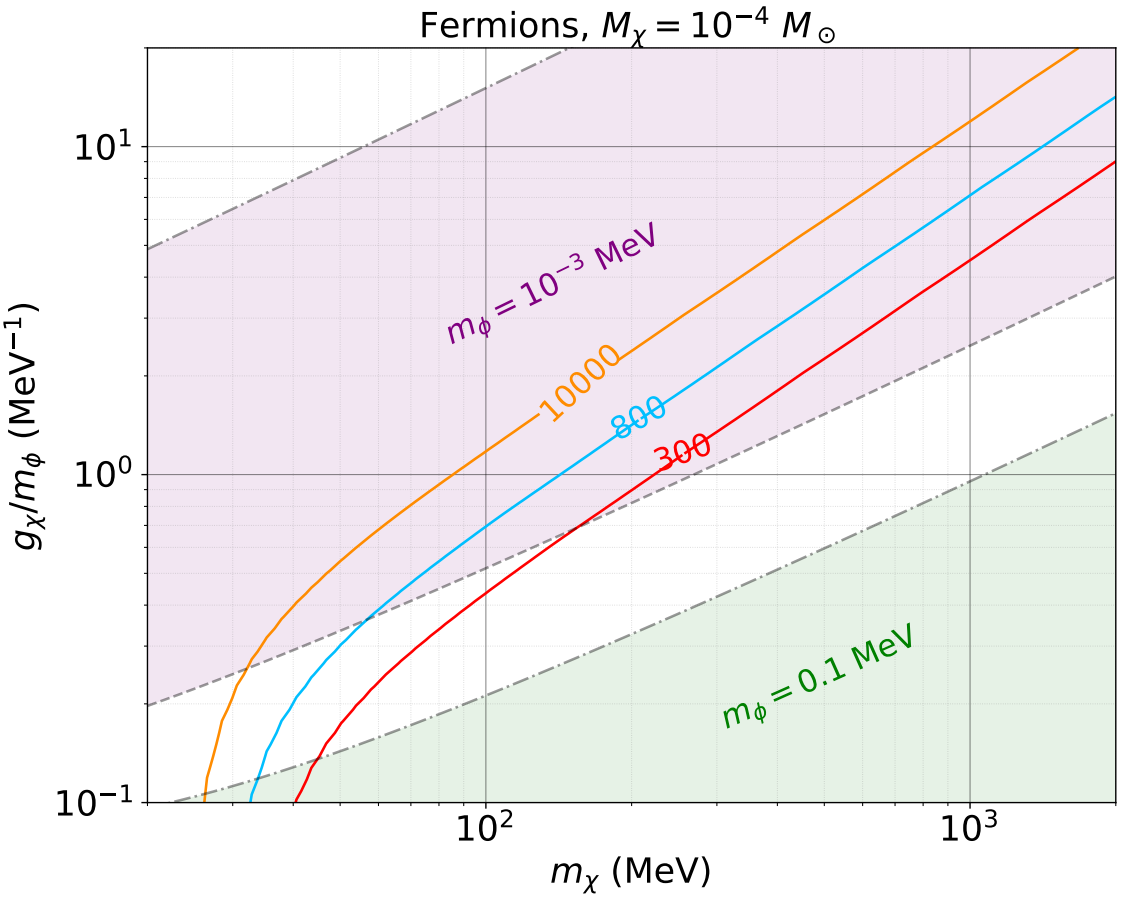

Figure 4.5: Contours of $\Lambda_{1.4M_\odot}$ for hybrid stars containing $10^{-4}\ M_\odot$ of fermionic DM. Regions above dash-dotted lines produce large cross-sections excluded by Bullet Cluster for given mediator masses m_ϕ, and the shaded regions between the dashed and dash-dotted lines correspond to the parameter space where the transport cross-section is adequate to provide an explanation of the DM density profiles in the cores of galaxies and clusters [211].

DM density in the cores of halos of galaxies and clusters, and these discrepancies have been discussed extensively in the literature. For a recent review see [365]. Collisions between DM particles can alleviate some of these issues if the transport cross-section is large enough. For example, a mildly velocity-dependent transport cross-section per unit mass, $\sigma_t/m \simeq 2$ cm^2/g on galactic scales, and $\sigma_t/m \simeq 0.1$ cm^2/g on cluster scales has been shown to provide a consistent solution to the dark matter deficit [211]. These cross-sections can be consistent with upper limits derived from observations of the Bullet Cluster which requires $\sigma_t/m < 1.25$ cm^2/g with estimated relative velocity $v_{rel} \approx 3000$ km/s [302] for velocity-dependent interactions. Although in general the tidal deformability provides a complementary constraint, in the scenario where χ is the sole dark matter particle with Yukawa interactions mediated by a vector boson, as in our simple model, a comparison of these different constraints is useful. To make this comparison we choose two values for the mediator mass: $m_\phi = 1$ keV (purple) and $m_\phi = 0.1$ MeV (green) in Fig. 4.5. The shaded parameter region corresponds to values of the transport cross-section that would make N-body simulations of halos of galaxies and clusters compatible with observations. Dashed curves are obtained by setting $\sigma_t/m \simeq 0.7$ cm^2/g for $v_{rel} = 4000$ km/s (a tighter constraint from Bullet Cluster mass-to-light ratio), and the dashed curve is obtained by setting $\sigma_t/m \simeq 1$ cm^2/g for $v_{rel} = 100$ km/s. The parameter space to the left of the dash-dotted curve violates the cross-section bound from the Bullet Cluster.

With more detections of BNS and black hole-neutron star mergers expected we anticipate that the limits on the tidal deformability will improve and provide stronger constraints. There is also the tantalizing possibility that as the detection sample grows, LIGO might detect a larger than expected variability in the tidal deformability for neutron stars implicating that some may have dark halos. We have also proposed new mechanisms for DM production and retention. These warrant further study to obtain quantitative estimates for the amount of DM accumulated and its dependence on the model parameters.

Finally, we note that our study only addressed how DM halos influence GW emissions through their effects on Λ before the dark halos overlap. The dynamics of larger halos or

later times during the merger will likely have other interesting observable signatures. We hope our study will motivate the inclusion of DM in numerical relativity simulations to study the complex hydrodynamic evolution of the merger of hybrid stars.

Chapter 5

DARK LEPTON SUPERFLUID IN PROTO-NEUTRON STARS

[1]

We find that sub-GeV neutrino portal bosons that carry lepton number can condense inside a proto-neutron star. These bosons are produced copiously and form a Bose-Einstein condensate for a range of as yet unconstrained coupling strengths to neutrinos. The condensate is a lepton number superfluid with transport properties that differ dramatically from those encountered in the ordinary dense baryonic matter. We discuss how this phase could alter the evolution of proto-neutron stars and comment on the implications for neutrino signals and nucleosynthesis.

5.1 Introduction

Recently, the possibility that dark matter particles may interact strongly with neutrinos has sparked strong interests [36, 58, 70, 52, 115, 225, 65, 32]. These interactions can generate stronger self-interactions between neutrinos mediated by new degrees of freedom [225, 65] and have been invoked to explain hints of anomalies in neutrino oscillation experiments [14, 15] and puzzling cosmological observations [53, 309, 310]. In this article we consider dark bosons that carry lepton number L but is otherwise uncharged with respect to the SM gauge group and demonstrate its novel implications in extreme astrophysical environments.

Proto-neutron stars (PNSs) provide a unique laboratory to study DM coupled to neutrinos. As noted in section 1.3, a PNS born in the aftermath of core-collapse supernovae explosion is hot ($T \simeq 30$ MeV) and contains large densities ($\rho \simeq 5 \times 10^{14}$ g/cm^3) of baryons and leptons. Detailed simulations have shown that neutrinos are trapped inside the PNS, and that

[1] this chapter is based on [308] which is submitted to Physical Review D.

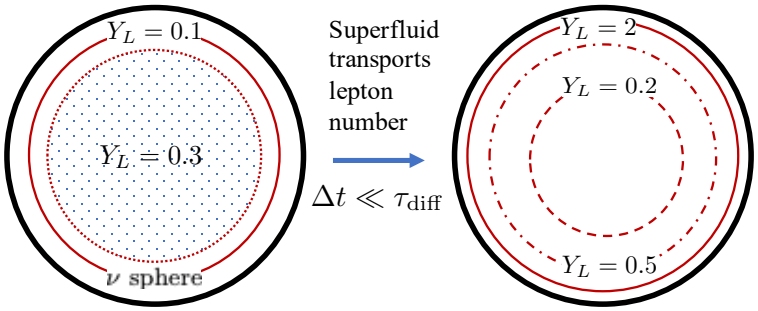

Figure 5.1: Superfluid transport of lepton number due to ϕ condensation rapidly quenches the spatial gradients in the lepton number chemical potential. It transforms the initial state with an approximately constant lepton fraction $Y_L \simeq 0.3$ (depicted on the left) to the state on the right.

their diffusion takes $\tau_{\rm diff} \sim$ tens of seconds [387, 80]. During this time, the hot and dense PNS matter supports a large chemical potential for lepton number ($\mu_L = \mu_{\nu_e} \simeq 100 - 200$ MeV) and a corresponding large excess of electron neutrinos. These conditions, which are not realized in any other environment in the universe, present an opportunity to study DM candidates that carry lepton number.

In this chapter we show that lepton number scalars, denoted by ϕ, will have important implications for PNSs. For a wide range of parameter space compatible with existing constraints, ϕ particles are rapidly produced in the PNS and thermalize to form a Bose-Einstein condensate. The condensate is a superfluid that transports lepton number from the core to the surface of PNS on timescales that are negligible compared to neutrino diffusion. This alters the radial distribution of lepton number (see fig. 5.1) and modifies the composition and neutrino transport properties of dense matter inside the PNS.

We introduce the lepton number scalar ϕ through a minimal model defined by the low-energy effective Lagrangian [58]

$$\mathcal{L}_{\text{eff, int}} \supset -\frac{g_{\alpha\beta}}{2}\nu_\alpha \nu_\beta \phi^* + \text{h.c.} - m_\phi^2 \phi^* \phi - \frac{\lambda}{4}(\phi^* \phi)^2. \tag{5.1}$$

Here, $g_{\alpha\beta}$ is the coupling between left-handed Weyl neutrinos $\nu_{\alpha,\beta}$ and the scalar ϕ that

carries lepton number 2. α, β are flavor indices and the quartic coupling λ characterizes the strength of self-interaction among ϕ's. In general, $g_{\alpha\beta}$ may involve all 3 flavors e, μ, τ. However, in what follows we focus on the flavor conserving coupling to electron neutrinos $g_{ee} = g$, and comment on the possible role of couplings to μ and τ neutrinos in our concluding remarks.

This coupling g may arise after electroweak symmetry breaking from the effective operator $(l\tilde{H})(l\tilde{H})\phi^*/\Lambda^2$ [74, 58], where $l = (\nu_e, e)^T$ is the SM lepton doublet, $\tilde{H} = i\sigma_2 H^*$ is the flipped SM Higgs doublet, and Λ is the high-energy scale associated with new physics. Since the Weinberg operator $(l\tilde{H})(l\tilde{H})$[378] carries lepton number 2, the Lagrangian eq. 5.1 conserves L. This effective operator is one of few dimension six operators that generates neutrino self-interactions. In contrast to conventional majoron models where the coupling is highly suppressed by neutrino Majorana masses [96, 157], in this scenario, the natural strength for the coupling $g \simeq (v/\Lambda)^2$ ($v = 246$ GeV is the electroweak scale) is expected to be large from the model building perspective [74, 58].

Laboratory constraints on the coupling $g_{\alpha\beta}$ are flavor dependent. For $g \equiv g_{ee}$, limits from exotic meson decays demand $g \lesssim 10^{-2}$ when $m_\phi \lesssim$ GeV, and double beta-decay experiments require $g \lesssim 10^{-4}$ when $m_\phi \lesssim$ MeV [289, 58, 115]. Astrophysical and cosmological bounds on the parameter space are also quite stringent. For $m_\phi \lesssim 10$ MeV and $g \gtrsim 10^{-10}$, a thermal population of $\phi's$ alters the expansion history of the early universe during and after weak decoupling. This spoils the concordance between the predictions of Big Bang nucleosynthesis (BBN) and observations of light element abundances [105, 65], and is also in tension with the observed cosmic microwave background (CMB) spectrum [225]. The supernovae cooling bound based on SN1987a – the core-collapse supernova occurred in the Large Magellanic Cloud in 1987 – excludes $g^{-11} \lesssim g \lesssim 10^{-6}$ when $m_\phi \lesssim 50$ MeV [190, 70]. This constraint arises because the duration of the observed neutrino signal is shortened when free streaming weakly interacting particles rapidly cool the PNS core subsequent to their thermal production [301].

In this chapter, we will focus on the as yet unconstrained region for ϕ's with mass $m_\phi \gtrsim 10$

MeV and a coupling to electron neutrinos in the range $10^{-6} \lesssim g \lesssim 10^{-2}$ to show that novel phenomena arise in the PNS that can probe new physics at energy scale $\Lambda \sim 1 - 10^4$ TeV.

5.2 ϕ condensation in the PNS

As noted earlier, the PNS is characterized by high baryon number density $n_B \simeq 1 - 3\ n_0$, where $n_0 = 0.16\ \text{fm}^{-3}$ is the nuclear saturation density, high temperature $T \sim 20 - 60$ MeV, and a lepton fraction $Y_L = n_L/n_B \simeq 0.3$. In this hot and dense environment lepton number scalars are produced rapidly through $\nu\nu \to \phi$. The rate of production is given by

$$\frac{\mathrm{d}n_{\nu\nu\to\phi}}{\mathrm{d}t} = \int \frac{\mathrm{d}^3p_1}{2E_{p_1}(2\pi)^3}\frac{\mathrm{d}^3p_2}{2E_{p_2}(2\pi)^3}\frac{\mathrm{d}^3k}{2E_k(2\pi)^3} \times \frac{\left|\mathcal{M}_{\nu\nu\to\phi}\right|^2}{2} f_1 f_2 (2\pi)^4 \delta^4(p_1 + p_2 - k)\,, \quad (5.2)$$

where $\left|\mathcal{M}_{\nu\nu\to\phi}\right|^2 = 4g^2(p_1 \cdot p_2)$ is the square of the tree level matrix element, and $f_{1,2} = 1/\left(1 + \exp\left[(E_{p_{1,2}} - \mu_L)/T\right]\right)$ are the Fermi-Dirac distribution functions for neutrinos. For $g > 10^{-6}$ and $T \simeq 10$ MeV, the timescale for transferring lepton number to the ϕ particles $\tau_{\text{prod}} \simeq n_L/\dot{n}_{\nu\nu\to\phi} \ll \tau_{\text{diff}}$. Further, most of the ϕ's produced have short mean free paths due to the inverse decay process hence are trapped and subsequently thermalize with the star. Qualitatively, the relaxation timescale can be calculated as

$$\begin{aligned}\frac{1}{\tau} &= \frac{1}{2E_k g_k}\int \frac{\mathrm{d}^3p_1}{2E_{p_1}(2\pi)^3}\frac{\mathrm{d}^3p_2}{2E_{p_2}(2\pi)^3} \times \frac{\left|\mathcal{M}_{\nu\nu\leftrightarrow\phi}\right|^2}{2} f_1 f_2 (2\pi)^4 \delta^4(p_1 + p_2 - k) \\ &= \frac{g^2 m_\phi^2}{16\pi g_k}\int_{\frac{E_k - k}{2}}^{\frac{E_k + k}{2}} \frac{\mathrm{d}E_1}{E_1^2} f_{E_1} f_{E_k - E_1},\end{aligned} \quad (5.3)$$

where $g_k = 1/(\exp((E_k - \mu_\phi)/T) - 1)$ denotes the Bose-Einstein distribution function of ϕ's. For a simple estimate we set all the distribution functions to 1 and find that the mean free path of ϕ's

$$\lambda_\phi = v\tau \sim 10^{-8}\ \left(\frac{10^{-3}}{g}\right)^2 \left(\frac{50\ \text{MeV}}{m_\phi}\right)^2 \left(\frac{T}{30\ \text{MeV}}\right)\ \text{km}\,. \quad (5.4)$$

Consequently, for the range of couplings considered in this study, ϕ's produced in PNS are in chemical and thermal equilibrium with neutrinos.

Since ϕ carries two units of lepton number, its chemical potential $\mu_\phi = 2\mu_L$. When $\mu_\phi > m_\phi$, there will be a macroscopic occupation of ϕ's in the zero-momentum state, and the ground state is a Bose-Einstein condensate. In the PNS where $\mu_L \simeq 200$ MeV at early times, we can expect condensation for $m_\phi \lesssim 2\mu_{L,max} \simeq 400$ MeV.

In the absence of repulsive forces between ϕ's, the density of the condensate grows rapidly in the core of the PNS. When the total mass of bosons in the core exceeds $M_{crit} \simeq m_{pl}^2/m_\phi \approx$ (100 MeV/m$_\phi$) 10^{-18} M$_\odot$ the boson clouds collapse to form a black hole. The black hole once formed is expected to subsequently consume the entire star [254, 201]. Thus, the very existence of neutron stars rules out such scenarios and viable models for ϕ must include repulsive self-interactions. Even a small quartic coupling λ in Eq. 5.1 alters the effective potential for ϕ's [173, 48, 213, 47]

$$V_{\rm eff}(\phi) = (m_\phi^2 - \mu_\phi^2)\phi^*\phi + \frac{\lambda}{4}(\phi^*\phi)^2\,, \tag{5.5}$$

and provides the necessary stabilization. When condensation occurs the finite vacuum expectation value (vev) of the scalar field that minimizes the effective potential above is given by

$$\langle\phi\rangle = \sqrt{2(\mu_\phi^2 - m_\phi^2)/\lambda}\,. \tag{5.6}$$

This vev breaks the global $U(1)_L$ symmetry and leads to superfluidity.

In the symmetry broken phase, the excitation spectrum is modified. The two degrees of freedom associated with the complex ϕ field manifest as fluctuations around the vev. Denoting the massless Goldstone mode as J, and the massive mode as σ, in the condensed phase we can write $\phi = (f + \sigma + iJ)/\sqrt{2}$, where $f = \sqrt{2}\langle\phi\rangle$. The dispersion relations for the goldstone mode (ω_-^ϕ) and the massive mode (ω_+^ϕ) are [173, 48, 213, 47][2]

$$\omega_\pm^\phi = \sqrt{E_p^2 + \mu_\phi^2 + \frac{\lambda f^2}{2} \pm \sqrt{\frac{\lambda^2 f^4}{16} + \mu_\phi^2(4E_p^2 + 2\lambda f^2)}}\,, \tag{5.7}$$

where $E_p = \sqrt{p^2 + m_\phi^2}$.

[2]See also appendix G.

The propagation of neutrinos is also modified in the superfluid phase because ν's directly couple to the condensate. When ϕ acquires a vev, the Yukawa term in eq. 5.1 becomes

$$\mathcal{L}_{\text{Yukawa}} \supset \frac{g}{2\sqrt{2}} (f + \sigma + iJ)\, \nu\nu + \text{h.c.}. \tag{5.8}$$

The term proportional to f, which would have led to a (left-handed) neutrino Majorana mass in the vacuum ($\mu_L = 0$), leads to pairings of electron neutrinos near their Fermi surface. This BCS-like pairing introduces a gap $\Delta = g\langle\phi\rangle$ in the neutrino excitation spectrum

$$\omega^{\nu}_{\pm} = \sqrt{\Delta^2 + (p \pm \mu_L)^2}\,. \tag{5.9}$$

For the viable range of coupling $g \lesssim 10^{-2}$, this gap is negligible compared to the temperature in PNS.

The grand potential per unit volume for neutrinos is

$$\Omega_\nu = \int \frac{\mathrm{d}^3 p}{(2\pi)^3} \left[\frac{1}{2}(\omega^{\nu}_{+} + \omega^{\nu}_{-}) + T \log\left(1 + e^{-\omega^{\nu}_{+}/T}\right) + T \log\left(1 + e^{-\omega^{\nu}_{-}/T}\right)\right], \tag{5.10}$$

and for ϕ's is

$$\Omega_\phi = \frac{f^2}{4}(m_\phi^2 - \mu_\phi^2) - \int \frac{\mathrm{d}^3 p}{(2\pi)^3} \left[\frac{1}{2}(\omega^{\phi}_{+} + \omega^{\phi}_{-}) + T \log\left(1 - e^{-\omega^{\phi}_{+}/T}\right) + T \log\left(1 - e^{-\omega^{\phi}_{-}/T}\right)\right]. \tag{5.11}$$

The first term on the RHS of Eq. 5.11 accounts for the condensate, and the second term contains the contribution from thermal excitations. For details see appendix G. UV divergences in eqs. 5.10 and 5.11 are regulated by imposing a momentum cutoff while demanding the Goldstone mode remains gapless with the vev given in eq. 5.6.

In fig. 5.2 we show the critical temperature as a function of the total lepton number density $n_L = \partial(\Omega_\nu + \Omega_\phi)/\partial\mu_L$. For $T > T_c$, the lepton number resides in the thermal population and the condensate amplitude vanishes $f = 0$. Note that the lepton number density in fig. 5.2 is in units of n_0, and in the PNS where the lepton fraction $Y_L \simeq 0.3$ we expect $n_L \simeq 0.1 - 0.3\ n_B$, and $n_B \simeq 1 - 3\ n_0$. Under these conditions the large T_c

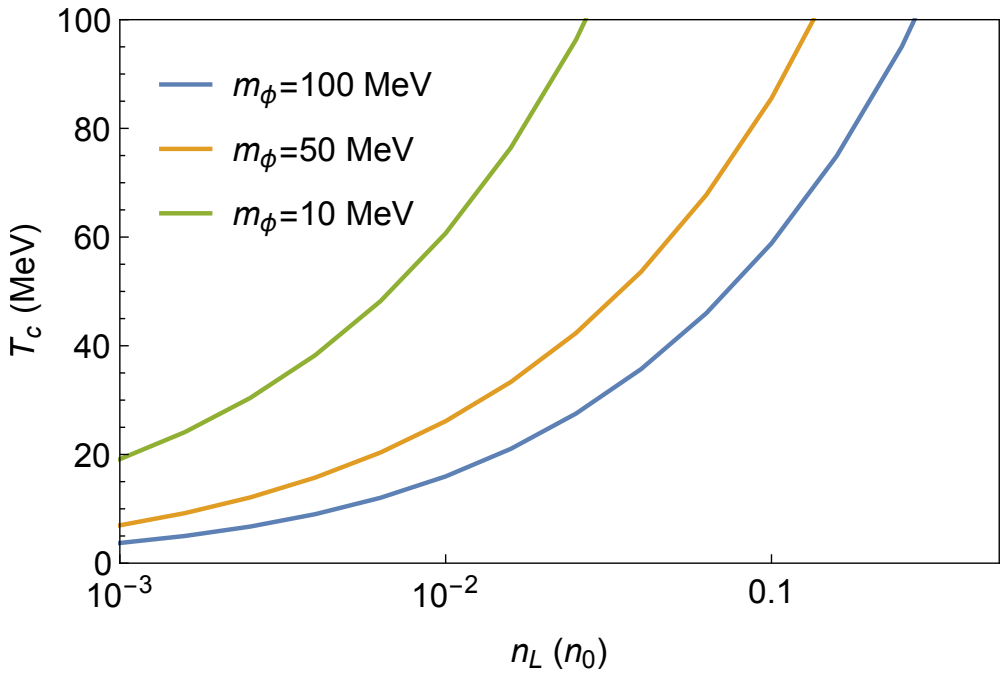

Figure 5.2: Critical temperature of the superfluid in a gas comprised solely of ϕ's.

indicates that condensation will persist even at the highest temperatures encountered in the PNS when the lepton fraction is large.

By accommodating a large fraction of the lepton number, the condensate alters the composition of hot and dense matter in the PNS. At given n_B, T, and Y_L, the baryonic and leptonic components are related by the conditions of beta-equilibrium and charge neutrality:

$$\mu_n - \mu_p = \mu_e - \mu_L \,, \tag{5.12}$$

$$n_p = n_e \,. \tag{5.13}$$

Above, subscripts n, p, e denotes neutrons, protons, and electrons. Number densities n_i include anti-particle contributions, e.g., $n_e = n_{e^-} - n_{e^+}$. In this work we treat electrons as non-interacting relativistic Fermi gas, and neglect muons for simplicity.

To obtain the composition of hot and dense matter in equilibrium we need to specify a baryonic equation of state $\mathcal{E}(n_n, n_p, T)$, the nuclear energy density as a function of the neutron

and proton number densities, and the temperature. For a given $\mathcal{E}(n_n, n_p, T)$, the nucleon chemical potentials are given by $\mu_n = (\partial\mathcal{E}(n_n, n_p)/\partial n_n)_{n_p,T}$, and $\mu_p = (\partial\mathcal{E}(n_n, n_p)/\partial n_p)_{n_n,T}$. In what follows we employ the Skyrme energy functional $\mathcal{E}(n_n, n_p, T)$ discussed in Ref. [350] and appendix B.3.

In fig. 5.3 we show the constituent particle fractions in the presence of ϕ's at $n_B = n_0$, $T = 20$ MeV, and $Y_L = 0.3$. The individual number densities are determined by chemical potentials μ_n, μ_p, μ_e, and μ_L which are obtained by solving eqs. 5.12 and 5.13, subject to the lepton number budget

$$n_L = n_B Y_L = n_e + n_L^\nu + n_L^\phi,$$

where $n_L^\nu = \partial\Omega_\nu/\partial\mu_L$ and $n_L^\phi = \partial\Omega_\phi/\partial\mu_L$ denote lepton number densities carried by ν's and ϕ's, respectively.

Effects of ϕ's on the dense matter composition shown in fig. 5.3 can be understood by noting that the condensate amplitude decreases with increasing m_ϕ. For a given value of m_ϕ, the condensate amplitude is calculated using eq. 5.6 and we have set $\lambda = 1$. For small m_ϕ, the condensate amplitude is large and it accommodates a large amount of lepton number as shown by the green curve. Consequently, the populations of e's (blue curve) and ν's (orange curve) are suppressed. Further, owing to charge neutrality eq. 5.13, the condensate lowers the proton fraction and amplifies the isospin asymmetry of PNS matter at early times. At larger m_ϕ, the lepton number in the condensate is smaller and vanishes when $m_\phi \geq 2\mu_L$. For the chosen parameters, this occurs at $m_\phi \simeq 230$ MeV. At finite temperature, a thermal bath of excitations also contributes to the lepton number density, and this contribution is shown by the red curve. It is interesting to note that for $m_\phi \lesssim 100$ MeV the ϕ condensation reduces the proton fraction by about a factor of 2.

5.3 Implications for neutrino transport

As discussed in section 1.3.1, in the standard scenario, the evolution of the PNS and the associated neutrino signal is largely determined by the diffusion of neutrinos [76, 296, 311].

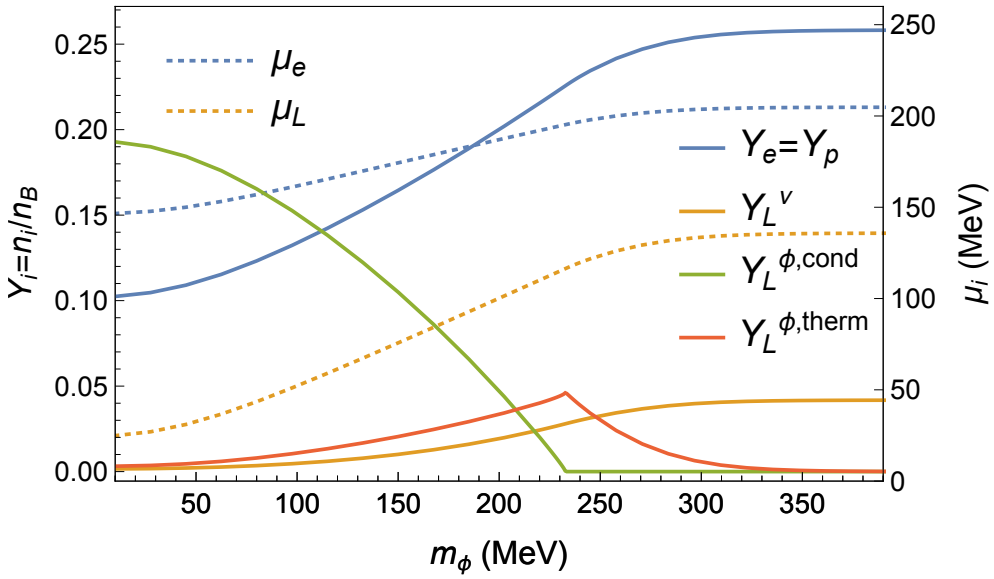

Figure 5.3: PNS composition as a function of m_ϕ at $n_B = n_0$ assuming $T = 20$ MeV and $Y_L = 0.3$. The green curve and red curve represent lepton number carried by the condensate and thermal ϕ's respectively. We took $\lambda = 1$. For $m_\phi \gtrsim 230$ MeV the L budget can no longer support the superfluid in this scenario.

Neutrino trapping during collapse leads to $Y_L \simeq 0.3$ in the bulk of the PNS, and $\mu_L \simeq 200$ MeV in the PNS core. The baryon density, temperature and lepton fraction profiles that roughly correspond to the state of the PNS at $t \simeq 1$ s (see fig. 1 of ref. [311]) are shown in the top panel of fig. 5.4. The spatial gradient of μ_L drives deleptonization by neutrino diffusion and simulations suggest that it takes about 20 seconds for μ_L to decrease substantially [311]. During this time, the lepton number current carried by neutrinos leads to heating in the core akin to Joule heating in ordinary conductors [76]. As we discuss below, ϕ condensation fundamentally alters lepton number transport in PNS.

A defining characteristic of a superfluid is that it supports dissipationless supercurrents that eliminate gradients in the chemical potential. Superflow redistributes the lepton number in the PNS on a short timescale $\tau \ll \tau_{\rm diff}$ without the associated Joule heating. Consequently, the PNS is characterized by a constant lepton number chemical potential in the star's gravitational field

$$\mu_L(r)\sqrt{g_{tt}(r)} = \mu_L^0 = \text{const}, \tag{5.14}$$

where $\mu_L(r)$ is the local chemical potential, and $g_{tt}(r)$ is the time-time component of the metric tensor. The value of μ_L^0 is set by the total lepton number ($N_{L,tot}$) in the star which at early times is $N_{L,tot} \approx 3 - 5 \times 10^{56}$.

The bottom panel of fig. 5.4 shows how the superfluid transport of lepton number alters the composition of the PNS. In the presence of the condensate, it ensures that the chemical potential $\mu_L(r)$ satisfies eq. 5.14. To obtain metric functions we solved the Tolman–Oppenheimer–Volkoff equation assuming the Skyrme equation of state mentioned earlier. At fixed $N_{L,tot}$, curves shown in the top panel reveals that $\mu_L(r)$ in the core is greatly reduced relative to the standard scenario, and is enhanced in the surface regions. Thus, in stark contrast to the standard scenario, the electron and the neutrino fractions are reduced in the core, and increase towards the surface of the PNS. A comparison between the solid and dashed curves in the lower panel reveals that the electron (and proton) fraction is reduced by about a factor of 2 in the core, and is enhanced in the low-density surface regions. The rapid increase in the neutrino fraction at intermediate radius is due to thermal effects and

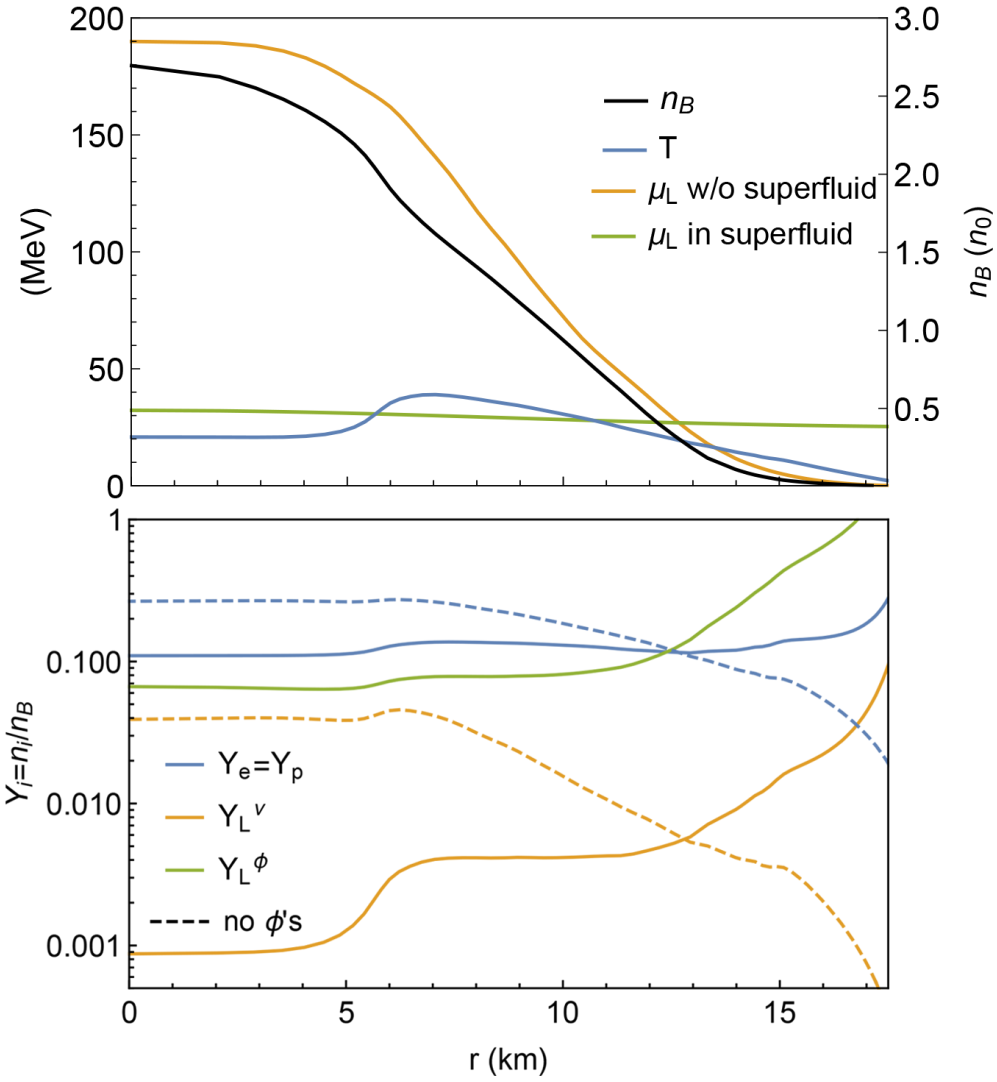

Figure 5.4: Superfluid transports L towards the surface of the star. Solid curves in the lower panel are obtained by distributing $N_{L,tot} \approx 4 \times 10^{56}$ according to eq. 5.14 in a $1.4 M_\odot$ star. The underlying temperature, baryon number, and lepton chemical potential profiles are shown in the top panel. We chose $m_\phi = 50$ MeV, $g = 10^{-3}$, and $\lambda = 1$.

is sensitive to the chosen temperature profile. We experimented with a few different initial profiles of T and μ_L, and found that qualitative features of lepton number transport by the superfluid seen in fig. 5.4 are robust.

The results shown in fig. 5.4 are obtained by setting $m_\phi = 50$ MeV and $\lambda = 1$. It is interesting that the ϕ superfluid can extend to large radii at early times and this is a generic feature for $m_\phi \lesssim 50$ MeV. For larger m_ϕ, the condensate recedes to smaller radius and the region of the PNS influenced by the lepton superfluid is diminished. We can also expect the spatial extent of the superfluid to decrease with time as neutrino diffusion in the outer (non-superfluid) regions of the PNS continuously saps lepton number, causing μ_L^0 in the condensate to decrease.

Condensation accelerates deleptonization of the PNS, especially during the early stages since the timescale for neutrino diffusion is now set by the neutrino mean free paths in the low density outer regions. However, a quantitative description of this time evolution will require self-consistent PNS simulations and is beyond the scope of this study. During this phase, temperature gradients in the PNS drive neutrino diffusion and all flavors of neutrinos contribute to the energy flux. We can expect the transport of energy in the condensate to differ from the standard scenario because the neutrino mean free paths are altered. In particular, we find that the mean free path due to the Cherenkov process $\nu \to \nu J$

$$\frac{1}{\lambda(E_p)} = \frac{1}{E_p}\int \frac{\mathrm{d}^3p'}{2E_{p'}(2\pi)^3}\frac{\mathrm{d}^3k'}{2E_{k'}(2\pi)^3} \times |\mathcal{M}_{\nu\to\nu J}|^2 (1 - f_{p'})(2\pi)^4\delta^4(p - p' - k')\,, \quad (5.15)$$

is significantly shorter than other processes previously considered. In eq. 5.15, $p = (E_p, \mathbf{p})$ is the four-momentum of the initial neutrino, and p', k' are the four-momenta of the neutrino in the final state and the Goldstone boson, respectively. This process is kinematically feasible because the Goldstone mode (c.f. eq. 5.7) exhibits a linear dispersion with velocity $v_J = \sqrt{(\mu_\phi^2 - m_\phi^2)/(3\mu_\phi^2 - m_\phi^2)} < 1$ at small momenta. However, with increasing momenta, when $|\mathbf{k}'| \gtrsim \langle\phi\rangle$ the dispersion relation resembles the vacuum mode of ϕ's and the process is kinematically forbidden. We therefore require that $|\mathbf{k}'| \lesssim \langle\phi\rangle$ in eq. 5.15.

Figure 5.5 shows the Cherenkov mean free paths for neutrinos and anti-neutrinos as

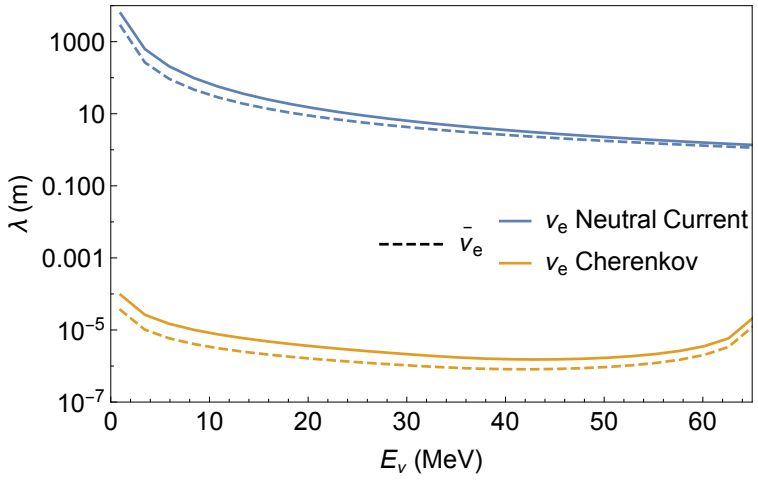

Figure 5.5: Neutrino mean free paths at $n_B = n_0$ in the condensate depicted in fig. 5.4, where $T \approx 27$ MeV and $\mu_L \approx 30$ MeV. As E_ν increases, $\nu \to \nu + J$ becomes forbidden at sufficiently large Goldstone momenta (see main text), resulting in the rising tail for the Cherenkov mean free path.

functions of their energies. For reference, the mean free paths due to neutral current reactions are also shown. These mean free paths are calculated assuming non-relativistic nucleons under the influence of mean-field potentials [307] obtained from the Skyrme model discussed earlier. Since μ and τ neutrinos do not couple to the Goldstone modes in our simple model we do not expect a similar reduction in their mean free paths.

The drastic shortening, by orders of magnitude, of the electron and anti-electron mean free paths suggests that energy transport in the PNS are affected by the condensate. It appears likely that while deleptonization is accelerated by condensation, the cooling of the PNS during the early times may be delayed.

The condensate could alter the neutrino energy spectrum at early times when the superfluid extends to low baryon density (such as the case shown in fig. 5.4). We find that for $m_\phi \lesssim 50$ MeV, condensation of ϕ's is likely to impact the location and temperature of the ν_e and $\bar{\nu}_e$ decoupling surfaces. Short mean free paths in condensed regions imply that

neutrino decoupling must occur at the outer edge of the condensate. In this region, we can expect a large thermal population of ν_e's and ϕ's due to the finite lepton chemical potential. Further, due to the strong coupling between ν_e's and ϕ's, we speculate that the decoupling of ν_e could occur in a thin layer and that the ν_e spectrum might contain a non-thermal component with energy close to $m_\phi/2 \sim 10$ MeV arising from decaying ϕ's. Note that because the population of ϕ^*'s is suppressed by $-2\mu_L$, the anti-electron neutrino signal does not receive similar non-thermal contributions. This enhanced difference between fluxes of ν_e and $\bar{\nu}_e$ would alter the neutron-to-proton ratio in the neutrino driven wind and therefore may have implications for nucleosynthesis [386]. However, as we have noted earlier these speculations neglect feedback effects and self-consistent PNS simulations [296, 80] will be needed to draw definitive conclusions about how the aforementioned effects will impact the temporal and spectral features of the neutrino signal.

5.4 Conclusion

Our main conclusion is that if lepton number scalars that couple to neutrinos exist in nature they will condense to form a superfluid in the PNS. For the conditions realized inside the PNS, condensation is favored for an interesting range of masses and couplings, and is likely to persist for several seconds during which lepton number remains trapped. We find that condensation dramatically alters the composition and transport properties of hot and dense PNS matter.

This first study of lepton number superfluidity in PNSs suggests that the thermodynamic and transport properties of matter are dramatically altered. The large spatial extent of the condensate, and shortened neutrino mean free paths in the condensed phase suggest that the energy spectrum and the luminosity of neutrinos will be affected, especially at early times. However, identifying unique observable signatures in the neutrino signal will require self-consistent PNS simulations that include lepton number scalars. Such studies could address how neutrino data from SN1987a, and future galactic supernovae can help either discover or

constrain a dark lepton sector.

We note that the model employed here neglected the diagonal and off-diagonal couplings of the ϕ to μ and τ neutrinos. Their inclusions could be interesting as it provides additional degrees to accommodate lepton number. It could have an impact during the infall phase of core-collapse [145] and the PNS evolution studied here. These issues are being investigated and will be reported in future works.

Finally, we note that dark superfluid of other forms could have interesting implications in different astrophysical settings. For instance, an additional dark superfluid component is used to revive Modified Newtonian Dynamics in explaining the dark matter in galaxies and clusters of galaxies [49, 50]. Recently, it is also hypothesized that a dark chiral condensate in the center of galaxies may resolve the "core-cusp" problem [18, 19].

Appendix A

HYDROSTATIC EQUILIBRIUM IN GENERAL RELATIVITY

In this appendix we summarize topics related to the global structure of relativistic stars. ρ instead of $\mathcal{E}$ shall be used to denote energy density.

A.1 Spherically symmetric configurations

We start with the following ansatz for the spherically symmetric and static spacetime metric:

$$\mathrm{d}s^2 = g_{\mu\nu}\mathrm{d}x^\mu \mathrm{d}x^\nu = e^{-\nu(r)}\mathrm{d}t^2 - e^{\lambda(r)}\mathrm{d}r^2 - r^2\mathrm{d}\theta^2 - r^2\sin^2\theta\mathrm{d}\phi^2 \tag{A.1}$$

The energy stress tensor for ideal and isotropic fluid takes the canonical form $T_{\mu\nu} = (p + \rho)u_\mu u_\nu - p\, g_{\mu\nu}$. For matter encountered in neutron stars, ideal and isotropic fluid is generally a good description even in the solid crustal phase where the anisotropic stress due to the lattice only makes up a subdominant contribution compared to the Fermi pressure arising from the degenerate neutron sea. It is then straightforward to solve the Einstein equations $G_{\mu\nu} = R_{\mu\nu} - \frac{1}{2}g_{\mu\nu}\, R = 8\pi T_{\mu\nu}$. The tt and rr components give

$$8\pi r^2\rho(r) = \frac{\mathrm{d}}{\mathrm{d}r}\left[r(1 - e^{\lambda(r)})\right], \tag{A.2}$$

$$\nu'(r) = \frac{2\left(M + 4\pi r^3 p(r)\right)}{r(r - 2M)}, \tag{A.3}$$

respectively. With the identification of the mass of the star

$$M(r) = \int_0^r 4\pi r'^2\rho(r')\mathrm{d}r' \tag{A.4}$$

we obtain

$$e^{\lambda(r)} = \left(1 - \frac{2M(r)}{r}\right)^{-1}. \tag{A.5}$$

The mass M defined above is the gravitational mass. This definition is appropriate since it leads to a g_{rr} that matches that of the Schwarzschild metric

$$\mathrm{d}s^2_{\text{Schwarzschild}} = \left(1 - \frac{2M}{r}\right)\mathrm{d}t^2 - \left(1 - \frac{2M}{r}\right)^{-1}\mathrm{d}r^2 - r^2\mathrm{d}\theta^2 - r^2\sin^2\theta\mathrm{d}\phi^2 \tag{A.6}$$

at the surface of the star. Combining eq. A.3 with the conservation of energy stress tensor $\nabla_\mu T_{\mu r} = 0$ which suggests

$$\nu'(r) = -\frac{2p'(r)}{p(r) + \rho(r)},$$

we arrive at the *Tolman-Oppenheimer-Volkoff* equations eq. 1.26.

Finally, the metric function $\nu(r)$ can be obtained from eq. A.3. The resulting integration constant is fixed by matching g_{tt} to $g_{tt}^{\text{Schwarzschild}}$ smoothly at the surface $r = R$.

A.1.1 Newtonian approximation

The TOV equation can be cast into the following form

$$\frac{\mathrm{d}p(r)}{\mathrm{d}r} = -\frac{M(r)\rho(r)}{r^2}\left(1 + \frac{p(r)}{\rho(r)}\right)\left(1 + \frac{4\pi r^3 p(r)}{M(r)}\right)\left(1 - \frac{2M(r)}{r}\right)^{-1}. \tag{A.7}$$

The first term (outside brackets) on the RHS is what would have been obtained had we worked in Newtonian gravity, where hydrostatic equilibrium can be simply understood from the "gradients of pressure balance gravity" analysis on arbitrary thin shells of matter. The tailing factors are general relativistic modifications. It is noteworthy that they all amplify the effects of gravity since each of them makes RHS a bit larger. The combined effects of these factors are moderate ($\lesssim 30\%$) for neutron stars and negligible for white dwarfs.

A.1.2 Physical quantities vs coordinates

Above, r, t are only coordinates. To get the physical (proper) quantities one needs to insert the correct factor of $\det g$. For example, given the profile of particle number density $n(r)$, the total particle number in a star is

$$N = 4\pi\int_0^R \mathrm{d}r r^2 n(r)\sqrt{g_{rr}(r)}. \tag{A.8}$$

A.1.3 thermodynamic potentials in curved spacetime

In chapters 4 and 5 we see the constancy of chemical potentials for an ensemble is modified in gravitational fields. This can be understood as a "redshift" effect. For a box of thermal ensemble of particles at radial coordinate r, its four-momentum $P^\mu = (E/\sqrt{g_{tt}}, 0, 0, 0)^T$ where the normalization $P^\mu P_\mu = E^2$ gives the total energy of the ensemble in local frames. Note that we assume the size of the box is much smaller than the curvature radius, so gravity does not affect internal states of the ensemble.

Static metrics such as eq. A.1 is time-translation invariant which implies the existence of time-like Killing vectors K^μ, such that $\nabla_\mu K_\nu + \nabla_\nu K_\mu = 0$. In this case the Killing vector is $K^\mu = (1, 0, 0, 0)$. Hence the quantity

$$E_0 \equiv P^\mu K_\mu = g_{tt} P^0 = E\sqrt{g_{tt}} = \text{const}, \tag{A.9}$$

is conserved for any free-fall observers (whose worldline are geodesics). Therefore, any quantity that represents some form of energy, such as temperature T and chemical potential μ, must follow similar relations in gravitational fields. This is because their conjugate quantities entropy density s and number density n are independent of gravitational fields, so local values of $T = \frac{\partial E_0}{\partial s}$ and $\mu = \frac{\partial E_0}{\partial n}$ shall have the same spacetime dependencies as E.

A.1.4 stability

While solutions to the TOV equations are in hydrostatic equilibrium, they are not always stable. Throughout this dissertation mass-radius relations shown are truncated at maximum masses because stars living on the branch thereafter are unstable against radial perturbations $\delta\rho(r, t)$. A sufficient but not necessary criterion is that the transition from a stable branch to an unstable one can only occur at local extrema where $\partial M/\partial \rho_c = 0$. To understand this, let us consider the radial oscillation frequencies of stellar normal modes ω_n. In stable configurations the frequency of any of the modes must be real or equivalently $\omega_n^2 > 0$, whereas in unstable stars at least one of the normal modes develops an imaginary part, i.e., $\omega_n^2 < 0$ (so that the mode contains a diverging component $\sim e^{|\omega| t}$). The boundary hence lies at

$\omega_n = 0$. This can only happen if a small perturbation in central energy density ρ_c does not change the mass of the stars. At very small (purely real) frequencies it takes a very long time for the oscillation to perturb a star in equilibrium to some other configurations $\rho(r) + \delta\rho(r)$, such that the new configuration specified by $\rho(r) + \delta\rho(r)$ must be another equilibrium state, in which $\delta\rho_c \neq 0$ (since different equilibria are by their central densities ρ_c). We also expect this slowly varying perturbation to conserve energy as its frequency $\omega_n \to 0$, hence the total energy $\delta M \to 0$. In other words, the transition $\omega_n = 0$ corresponds to a local minimum or maximum of the mass.

One may further show that an equilibrium configuration is stable if and only if the mass defined in eq. A.4 is stationary (and in fact a minimum) with respect to *all* perturbations $\delta\rho(r)$ that leaves the total particle number eq. A.8 invariant. Systematic investigations of radial oscillations of compact stars with uniform entropy yielded the following empirical criterion: with increasing central densities, one of the stable radial modes becomes unstable if the mass-radius curve bends counter-clockwise; if the curve bends clockwise, then one of unstable normal modes becomes stable [33]. To establish the stability of different branches of neutron stars, we may either start from the very low density Newtonian white dwarf branch and use the above criterion, or thorough observational evidence of pulsars with masses and radii within the predicted range of the normal branch as predicted by most physical nuclear EOSs.

A.2 Tidally deformed static configurations

In Newtonian gravity the leading contribution to tidal fields $\mathcal{E}_{ij} = \frac{\partial^2\phi}{\partial x^i \partial x^j}$ arises at the quadrupole order. The same has to hold in relativistic stars so that their weak-field slow-motion limits reproduce Newtonian stars. Hence we decompose the metric perturbations in

terms of spherical harmonics Y_{lm} and focus on $l = 2$:

$$\begin{aligned} g_{\mu\nu} &= \overset{(0)}{g}_{\mu\nu} + h_{\mu\nu}, \\ \overset{(0)}{g}_{\mu\nu} &= \mathrm{diag}\left(e^{-\nu(r)},\ -e^{\lambda(r)},\ -r^2,\ -r^2\sin^2\theta\right), \\ h_{\mu\nu} &= \mathrm{diag}\left(e^{-\nu(r)}H_0(r),\ e^{\lambda(r)}H_1(r),\ K(r)r^2,\ K(r)r^2\sin^2\theta\right)Y_{2m}. \end{aligned} \tag{A.10}$$

Most of the interesting physics occurs when the orbital separation becomes comparable to the size of compact stars in merging binaries. In the so-called *buffer zone* of each component star where $\lambda_{\rm GW} \gg r \gg R_{\rm star}(\gtrsim R_{\rm curv})$, gravitational radiations are unimportant and gravity is not too strong. For each star tidal fields due to its companion can be treated as a perturbation. The diagonal temporal component of the metric tensor in this region admits the following expansion [362]:

$$\frac{1-g_{tt}}{2} = -\frac{M}{r} - \frac{3Q_{ij}}{2r^3}(n^i n^j - \frac{1}{3}\delta^{ij}) + \mathcal{O}(\frac{1}{r}) + \frac{1}{2}\mathcal{E}_{ij}x^i x^j + \mathcal{O}(r^3) \tag{A.11}$$

where Q_{ij} is identified as the quadrupole moment and $\mathcal{E}_{ij}$ is the tidal field. The general plan to obtain tidal deformability therefore is to solve the perturbed metric $H_0(r)$ from linearized Einstein's equations, and extracting the tidal field and quadrupole moment from the expansion of H_0 in the buffer zone.

We start by noting that in the linearized gravity the inverse metric tensor is

$$\begin{aligned} g^{\mu\nu} &= \overset{(0)}{g}^{\mu\nu} - h^{\mu\nu}, \\ h^{\mu\nu} &= \overset{(0)}{g}^{\mu\sigma}\overset{(0)}{g}^{\nu\tau}h_{\sigma\tau}. \end{aligned} \tag{A.12}$$

At order $\mathcal{O}(h)$ the Christoffel symbols are found to be

$$\begin{aligned} \Gamma^{\lambda}_{\mu\nu} = \overset{(0)}{\Gamma}{}^{\lambda}_{\mu\nu} + \overset{(1)}{\Gamma}{}^{\lambda}_{\mu\nu} &= \frac{1}{2}\overset{(0)}{g}{}^{\lambda\sigma}\left[\frac{\partial \overset{(0)}{g}{}^{\mu\sigma}}{\partial x^\nu} + \frac{\partial \overset{(0)}{g}{}^{\nu\sigma}}{\partial x^\mu} - \frac{\partial \overset{(0)}{g}{}^{\mu\nu}}{\partial x^\sigma}\right] \\ &\quad - \frac{1}{2}h^{\lambda\sigma}\left[\frac{\partial \overset{(0)}{g}{}^{\mu\sigma}}{\partial x^\nu} + \frac{\partial \overset{(0)}{g}{}^{\nu\sigma}}{\partial x^\mu} - \frac{\partial \overset{(0)}{g}{}^{\mu\nu}}{\partial x^\sigma}\right] + \frac{1}{2}\overset{(0)}{g}{}^{\lambda\sigma}\left[\frac{\partial h_{\mu\sigma}}{\partial x^\nu} + \frac{\partial h_{\nu\sigma}}{\partial x^\mu} - \frac{\partial h_{\mu\nu}}{\partial x^\sigma}\right], \end{aligned} \tag{A.13}$$

which lead to the Riemann tensor

$$R^{\lambda}_{\mu\nu\sigma} = \overset{(0)}{R}{}^{\lambda}_{\mu\nu\sigma} + \overset{(1)}{R}{}^{\lambda}_{\mu\nu\sigma} = \left[\frac{\partial \overset{(0)}{\Gamma}{}^{\lambda}_{\mu\sigma}}{\partial x^{\nu}} - \frac{\partial \overset{(0)}{\Gamma}{}^{\lambda}_{\mu\nu}}{\partial x^{\sigma}} + \overset{(0)}{\Gamma}{}^{\lambda}_{\nu\eta}\overset{(0)}{\Gamma}{}^{\eta}_{\mu\sigma} - \overset{(0)}{\Gamma}{}^{\lambda}_{\eta\sigma}\overset{(0)}{\Gamma}{}^{\eta}_{\mu\nu}\right] + \left[\frac{\partial \overset{(1)}{\Gamma}{}^{\lambda}_{\mu\sigma}}{\partial x^{\nu}} - \frac{\partial \overset{(1)}{\Gamma}{}^{\lambda}_{\mu\nu}}{\partial x^{\sigma}} + \overset{(1)}{\Gamma}{}^{\lambda}_{\nu\eta}\overset{(0)}{\Gamma}{}^{\eta}_{\mu\sigma} + \overset{(0)}{\Gamma}{}^{\lambda}_{\nu\eta}\overset{(1)}{\Gamma}{}^{\eta}_{\mu\sigma} - (\overset{(1)}{\Gamma}{}^{\lambda}_{\eta\sigma}\overset{(0)}{\Gamma}{}^{\eta}_{\mu\nu} + \overset{(0)}{\Gamma}{}^{\lambda}_{\eta\sigma}\overset{(1)}{\Gamma}{}^{\eta}_{\mu\nu})\right], \tag{A.14}$$

From which it follows that

$$\overset{(1)}{R}{}^{\mu}_{\nu} = g^{\mu\lambda}\overset{(1)}{R}{}^{\sigma}_{\nu\sigma\lambda} - h^{\mu\lambda}\overset{(0)}{R}{}^{\sigma}_{\nu\sigma\lambda}. \tag{A.15}$$

The curvature scalar is given by

$$R = g^{\mu\nu}R_{\mu\nu} = \overset{(0)}{R} + \overset{(1)}{R} = \overset{(0)}{g}{}^{\mu\nu}\overset{(0)}{R}_{\mu\nu} + \left[-h^{\mu\nu}\overset{(0)}{R}_{\mu\nu} + \overset{(0)}{g}{}^{\mu\nu}\overset{(1)}{R}_{\mu\nu}\right], \tag{A.16}$$

and the perturbed Einstein tensor is

$$\overset{(1)}{G}{}^{\nu}_{\mu} = \left[\overset{(1)}{R}{}^{\nu}_{\mu} - \frac{1}{2}\delta^{\nu}_{\mu}\overset{(1)}{R}\right]. \tag{A.17}$$

The Lagrange perturbation is most suitable as it guarantees the perturbation $\delta\rho/\rho$ stays finite and small in the vicinity of perturbed stellar boundaries that were vacuum in the unperturbed configuration. So the perturbed stress-energy tensor is

$$\overset{(1)}{T}{}^{\mu}_{\nu} = \mathrm{diag}\left(\frac{\mathrm{d}\rho}{\mathrm{d}p}\delta p, -\delta p, -\delta p, -\delta p\right) Y_{2m} \tag{A.18}$$

The zeroth order Einstein equation is already solved which yielded the TOV equations. We only need to solve the field equations at order $\mathcal{O}(h)$: $\overset{(1)}{G}{}^{\mu}_{\nu} = 8\pi\overset{(1)}{T}{}^{\mu}_{\nu}$. The diagonal angular components $\overset{(1)}{T}{}^{\theta}_{\theta} = \overset{(1)}{T}{}^{\phi}_{\phi}$ implies that $H_0(r) = H_1(r) = H(r)$. Next, from $\overset{(1)}{G}{}^{\theta}_{r} = 0$, we have

$$K'(r) = H'(r) - H(r)\nu'(r). \tag{A.19}$$

This relation allows us to substitute H and its derivatives for K' and K''. Further, the $\theta\theta$ component of the linearized equation

$$\delta p = -\frac{H(r)e^{-\lambda(r)}\left(\lambda'(r) - \nu'(r)\right)}{16\pi r}. \tag{A.20}$$

can be used to eliminate δp. We then subtract the rr component of the field equations from the tt component, and finally arrive at an equation for $H(r)$:

$$H''(r)+H'(r)\left(\frac{2}{r}-\frac{\lambda'(r)+\nu'(r)}{2}\right)-H(r)\Big[\frac{\mathrm{d}\rho}{\mathrm{d}p}\left(\frac{\lambda'(r)}{2r}-\frac{\nu'(r)}{2r}\right)+\frac{6e^{\lambda(r)}}{r^2} \\ -\frac{1}{2}\lambda'(r)\nu'(r)+\frac{7\nu'(r)}{2r}-\frac{3\lambda'(r)}{2r}+\nu''(r)+\frac{1}{2}\nu'^2(r)\Big]=0. \quad \text{(A.21)}$$

As discussed earlier the metric functions λ and ν are obtained from the 0th order field equations derived in the previous section. Applying those results, A.21 can be expressed as

$$H''(r)+\left[\frac{2}{r}+e^{\lambda(r)}\left(\frac{2M(r)}{r^2}+4\pi r(p-\rho)\right)\right]H'(r) \\ +\left[4\pi\left(9p+5\rho+\frac{\mathrm{d}\rho}{\mathrm{d}p}(p+\rho)\right)e^{\lambda(r)}-\frac{6e^{\lambda(r)}}{r^2}-\nu'^2(r)\right]H(r)=0. \quad \text{(A.22)}$$

This is valid in the interior of the star. Setting $\rho=p=0$ we obtain an expression valid for the buffer zone. Note that since outside the star the zeroth order equation yields the Schwarzschild metric, we have $e^{\nu}=e^{\lambda}$, and hence $\nu'=\lambda'=-2Me^{\lambda}/r^2$ (where M is the total mass $M(R)$). Rewritten in terms of $x=r/M-1$, the metric perturbation function H outside the star satisfies

$$(x^2-1)H''+2xH'-(6+\frac{4}{x^2-1})H=0. \quad \text{(A.23)}$$

This is the associated Legendre equation with $l=m=2$. The most general solution is

$$H(r)=c_1(\frac{r}{M})^2(1-\frac{2M}{r})\left[-\frac{M(M-r)(2M^2+6Mr-3r^2)}{r^2(2M-r)^2}-\frac{3}{2}\log(\frac{r-2M}{r})\right] \\ +3c_2(\frac{r}{M})^2(1-\frac{2M}{r}). \quad \text{(A.24)}$$

Its expansion takes the form:

$$H=-c_1\frac{8}{5}(\frac{M}{r})^3+\mathcal{O}((\frac{1}{r})^3)-3c_2(\frac{r}{M})^2+\mathcal{O}(r) \quad \text{(A.25)}$$

Now relations between c_1 and Q_{ij}, c_2 and $\mathcal{E}_{ij}$ can be identified and they are

$$c_1=-\frac{15}{8}\frac{Q_{ij}}{M^3},\ c_2=\frac{1}{3}\mathcal{E}_{ij}M^2.$$

leading to

$$\lambda = \frac{8}{45}\frac{c_1}{c_2}M^5, \quad k_2 = \frac{3}{2}\lambda R^{-5} = \frac{4}{15}\frac{c_1}{c_2}C^5. \tag{A.26}$$

Where $C = M/R$ is the compactness of the neutron star. In order to solve k_2 we numerically integrate equation A.22, and match the boundary conditions

$$H_{\rm int}(R) = H_{\rm ext}(R),\ H'_{\rm int}(R) = H'_{\rm ext}(R) \tag{A.27}$$

This procedure can be simplified by noting that eq. A.22 is homogeneous hence H are H' are scale invariant. This is expected in our linear analysis since the overall amplitudes of tidal fields and induced quadrupole moments are set by the companion stars and have no bearing on the proportionality coefficient λ. Only the combination H'/H matters. Define $y = rH'(r)/H(r)$, eq. A.22 can be rewritten as

$$\begin{aligned}\frac{dy(r)}{dr} =& -\frac{y(r)^2}{r} - \frac{y(r)g_{rr}(r)}{r}\left[1 + 4\pi r^2\Big(p(r) - \rho(r)\Big)\right] \\ &- 4\pi r\left[9p(r) + 5\rho(r) + \frac{\mathrm{d}\rho}{\mathrm{d}p}\Big(p(r) + \rho(r)\Big)\right]g_{rr}(r) + r\left[\frac{6g_{rr}(r)}{r^2} + \left(\frac{d\ln g_{tt}(r)}{dr}\right)^2\right],\end{aligned} \tag{A.28}$$

This is eq. 2.7. The expression for c_1/c_2 now becomes

$$\begin{aligned}\frac{c_1}{c_2} =& 6(1-2C)^2[2(1-C) + (2C-1)y] \times \Bigg\{4C^3\Big[13 - 11y + 2C^2(1+y) + C(-2+3y)\Big] \\ &+ 2C\Big[6 - 3y + 3C(5y-8)\Big] + 3(1-2C)^2\Big[2 + 2C(y-1) - y\Big]\log(1-2C)\Bigg\}^{-1},\end{aligned} \tag{A.29}$$

Where $y = y(R) = RH'(R)/H(R)$. To find the boundary condition for $y(r=0)$ note that near $r = 0$ the solution to A.22 is

$$H(r_0) = ar_0^2 + \mathcal{O}(r_0^3), \quad H'(r_0) = 2ar_0 + \mathcal{O}(r_0^2),$$

Hence $y(0) = 2$.

A.3 Numerical notes

Often times the equation of state is specified by a set of tabulated data, which needs to be interpolated to reconstruct a continuous function $p(\rho)$. It turns out, however, adaptive ODE solvers (e.g., those from the Runge-Kutta family) may struggle at the boundaries of neighboring interpolated (p, ρ) pairs: the step size keeps shrinking to avoid crossing the boundary. It is thus easier to integrate the TOV equations interval-by-interval when they are transformed into a form such that p is the independent variable

$$\begin{aligned} \frac{\mathrm{d}r}{\mathrm{d}p} &= -\frac{r\left(1-\dfrac{2M}{r}\right)}{(\rho+p)\left(\dfrac{M}{r}+4\pi r^2 p\right)}, \\ \frac{\mathrm{d}M}{\mathrm{d}p} &= 4\pi\rho r^2 \frac{\mathrm{d}r}{\mathrm{d}p}. \end{aligned} \tag{A.30}$$

Now the radius of the star can be obtained explicitly from $R = r(p = 0)$. To initiate numerical solvers at $r = 0$, we expand the two equations near the center

$$\begin{aligned} \frac{\mathrm{d}r^2}{\mathrm{d}p} &= \frac{3}{2\pi\rho(3p+\rho)(p+\rho)}, \\ M &= \frac{4}{3}\pi\rho_0 r^2. \end{aligned}$$

We then take a small step of size $\mathrm{d}p$ and explicitly perform the integration to obtain:

$$\begin{aligned} r(p_1)^2 &= \frac{3}{2\pi\rho_0}\left[\log\frac{p_1+\rho_0}{p_0+\rho_0} - \log\frac{3p_1+\rho_0}{3p_0+\rho_0}\right], \\ M(p_1) &= \frac{4}{3}\pi\rho_0 r(p_1)^3. \end{aligned} \tag{A.31}$$

where $p_1 = p_0 - dp$, and $\rho_0 = \rho(p_0)$.

Appendix B

SUMMARY OF EQUATIONS OF STATE

B.1 Thermodynamics

Given the grand potential $\Omega(T, \mu_i)$ specified by temperature T and chemical potential μ_i of species i, the energy density $\mathcal{E}$, entropy density s and number densities n_i for species i are given by

$$\begin{aligned} n_i &= -\frac{\partial(\Omega/V)}{\partial \mu_i}, \quad s = -\frac{\partial(\Omega/V)}{\partial T}, \\ \mathcal{E} &= \Omega/V + Ts + \sum_i \mu_i n_i \\ p &= -\Omega/V. \end{aligned} \tag{B.1}$$

Stability requires that the (isentropic) speed of sound is greater than zero:

$$C_s = c_s^2 = \left(\frac{\mathrm{d}P}{\mathrm{d}\mathcal{E}}\right)_s = \frac{P'(n)}{\mathcal{E}'(n)} \geq 0. \tag{B.2}$$

B.2 Free Fermi gas

Although insufficient for studying neutron stars, the free Fermi gas model is a relatively intuitive 0^{th} order approximation to the compact star composition. In fact it provides fairly good descriptions for white dwarfs and certain dark matter models. This appendix summarizes the results of

$$n = \frac{g}{(2\pi)^3} \int f(E_p) \mathrm{d}^3 p, \tag{B.3}$$

$$\mathcal{E} = \frac{g}{(2\pi)^3} \int E_p f(E_p) \mathrm{d}^3 p, \tag{B.4}$$

$$s = \frac{g}{(2\pi)^3} \int \left[f \log f - (1-f) \log(1-f) \right] \mathrm{d}^3 p, \tag{B.5}$$

$$p = \mu n - \mathcal{E} + Ts; \tag{B.6}$$

assuming different kinematics. Above, g is the particle degeneracy parameter and f_E the Fermi-Dirac distribution function

$$f_E = \frac{1}{1 + \exp\left[E(p) - \mu)/T\right]}.$$

Except for the finite temperature arbitrary relativistic case, thermodynamic integrals above can be evaluated in closed forms.

B.2.1 $T = 0$

Regardless of the kinematics, at zero temperature

$$n = \frac{g}{2\pi^2}\int_0^{p_F} p^2 \mathrm{d}p = g\frac{p_F^3}{6\pi^2}. \tag{B.7}$$

arbitrary relativity

For convenience define the dimensionless quantity $x = p_F/m$.

$$\mathcal{E} = \frac{g}{2\pi^2}\int_0^{p_F} \mathrm{d}p\; p^2\sqrt{p^2+m^2} = \frac{g\; m^4}{16\pi}\left[x\sqrt{x^2+1}\left(2x^2+1\right) - \sinh^{-1}(x)\right], \tag{B.8}$$

$$p = \frac{g}{6\pi^2}\int_0^{p_F} \frac{p^4\mathrm{d}p}{\sqrt{p^2+m^2}} = \frac{g\; m^4}{48\pi}\left[x\left(2x^2-3\right)\sqrt{x^2+1} + 3\sinh^{-1}(x)\right]. \tag{B.9}$$

non-relativistic

$$\mathcal{E} = \frac{gp_F^3}{20\pi^2 m} = \frac{3\left(6\pi^2/g\right)^{2/3}}{10\pi^2 m}n^{5/3}, \quad p = \frac{gp_F^3}{60\pi^2 m} = \frac{\left(6\pi^2/g\right)^{2/3}}{5\pi^2 m}n^{5/3}. \tag{B.10}$$

ultra-relativistic

$$\mathcal{E} = \frac{g}{8\pi^2}\mu^4 = \frac{3}{2}\left(\frac{3\pi^2}{4g^2}\right)^{1/3} n^{4/3}, \quad p = \frac{g}{24\pi^2}\mu^4 = \frac{1}{2}\left(\frac{3\pi^2}{4g^2}\right)^{1/3} n^{4/3}. \tag{B.11}$$

B.2.2 Finite temperature

non-relativistic

Define $\alpha = T/m$, $x = p/T$, $y = \mu/T$,

$$n = \frac{gT^3}{2\pi^2}\int_0^\infty \mathrm{d}x \frac{x^2}{1+\exp\left(\alpha x^2/2 - y\right)} = -\frac{gT^3}{2\sqrt{2}\pi^{3/2}\alpha^{3/2}}\mathrm{Li}_{\frac{3}{2}}\left(-e^y\right), \tag{B.12}$$

$$\mathcal{E} = \frac{gT^4}{2\pi^2}\int_0^\infty \mathrm{d}x \frac{ax^4/2}{1+\exp\left(\alpha x^2/2 - y\right)} = -\frac{3gT^4}{4\sqrt{2}\pi^{3/2}\alpha^{3/2}}\mathrm{Li}_{\frac{5}{2}}\left(-e^y\right), \tag{B.13}$$

$$p = \frac{2}{3}\mathcal{E}, \tag{B.14}$$

$$s = \frac{gT^3}{2\pi^2}\int_0^\infty \frac{-x^2 y + 5\alpha x^4/6}{1+\exp\left(\alpha x^2/2 - y\right)} = \frac{gT^3}{4\sqrt{2}\pi^{3/2}\alpha^{3/2} n}\left[2y\mathrm{Li}_{\frac{3}{2}}(-e^y) - 5\mathrm{Li}_{\frac{5}{2}}(-e^y)\right]. \tag{B.15}$$

In obtaining the integrand for the entropy density, the relation $s = (\mathcal{E} + p - \mu n)/T$ is used. Li_n are polylograithm functions of order n.

ultra-relativistic

With $x = p/T$ and $y = \mu/T$,

$$n = \frac{gT^3}{2\pi^2}\int_0^\infty \mathrm{d}x \frac{x^2}{1+\exp\left(x - y\right)} = \frac{gT^3}{3\pi^2}\mathrm{Li}_3\left(-e^y\right) \tag{B.16}$$

$$\mathcal{E} = \frac{gT^4}{2\pi^2}\int_0^\infty \mathrm{d}x \frac{x^3}{1+\exp\left(x - y\right)} = -\frac{3gT^4}{\pi^2}\mathrm{Li}_4\left(-e^y\right) \tag{B.17}$$

$$p = \frac{1}{3}\mathcal{E}, \tag{B.18}$$

$$s = \frac{gT^3}{2\pi^2}\int_0^\infty \frac{\frac{4x^3}{3} - x^2 y}{1+\exp(x - y)} = \frac{gT^3}{2\pi^2}\left[2y\mathrm{Li}_3\left(-e^y\right) - 8\mathrm{Li}_4\left(-e^y\right)\right] \tag{B.19}$$

Sommerfeld Expansion

At low temperature ($T \ll \mu$, or $y \ll 1$) the Fermi surface "smoothed out" with width $\sim T$. This allows the following expansion

$$\int_0^\infty \frac{f(x)}{1+\exp\left(x - y\right)}\mathrm{d}x = \int_0^y f(x)\mathrm{d}x + \frac{\pi^2}{6}f'(y) + \frac{7\pi^4}{360}f'''(y) + \ldots \tag{B.20}$$

B.3 Skyrme

Tony Skyrme discovered that nucleons, although not explicitly included in eq. 1.9, emerges as solitons from the chiral Lagrangian eq. 1.9 [340][341]. By working out the topological

properties of the (non-relativistic) excitation carrying integer baryon number he was able to write down an effective description for nucleon interactions. In it nuclear forces are mediated by contact interactions. This approach was further promoted in nuclear physics by mean field studies due to Brinks and Vautherine [371, 370].

For homogeneous nuclear matter the Skyrme functional specifies the energy density as a function of neutron and proton number densities n_n and n_p. Here we pick the parameterization

$$\mathcal{E}(n_n,n_p)=\frac{\tau_n}{2m_n}+\frac{\tau_p}{2m_p}+(n_n+n_p)(\tau_n+\tau_p)\left[\frac{t_1}{4}\left(1+\frac{x_1}{2}\right)+\frac{t_2}{4}\left(1+\frac{x_2}{2}\right)\right]$$
$$+(n_n\tau_n+n_p\tau_p)\left[\frac{t_2}{4}\left(\frac{1}{2}+x_2\right)-\frac{t_1}{4}\left(\frac{1}{2}+x_1\right)\right]+\frac{t_0}{2}\left[(n_n+n_p)^2\left(1+\frac{x_0}{2}\right)-(n_n^2+n_p^2)\left(\frac{1}{2}+x_0\right)\right]$$
$$+\frac{t_3}{12}\left[(n_n+n_p)^2\left(1+\frac{x_3}{2}\right)-(n_n^2+n_p^2)\left(\frac{1}{2}+x_3\right)\right](n_n+n_p)^\epsilon \quad \text{(B.21)}$$

Above, τ_i are kinetic energy densities, and $t_{1,2}, x_{0,1,2,3}, \epsilon$ are free parameters and a particular set that fitted to APR EOS can be found in **??**. Because of τ-dependent terms in eq. B.21, nucleon masses are modified in the medium. The effective masses $m^*_{n,p}$ are functions of densities and may be obtained by absorbing all the τ-dependent terms into $\frac{\tau_i}{2m_i^*}$. They are found to be

$$m_n^*/m_n=\frac{4}{4+n_n\left[t_1(1-x_1)+3t_2(1+x_2)\right]+n_p\left[t_1(2+x_1)+t_2(2+x_2)\right]},$$
$$m_p^*/m_p=\frac{4}{4+n_p\left[t_1(1-x_1)+3t_2(1+x_2)\right]+n_n\left[t_1(2+x_1)+t_2(2+x_2)\right]}$$

At the mean field level, identical particles all experience the same potential given by $U_i = \partial\mathcal{E}/\partial n_i$. The results are

$$U_n=\frac{1}{2}\Bigg\{t_0\left[n_n(1-x_0)+n_p(2+x_0)\right]+\frac{1}{4}\left[\tau_n\left(t_1(1-x_1)+3t_2(1+x_2)\right)+\tau_p\left(t_1(2+x_1)+t_2(2+x_2)\right)\right]$$
$$+\frac{t_3}{12}(n_n+n_p)^{\epsilon-1}\left[-n_n^2(-1+x_3)(2+\epsilon)+n_p^2\left(4+\epsilon-x_3(\epsilon-2)\right)+2n_nn_p\left((x_3+2)\epsilon+3\right)\right]\Bigg\}$$

Swapping the labels $n \leftrightarrow p$ yields U_p. The single particle excitation thus takes the following form in this mean-field treatment:

$$E_i(k)=\frac{k^2}{2m_i^*}+U_i. \quad \text{(B.22)}$$

Implicit density dependencies in m^* and U_i through τ_i require solving

$$n_i = \frac{1}{\pi^2}\int_0^\infty \frac{k^2}{1+\exp\left[(E_i(k)-\mu_i)/T\right]}\mathrm{d}k \tag{B.23}$$

consistently by iterations. Note that with the identification $\alpha = T/m_i^*$ and $y = (\mu_i - U_i)/T$ the integral on the right hand side can be evaluated in closed form (c.f. eq. B.16). Once converged to the desired accuracy the EOS can be obtained using the expressions below eq. B.16 by noting that kinetic energy densities

$$\tau_i = \frac{1}{\pi^2}\int_0^\infty \frac{k^4}{1+\exp\left[(E_i(k)-\mu_i)/T\right]}\mathrm{d}k \tag{B.24}$$

and the pressure $p \neq \frac{2}{3}\mathcal{E}$ due to interactions. The same procedure can be easily generalized to zero temperature where f_E becomes a step function and the integral limits on k is restricted to $0 \leq k \leq k_F$.

B.4 Polytropes

The polytropic parameterization of EOS assumes the following form for pressure versus number density $p(n)$:

$$p(n) = k\left(\frac{n}{\widetilde{n}}\right)^\gamma = k\bar{n}^\gamma$$

where $\widetilde{n}$ is an arbitrary constant such that $\bar{n} = n/\widetilde{n}$ is dimensionless. For neutron star EOS the nuclear saturation density $\widetilde{n} = n_s$ is a convenient choice. The polytropic parameterization is widely used before physical calculations of dense nuclear matter EOS can be carried out. Notably, non-relativistic free Fermi gas EOS has polytropic index $\gamma = 5/3$, and for ultra-relativistic Fermi gas $\gamma = 4/3$, see appendix B.2. Stability requires $\gamma > 1$. The energy density follows from thermodynamics and is

$$\mathcal{E}(n) = \frac{k}{\gamma - 1}\bar{n}^\gamma + \bar{n}\mathcal{E}_0,$$

where $\mathcal{E}_0$ is an integration constant. If the polytrope is to be used in conjunction with other low density EOSs, continuity at the boundary uniquely fixes the constants $k, \mathcal{E}_0$. In

the absence of another low density parameterization, $\mathcal{E}_0 = m_N\widetilde{n}$ such that the energy per particle approaches nucleon rest mass m_N as $n \to 0$.

All physical EOSs, for which $\gamma > 1$ so that $\mathcal{E}(n)$ is positive and increasing, constraints from thermodynamics are satisfied. The speed of sound in this construction is given by

$$c_s^2 = \frac{\mathrm{d}p}{\mathrm{d}\bar{n}} \Big/ \frac{\mathrm{d}\mathcal{E}}{\mathrm{d}\bar{n}} = \frac{\gamma p}{p + \mathcal{E}}.$$

B.4.1 GCR double polytrope

Another ingenious extension of polytrope is the double polytrope parameterization for energy per particle [149]

$$E(n) = a\left(\frac{n}{n_0}\right)^{\alpha} + b\left(\frac{n}{n_0}\right)^{\beta}. \tag{B.25}$$

Gandolfi, Carlson, and Reddy found that results of χEFT-based pure neutron matter quantum Monte Carlo calculations can be fitted with the form above to good accuracy. Equation B.25 provides a concise and elegant parameterization for realistic neutron-matter EOSs.

$3N$ force	E_{sym} (MeV)	L (MeV)	a (MeV)	α	b (MeV)	β
none	30.5	31.3	12.7	0.49	1.78	2.26
$V_{2\pi}^{PW} + V_{\mu=150}^{R}$	32.1	40.8	12.7	0.48	3.45	2.12
$V_{2\pi}^{PW} + V_{\mu=300}^{R}$	32.0	40.6	12.8	0.488	3.19	2.20
$V_{3\pi} + V_R$	32.0	44.0	13.0	0.49	3.21	2.47
$V_{2\pi}^{PW} + V_{\mu=150}^{R}$	33.7	51.5	12.6	0.475	5.16	2.12
$V_{3\pi} + V_R$	33.8	56.2	13.0	0.50	4.71	2.49
UIX	35.1	63.6	13.4	0.514	5.62	2.436

Table B.1: Double polytropic fittings eq. B.25 for selected 3-body interactions listed in [149].

The EOS follows as

$$\begin{aligned}\mathcal{E} &= a\left(\frac{n}{n_0}\right)^{\alpha+1} n_0 + b\left(\frac{n}{n_0}\right)^{\beta+1} n_0 + nm_n, \\ p &= a\alpha n_0\left(\frac{n}{n_0}\right)^{\alpha+1} + b\beta n_0\left(\frac{n}{n_0}\right)^{\beta+1}.\end{aligned} \tag{B.26}$$

B.5 Speed of sound

The speed of sound (squared $C_s = c_s^2 = \partial p/\partial\mathcal{E}$ parameterization of equation of state is a simple but well-motivated parameterization for the high density phase of QCD matter. Bounded from below $C_s \geq 0$ from stability requirements and from above $C_s \leq 1$ due to causality, the speed of sound parameterization can represent the most general EOS consistent with known physics. It relates the rate of change of pressure to that of energy density therefore directly controls the stiffness of EOSs. Moreover, calculations in perturbative QCD suggest that C_s approaches 1/3 from below at asymptotic densities $n_B \gtrsim 50n_0$. This provides a bit of hint for possible behaviors of C_s at densities achieved in neutron stars interiors where $n_B \lesssim 10n_0$.

The C_s parameterization is used to describe high density EOS starting from $n = n0$ (not to be confused with the saturation density n_0), $p = p_0$ and $\mathcal{E} = \mathcal{E}_0$. Given a general function $C_s(\mathcal{E})$, we have

$$p(\mathcal{E}) - p0 = \int_{\mathcal{E}_0}^{\mathcal{E}} C_s(\mathcal{E}')\mathrm{d}\mathcal{E}',$$

so that

$$\frac{\mathrm{d}\mathcal{E}}{\mathrm{d}n} = \frac{p+\mathcal{E}}{n} = \frac{p_0 + \int_{\mathcal{E}_0}^{\mathcal{E}} C_s(\mathcal{E}')\mathrm{d}\mathcal{E}' + \mathcal{E}}{n}, \tag{B.27}$$

from which we obtain

$$n = n0\exp\left[\int_{\mathcal{E}_0}^{\mathcal{E}} \frac{\mathrm{d}\mathcal{E}'}{p_0 + \int_{\mathcal{E}_0}^{\mathcal{E}'} C_s(\mathcal{E}'')\mathrm{d}\mathcal{E}'' + \mathcal{E}'}\right]. \tag{B.28}$$

Consider a special case

- constant C_s:

$$\mathcal{E} = \frac{1}{1+C_s}\left[(C_s\mathcal{E}_0 - p_0) + \left(\frac{n}{n0}\right)^{C_s+1}(p_0+\mathcal{E}_0)\right], \tag{B.29}$$

$$p = p_0 + C_s(\mathcal{E}-\mathcal{E}_0). \tag{B.30}$$

B.6 Note on tabulated EOS Data

Here we present somewhat tighter constraints on tabulated EOS data, required to ensure convexity, than we have seen presented in the literature. Suppose we have an interval with tabulated density, pressure, and energy $n_{0,1}$, $P_{0,1}$, and $\mathcal{E}_{0,1}$. If these data come from an equation of state that satisfies thermodynamic convexity $\mathrm{d}^2\mathcal{E}/\mathrm{d}n^2 = \mathrm{d}P/\mathrm{d}n/n \geq 0$ and causality $\mathrm{d}\mathcal{E}/\mathrm{d}P \geq 1$, then each interval must satisfy the following conditions:

$$P_1 - P_0 \leq \mathcal{E}_1 - \mathcal{E}_0, \quad \frac{\mathcal{E}_1+P_1}{\sqrt{(\mathcal{E}_0+P_0)(E_0+2P_1-P_0)}} \leq \frac{n_1}{n_0} \leq \frac{\sqrt{(\mathcal{E}_1+P_1)(\mathcal{E}_1+2P_0-P_1)}}{\mathcal{E}_0+P_0}. \tag{B.31}$$

The tabulated data in [336] used for the outer crust in chapter 2 required some minor corrections to ensure these constraints are met.

Appendix C

COMPRESSIBLE LIQUID DROP MODEL

C.1 Surface Term in the CLDM

The implementation of the CLDM in chapter 2 includes a surface contribution to the nuclei energy. We employ the following surface term with an effective surface tension $\sigma(n_n^i, n_p^i) = \sigma_0/(1 - C_{\rm sym} f(x_p)) \approx \sigma_0(1 - C_{\rm sym}\beta^2 + \mathcal{O}(\beta^4))$ following [236] (see also [348]):

$$E = 4\pi r_p^2\, \sigma_0 \frac{1}{1 - \frac{C_{\rm sym}}{96}\left(16 - x_p^{-3} - (1-x_p)^{-3}\right)} \tag{C.1a}$$

$$= 4\pi r_p^2\, \sigma_0 \left(1 - C_{\rm sym}\beta^2 + \mathcal{O}(\beta^4)\right), \tag{C.1b}$$

where $x_p = n_p^i/(n_p^i + n_n^i)$ is the proton fraction in the nucleus, and $\beta = (n_n^i - n_p^i)/(n_p^i + n_n^i) = 1 - 2x_p$. We parameterize this as $C_{\rm sym} = \sigma_\delta/\sigma_0$ where $\sigma_\delta \approx 1.38\,\mathrm{MeV/fm^2}$ is held fixed as a parameter of the theory, and σ_0 is varied to smoothly match the tabulated outer-crust data.

Appendix D

FUTURE GW CONSTRAINTS FOR SELECTED EOS MODELS

D.1 Comparison with Piecewise Polytropes

In fig. D.1 we compare the constraints obtained on the total pressure $P(n_B)$ of nuclear matter in β-equilibrium using our `Central` unified parameterization with those obtained using the piecewise polytropic EOS in [306]. To better compare these, we do the following:

1. Fit the parameters of the polytrope to best match our `Central` EOS: $\log(p_1) = 34.3$, $\Gamma_1 = 2.60$, $\Gamma_2 = 3.81$, and $\Gamma_3 = 2.91$.

2. We use the same speed-of-sound core parameterization with $E_c = 350.0\,\mathrm{MeV/fm^3}$, $E_{\max} = 800.0\,\mathrm{MeV/fm^3}$, $C_{\max} = 0.8$ as our `Central` EOS.

3. We start with a bare "Nuclear" constraint by computing the 1.2σ covariance matrix of the parameters from Table III of [306] over the following EOS models that have a small pressure $P(n_0) < 3\,\mathrm{MeV/fm^3}$ at saturation density: PAL6, SLy, APR1, APR2, APR3, APR4, FPS, WFF1, WFF2, WFF3, BBB2, BPAL12, ENG, MPA1, BGN1H1, PCL2, ALF1, ALF2, ALF3, and ALF4. (This excludes some models with hyperon (GNH3, H1-7), pion (PS), and kaon (GS1-2) condensates, as well as the strange-quark matter models MS1-2, which all have significantly higher saturation pressures $P(n_0) > 3\,\mathrm{MeV/fm^3}$). This gives similar bare "Nuclear" errors as our `Central` model at and above saturation density.

We note that the constraints on P are very similar to those from our "Nuclear" parameter set. To obtain this, however, it was critical to use correlated errors in the polytrope parameters. To this end, taking a polytropic EOS with uncorrelated priors is inadvisable. Only

once correlated priors are used does the polytropic equation of state provides constraints comparable to those that can be obtained from our nuclear parameterization.

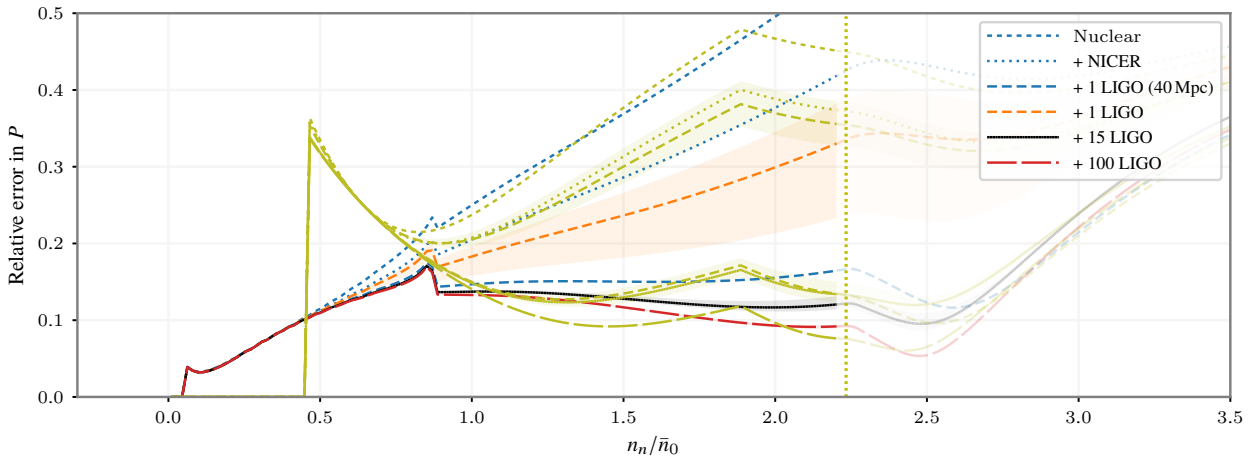

Figure D.1: Relative constraints on the pressure P of nuclear matter in β-equilibrium for the `Central` EOS (dark curves) and a polytropic EOS (light curves) with the same form as [306] with parameters fit to give a similar mass-radius curve, but using the same core EOS as ours. (Note: Kinks in these curves occur when the form of the EOS changes - for example, just below $n = 2n_0$, the from of the polytrope [306] changes.)

D.2 Comparison plots for selected EOS models

On the following pages, we provide comparison plots for all of the EOS models discussed in chapter 2.

Central

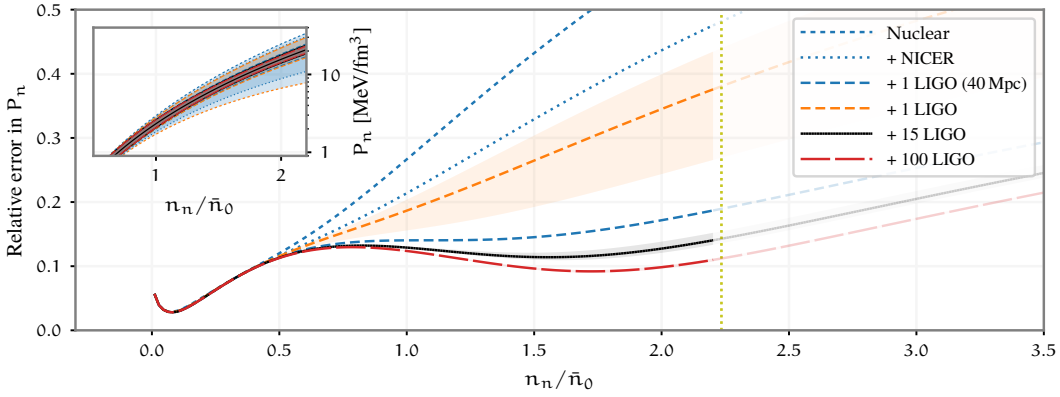
Relative error in P_n
P_n [MeV/fm^3]
$n_n/\bar{n}_0$
Nuclear
+ NICER
+ 1 LIGO (40 Mpc)
+ 1 LIGO
+ 15 LIGO
+ 100 LIGO

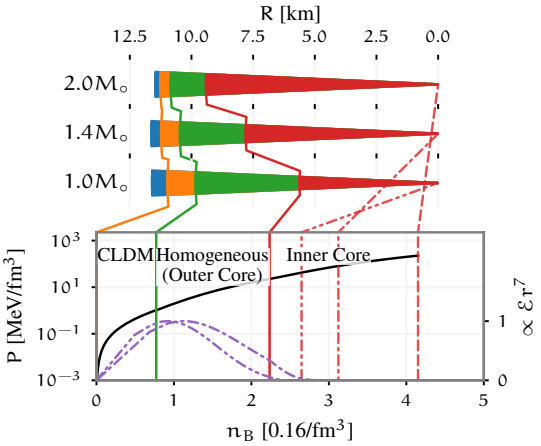
R [km]
2.0M$_\odot$
1.4M$_\odot$
1.0M$_\odot$
P [MeV/fm^3]
CLDM
Homogeneous (Outer Core)
Inner Core
$\propto \varepsilon r^7$
n_B [0.16/fm^3]

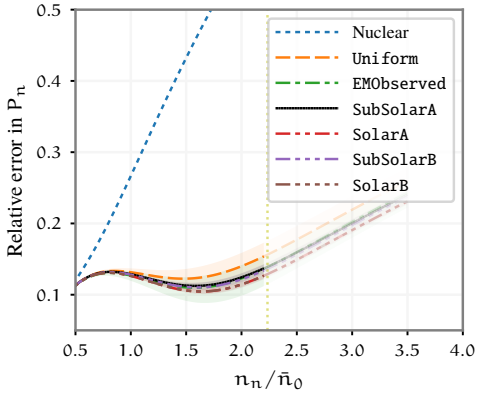
Relative error in P_n
$n_n/\bar{n}_0$
Nuclear
Uniform
EMObserved
SubSolarA
SolarA
SubSolarB
SolarB

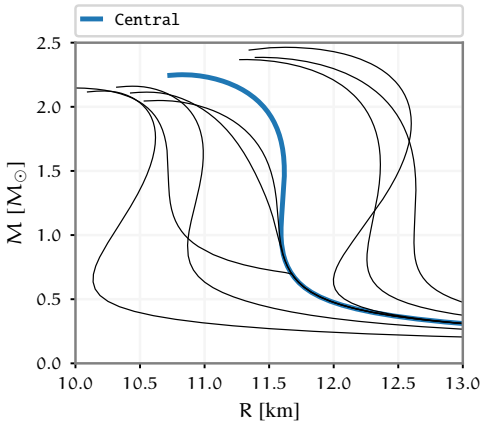
Central
M [M$_\odot$]
R [km]

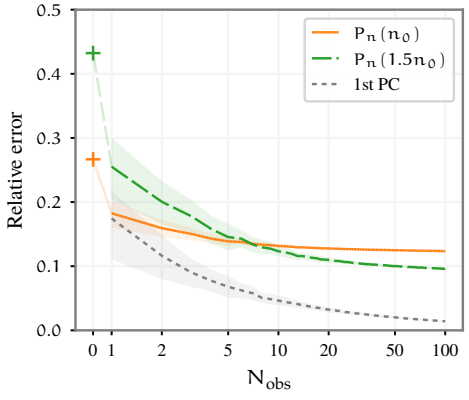
Relative error
N_{obs}
$P_n(n_0)$
$P_n(1.5n_0)$
1st PC

Soft

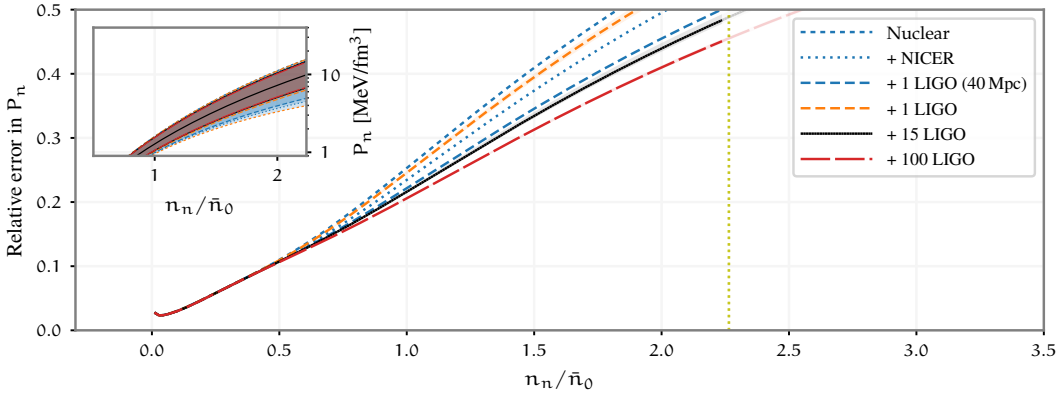
Relative error in P_n
P_n [MeV/fm^3]
$n_n/\bar{n}_0$
Nuclear
+ NICER
+ 1 LIGO (40 Mpc)
+ 1 LIGO
+ 15 LIGO
+ 100 LIGO

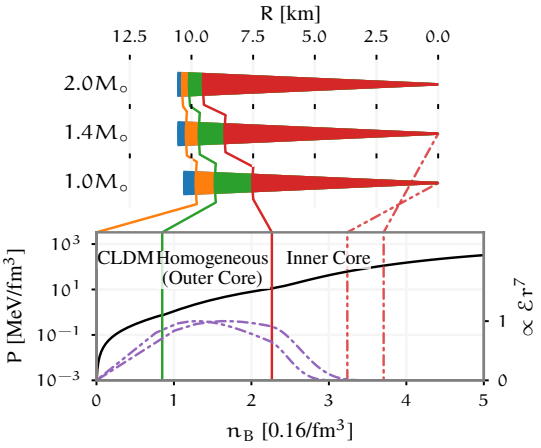
R [km]
2.0$M_\odot$
1.4$M_\odot$
1.0$M_\odot$
P [MeV/fm^3]
CLDM
Homogeneous (Outer Core)
Inner Core
$\propto \mathcal{E}r^7$
n_B [0.16/fm^3]

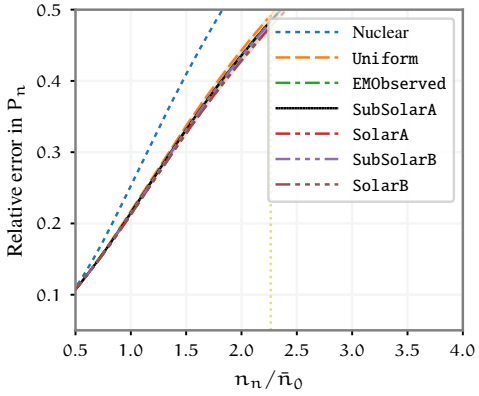
Relative error in P_n
$n_n/\bar{n}_0$
Nuclear
Uniform
EMObserved
SubSolarA
SolarA
SubSolarB
SolarB

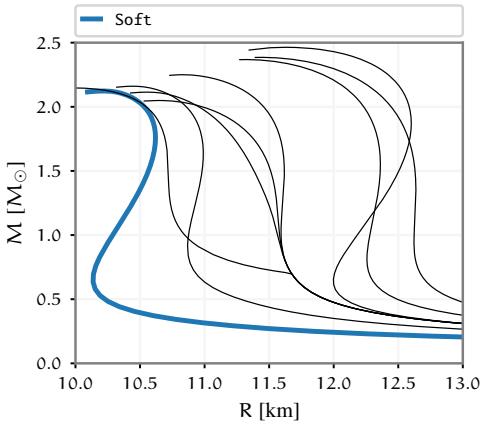
Soft
M [$M_\odot$]
R [km]

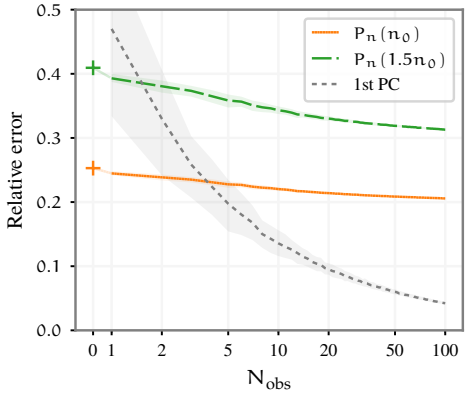
Relative error
$P_n(n_0)$
$P_n(1.5n_0)$
1st PC
N_{obs}

Stiff_Soft

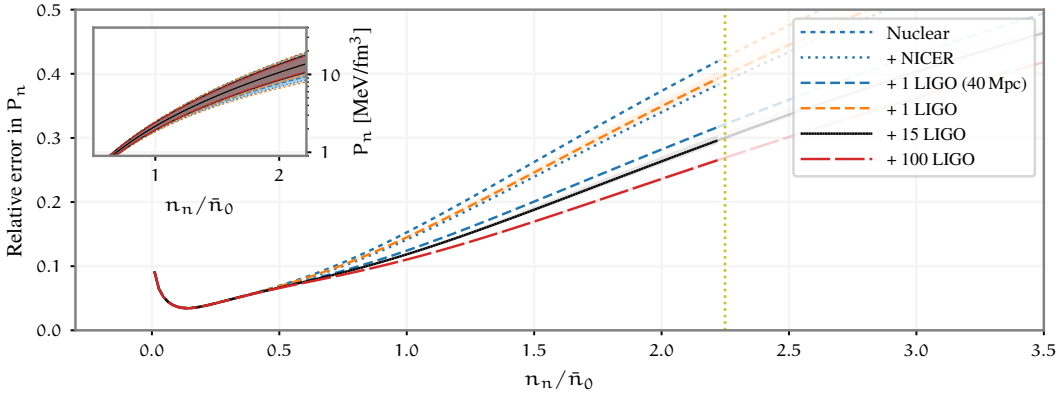
Relative error in P_n
P_n [MeV/fm^3]
$n_n/\bar{n}_0$
Nuclear
+ NICER
+ 1 LIGO (40 Mpc)
+ 1 LIGO
+ 15 LIGO
+ 100 LIGO

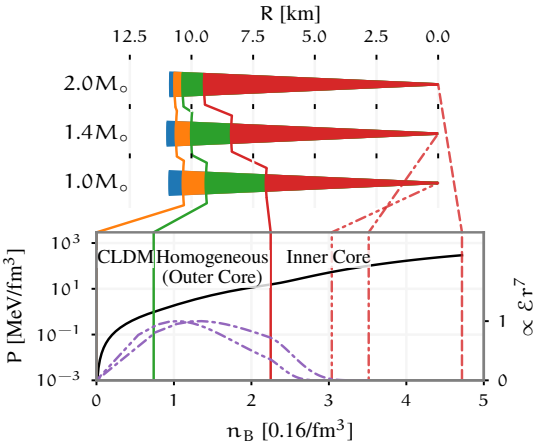
R [km]
2.0$M_\odot$
1.4$M_\odot$
1.0$M_\odot$
CLDM
Homogeneous (Outer Core)
Inner Core
P [MeV/fm^3]
$\propto \mathcal{E} r^7$
n_B [0.16/fm^3]

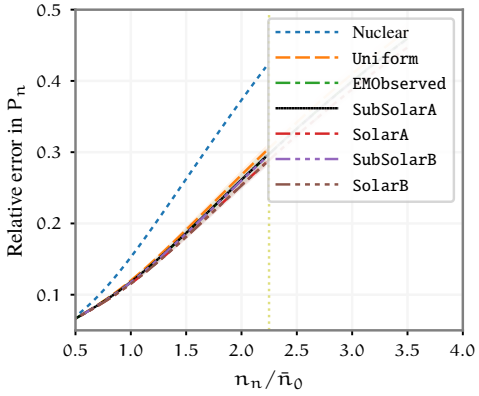
Relative error in P_n
$n_n/\bar{n}_0$
Nuclear
Uniform
EMObserved
SubSolarA
SolarA
SubSolarB
SolarB

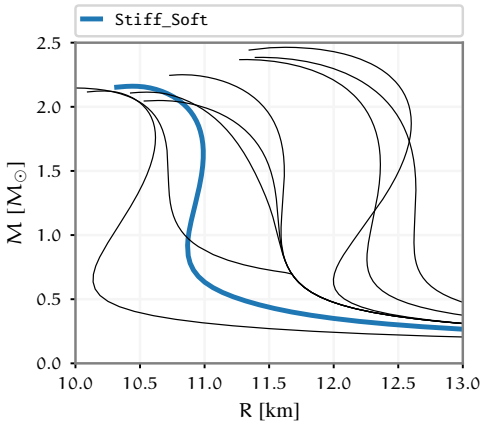
Stiff_Soft
M [$M_\odot$]
R [km]

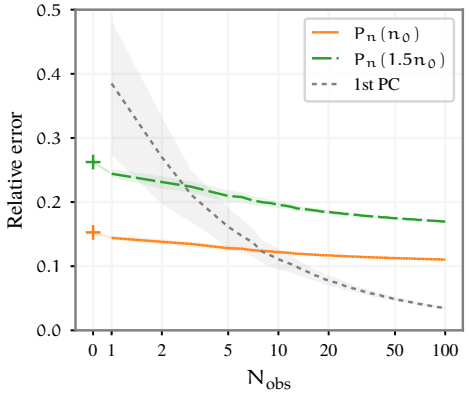
Relative error
N_{obs}
$P_n(n_0)$
$P_n(1.5n_0)$
1st PC

Soft_Stiff

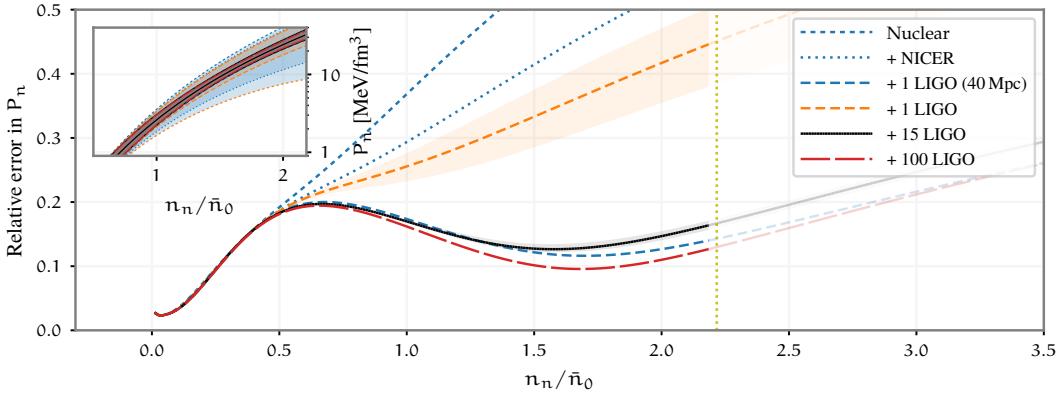
Relative error in P_n
$n_n/\bar{n}_0$
P_n [MeV/fm^3]
Nuclear
+ NICER
+ 1 LIGO (40 Mpc)
+ 1 LIGO
+ 15 LIGO
+ 100 LIGO

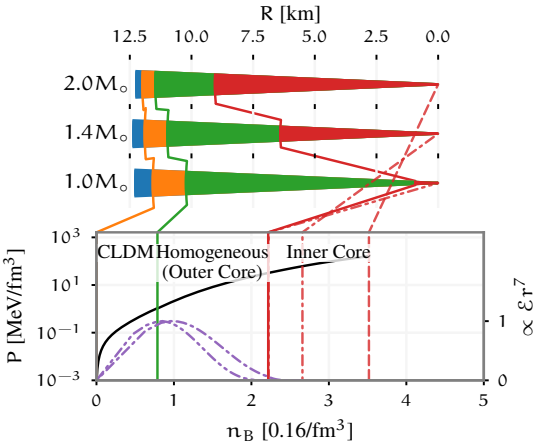
R [km]
2.0M$_\odot$
1.4M$_\odot$
1.0M$_\odot$
P [MeV/fm^3]
CLDM
Homogeneous (Outer Core)
Inner Core
$\propto \mathcal{E}r^7$
n_B [0.16/fm^3]

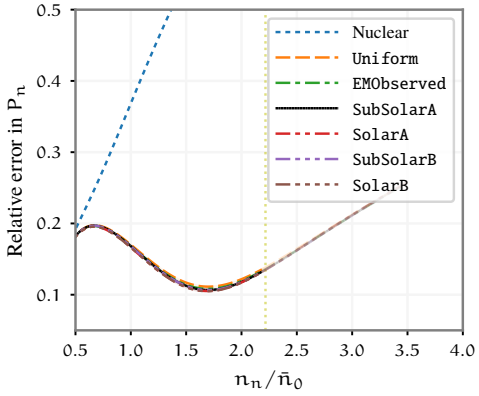
Relative error in P_n
$n_n/\bar{n}_0$
Nuclear
Uniform
EMObserved
SubSolarA
SolarA
SubSolarB
SolarB

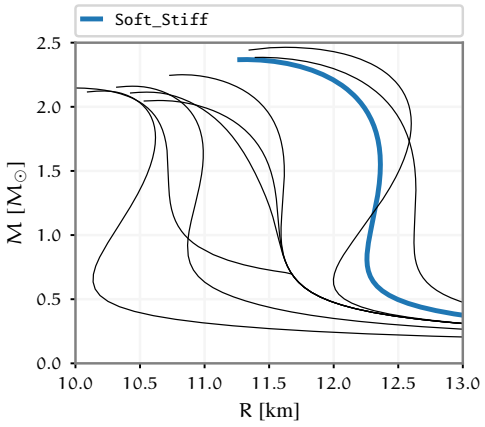
Soft_Stiff
M [M$_\odot$]
R [km]

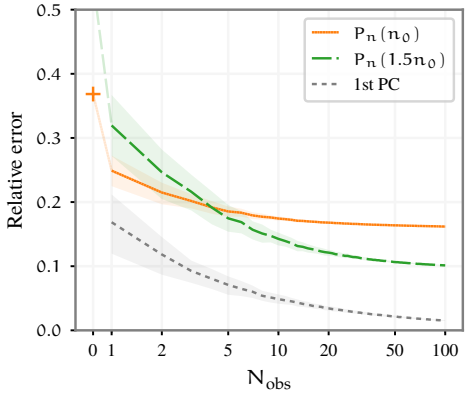
Relative error
N_{obs}
$P_n(n_0)$
$P_n(1.5n_0)$
1st PC

Stiff

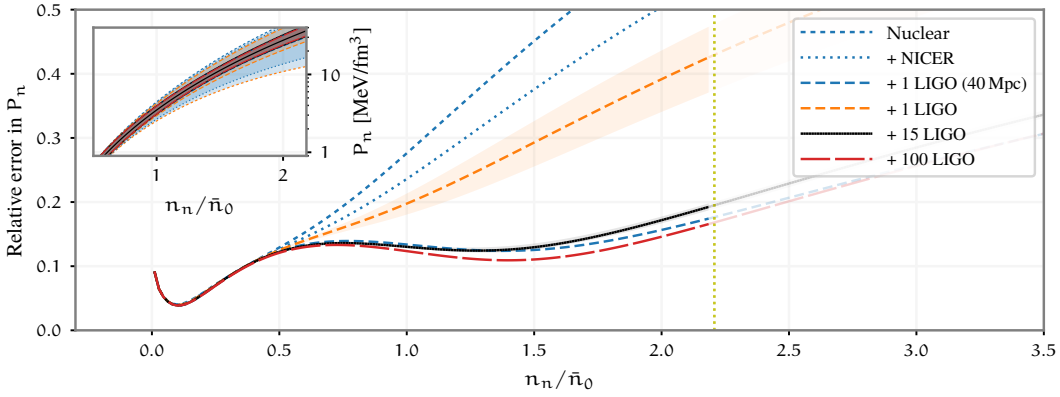
Relative error in P_n
$n_n/\bar{n}_0$
P_n [MeV/fm^3]
Nuclear
+ NICER
+ 1 LIGO (40 Mpc)
+ 1 LIGO
+ 15 LIGO
+ 100 LIGO

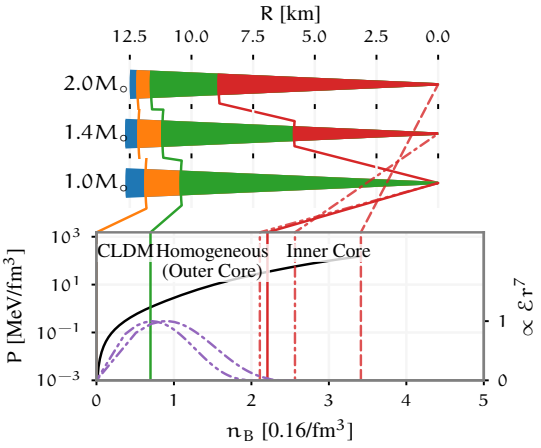
R [km]
2.0$M_\odot$
1.4$M_\odot$
1.0$M_\odot$
CLDM
Homogeneous (Outer Core)
Inner Core
P [MeV/fm^3]
$\propto \mathcal{E}r^7$
n_B [0.16/fm^3]

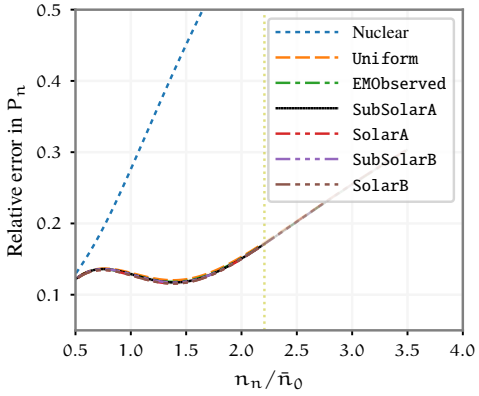
Relative error in P_n
$n_n/\bar{n}_0$
Nuclear
Uniform
EMObserved
SubSolarA
SolarA
SubSolarB
SolarB

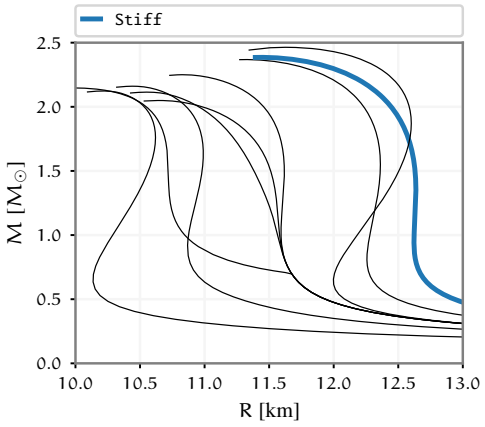
Stiff
M [$M_\odot$]
R [km]

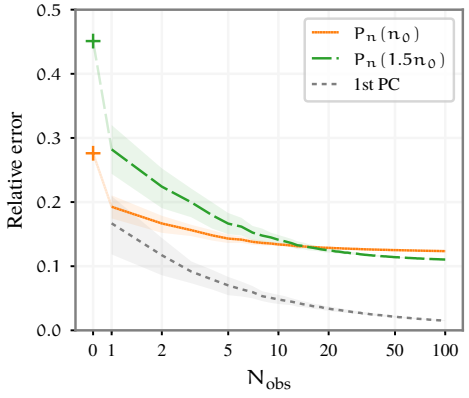
Relative error
N_{obs}
$P_n(n_0)$
$P_n(1.5n_0)$
1st PC

Low_C_{max}

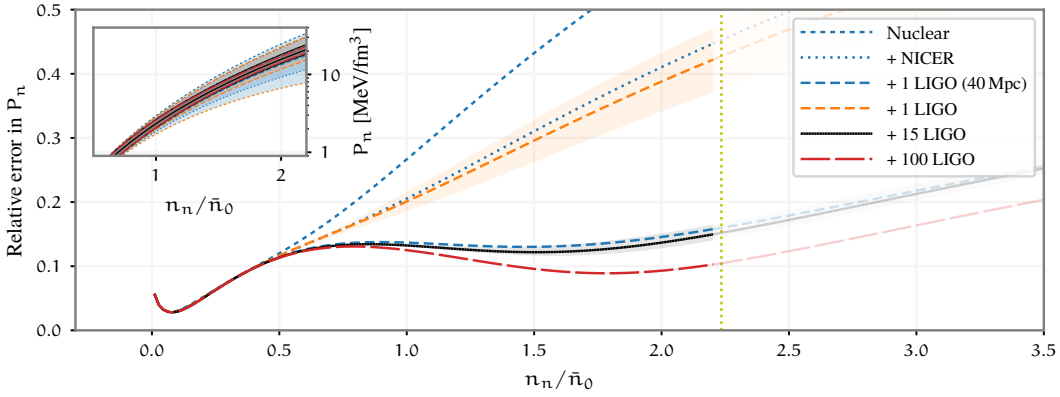
Relative error in P_n
P_n [MeV/fm^3]
$n_n/\bar{n}_0$
Nuclear
+ NICER
+ 1 LIGO (40 Mpc)
+ 1 LIGO
+ 15 LIGO
+ 100 LIGO

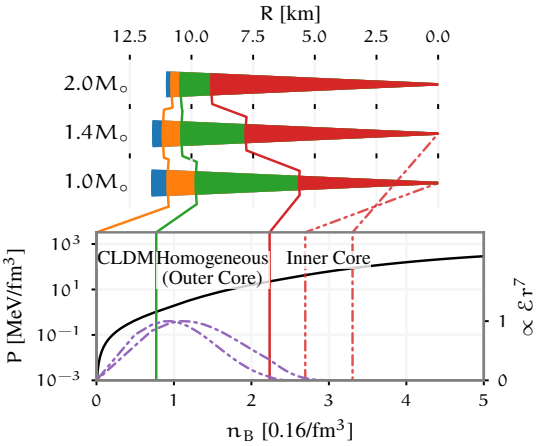
R [km]
2.0$M_\odot$
1.4$M_\odot$
1.0$M_\odot$
P [MeV/fm^3]
CLDM
Homogeneous (Outer Core)
Inner Core
$\propto \mathcal{E} r^7$
n_B [0.16/fm^3]

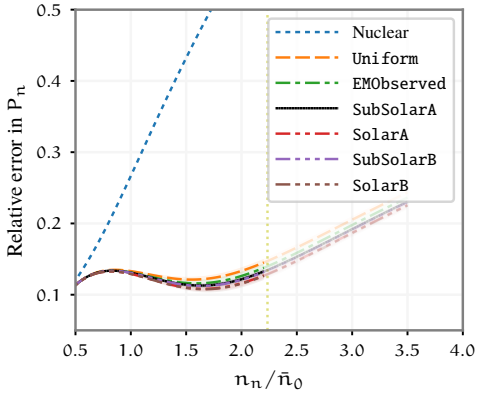
Relative error in P_n
$n_n/\bar{n}_0$
Nuclear
Uniform
EMObserved
SubSolarA
SolarA
SubSolarB
SolarB

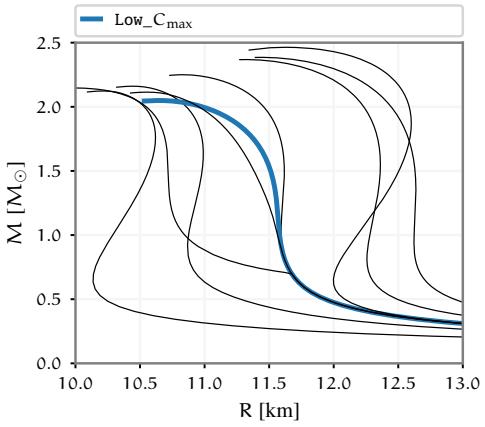
Low_C_{max}
M [$M_\odot$]
R [km]

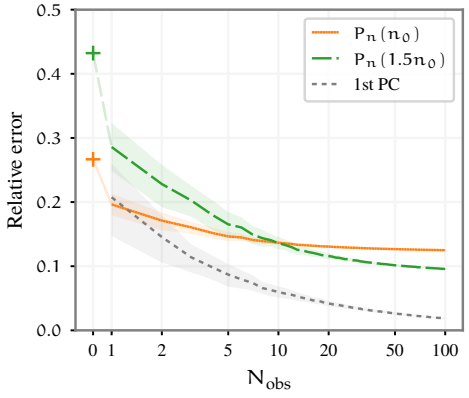
Relative error
N_{obs}
$P_n(n_0)$
$P_n(1.5n_0)$
1st PC

High_$\mathcal{E}_c$

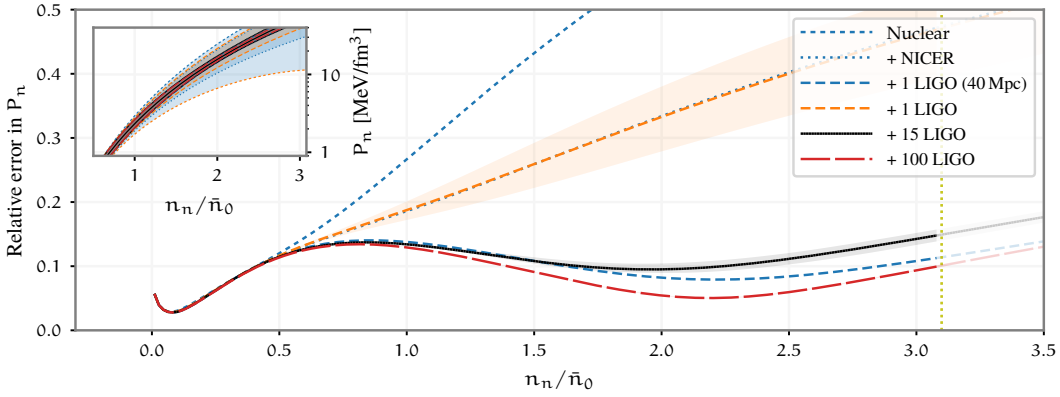

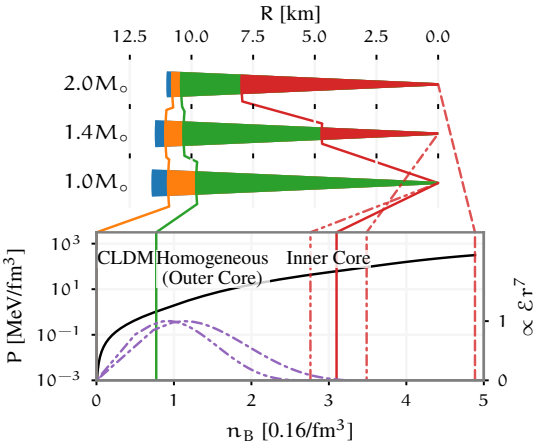

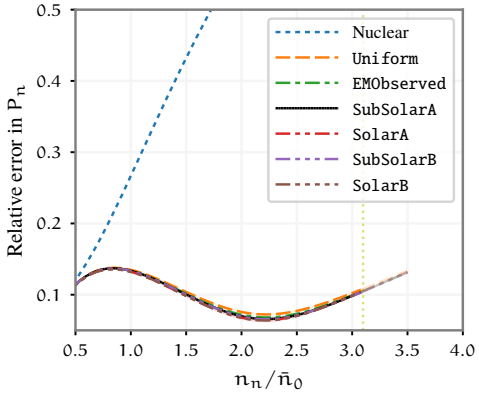

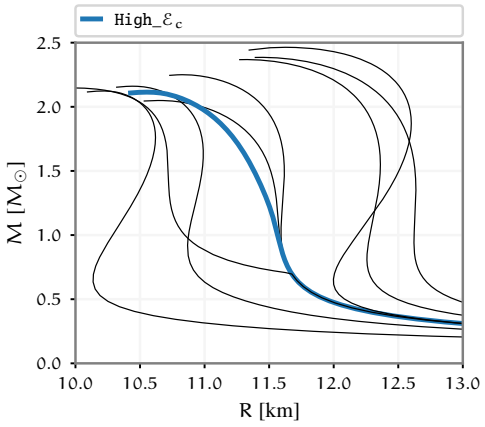

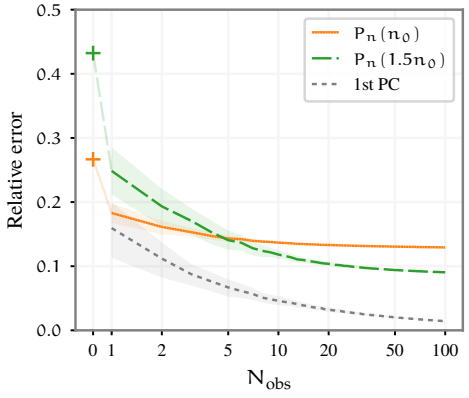

Low_$\mathcal{E}_c$

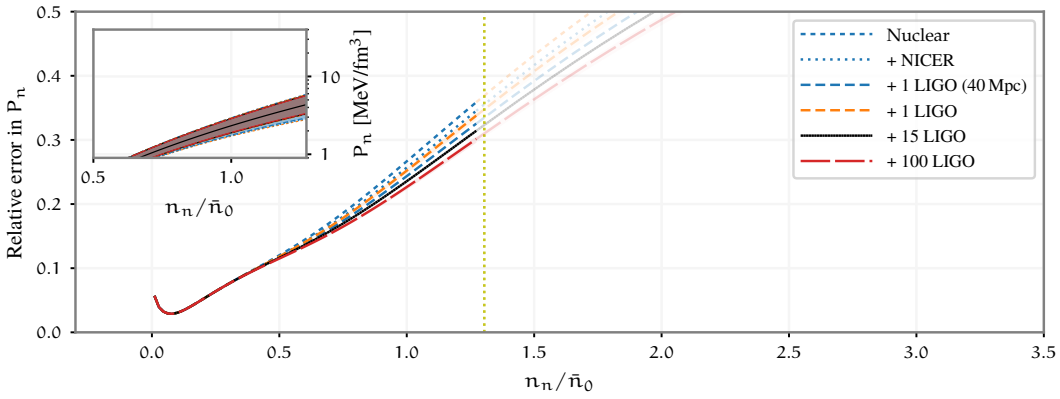

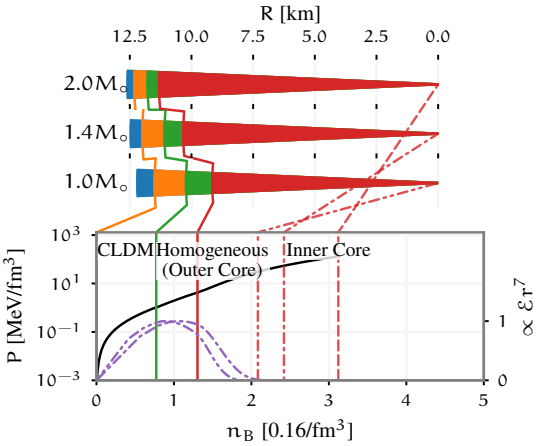

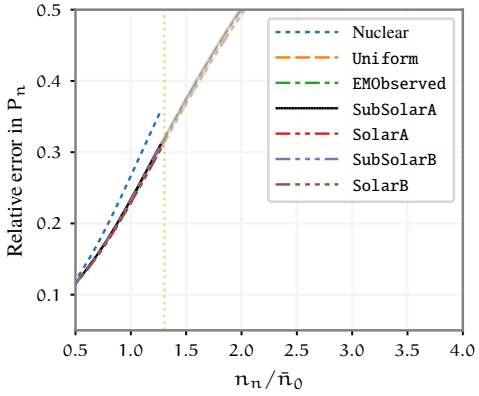

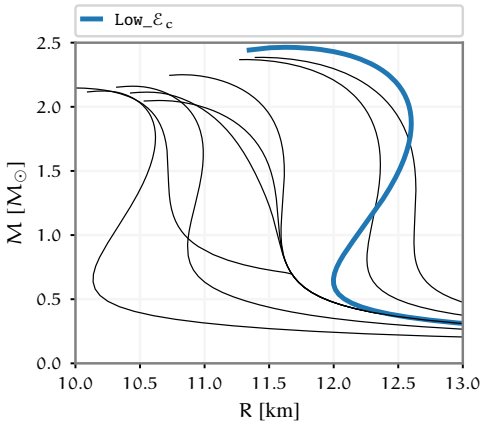

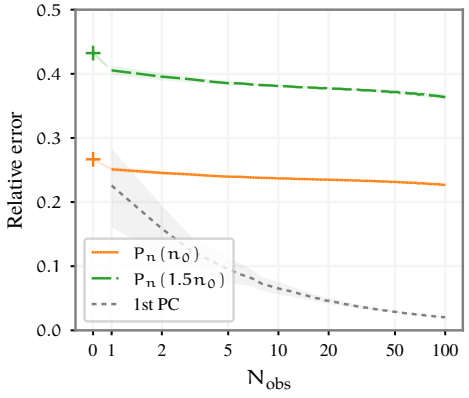

Core_trans

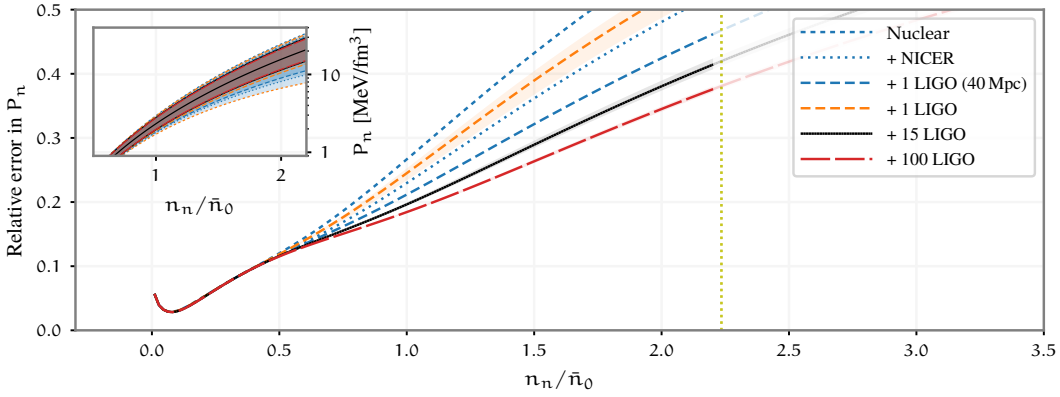
Relative error in P_n
$n_n/\bar{n}_0$
P_n [MeV/fm^3]
Nuclear
+ NICER
+ 1 LIGO (40 Mpc)
+ 1 LIGO
+ 15 LIGO
+ 100 LIGO

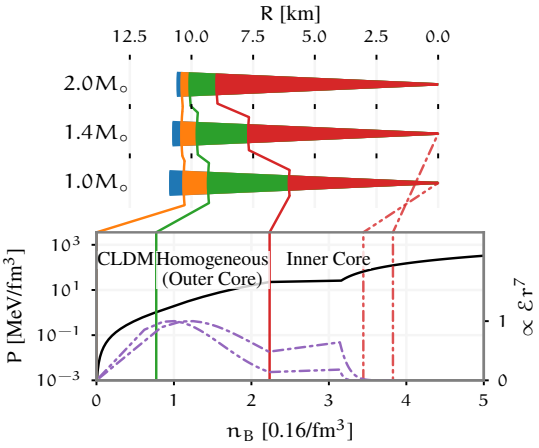
R [km]
2.0$M_\odot$
1.4$M_\odot$
1.0$M_\odot$
P [MeV/fm^3]
CLDM
Homogeneous (Outer Core)
Inner Core
$\propto \mathcal{E}r^7$
n_B [0.16/fm^3]

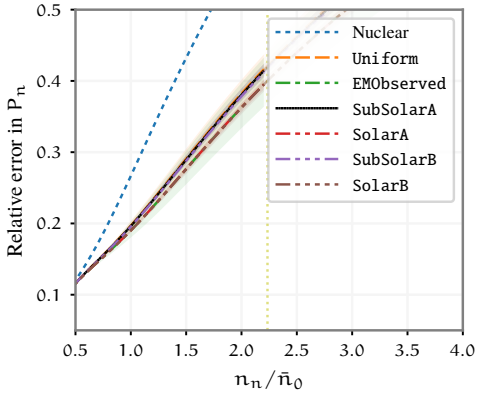
Relative error in P_n
$n_n/\bar{n}_0$
Nuclear
Uniform
EMObserved
SubSolarA
SolarA
SubSolarB
SolarB

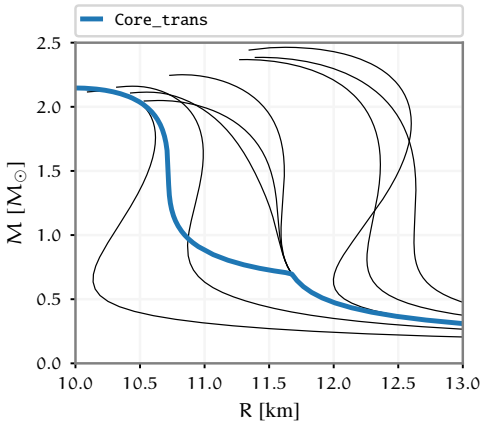
Core_trans
M [$M_\odot$]
R [km]

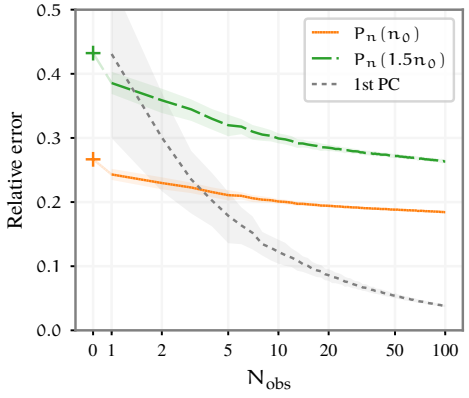
Relative error
N_{obs}
$P_n(n_0)$
$P_n(1.5n_0)$
1st PC

Appendix E

CONSTRAINTS FOR INTERACTING DARK BARYONS

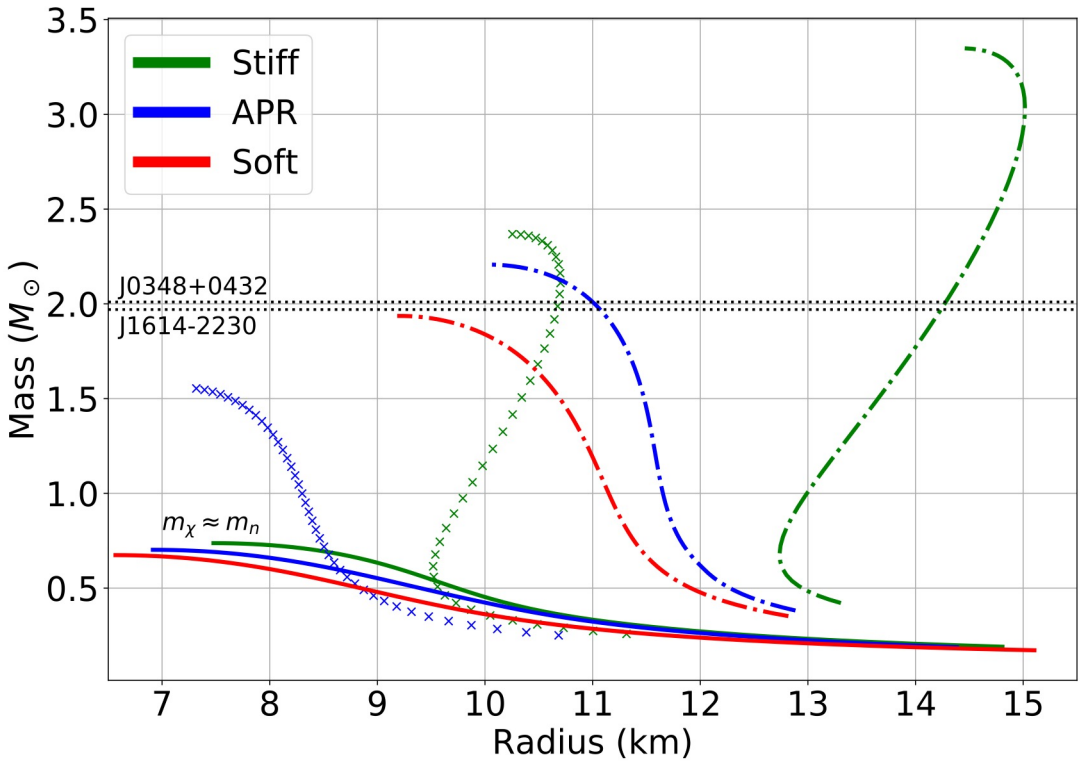

Figure E.1: Mass-radius relations for neutron stars containing mirror neutrons. The dark neutron is assumed to experience the same interactions neutrons do. Reductions to maximum allowed masses remain large. While this scenario cannot be stringently ruled out by the observed massive neutron stars, only extremely stiff equations of state (such as the green curve which shifts to the causal EOS at $n_B > 1.5n_0$) can evade the constraint.

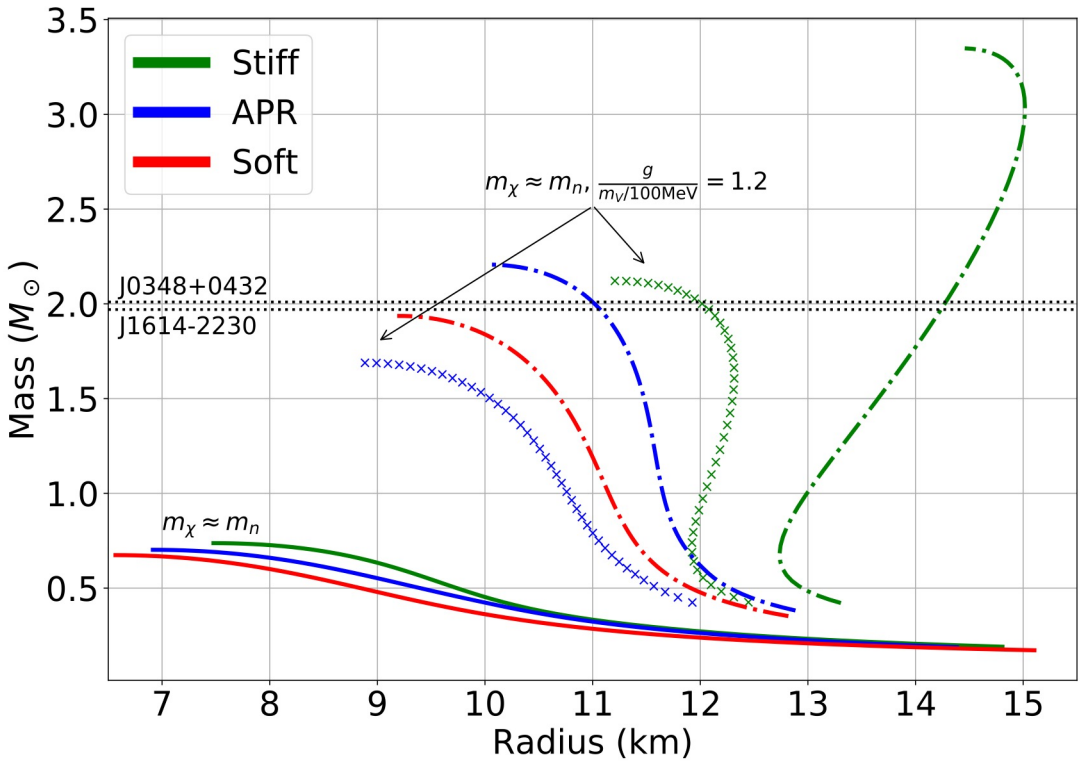

Figure E.2: Maximum allowed mass as a function of self-repulsion strengths for representative underlying nuclear equations of state. The interaction is mediated by a massive dark $U(1)$ force carrier V^μ.

$$\mathcal{L}_{\text{eff}} \supset \bar{\chi}(i\partial\!\!\!/ + g_\chi V\!\!\!/ - m_\chi)\chi - \frac{1}{2}m_V^2 V^\mu V_\mu - \frac{1}{4}V^{\mu\nu}V_{\mu\nu}, \quad V_{\mu\nu} = (\partial_\mu V_\nu - \partial_\nu V_\nu)$$

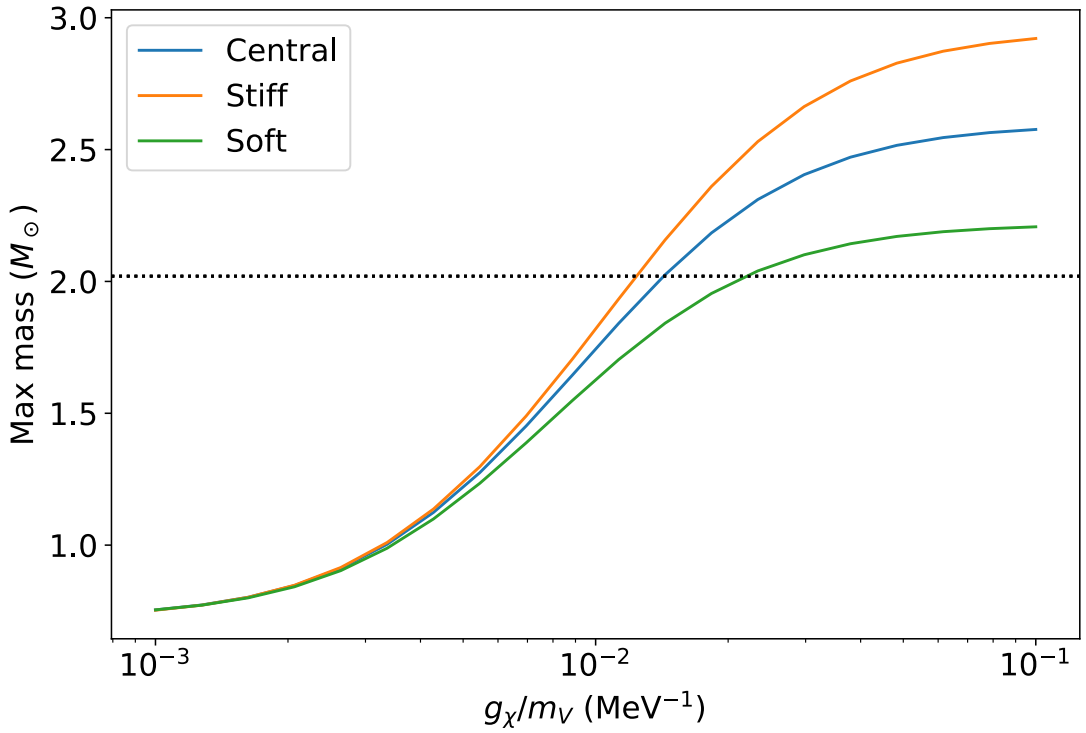

Figure E.3: Maximum neutron star masses as functions of self-repulsion strengths in the presence of a dark $U(1)$ mediator.

Appendix F

RATES AND MEAN FREE PATHS OF DARK LEPTON SCALARS

This appendix details the calculation of the scalar reaction rates and mean free paths in chapter 5.

F.1 ϕ production rate and emissivity

The emissivity (energy radiated per unit volume per unit time) and production rate of ϕ's can be evaluated as

$$\dot{\epsilon}_\phi = \frac{g^2 m_\phi^2 T^3}{32\pi^3}\int_0^\infty \mathrm{d}x_1 \int_{z/(4x_1)}^\infty \mathrm{d}x_2 \; \frac{x_1+x_2}{[\exp(x_1-y_1)+1][\exp(x_2-y_2)+1]},$$
$$\dot{n}_\phi = \frac{g^2 m_\phi^2 T^2}{32\pi^3}\int_0^\infty \mathrm{d}x_1 \int_{z/(4x_1)}^\infty \mathrm{d}x_2 \; \frac{1}{[\exp(x_1-y_1)+1][\exp(x_2-y_2)+1]}.$$

where $x_i = p_i/T$, $y_i = \mu_i/T$ and $z = m_\phi^2/T^2$.

The integral over x_2 for $\dot{\mathcal{E}}_\phi$ can be evaluated in closed form in terms of the polylogarithmic functions $\mathrm{Li}_n(x)$, leading to

$$\dot{\epsilon}_\phi = \frac{g^2 m_\phi^2 T^3}{32\pi^3}\int_0^\infty \mathrm{d}x_1 \frac{\left(x_1+\frac{z}{4x_1}\right)\log\left(1+e^{y_2-\frac{z}{4x_1}}\right) - \mathrm{Li}_2\left(-e^{y_2-\frac{z}{4x_1}}\right)}{e^{(x_1-y_1)}+1}.$$

For an estimate,

$$\dot{\epsilon}_\phi \approx 10^{58}\ \mathrm{ergs/s/km}^3 \times \left(\frac{g}{10^{-3}}\right)^2\left(\frac{m_\phi}{50\ \mathrm{MeV}}\right)^2\left(\frac{T}{30\ \mathrm{MeV}}\right)^3 \mathcal{I}_1(\mu, m_\phi, T),$$
$$\dot{n}_\phi \approx 10^{61}\mathrm{s}^{-1}\mathrm{km}^{-3} \times \left(\frac{g}{10^{-3}}\right)^2\left(\frac{m_\phi}{50\ \mathrm{MeV}}\right)^2\left(\frac{T}{30\ \mathrm{MeV}}\right)^2 \mathcal{I}_2(\mu, m_\phi, T).$$

This rate is unrealistically large since the inverse decay reaction is ignored. For a 0th order approximation we may insert into the integrand a factor $e^{-\Gamma(E_k)R_\nu}$ where R_ν is the size

of the neutrino sphere. Note also the production rate approaches 0 in the limit $m_\phi \to 0$ because massless neutrinos are assumed. For light scalars $m_\phi \lesssim$ keV the neutrino masses have to be taken into consideration.

F.2 Relaxation time

The rate of change of the particle number of interests is given by

$$\frac{\mathrm{d}n_\phi}{\mathrm{d}t} = \int \frac{\mathrm{d}^3p_1}{2E_{p_1}(2\pi)^3}\frac{\mathrm{d}^3p_2}{2E_{p_2}(2\pi)^3}\frac{\mathrm{d}^3k}{2E_k(2\pi)^3}\frac{\left|\mathcal{M}_{\nu\nu\leftrightarrow\phi}\right|^2}{2} \times \left[f_1 f_2(1+g) - (1-f_1)(1-f_2)g\right](2\pi)^4\delta^4(p_1+p_2-k)$$

We already know that ϕ's are produced on very short time scales. We are now interested in understanding how fast ϕ's come into equilibrium with neutrinos for a small deviation in its distribution function $\delta g = g - g_0$, where $g_0 = 1/(\exp\left[(E_k - \mu_\phi)/T\right] - 1)$ is the equilibrium Bose-Einstein distribution function.

In this case, we may linearize the phase space factor by taking $f_{1,2}$ to be the equilibrium Fermi-Dirac distribution of neutrinos and obtain

$$f_1 f_2(1+g) - (1-f_1)(1-f_2)g \approx \frac{f_1 f_2}{g_0}\delta g.$$

So we arrived at

$$\frac{\mathrm{d}n_\phi}{\mathrm{d}t} = \int \frac{\mathrm{d}^3p_1}{2E_{p_1}(2\pi)^3}\frac{\mathrm{d}^3p_2}{2E_{p_2}(2\pi)^3}\frac{\mathrm{d}^3k}{2E_k(2\pi)^3}\frac{\left|\mathcal{M}_{\nu\nu\leftrightarrow\phi}\right|^2}{2}\left[\frac{f_1 f_2}{g_0}\delta g\right](2\pi)^4\delta^4(p_1+p_2-k) \quad \text{(F.1)}$$

The relaxation time τ is defined as the characteristic time scale for the system to return to equilibrium, i.e., $\delta g(E_k) \to \exp\left[-t/\tau(E_k)\right]$, through

$$\frac{\mathrm{d}n_\phi}{\mathrm{d}t} = \int \frac{\mathrm{d}^3k}{(2\pi)^3}\frac{\delta g}{\tau}.$$

Comparing this with eq. F.1 yields eq. 5.3. The evaluation of eq. 5.3 follows similar approaches discussed above, with the exception that now the kinematic puts extra constraints on p when the scalar momentum is held fixed.

F.3 Cherenkov mean free path

At small momenta the Goldstone excitation can be expanded as

$$\omega_\phi^- \approx \sqrt{\frac{\mu^2 - M^2}{3\mu^2 - M^2}}p + \frac{\mu^4}{(3\mu^2 - M^2)^3}\sqrt{\frac{3\mu^2 - M^2}{\mu^2 - M^2}}p^3 + \mathcal{O}(p^5). \tag{F.2}$$

Keeping only the leading term the majoron exhibits a linear dispersion relation with velocity $\alpha = \sqrt{(\mu^2 - M^2)\,/\,(3\mu^2 - M^2)}$. Hence the Cherenkov process may proceed.

With the amplitude $\mathcal{M} = 4g^2(p \cdot p')$ the Cherenkov rate

$$\begin{aligned}
\Gamma_{\nu\to\nu J} &= \frac{1}{E_p}\int \frac{\mathrm{d}^3p'}{2E_{p'}(2\pi)^3}\frac{\mathrm{d}^3k'}{2E_{k'}(2\pi)^3} \times \left|\mathcal{M}_{\nu\to\nu J}\right|^2 (1 - f_{p'})(2\pi)^4\delta^4(p - p' - k') \\
&= \frac{g^2}{2E_pE_{k'}}(2\pi)\int \frac{\mathrm{d}^3p'}{2E_{p'}(2\pi)^3} \times [pp'(1 - \cos\theta)]\,(1 - f_{p'})\delta(p - p' - \alpha k') \\
&= \frac{g^2}{8\pi}\int \mathrm{d}p'\frac{(p')^2p'p}{pp'\alpha k'}\frac{k'}{\alpha pp'}(1 - f_{p'})\int_{-1}^{1}\mathrm{d}\cos\theta(1 - \cos\theta)\delta(\cos\theta - \cos\theta_0) \\
&= \frac{g^2}{8\pi\alpha^2}\frac{1}{p^2}\int_{\frac{1-\alpha}{1+\alpha}p}^{p}\mathrm{d}p'\left(\frac{1}{\alpha^2} - 1\right)(p - p')^2(1 - f_{p'})
\end{aligned}$$

The lower limit of the p' integral was obtained from the requirement

$$-1 \le \cos\theta = 1 - \frac{k'^2}{2pp'}(1 - \alpha^2) \le 1. \tag{F.3}$$

Appendix G

FIELD THEORY AT FINITE T AND μ

Here we work out the thermodynamics of the scalar field theory studied in chapter 5 defined by the Lagrangian

$$\mathcal{L}_\phi = (\partial^\mu \phi^*)(\partial_\mu \phi) - m_\phi^2 \phi^* \phi - \frac{\lambda}{4}(\phi^* \phi)^2, \tag{G.1}$$

and that for the neutrinos defined by

$$\mathcal{L}_{\nu_L} = i\nu_L^\dagger \bar{\sigma}^\mu \partial_\mu \nu_L + \mathcal{L}_{\nu_L,\Delta}$$

where the Yukawa coupling to ϕ results in a Majorana mass (in the absence of Fermi surfaces) term when the scalars condense

$$L_{\nu_L,\Delta} = -\frac{i\Delta}{2}\left(\nu_L^T \sigma_2 \nu_L - \nu_L^\dagger \sigma_2 \nu_L^*\right).$$

We first derive some general results. Statistical properties of ensembles of particles ϕ (for this purpose, either bosons or fermions) can be conveniently described by the grand canonical partition function

$$Z = \mathrm{tr} e^{-\beta(H-\mu N)} = \langle\phi|\, e^{-\beta \int \mathrm{d}^3x(\mathcal{H}-\mu\mathcal{N})}\, |\phi\rangle\ .$$

Here, $\mathcal{H}$ and $\mathcal{N}$ are the Hamiltonian density operator and the particle number operator respectively, and $\beta = 1/T$ is the inverse temperature. A very similar expression arises in quantum theories when transition amplitudes are evaluated with functional integrals

$$\langle \phi_f, t_f | \phi_i, t_i \rangle = \langle \phi_f |\, e^{-iH(t_f - t_i)}\, |\phi_i\rangle = \int_{\phi(t=t_i)=\phi_i}^{\phi(t=t_f)=\phi_f} \mathcal{D}\pi \mathcal{D}\phi \exp\left[i \int \mathrm{d}^4x (\pi\dot{\phi} - \mathcal{H}) \right].$$

where π is the conjugate momentum of ϕ. The equation above suggests that when evaluated in the Euclidean spacetime with a compactified temporal dimension, i.e., $\tau = it$ with periodicity $\tau = \tau + \beta$, path integrals of the transition amplitude over closed trajectories in the

field configuration space ($|\phi_f| = |\phi_i|$) yield the finite temperature grand partition function of the ϕ field. That is,

$$Z = \int_{\phi(t_i)=\pm\phi(t_f)} \mathcal{D}\pi\mathcal{D}\phi \exp\left[\int_0^\beta \mathrm{d}\tau \int \mathrm{d}^3x (i\pi\partial_\tau\phi - \mathcal{H} + \mu\mathcal{N})\right]$$

Above, the boundary conditions account for the spin-statistics of the underlying fields. Boson fields are periodic in the Euclidean temporal direction whereas fermions are anti-periodic. These choices guarantee time-ordered operator products satisfy the correct commutation/anti-commutation relations.

Oftentimes it is convenient to work in the momentum space. The compactified Euclidean time direction implies discretization of (Euclidean) energies $\omega_n \equiv p^0$. Periodic and anti-periodic boundary conditions for bosons and fermions then lead to

$$\omega_n = \begin{cases} 2n\pi/\beta, & \text{bosons} \\ (2n+1)\pi/\beta, & \text{fermions.} \end{cases} \tag{G.2}$$

with $n \in \mathbb{Z}$.

Chemical potentials are associated with conserved charges. For either fermionic or bosonic fields the conserved charge corresponds to the temporal component of the Noether current

$$J^\mu = \sum_i \frac{\partial\mathcal{L}}{\partial(\partial_\mu\phi_i)} \frac{\delta\phi_i}{\delta\alpha}.$$

For a complex scalar field theory that is invariant under a global $U(1)$ transformation $\phi \to e^{-i\alpha}\phi$,

$$J^\mu = -i\phi\partial^\mu\phi^* + i\phi^*\partial^\mu\phi,$$

whereas for a Dirac fermionic field ψ,

$$J^\mu = i\bar{\psi}\gamma^\mu\psi.$$

These suggest that chemical potentials are added to the Lagrangian as temporal components of gauge fields.

G.1 Fermions

The Lagrangian for neutrinos after ϕ develops a vev is

$$\mathcal{L} = i\nu_L^\dagger \bar{\sigma}^\mu \partial_\mu \nu_L - \frac{i\Delta}{2}\left(\nu_L^T \sigma_2 \nu_L - \nu_L^\dagger \sigma_2 \nu_L^*\right) = \frac{i}{2}\left(\nu_L^\dagger \bar{\sigma}^\mu \partial_\mu \nu_L + \nu_L^{c\,\dagger} \sigma^\mu \partial_\mu \nu_L^c\right) + \frac{\Delta}{2}\left(\nu_L^{c\,\dagger}\nu_L + \nu_L^\dagger \nu_L^c\right),$$

We performed integrations by part to get the kinetic term of $\nu_L^c = i\sigma_2 \nu_L^*$. The conserved charge for ν_L is $\mathcal{Q} = \nu_L^\dagger \nu_L = -\nu_L^{c\,\dagger}\nu_L^c$. Putting everything together we can express the exponent in a way that is symmetric with respect to ν_L and ν_L^c:

$$\begin{aligned}\pi_{\nu_L}\dot{\nu}_L + \pi_{\nu_L^c}\dot{\nu}_L^c - \mathcal{H} + \mu\mathcal{Q} = &-\frac{1}{2}\left(\nu_L^\dagger \partial_\tau \nu_L + \nu_L^{c\,\dagger}\partial_\tau \nu_L^c\right) + \frac{i}{2}\left(\nu_L^\dagger \sigma^i \partial_i \nu_L - \nu_L^{c\,\dagger}\sigma^i \partial_i \nu_L^c\right) \\ &+ \frac{\Delta}{2}\left(\nu_L^{c\,\dagger}\nu_L + \nu_L^\dagger \nu_L^c\right) + \frac{\mu}{2}\left(\nu_L^\dagger \nu_L - \nu_L^{c\,\dagger}\nu_L^c\right).\end{aligned}$$

It is convenient to work in momentum space. Putting the system in a box of volume V, the Fourier modes of neutrinos and anti-neutrinos take the form

$$\nu(x) = \frac{1}{\sqrt{V}}\sum_n \sum_{\mathbf{p}} e^{i(w_n\tau + \mathbf{px})}\widetilde{\nu}_n(\mathbf{p}) \tag{G.3}$$

$$\nu^c(t,\mathbf{x}) = \frac{1}{\sqrt{V}}\sum_n \sum_{\mathbf{p}} e^{-i(w_n\tau + \mathbf{px})}(i\sigma_2 \widetilde{\nu}_n^*(\mathbf{p})) = \frac{1}{\sqrt{V}}\sum_n \sum_{\mathbf{p}} e^{i(w_n\tau + \mathbf{px})}\widetilde{\nu}_{-n+1}^c(-\mathbf{p}) \tag{G.4}$$

Now in the basis $N_n(\mathbf{p}) = (\widetilde{\nu}_n(\mathbf{p}), \widetilde{\nu}_{-n+1}^c(-\mathbf{p}))^T$, the grand canonical partition function becomes

$$Z = \int \prod_{n,\mathbf{p}} \mathcal{D}iN_n^\dagger \mathcal{D}N_n(\mathbf{p}) \exp\left[\int_0^\beta \mathrm{d}\tau \int \mathrm{d}^3x \sum_{n,\mathbf{p}} iN_n^\dagger(-\mathbf{p})DN_n(\mathbf{p})\right] = \det D,$$

$$D = \frac{i}{2}\beta \begin{pmatrix} i\omega_n + \sigma\cdot\mathbf{p} - \mu & -\Delta \\ -\Delta & i\omega_n - \sigma\cdot\mathbf{p} + \mu \end{pmatrix}. \tag{G.5}$$

Had we start from a 4-component Dirac fermion with (i.e., including the sterile state ν_R) $\psi = (\nu_L, \nu_R)^T$, the sign of the chemical potential μ in the lower 2×2 diagonal block would become positive. This can be seen from the charge density operator $\mathcal{Q} = j^0(x) = \bar{\psi}\gamma^0\psi = \nu_L^\dagger\nu_L + \nu_R^\dagger\nu_R$. For the 4 component Majorana spinor $N = (\nu_L, i\sigma_2\nu_L^*)^T$, the temporal component of Noether currents vanishes $j^0 = \nu_L^\dagger\nu_L + \nu_L^{c\,\dagger}\nu_L^c = 0$.

It then follows that

$$\log Z = \log(\det D) = \log\left[\beta^2(\Delta^2 + (\mu - p)^2 + \omega_n^2)\right] + \log\left[\beta^2(\Delta^2 + (\mu + p)^2 + \omega_n^2)\right].$$

To get rid of Matsubara frequencies note that the logarithms functions above can be expressed as

$$\log(x^2 + \beta^2\omega_n^2) = \int_1^{x^2} \frac{\mathrm{d}z^2}{z^2 + \beta^2\omega_n^2} + \text{const.}$$

The constant term is independent of T or V therefore irrelevant for thermodynamics. The summation over n can then be performed as

$$\sum_n \frac{1}{(2n+1)^2\pi^2 + x^2} = \frac{1}{x}\left(\frac{1}{2} - \frac{1}{1 + \exp(x)}\right).$$

So we arrive at

$$\Omega_{F,0} = -\beta^{-1}\log Z = -V\int \frac{\mathrm{d}^3p}{(2\pi)^3}\frac{1}{2}\left\{\sqrt{\Delta^2 + (\mu - p)^2} + \sqrt{\Delta^2 + (\mu + p)^2}\right.$$
$$\left. + 2\beta^{-1}\log\left[1 + \exp\left(-\beta\sqrt{\Delta^2 + (\mu - p)^2}\right)\right] + 2\beta^{-1}\log\left[1 + \exp\left(-\beta\sqrt{\Delta^2 + (\mu + p)^2}\right)\right]\right\}$$

In the $\Delta \to 0$ limit we recover the massless Weyl fermion grand potential

$$\Omega_{F,0}(f = 0)/V = -\frac{1}{2}\int \frac{\mathrm{d}^3p}{(2\pi)^3}\left\{2p + 2T\log\left[1 + e^{-\beta(p-\mu)}\right] + 2T\log\left[1 + e^{-\beta(p+\mu)}\right]\right\}.$$

The UV divergence becomes apparent once a momentum cutoff Λ is imposed:

$$\Omega_{F,0} = -\frac{1}{2\pi^2}\left[\frac{\Lambda^4}{4} + \frac{\Delta^2}{4}\Lambda^2 + \frac{\Delta^4 - 4\Delta^2\mu^2}{8}\log(\Lambda/K)\right] + \text{finite.}$$

G.2 Bosons

We now return to the bosons eq. G.1. The conjugate momenta are $\pi_\phi = \partial_t\phi^*$ and $\pi_{\phi^*} = \partial_t\phi$. So we obtain

$$\mathcal{H} = \pi_\phi\dot{\phi} + \pi_{\phi^*}\dot{\phi}^* - \mathcal{L} = \pi_\phi\pi_{\phi^*} + \partial^i\phi^*\partial_i\phi + m_\phi^2\phi^*\phi + \frac{\lambda}{4}(\phi^*\phi)^2.$$

The charge density operator is given by

$$\mathcal{Q} = i(\phi^*\partial_t\phi - \phi\partial_t\phi^*) = i(\phi^*\pi_{\phi^*} - \phi\pi_\phi).$$

Now we have all the ingredients to compute

$$\mathcal{L}' = i\sum_k \pi_k\partial_\tau\phi_k - \mathcal{H} + \mu\mathcal{N} = \pi_\phi\dot{\phi} + \pi_{\phi^*}\dot{\phi}^* - \pi_\phi\pi_{\phi^*} - \partial^i\phi^*\partial_i\phi - m_\phi^2\phi^*\phi - \frac{\lambda}{4}(\phi^*\phi)^2 + i\mu(\phi^*\pi_{\phi^*} - \phi\pi_\phi).$$

Rewriting the ϕ field in terms of its Cartesian components,

$$\phi = \frac{1}{\sqrt{2}}(\phi_1 + i\phi_2), \quad \phi^* = \frac{1}{\sqrt{2}}(\phi_1 - i\phi_2),$$

we can integrate out the momenta in $\mathcal{L}'$ and obtain

$$\mathcal{L}'' = \frac{1}{2}(i\partial_\tau\phi_1 + \mu\phi_2)^2 + \frac{1}{2}(i\partial_\tau\phi_2 - \mu\phi_1)^2 - \frac{1}{2}\left((\partial^i\phi_1)^2 + (\partial^i\phi_2)^2\right) - \frac{1}{2}m_\phi^2(\phi_1^2+\phi_2^2) - \frac{\lambda}{16}(\phi_1^2+\phi_2^2)^2.$$

In momentum space ϕ_i can be expand around the vev $\langle\phi\rangle = f/\sqrt{2}$ as

$$\begin{aligned}\phi_1 &= f\cos\theta + \sqrt{\frac{\beta}{V}}\sum_{n,\mathbf{p}} e^{i(w_n\tau + \mathbf{px})}\widetilde{\phi}_{1,n}(\mathbf{p}),\\ \phi_2 &= f\sin\theta + \sqrt{\frac{\beta}{V}}\sum_{n,\mathbf{p}} e^{i(w_n\tau + \mathbf{px})}\widetilde{\phi}_{2,n}(\mathbf{p})\end{aligned} \tag{G.6}$$

In the absence of quartic couplings an exact result may be obtained. We shall treat λ perturbatively. Since θ parameterize the flat direction of the Mexican hat potential, we may utilize the shift symmetry and study the excitation spectrum around $\theta = 0$. At leading order the expansion of the quartic interaction leads to the following terms that survive the Gaussian integral

$$\frac{\lambda}{16}(\phi_1^2+\phi_2^2)^2 = \frac{3\lambda}{8}f^2\widetilde{\phi}_{1,-n}(-\mathbf{p})\phi_{1,n}(\mathbf{p}) + \frac{\lambda}{8}f^2\widetilde{\phi}_{2,-n}(-\mathbf{p})\phi_{2,n}(\mathbf{p}) + \mathcal{O}(\widetilde{\phi}_i^3).$$

Now the partition function takes the following form in the basis $\Phi_n(\mathbf{p}) = (\widetilde{\phi}_{1,n}(\mathbf{p}), \widetilde{\phi}_{2,n}(\mathbf{p}))^T$:

$$\begin{aligned}Z &= \int\prod_{n,\mathbf{p}}\mathcal{D}\phi_{1,n}(\mathbf{p})\mathcal{D}\phi_{2,n}(\mathbf{p})\exp\left[\frac{\beta V}{4}f^2(\mu^2 - m_\phi^2) - \frac{1}{2}\sum_{n,\mathbf{p}}\Phi_{-n}(-\mathbf{p})D\Phi_n(\mathbf{p})\right] = e^{\frac{\beta V}{4}f^2(\mu^2-m_\phi^2)}(\det D)^{-\frac{1}{2}},\\ D &= \beta^2\begin{pmatrix}\omega_n^2 + p^2 + m_\phi^2 - \mu^2 + \frac{3\lambda}{4}f^2 & -2\omega_n\mu\\ 2\omega_n\mu & \omega_n^2 + p^2 + m_\phi^2 - \mu^2 + \frac{\lambda}{4}f^2\end{pmatrix}.\end{aligned} \tag{G.7}$$

The roots of the characteristic polynomial of D allows us to write

$$-\frac{1}{2}\log\det D = \log\beta^2\left(\omega_n^2+\omega_+^2\right)+\log\beta^2\left(\omega_n^2+\omega_-^2\right)$$

with

$$\omega_\pm^2 = \left(E_p^2+\mu^2+\frac{\lambda}{2}f^2 \pm \sqrt{\frac{\lambda^2 f^4}{16}+\mu^2(4E_p^2+2\lambda f^2)}\right). \tag{G.8}$$

We have defined the free particle energy $E_p = \sqrt{p^2+m_\phi^2}$. Applying the usual bag of tricks we can carry out the sum over Matasubara frequencies and obtain

$$\begin{aligned}
\Omega_{B,0} &= -\beta^{-1}\log Z = \frac{V}{4}f^2(m_\phi^2-\mu^2)+\frac{1}{2}\beta^{-1}\sum_{n,\mathbf{p}}\log\det D \\
&= \frac{V}{4}f^2(m_\phi^2-\mu^2)+\frac{1}{2}\beta^{-1}\sum_{n,\mathbf{p}}\sum_{\omega_\pm}\int_1^{\beta^2\omega_\pm^2}\frac{\mathrm{d}x^2}{x^2+(2n\pi)^2}+\text{const} \\
&= \frac{V}{4}f^2(m_\phi^2-\mu^2)+\beta^{-1}\sum_{\mathbf{p}}\sum_{\omega_\pm}\left(\frac{1}{2}\beta\omega_\pm+\log\left(1-e^{-\beta\omega_\pm}\right)\right) \\
&= \frac{V}{4}f^2(m_\phi^2-\mu^2)+V\int\frac{\mathrm{d}^3p}{(2\pi)^3}\left[\frac{1}{2}(\omega_++\omega_-)+\beta^{-1}\log\left(1-e^{-\beta\omega_+}\right)+\beta^{-1}\log\left(1-e^{-\beta\omega_-}\right)\right].
\end{aligned} \tag{G.9}$$

The thermodynamic limit $V\to\infty$ is taken in obtaining the last line, so the sum over discrete momenta is replaced by a continuous integral. In the absence of the condensate f the dispersion relations reduce to $\omega_\pm = E\pm\mu$, thus we recover the usual Bose-Einstein statistic:

$$\Omega_{B,0}(f=0) = V\int\frac{\mathrm{d}^3p}{(\pi)^3}\left\{E_p+T\log\left[1-e^{-\beta(E_p-\mu)}\right]+T\log\left[1-e^{-\beta(E_p+\mu)}\right]\right\}.$$

BIBLIOGRAPHY

[1] R. Aaij et al. Measurement of the ratio of the $B^0 \to D^{*-}\tau^+\nu_\tau$ and $B^0 \to D^{*-}\mu^+\nu_\mu$ branching fractions using three-prong τ-lepton decays. *Phys. Rev. Lett.*, 120(17):171802, 2018.

[2] B. P. Abbott et al. Observation of Gravitational Waves from a Binary Black Hole Merger. *Phys. Rev. Lett.*, 116(6):061102, 2016.

[3] B. P. Abbott et al. A gravitational-wave standard siren measurement of the Hubble constant. *Nature*, 551(7678):85–88, 2017.

[4] B. P. Abbott et al. GW170817: Observation of Gravitational Waves from a Binary Neutron Star Inspiral. *Phys. Rev. Lett.*, 119(16):161101, 2017.

[5] B. P. Abbott et al. GW170817: Measurements of neutron star radii and equation of state. *Phys. Rev. Lett.*, 121(16):161101, 2018.

[6] B. P. Abbott et al. GWTC-1: A Gravitational-Wave Transient Catalog of Compact Binary Mergers Observed by LIGO and Virgo during the First and Second Observing Runs. 2018.

[7] B. P. Abbott et al. Prospects for Observing and Localizing Gravitational-Wave Transients with Advanced LIGO, Advanced Virgo and KAGRA. *Living Rev. Rel.*, 21(1):3, 2018.

[8] B. P. Abbott et al. Properties of the binary neutron star merger GW170817. *Phys. Rev.*, X9(1):011001, 2019.

[9] R. Abbott et al. All-sky Search for Continuous Gravitational Waves from Isolated Neutron Stars in the Early O3 LIGO Data. 7 2021.

[10] B. Abi et al. Measurement of the Positive Muon Anomalous Magnetic Moment to 0.46 ppm. *Phys. Rev. Lett.*, 126(14):141801, 2021.

[11] Stephen L. Adler. Axial vector vertex in spinor electrodynamics. *Phys. Rev.*, 177:2426–2438, 1969.

[12] Michalis Agathos, Jeroen Meidam, Walter Del Pozzo, Tjonnie G. F. Li, Marco Tompitak, John Veitch, Salvatore Vitale, and Chris Van Den Broeck. Constraining the neutron star equation of state with gravitational wave signals from coalescing binary neutron stars. *Phys. Rev. D*, D92(2):023012, 2015.

[13] N. Aghanim et al. Planck 2018 results. VI. Cosmological parameters. *Astron. Astrophys.*, 641:A6, 2020.

[14] A. Aguilar-Arevalo et al. Evidence for neutrino oscillations from the observation of $\bar{\nu}_e$ appearance in a $\bar{\nu}_\mu$ beam. *Phys. Rev. D*, 64:112007, 2001.

[15] A. A. Aguilar-Arevalo et al. Significant Excess of ElectronLike Events in the MiniBooNE Short-Baseline Neutrino Experiment. *Phys. Rev. Lett.*, 121(22):221801, 2018.

[16] P. Ajith and Sukanta Bose. Estimating the parameters of non-spinning binary black holes using ground-based gravitational-wave detectors: Statistical errors. *Phys. Rev.*, D79:084032, 2009.

[17] A. Akmal, V. R. Pandharipande, and D. G. Ravenhall. The Equation of state of nucleon matter and neutron star structure. *Phys. Rev. C*, 58:1804–1828, 1998.

[18] Stephon Alexander, Jason J. Bramburger, and Evan McDonough. Dark Disk Substructure and Superfluid Dark Matter. *Phys. Lett. B*, 797:134871, 2019.

[19] Stephon Alexander, Evan McDonough, and David N. Spergel. Strongly-Interacting Ultralight Millicharged Particle (STUMP) Neutron Stars as Dark Matter Halos. 11 2020.

[20] Mark Alford. Raised in discussions at the INT-16-2b program.

[21] Mark G. Alford, Andreas Schmitt, Krishna Rajagopal, and Thomas Schäfer. Color superconductivity in dense quark matter. *Rev. Mod. Phys.*, 80:1455–1515, 2008.

[22] Pau Amaro-Seoane et al. Laser Interferometer Space Antenna. 2 2017.

[23] P. W. ANDERSON and N. ITOH. Pulsar glitches and restlessness as a hard superfluidity phenomenon. *Nature*, 256(5512):25–27, jul 1975.

[24] J. Antoniadis, P. C. C. Freire, N. Wex, T. M. Tauris, R. S. Lynch, M. H. van Kerkwijk, M. Kramer, C. Bassa, V. S. Dhillon, T. Driebe, and et al. A massive pulsar in a compact relativistic binary. *Science*, 340(6131):1233232–1233232, Apr 2013.

[25] John Antoniadis et al. A Massive Pulsar in a Compact Relativistic Binary. *Science*, 340:6131, 2013.

[26] Jonathan M. Arnold, Bartosz Fornal, and Mark B. Wise. Simplified models with baryon number violation but no proton decay. *Phys. Rev.*, D87:075004, 2013.

[27] S. Arzumanov, L. Bondarenko, S. Chernyavsky, P. Geltenbort, V. Morozov, V. V. Nesvizhevsky, Yu. Panin, and A. Strepetov. A measurement of the neutron lifetime using the method of storage of ultracold neutrons and detection of inelastically up-scattered neutrons. *Phys. Lett.*, B745:79–89, 2015.

[28] W. Baade and F. Zwicky. Cosmic rays from super-novae. *Proceedings of the National Academy of Sciences*, 20(5):259–263, may 1934.

[29] W. Baade and F. Zwicky. On super-novae. *Proceedings of the National Academy of Sciences*, 20(5):254–259, may 1934.

[30] W. Baade and F. Zwicky. Remarks on super-novae and cosmic rays. *Physical Review*, 46(1):76–77, jul 1934.

[31] Horace W. Babcock. The rotation of the andromeda nebula. *Lick Observatory Bulletins*, 19:41–51, 1939.

[32] Andreas Bally, Sudip Jana, and Andreas Trautner. Neutrino self-interactions and XENON1T electron recoil excess. *Phys. Rev. Lett.*, 125(16):161802, 2020.

[33] James M. Bardeen, Kip S. Thorne, and David W. Meltzer. A catalogue of methods for studying the normal modes of radial pulsation of general-relativistic stellar models. *The Astrophysical Journal*, 145:505, aug 1966.

[34] John Bardeen, L. N. Cooper, and J. R. Schrieffer. Theory of superconductivity. *Phys. Rev.*, 108:1175–1204, 1957.

[35] Rennan Barkana. Possible interaction between baryons and dark-matter particles revealed by the first stars. *Nature*, 555:71 EP –, 02 2018.

[36] Brian Batell, Tao Han, David McKeen, and Barmak Shams Es Haghi. Thermal Dark Matter Through the Dirac Neutrino Portal. *Phys. Rev. D*, 97(7):075016, 2018.

[37] A. Bauswein and N. Stergioulas. Unified picture of the post-merger dynamics and gravitational wave emission in neutron star mergers. *Physical Review D*, 91(12), jun 2015.

[38] G. Baym, H. Monien, C. J. Pethick, and D. G. Ravenhall. Transverse Interactions and Transport in Relativistic Quark - Gluon and Electromagnetic Plasmas. *Phys. Rev. Lett.*, 64:1867–1870, 1990.

[39] G. Baym, C. Pethick, and P. Sutherland. The Ground State of Matter at High Densities: Equation of State and Stellar Models. *Astrophys. J.*, 170:299, December 1971.

[40] S. R. Beane, Paulo F. Bedaque, L. Childress, A. Kryjevski, J. McGuire, and U. van Kolck. Singular potentials and limit cycles. *Phys. Rev. A*, 64:042103, 2001.

[41] S. R. Beane, Paulo F. Bedaque, M. J. Savage, and U. van Kolck. Towards a perturbative theory of nuclear forces. *Nucl. Phys. A*, 700:377–402, 2002.

[42] Silas R. Beane, David B. Kaplan, and Aleksi Vuorinen. Perturbative nuclear physics. *Phys. Rev. C*, 80:011001, 2009.

[43] Paulo Bedaque and Andrew W. Steiner. Sound velocity bound and neutron stars. *Phys. Rev. Lett.*, 114:031103, January 2015.

[44] Jacob D. Bekenstein. Relativistic gravitation theory for the MOND paradigm. *Phys. Rev. D*, 70:083509, 2004. [Erratum: Phys.Rev.D 71, 069901 (2005)].

[45] J. S. Bell and R. Jackiw. A PCAC puzzle: $\pi^0 \to \gamma\gamma$ in the σ model. *Nuovo Cim. A*, 60:47–61, 1969.

[46] Nicole F. Bell, Andrew Melatos, and Kalliopi Petraki. Realistic neutron star constraints on bosonic asymmetric dark matter. *Phys. Rev.*, D87(12):123507, 2013.

[47] Michel Le Bellac. *Thermal Field Theory*. Cambridge Monographs on Mathematical Physics. Cambridge University Press, 3 2011.

[48] Katherine M. Benson, Jeremy Bernstein, and Scott Dodelson. Phase structure and the effective potential at fixed charge. *Phys. Rev. D*, 44:2480–2497, 1991.

[49] Lasha Berezhiani and Justin Khoury. Theory of dark matter superfluidity. *Phys. Rev. D*, 92:103510, 2015.

[50] Lasha Berezhiani and Justin Khoury. Dark Matter Superfluidity and Galactic Dynamics. *Phys. Lett. B*, 753:639–643, 2016.

[51] Zurab Berezhiani and Luis Bento. Neutron - mirror neutron oscillations: How fast might they be? *Phys. Rev. Lett.*, 96:081801, 2006.

[52] Asher Berlin and Nikita Blinov. Thermal neutrino portal to sub-MeV dark matter. *Phys. Rev. D*, 99(9):095030, 2019.

[53] Jose Luis Bernal, Licia Verde, and Adam G. Riess. The trouble with H_0. *JCAP*, 10:019, 2016.

[54] V. BERNARD, N. KAISER, and ULF-G. MEIßNER. CHIRAL DYNAMICS IN NUCLEONS AND NUCLEI. *International Journal of Modern Physics E*, 04(02):193–344, jun 1995.

[55] Véronique Bernard, Norbert Kaiser, Joachim Kambor, and Ulf-G. Meißner. Chiral structure of the nucleon. *Nuclear Physics B*, 388(2):315–345, 1992.

[56] Sebastiano Bernuzzi. Quasiuniversal properties of neutron star mergers. *Physical Review Letters*, 112(20), 2014.

[57] Sebastiano Bernuzzi. Modeling the complete gravitational wave spectrum of neutron star mergers. *Physical Review Letters*, 115(9), 2015.

[58] Jeffrey M. Berryman, André De Gouvêa, Kevin J. Kelly, and Yue Zhang. Lepton-Number-Charged Scalars and Neutrino Beamstrahlung. *Phys. Rev. D*, 97(7):075030, 2018.

[59] Bridget Bertoni, Seyda Ipek, David McKeen, and Ann E. Nelson. Constraints and consequences of reducing small scale structure via large dark matter-neutrino interactions. *JHEP*, 04:170, 2015.

[60] Bridget Bertoni, Ann E. Nelson, and Sanjay Reddy. Dark Matter Thermalization in Neutron Stars. *Phys. Rev. D*, 88:123505, 2013.

[61] H. A. Bethe and J. R. Wilson. Revival of a stalled supernova shock by neutrino heating. *The Astrophysical Journal*, 295:14, aug 1985.

[62] Lars Bildsten and Curt Cutler. Tidal interactions of inspiraling compact binaries. *The Astrophysical Journal*, 400:175, nov 1992.

[63] R. M. Bionta et al. Observation of a Neutrino Burst in Coincidence with Supernova SN 1987a in the Large Magellanic Cloud. *Phys. Rev. Lett.*, 58:1494, 1987.

[64] Michael C. Birse. Power counting with one-pion exchange. *Phys. Rev. C*, 74:014003, 2006.

[65] Nikita Blinov, Kevin James Kelly, Gordan Z Krnjaic, and Samuel D McDermott. Constraining the Self-Interacting Neutrino Interpretation of the Hubble Tension. *Phys. Rev. Lett.*, 123(19):191102, 2019.

[66] Sukanta Bose, Kabir Chakravarti, Luciano Rezzolla, B. S. Sathyaprakash, and Kentaro Takami. Neutron-star Radius from a Population of Binary Neutron Star Mergers. *Phys. Rev. Lett.*, 120(3):031102, 2018.

[67] S. M. Boucenna and S. Morisi. Theories relating baryon asymmetry and dark matter: A mini review. *Front.in Phys.*, 1:33, 2014.

[68] Judd D. Bowman, Alan E. E. Rogers, Raul A. Monsalve, Thomas J. Mozdzen, and Nivedita Mahesh. An absorption profile centred at 78 megahertz in the sky-averaged spectrum. *Nature*, 555:67 EP –, 02 2018.

[69] Edward F. Brown, Andrew Cumming, Farrukh J. Fattoyev, C. J. Horowitz, Dany Page, and Sanjay Reddy. Rapid neutrino cooling in the neutron star MXB 1659-29. *Phys. Rev. Lett.*, 120(18):182701, 2018.

[70] Tim Brune and Heinrich Päs. Massive Majorons and constraints on the Majoron-neutrino coupling. *Phys. Rev. D*, 99(9):096005, 2019.

[71] Matthew R. Buckley, Jesús Zavala, Francis-Yan Cyr-Racine, Kris Sigurdson, and Mark Vogelsberger. Scattering, Damping, and Acoustic Oscillations: Simulating the Structure of Dark Matter Halos with Relativistic Force Carriers. *Phys. Rev.*, D90(4):043524, 2014.

[72] Aurel Bulgac, Michael Mcneil Forbes, Shi Jin, Rodrigo Navarro Perez, and Nicolas Schunck. Minimal nuclear energy density functional. *Phys. Rev. C*, 97(4):044313, 2018.

[73] Alessandra Buonanno, Bala Iyer, Evan Ochsner, Yi Pan, and B. S. Sathyaprakash. Comparison of post-Newtonian templates for compact binary inspiral signals in gravitational-wave detectors. *Phys. Rev.*, D80:084043, 2009.

[74] C. P. Burgess and J. M. Cline. New class of majoron-emitting double-βdecays. *Physical Review D*, 49(11):5925–5944, jun 1994.

[75] A. Burrows and J. M. Lattimer. The effect of trapped lepton number and entropy on the outcome of stellar collapse. *The Astrophysical Journal*, 270:735, jul 1983.

[76] A. Burrows and J. M. Lattimer. The birth of neutron stars. *The Astrophysical Journal*, 307:178, aug 1986.

[77] A. Burrows, E. Livne, L. Dessart, C. D. Ott, and J. Murphy. A new mechanism for core-collapse supernova explosions. *The Astrophysical Journal*, 640(2):878–890, apr 2006.

[78] Adam Burrows. Convection and the mechanism of type II supernovae. *The Astrophysical Journal*, 318:L57, jul 1987.

[79] Adam Burrows. Pulsar recoil and gravitational radiation due to asymmetrical stellar collapse and explosion. *Physical Review Letters*, 76(3):352–355, 1996.

[80] Adam Burrows. Colloquium: Perspectives on core-collapse supernova theory. *Rev. Mod. Phys.*, 85:245, 2013.

[81] Adam Burrows and James M. Lattimer. Neutrinos from sn 1987a. *The Astrophysical Journal*, 318:L63, Jul 1987.

[82] J. Byrne and P. G. Dawber. J. Byrne and P. G. Dawber and C. G. Habeck and S. J. Smidt and J. A. Spain and A. P. Williams. *Europhys. Lett.*, 33:187, 1996.

[83] J. Byrne et al. Measurement of the neutron lifetime by counting trapped protons. *Phys. Rev. Lett.*, 65:289–292, 1990.

[84] Curtis G. Callan, Jr., Sidney R. Coleman, J. Wess, and Bruno Zumino. Structure of phenomenological Lagrangians. 2. *Phys. Rev.*, 177:2247–2250, 1969.

[85] Curtis G. Callan, Jr., Roger F. Dashen, and David J. Gross. A Theory of Hadronic Structure. *Phys. Rev. D*, 19:1826, 1979.

[86] Christian Y. Cardall, Madappa Prakash, and James M. Lattimer. Effects of strong magnetic fields on neutron star structure. *Astrophys. J.*, 554:322–339, 2001.

[87] A. Catuneanu, C. O. Heinke, G. R. Sivakoff, W. C. G. Ho, and M. Servillat. MASS/RADIUS CONSTRAINTS ON THE QUIESCENT NEUTRON STAR IN m13 USING HYDROGEN AND HELIUM ATMOSPHERES. *The Astrophysical Journal*, 764(2):145, feb 2013.

[88] M. Cermeño, M. Ángeles Pérez-García, and Joseph Silk. Fermionic Light Dark Matter Particles and the New Physics of Neutron Stars. *Publ. Astron. Soc. Austral.*, 34:e043, 2017.

[89] N. Chamel, S. Naimi, E. Khan, and J. Margueron. Validity of the wigner-seitz approximation in neutron star crust. *Phys. Rev. C*, 75:055806, May 2007.

[90] Nicolas Chamel and Paweł Haensel. Physics of neutron star crusts. *Living Rev. Relativity*, 11(10), 2008.

[91] Jae Hyeok Chang, Rouven Essig, and Samuel D. McDermott. Revisiting Supernova 1987A Constraints on Dark Photons. *JHEP*, 01:107, 2017.

[92] Jae Hyeok Chang, Rouven Essig, and Samuel D. McDermott. Supernova 1987A Constraints on Sub-GeV Dark Sectors, Millicharged Particles, the QCD Axion, and an Axion-like Particle. 2018.

[93] Hsin-Yu Chen, Maya Fishbach, and Daniel E. Holz. A two per cent Hubble constant measurement from standard sirens within five years. *Nature*, 562(7728):545–547, 2018.

[94] Aleksey Cherman, Srimoyee Sen, and Laurence G. Yaffe. Anyonic particle-vortex statistics and the nature of dense quark matter. *Phys. Rev. D*, 100(3):034015, 2019.

[95] Paul M. Chesler and Laurence G. Yaffe. Holography and colliding gravitational shock waves in asymptotically AdS_5 spacetime. *Phys. Rev. Lett.*, 106:021601, 2011.

[96] Y. Chikashige, Rabindra N. Mohapatra, and R. D. Peccei. Are There Real Goldstone Bosons Associated with Broken Lepton Number? *Phys. Lett. B*, 98:265–268, 1981.

[97] Krzysztof Cichy, Elena Garcia-Ramos, and Karl Jansen. Chiral condensate from the twisted mass Dirac operator spectrum. *JHEP*, 10:175, 2013.

[98] Douglas Clowe, Maruša Bradač, Anthony H. Gonzalez, Maxim Markevitch, Scott W. Randall, Christine Jones, and Dennis Zaritsky. A direct empirical proof of the existence of dark matter. *The Astrophysical Journal*, 648(2):L109–L113, Aug 2006.

[99] Douglas Clowe, Anthony Gonzalez, and Maxim Markevitch. Weak lensing mass reconstruction of the interacting cluster 1E0657-558: Direct evidence for the existence of dark matter. *Astrophys. J.*, 604:596–603, 2004.

[100] Sidney R. Coleman, J. Wess, and Bruno Zumino. Structure of phenomenological Lagrangians. 1. *Phys. Rev.*, 177:2239–2247, 1969.

[101] Gregory B. Cook, Stuart L. Shapiro, and Saul A. Teukolsky. Rapidly rotating neutron stars in general relativity: Realistic equations of state. *The Astrophysical Journal*, 424:823, apr 1994.

[102] Leon N. Cooper. Bound electron pairs in a degenerate Fermi gas. *Phys. Rev.*, 104:1189–1190, 1956.

[103] Peter Creasey, Omid Sameie, Laura V. Sales, Hai-Bo Yu, Mark Vogelsberger, and Jesús Zavala. Spreading out and staying sharp – creating diverse rotation curves via baryonic and self-interaction effects. *Mon. Not. Roy. Astron. Soc.*, 468(2):2283–2295, 2017.

[104] H. T. Cromartie et al. Relativistic Shapiro delay measurements of an extremely massive millisecond pulsar. *Nature Astron.*, 4(1):72–76, 2019.

[105] Richard H. Cyburt, Brian D. Fields, Keith A. Olive, and Tsung-Han Yeh. Big Bang Nucleosynthesis: 2015. *Rev. Mod. Phys.*, 88:015004, 2016.

[106] Andrzej Czarnecki, William J. Marciano, and Alberto Sirlin. The Neutron Lifetime and Axial Coupling Connection. 2018.

[107] Thibault Damour, Alessandro Nagar, and Loic Villain. Measurability of the tidal polarizability of neutron stars in late-inspiral gravitational-wave signals. *Phys. Rev.*, D85:123007, 2012.

[108] Arthur Davidsen, Stuart Bowyer, and William Welch. Observational evidence that the coma cluster is not bound by ionized intracluster gas. *The Astrophysical Journal*, 186:L119, dec 1973.

[109] Hooman Davoudiasl. Nucleon Decay into a Dark Sector. *Phys. Rev. Lett.*, 114(5):051802, 2015.

[110] Hooman Davoudiasl and Rabindra N. Mohapatra. On Relating the Genesis of Cosmic Baryons and Dark Matter. *New J. Phys.*, 14:095011, 2012.

[111] Hooman Davoudiasl, David E. Morrissey, Kris Sigurdson, and Sean Tulin. Hylogenesis: A Unified Origin for Baryonic Visible Matter and Antibaryonic Dark Matter. *Phys. Rev. Lett.*, 105:211304, 2010.

[112] Hooman Davoudiasl, David E. Morrissey, Kris Sigurdson, and Sean Tulin. Baryon Destruction by Asymmetric Dark Matter. *Phys. Rev.*, D84:096008, 2011.

[113] Soumi De, Daniel Finstad, James M. Lattimer, Duncan A. Brown, Edo Berger, and Christopher M. Biwer. Constraining the nuclear equation of state with GW170817. *Phys. Rev. Lett.*, 121(9):091102, 2018.

[114] Soumi De, Daniel Finstad, James M. Lattimer, Duncan A. Brown, Edo Berger, and Christopher M. Biwer. Tidal deformabilities and radii of neutron stars from the observation of gw170817. *Phys. Rev. Lett.*, 121:091102, Aug 2018.

[115] André de Gouvêa, P. S. Bhupal Dev, Bhaskar Dutta, Tathagata Ghosh, Tao Han, and Yongchao Zhang. Leptonic Scalars at the LHC. *JHEP*, 07:142, 2020.

[116] W. Del Pozzo, T. G. F. Li, M. Agathos, C. Van Den Broeck, and S. Vitale. Demonstrating the Feasibility of Probing the Neutron-Star Equation of State with Second-Generation Gravitational-Wave Detectors. *Physical Review Letters*, 111(7):071101, August 2013.

[117] P. B. Demorest, T. Pennucci, S. M. Ransom, M. S. E. Roberts, and J. W. T. Hessels. A two-solar-mass neutron star measured using shapiro delay. *Nature*, 467(7319):1081–1083, Oct 2010.

[118] Paul Demorest, Tim Pennucci, Scott Ransom, Mallory Roberts, and Jason Hessels. Shapiro Delay Measurement of A Two Solar Mass Neutron Star. *Nature*, 467:1081–1083, 2010.

[119] Arianna Di Cintio, Michael Tremmel, Fabio Governato, Andrew Pontzen, Jesús Zavala, Alexander Bastidas Fry, Alyson Brooks, and Mark Vogelsberger. A rumble in the dark: signatures of self-interacting dark matter in supermassive black hole dynamics and galaxy density profiles. *Mon. Not. Roy. Astron. Soc.*, 469(3):2845–2854, 2017.

[120] Tim Dietrich, Sebastiano Bernuzzi, and Wolfgang Tichy. Closed-form tidal approximants for binary neutron star gravitational waveforms constructed from high-resolution numerical relativity simulations. *Phys. Rev.*, D96(12):121501(R), 2017.

[121] Scott Dodelson and Lawrence M. Widrow. Sterile-neutrinos as dark matter. *Phys. Rev. Lett.*, 72:17–20, 1994.

[122] Michal Dominik, Krzysztof Belczynski, Christopher Fryer, Daniel Holz, Emanuele Berti, Tomasz Bulik, Ilya Mandel, and Richard O'Shaughnessy. Double Compact Objects I: The Significance of the Common Envelope on Merger Rates. *Astrophys. J.*, 759:52, 2012.

[123] Jeff A. Dror, Robert Lasenby, and Maxim Pospelov. New constraints on light vectors coupled to anomalous currents. *Phys. Rev. Lett.*, 119(14):141803, 2017.

[124] Jeff A. Dror, Robert Lasenby, and Maxim Pospelov. Light vectors coupled to bosonic currents. *Phys. Rev.*, D99(5):055016, 2019.

[125] Michael Duerr, Kai Schmidt-Hoberg, and Sebastian Wild. Self-interacting dark matter with a stable vector mediator. unpublished, 2018.

[126] M. Dutra, O. Lourenco, J. S. Sa Martins, A. Delfino, J. R. Stone, and P. D. Stevenson. Skyrme Interaction and Nuclear Matter Constraints. *Phys. Rev. C*, 85:035201, 2012.

[127] Albert Einstein. Über Gravitationswellen. *Sitzungsber. Preuss. Akad. Wiss. Berlin (Math. Phys.)*, 1918:154–167, 1918.

[128] John Ellis, Andi Hektor, Gert Hütsi, Kristjan Kannike, Luca Marzola, Martti Raidal, and Ville Vaskonen. Search for Dark Matter Effects on Gravitational Signals from Neutron Star Mergers. *Phys. Lett.*, B781:607–610, 2018.

[129] John R. Ellis, J. S. Hagelin, Dimitri V. Nanopoulos, Keith A. Olive, and M. Srednicki. Supersymmetric Relics from the Big Bang. *Nucl. Phys. B*, 238:453–476, 1984.

[130] John R. Ellis and Keith A. Olive. Constraints on Light Particles From Supernova SN 1987a. *Phys. Lett.*, B193:525, 1987.

[131] Georg P. Engel, Leonardo Giusti, Stefano Lottini, and Rainer Sommer. Chiral Symmetry Breaking in QCD with Two Light Flavors. *Phys. Rev. Lett.*, 114(11):112001, 2015.

[132] Georg P. Engel, Leonardo Giusti, Stefano Lottini, and Rainer Sommer. Spectral density of the Dirac operator in two-flavor QCD. *Phys. Rev. D*, 91(5):054505, 2015.

[133] R. Epstein. The generation of gravitational radiation by escaping supernova neutrinos. *The Astrophysical Journal*, 223:1037, aug 1978.

[134] B. P. Abbott et al. LIGO Scientific Collaboration and Virgo Collaboration. Search for post-merger gravitational waves from the remnant of the binary neutron star merger GW170817. *The Astrophysical Journal*, 851(1):L16, dec 2017.

[135] Pavel Fileviez Pérez, Elliot Golias, Rui-Hao Li, and Clara Murgui. Leptophobic Dark Matter and the Baryon Number Violation Scale. *Phys. Rev.*, D99(3):035009, 2019.

[136] Eanna E. Flanagan and Tanja Hinderer. Constraining neutron star tidal Love numbers with gravitational wave detectors. *Phys. Rev.*, D77:021502, 2008.

[137] Sean Fleming, Thomas Mehen, and Iain W. Stewart. NNLO corrections to nucleon-nucleon scattering and perturbative pions. *Nucl. Phys. A*, 677:313–366, 2000.

[138] Michael McNeil Forbes, Sukanta Bose, Sanjay Reddy, Dake Zhou, Arunava Mukherjee, and Soumi De. Constraining the neutron-matter equation of state with gravitational waves. *Phys. Rev. D*, 100(8):083010, 2019.

[139] Bartosz Fornal and Benjamin Grinstein. Dark Matter Interpretation of the Neutron Decay Anomaly. *Phys. Rev. Lett.*, 120(19):191801, 2018.

[140] M. Fortin, C. Providência, A. R. Raduta, F. Gulminelli, J. L Zdunik, P. Haensel, and M. Bejger. Neutron star radii and crusts: uncertainties and unified equations of state. *Phys. Rev. C*, 94:035804, 2016.

[141] Patrick J. Fox, Jia Liu, David Tucker-Smith, and Neal Weiner. An Effective Z'. *Phys. Rev.*, D84:115006, 2011.

[142] J. L. Friedman, L. Parker, and J. R. Ipser. Rapidly rotating neutron star models. *The Astrophysical Journal*, 304:115, may 1986.

[143] H. Fukaya, S. Aoki, T. W. Chiu, S. Hashimoto, T. Kaneko, J. Noaki, T. Onogi, and N. Yamada. Determination of the chiral condensate from QCD Dirac spectrum on the lattice. *Phys. Rev. D*, 83:074501, 2011.

[144] H. Fukaya, S. Aoki, S. Hashimoto, T. Kaneko, J. Noaki, T. Onogi, and N. Yamada. Determination of the chiral condensate from 2+1-flavor lattice QCD. *Phys. Rev. Lett.*, 104:122002, 2010. [Erratum: Phys.Rev.Lett. 105, 159901 (2010)].

[145] G. M. Fuller, R. Mayle, and J. R. Wilson. The Majoron model and stellar collapse. *Astrophys. J.*, 332:826, 1988.

[146] S. Gandolfi, J. Carlson, S. Reddy, A. W. Steiner, and R. B. Wiringa. The equation of state of neutron matter, symmetry energy, and neutron star structure. *Eur. Phys. J.*, A50:10, 2014.

[147] S. Gandolfi, J. Carlson, S. Reddy, A.W. Steiner, and R.B. Wiringa. The equation of state of neutron matter, symmetry energy and neutron star structure. *The European Physical Journal A*, 50(2):10, 2014.

[148] S. Gandolfi, J. Carlson, and Sanjay Reddy. Maximum mass and radius of neutron stars, and the nuclear symmetry energy. *Phys. Rev. C*, 85:032801, March 2012.

[149] S. Gandolfi, J. Carlson, and Sanjay Reddy. Maximum mass and radius of neutron stars, and the nuclear symmetry energy. *Physical Review C*, 85(3), Mar 2012.

[150] S. Gandolfi, J. Carlson, and Sanjay Reddy. The maximum mass and radius of neutron stars and the nuclear symmetry energy. *Phys. Rev.*, C85:032801, 2012.

[151] S. Gandolfi, A. Yu. Illarionov, S. Fantoni, J. C. Miller, F. Pederiva, and K. E. Schmidt. Microscopic calculation of the equation of state of nuclear matter and neutron star structure. *MNRAS*, 404(1):L35–L39, 2010.

[152] S. Gandolfi, A. Yu. Illarionov, K. E. Schmidt, F. Pederiva, and S. Fantoni. Quantum Monte Carlo calculation of the equation of state of neutron matter. *Phys. Rev. C*, 79:054005, May 2009.

[153] S. Gandolfi, A. Lovato, J. Carlson, and Kevin E. Schmidt. From the lightest nuclei to the equation of state of asymmetric nuclear matter with realistic nuclear interactions. *Phys. Rev. C*, 90:061306, 2014.

[154] Stefano Gandolfi, Alexandros Gezerlis, and Joe Carlson. Neutron matter from low to high density. *Annual Review of Nuclear and Particle Science*, 65(1):303–328, 2015.

[155] J. Gasser, M.E. Sainio, and A. Švarc. Nucleons with chiral loops. *Nuclear Physics B*, 307(4):779–853, 1988.

[156] Murray Gell-Mann and M Levy. The axial vector current in beta decay. *Nuovo Cim.*, 16:705, 1960.

[157] G. B. Gelmini and M. Roncadelli. Left-Handed Neutrino Mass Scale and Spontaneously Broken Lepton Number. *Phys. Lett. B*, 99:411–415, 1981.

[158] Howard Georgi. An Effective Field Theory for Heavy Quarks at Low-energies. *Phys. Lett. B*, 240:447–450, 1990.

[159] Leonardo Giusti and Martin Luscher. Chiral symmetry breaking and the Banks-Casher relation in lattice QCD with Wilson quarks. *JHEP*, 03:013, 2009.

[160] Kostas Glampedakis and Leonardo Gualtieri. Gravitational waves from single neutron stars: an advanced detector era survey. *Astrophys. Space Sci. Libr.*, 457:673–736, 2018.

[161] N.K. Glendenning. *Compact Stars: Nuclear Physics, Particle Physics, and General Relativity*. Astronomy and Astrophysics Library. Springer New York, 2000.

[162] H. Goldberg. Constraint on the Photino Mass from Cosmology. *Phys. Rev. Lett.*, 50:1419, 1983. [Erratum: Phys.Rev.Lett. 103, 099905 (2009)].

[163] I. Goldman and S. Nussinov. Weakly Interacting Massive Particles and Neutron Stars. *Phys. Rev.*, D40:3221–3230, 1989.

[164] J. Goldstone. Field Theories with Superconductor Solutions. *Nuovo Cim.*, 19:154–164, 1961.

[165] Jeffrey Goldstone, Abdus Salam, and Steven Weinberg. Broken Symmetries. *Phys. Rev.*, 127:965–970, 1962.

[166] C. Gonzalez-Boquera, M. Centelles, X. Viñas, and A. Rios. Higher-order symmetry energy and neutron star core-crust transition with gogny forces. *Phys. Rev. C*, 96:065806, Dec 2017.

[167] Andrew Gould, Bruce T. Draine, Roger W. Romani, and Shmuel Nussinov. Neutron Stars: Graveyard of Charged Dark Matter. *Phys. Lett.*, B238:337–343, 1990.

[168] F. Governato, A. Zolotov, A. Pontzen, C. Christensen, S. H. Oh, A. M. Brooks, T. Quinn, S. Shen, and J. Wadsley. Cuspy no more: how outflows affect the central dark matter and baryon distribution in Λ cold dark matter galaxies. *Monthly Notices of the Royal Astronomical Society*, 422(2):1231–1240, mar 2012.

[169] Benjamín Grinstein, Chris Kouvaris, and Niklas Grønlund Nielsen. Neutron Star Stability in Light of the Neutron Decay Anomaly. 2018.

[170] David J. Gross, Robert D. Pisarski, and Laurence G. Yaffe. QCD and Instantons at Finite Temperature. *Rev. Mod. Phys.*, 53:43, 1981.

[171] David J. Gross and Frank Wilczek. Ultraviolet Behavior of Nonabelian Gauge Theories. *Phys. Rev. Lett.*, 30:1343–1346, 1973.

[172] Sebastien Guillot, Mathieu Servillat, Natalie A. Webb, and Robert E. Rutledge. MEASUREMENT OF THE RADIUS OF NEUTRON STARS WITH HIGH SIGNAL-TO-NOISE QUIESCENT LOW-MASS x-RAY BINARIES IN GLOBULAR CLUSTERS. *The Astrophysical Journal*, 772(1):7, jun 2013.

[173] Howard E. Haber and H. Arthur Weldon. Finite Temperature Symmetry Breaking as Bose-Einstein Condensation. *Phys. Rev. D*, 25:502, 1982.

[174] P. Haensel, A. Y. Potekhin, and D. G. Yakovlev. *Neutron Stars 1*, volume 326 of *Astrophysics and Space Science Library*. Springer-Verlag, New York, 1 edition, 2007.

[175] P. Haensel and J. L. Zdunik. A submillisecond pulsar and the equation of state of dense matter. *Nature*, 340(6235):617–619, aug 1989.

[176] R. Hagedorn. Statistical thermodynamics of strong interactions at high-energies. *Nuovo Cim. Suppl.*, 3:147–186, 1965.

[177] R. Hagedorn and J. Ranft. Statistical thermodynamics of strong interactions at high-energies. 2. Momentum spectra of particles produced in pp-collisions. *Nuovo Cim. Suppl.*, 6:169–354, 1968.

[178] James B. Hartle. Slowly rotating relativistic stars. 1. Equations of structure. *Astrophys. J.*, 150:1005–1029, 1967.

[179] James B. Hartle. Slowly-rotating relativistic stars.iv. rotational energy and moment of inertia for stars in differential rotation. *The Astrophysical Journal*, 161:111, Jul 1970.

[180] James B. Hartle and Kip S. Thorne. Slowly Rotating Relativistic Stars. II. Models for Neutron Stars and Supermassive Stars. *Astrophys. J.*, 153:807, 1968.

[181] Stephen Hawking. Gravitationally collapsed objects of very low mass. *Mon. Not. Roy. Astron. Soc.*, 152:75, 1971.

[182] K. Hebeler, J. D. Holt, J. Menendez, and A. Schwenk. Nuclear forces and their impact on neutron-rich nuclei and neutron-rich matter. *Ann. Rev. Nucl. Part. Sci.*, 65:457–484, 2015.

[183] K. Hebeler, J. M. Lattimer, C. J. Pethick, and A. Schwenk. Constraints on neutron star radii based on chiral effective field theory interactions. *Phys. Rev. Lett.*, 105:161102, 2010.

[184] K. Hebeler, J. M. Lattimer, C. J. Pethick, and A. Schwenk. Equation of State and Neutron Star Properties Constrained by Nuclear Physics and Observation. *Astrophys. J.*, 773(1):11, 2013.

[185] K. Hebeler, J. M. Lattimer, C. J. Pethick, and A. Schwenk. Equation of state and neutron star properties constrained by nuclear physics and observation. *Astrophys. J.*, 773:11, 2013.

[186] K. Hebeler and A. Schwenk. Chiral three-nucleon forces and neutron matter. *Phys. Rev. C*, 82:014314, July 2010.

[187] Dennis J. Hegyi and Keith A. Olive. Can galactic halos be made of baryons? *Physics Letters B*, 126(1-2):28–32, jun 1983.

[188] C. O. Heinke, H. N. Cohn, P. M. Lugger, N. A. Webb, W. C. G. Ho, J. Anderson, S. Campana, S. Bogdanov, D. Haggard, A. M. Cool, and J. E. Grindlay. Improved mass and radius constraints for quiescent neutron stars in ω cen and NGC 6397. *Monthly Notices of the Royal Astronomical Society*, 444(1):443–456, aug 2014.

[189] Carl W. Helstrom. *Elements of signal detection and estimation*. Prentice-Hall, Inc., Upper Saddle River, NJ, USA, 1995.

[190] Lucien Heurtier and Yongchao Zhang. Supernova Constraints on Massive (Pseudo)Scalar Coupling to Neutrinos. *JCAP*, 02:042, 2017.

[191] A. HEWISH, S. J. BELL, J. D. H. PILKINGTON, P. F. SCOTT, and R. A. COLLINS. Observation of a rapidly pulsating radio source. *Nature*, 217(5130):709–713, feb 1968.

[192] Tanja Hinderer. Tidal Love numbers of neutron stars. *Astrophys. J.*, 677:1216–1220, 2008.

[193] K. Hirata et al. Observation of a Neutrino Burst from the Supernova SN 1987a. *Phys. Rev. Lett.*, 58:1490–1493, 1987.

[194] S. Hirose et al. Measurement of the τ lepton polarization and $R(D^*)$ in the decay $\bar{B} \to D^* \tau^- \bar{\nu}_\tau$. *Phys. Rev. Lett.*, 118(21):211801, 2017.

[195] Bob Holdom. Two U(1)'s and Epsilon Charge Shifts. *Phys. Lett. B*, 166:196–198, 1986.

[196] C. J. Horowitz, Z. Ahmed, C.-M. Jen, A. Rakhman, P. A. Souder, M. M. Dalton, N. Liyanage, K. D. Paschke, K. Saenboonruang, R. Silwal, G. B. Franklin, M. Friend, B. Quinn, K. S. Kumar, D. McNulty, L. Mercado, S. Riordan, J. Wexler, R. W. Michaels, and G. M. Urciuoli. Weak charge form factor and radius of ^{208}pb through parity violation in electron scattering. *Phys. Rev. C*, 85(3):032501, March 2012.

[197] C. J. Horowitz, E. F. Brown, Y. Kim, W. G. Lynch, R. Michaels, A. Ono, J. Piekarewicz, M. B. Tsang, and H. H. Wolter. A way forward in the study of the symmetry energy: Experiment, theory, and observation. *Journal of Physics G: Nuclear and Particle Physics*, 41:093001, 2014.

[198] C.J. Horowitz, K.S. Kumar, and R. Michaels. Electroweak measurements of neutron densities in CREX and PREX at JLab, USA. *The European Physical Journal A*, 50(2), 2014.

[199] Kerson Huang and Steven Weinberg. Ultimate temperature and the early universe. *Phys. Rev. Lett.*, 25:895–897, 1970.

[200] R. A. Hulse and J. H. Taylor. Discovery of a pulsar in a binary system. *The Astrophysical Journal*, 195:L51, jan 1975.

[201] Alan O. Jamison. Effects of gravitational confinement on bosonic asymmetric dark matter in stars. *Phys. Rev. D*, 88:035004, 2013.

[202] Elizabeth Ellen Jenkins and Aneesh V. Manohar. Baryon chiral perturbation theory using a heavy fermion Lagrangian. *Phys. Lett. B*, 255:558–562, 1991.

[203] Gerard Jungman, Marc Kamionkowski, and Kim Griest. Supersymmetric dark matter. *Phys. Rept.*, 267:195–373, 1996.

[204] D. B. Kaplan and A. E. Nelson. Strange Goings on in Dense Nucleonic Matter. *Phys. Lett. B*, 175:57–63, 1986.

[205] David B. Kaplan. Chiral Symmetry and Lattice Fermions. In *Les Houches Summer School: Session 93: Modern perspectives in lattice QCD: Quantum field theory and high performance computing*, 12 2009.

[206] David B. Kaplan, Martin J. Savage, and Mark B. Wise. Nucleon - nucleon scattering from effective field theory. *Nucl. Phys. B*, 478:629–659, 1996.

[207] David B. Kaplan, Martin J. Savage, and Mark B. Wise. A New expansion for nucleon-nucleon interactions. *Phys. Lett. B*, 424:390–396, 1998.

[208] David B. Kaplan, Martin J. Savage, and Mark B. Wise. Two nucleon systems from effective field theory. *Nucl. Phys. B*, 534:329–355, 1998.

[209] David E. Kaplan, Gordan Z. Krnjaic, Keith R. Rehermann, and Christopher M. Wells. Atomic Dark Matter. *JCAP*, 1005:021, 2010.

[210] David E. Kaplan, Markus A. Luty, and Kathryn M. Zurek. Asymmetric dark matter. *Physical Review D*, 79(11), Jun 2009.

[211] Manoj Kaplinghat, Sean Tulin, and Hai-Bo Yu. Dark Matter Halos as Particle Colliders: Unified Solution to Small-Scale Structure Puzzles from Dwarfs to Clusters. *Phys. Rev. Lett.*, 116(4):041302, 2016.

[212] J. C. Kapteyn. First attempt at a theory of the arrangement and motion of the sidereal system. *The Astrophysical Journal*, 55:302, may 1922.

[213] J. I. Kapusta and Charles Gale. *Finite-temperature field theory: Principles and applications*. Cambridge Monographs on Mathematical Physics. Cambridge University Press, 2011.

[214] Victoria M. Kaspi and Andrei Beloborodov. Magnetars. *Ann. Rev. Astron. Astrophys.*, 55:261–301, 2017.

[215] Anatoly A. Klypin, Andrey V. Kravtsov, Octavio Valenzuela, and Francisco Prada. Where are the missing Galactic satellites? *Astrophys. J.*, 522:82–92, 1999.

[216] John Kogut. Hamiltonian formulation of wilson's lattice gauge theories. *Physical Review D*, 11(2):395–408, 1975.

[217] Joachim Kopp, Ranjan Laha, Toby Opferkuch, and William Shepherd. CuckooÕs eggs in neutron stars: can LIGO hear chirps from the dark sector? *JHEP*, 11:096, 2018.

[218] Kei Kotake, Naofumi Ohnishi, and Shoichi Yamada. Gravitational Radiation from Standing Accretion Shock Instability in Core-Collapse Supernovae. *Astrophys. J.*, 655:406–415, 2007.

[219] Chris Kouvaris. The Dark Side of Neutron Stars. *Adv. High Energy Phys.*, 2013:856196, 2013.

[220] Chris Kouvaris and Niklas Grønlund Nielsen. Asymmetric dark matter stars. *Physical Review D*, 92(6), Sep 2015.

[221] Chris Kouvaris and Peter Tinyakov. Can neutron stars constrain dark matter? *Phys. Rev. D*, 82:063531, Sep 2010.

[222] Chris Kouvaris and Peter Tinyakov. Can Neutron stars constrain Dark Matter? *Phys. Rev.*, D82:063531, 2010.

[223] Chris Kouvaris and Peter Tinyakov. Constraining Asymmetric Dark Matter through observations of compact stars. *Phys. Rev.*, D83:083512, 2011.

[224] A. J. Krasznahorkay et al. Observation of Anomalous Internal Pair Creation in Be8 : A Possible Indication of a Light, Neutral Boson. *Phys. Rev. Lett.*, 116(4):042501, 2016.

[225] Christina D. Kreisch, Francis-Yan Cyr-Racine, and Olivier Doré. Neutrino puzzle: Anomalies, interactions, and cosmological tensions. *Phys. Rev. D*, 101(12):123505, 2020.

[226] T. Krüger, I. Tews, K. Hebeler, and A. Schwenk. Neutron matter from chiral effective field theory interactions. *Phys. Rev. C*, 88:025802, 2013.

[227] Benjamin D. Lackey, Koutarou Kyutoku, Masaru Shibata, Patrick R. Brady, and John L. Friedman. Extracting equation of state parameters from black hole-neutron star mergers. I. Nonspinning black holes. *Phys. Rev.*, D85:044061, 2012.

[228] Frederick K. Lamb, Stratos Boutloukos, Sandor Van Wassenhove, Robert T. Chamberlain, Ka Ho Lo, Alexander Clare, Wenfei Yu, and M. Coleman Miller. A MODEL FOR THE WAVEFORM BEHAVIOR OF ACCRETING MILLISECOND x-RAY PULSARS: NEARLY ALIGNED MAGNETIC FIELDS AND MOVING EMISSION REGIONS. *The Astrophysical Journal*, 706(1):417–435, oct 2009.

[229] Frederick K. Lamb, Stratos Boutloukos, Sandor Van Wassenhove, Robert T. Chamberlain, Ka Ho Lo, and M. Coleman Miller. ORIGIN OF INTERMITTENT ACCRETION-POWERED x-RAY OSCILLATIONS IN NEUTRON STARS WITH MILLISECOND SPIN PERIODS. *The Astrophysical Journal*, 705(1):L36–L39, oct 2009.

[230] Paul D. Lasky. Gravitational waves from neutron stars: A review. *Publications of the Astronomical Society of Australia*, 32, 2015.

[231] J. M. Lattimer and M. Prakash. The physics of neutron stars. *Science*, 304:536–542, 2004.

[232] J. M. Lattimer and M. Prakash. What a Two Solar Mass Neutron Star Really Means. *ArXiv e-prints*, December 2010.

[233] James M. Lattimer. The nuclear equation of state and neutron star masses. *Annual Review of Nuclear and Particle Science*, 62(1):485–515, Nov 2012.

[234] James M. Lattimer, Madappa Prakash, Dieter Masak, and Amos Yahil. Rapidly rotating pulsars and the equation of state. *The Astrophysical Journal*, 355:241, may 1990.

[235] James M. Lattimer and Andrew W. Steiner. Constraints on the symmetry energy using the mass-radius relation of neutron stars. *The European Physical Journal A*, 50(2):40, 2014.

[236] J.M. Lattimer, C.J. Pethick, D.G. Ravenhall, and D.Q. Lamb. Physical properties of hot, dense matter: The general case. *Nuclear Physics A*, 432(3):646 – 742, 1985.

[237] J. M. Leblanc and J. R. Wilson. A numerical example of the collapse of a rotating magnetized star. *The Astrophysical Journal*, 161:541, aug 1970.

[238] C.-H. Lee, T. T. S. Kuo, G. Q. Li, and G. E. Brown. Nuclear symmetry energy. *Phys. Rev. C*, 57:3488–3491, Jun 1998.

[239] S.-C. Leung, M.-C. Chu, and L.-M. Lin. Dark-matter admixed neutron stars. *Physical Review D*, 84(10), Nov 2011.

[240] Bao-An Li, Lie-Wen Chen, and Che Ming Ko. Recent progress and new challenges in isospin physics with heavy-ion reactions. *Physics Reports*, 464(4):113 – 281, 2008.

[241] Jung-Tsung Li, George M. Fuller, and Chad T. Kishimoto. Neutrino Burst-Generated Gravitational Radiation From Collapsing Supermassive Stars. *Phys. Rev. D*, 98(2):023002, 2018.

[242] Bennett Link. Constraining hadronic superfluidity with neutron star precession. *Phys. Rev. Lett.*, 91:101101, 2003.

[243] Abraham Loeb and Neal Weiner. Cores in dwarf galaxies from dark matter with a yukawa potential. *Phys. Rev. Lett.*, 106:171302, Apr 2011.

[244] Love. The yielding of the earth to disturbing forces. *Proceedings of the Royal Society of London A: Mathematical, Physical and Engineering Sciences*, 82(551):73–88, 1909.

[245] J. E. Lynn, I. Tews, J. Carlson, S. Gandolfi, A. Gezerlis, K. E. Schmidt, and A. Schwenk. Chiral three-nucleon interactions in light nuclei, neutron-α scattering, and neutron matter, 2015.

[246] R. Machleidt and D. R. Entem. Chiral effective field theory and nuclear forces. *Phys. Rept.*, 503:1–75, 2011.

[247] Michele Maggiore et al. Science Case for the Einstein Telescope. *JCAP*, 03:050, 2020.

[248] W. Mampe, L. N. Bondarenko, V. I. Morozov, Yu. N. Panin, and A. I. Fomin. Measuring neutron lifetime by storing ultracold neutrons and detecting inelastically scattered neutrons. *JETP Lett.*, 57:82–87, 1993. [Pisma Zh. Eksp. Teor. Fiz.57,77(1993)].

[249] R. N. Manchester, G. B. Hobbs, A. Teoh, and M. Hobbs. The australia telescope national facility pulsar catalogue. *The Astronomical Journal*, 129(4):1993–2006, apr 2005.

[250] Jérôme Margueron, Rudiney Hoffmann Casali, and Francesca Gulminelli. Equation of state for dense nucleonic matter from metamodeling. I. foundational aspects. *Phys. Rev. C*, 97:025805, Feb 2018.

[251] Maxim Markevitch, A. H. Gonzalez, D. Clowe, A. Vikhlinin, L. David, W. Forman, C. Jones, S. Murray, and W. Tucker. Direct constraints on the dark matter self-interaction cross-section from the merging galaxy cluster 1E0657-56. *Astrophys. J.*, 606:819–824, 2004.

[252] Stephen P. Martin. A Supersymmetry primer. *Adv. Ser. Direct. High Energy Phys.*, 18:1–98, 1998.

[253] Andrea Maselli, Pantelis Pnigouras, Niklas Grønlund Nielsen, Chris Kouvaris, and Kostas D. Kokkotas. Dark stars: Gravitational and electromagnetic observables. *Physical Review D*, 96(2), Jul 2017.

[254] Samuel D. McDermott, Hai-Bo Yu, and Kathryn M. Zurek. Constraints on Scalar Asymmetric Dark Matter from Black Hole Formation in Neutron Stars. *Phys. Rev. D*, 85:023519, 2012.

[255] David McKeen and Ann E. Nelson. CP Violating Baryon Oscillations. *Phys. Rev.*, D94(7):076002, 2016.

[256] David McKeen, Ann E. Nelson, Sanjay Reddy, and Dake Zhou. Neutron stars exclude light dark baryons. *Phys. Rev. Lett.*, 121(6):061802, 2018.

[257] Larry McLerran and Robert D. Pisarski. Phases of cold, dense quarks at large N(c). *Nucl. Phys. A*, 796:83–100, 2007.

[258] Larry McLerran and Sanjay Reddy. Quarkyonic Matter and Neutron Stars. *Phys. Rev. Lett.*, 122(12):122701, 2019.

[259] David Merritt. The distribution of dark matter in the coma cluster. *The Astrophysical Journal*, 313:121, feb 1987.

[260] M. Milgrom. A Modification of the Newtonian dynamics as a possible alternative to the hidden mass hypothesis. *Astrophys. J.*, 270:365–370, 1983.

[261] M. C. Miller. The case for PSR J1614–2230 as a NICER target. *Astrophys. J.*, 822(1):27, 2016.

[262] M. C. Miller et al. PSR J0030+0451 Mass and Radius from $NICER$ Data and Implications for the Properties of Neutron Star Matter. *Astrophys. J. Lett.*, 887(1):L24, 2019.

[263] M. C. Miller et al. The Radius of PSR J0740+6620 from NICER and XMM-Newton Data. 5 2021.

[264] M. C. Miller and Frederick K. Lamb. Observational constraints on neutron star masses and radii. *The European Physical Journal A*, 52(3):63, mar 2016.

[265] M. Coleman Miller and Frederick K. Lamb. Bounds on the compactness of neutron stars from brightness oscillations during x-ray bursts. *The Astrophysical Journal*, 499(1):L37–L40, may 1998.

[266] M. Coleman Miller and Frederick K. Lamb. DETERMINING NEUTRON STAR PROPERTIES BY FITTING OBLATE-STAR WAVEFORM MODELS TO x-RAY BURST OSCILLATIONS. *The Astrophysical Journal*, 808(1):31, jul 2015.

[267] Chiara M. F. Mingarelli, T. Joseph W. Lazio, Alberto Sesana, Jenny E. Greene, Justin A. Ellis, Chung-Pei Ma, Steve Croft, Sarah Burke-Spolaor, and Stephen R. Taylor. The local nanohertz gravitational-wave landscape from supermassive black hole binaries. *Nature Astronomy*, 1(12):886–892, nov 2017.

[268] B. Moore, S. Ghigna, F. Governato, G. Lake, Thomas R. Quinn, J. Stadel, and P. Tozzi. Dark matter substructure within galactic halos. *Astrophys. J. Lett.*, 524:L19–L22, 1999.

[269] Ben Moore. Evidence against dissipation-less dark matter from observations of galaxy haloes. *Nature*, 370(6491):629–631, aug 1994.

[270] E. Mueller and H. T. Janka. Gravitational radiation from convective instabilities in Type II supernova explosions. **??***jnlA&A*, 317:140–163, January 1997.

[271] Remya Nair, Sukanta Bose, and Tarun Deep Saini. Measuring the Hubble constant: Gravitational wave observations meet galaxy clustering. *Phys. Rev.*, D98(2):023502, 2018.

[272] J. Nättilä and P. Pihajoki. Radiation from rapidly rotating oblate neutron stars. *Astronomy & Astrophysics*, 615:A50, jul 2018.

[273] Julio F. Navarro, Carlos S. Frenk, and Simon D. M. White. A universal density profile from hierarchical clustering. *The Astrophysical Journal*, 490(2):493–508, dec 1997.

[274] J. W. Negele and D. Vautherin. Neutron star matter at sub-nuclear densities. *Nuclear Physics A*, 207(2):298–320, January 1973.

[275] G. Nelemans, L. R. Yungelson, and Simon F. Portegies Zwart. The gravitational wave signal from the galactic disk population of binaries containing two compact objects. *Astron. Astrophys.*, 375:890–898, 2001.

[276] Ann Nelson, Sanjay Reddy, and Dake Zhou. Dark halos around neutron stars and gravitational waves. *JCAP*, 1907(07):012, 2019.

[277] A. Nogga, R. G. E. Timmermans, and U. van Kolck. Renormalization of one-pion exchange and power counting. *Phys. Rev. C*, 72:054006, 2005.

[278] Ken'ichi Nomoto and Masa-aki Hashimoto. Presupernova evolution of massive stars. *Physics Reports*, 163(1):13–36, 1988.

[279] S. A. Olausen and V. M. Kaspi. THE McGILL MAGNETAR CATALOG. *The Astrophysical Journal Supplement Series*, 212(1):6, apr 2014.

[280] J. H. Oort. The force exerted by the stellar system in the direction perpendicular to the galactic plane and some related problems. **??***jnlBulletin Astronomical Institute of the Netherlands*, 6:249, August 1932.

[281] J. H. Oort. Some problems concerning the structure and dynamics of the galactic system and the elliptical nebulae NGC 3115 and 4494. *The Astrophysical Journal*, 91:273, apr 1940.

[282] J. R. Oppenheimer and G. M. Volkoff. On Massive neutron cores. *Phys. Rev.*, 55:374–381, 1939.

[283] C. Ordonez and U. van Kolck. Chiral lagrangians and nuclear forces. *Phys. Lett. B*, 291:459–464, 1992.

[284] Feryal Özel and Paulo Freire. Masses, Radii, and the Equation of State of Neutron Stars. *Ann. Rev. Astron. Astrophys.*, 54:401–440, 2016.

[285] F. PACINI. Energy emission from a neutron star. *Nature*, 216(5115):567–568, Nov 1967.

[286] Dany Page and Sanjay Reddy. Dense Matter in Compact Stars: Theoretical Developments and Observational Constraints. *Annual Review of Nuclear and Particle Science*, 56:327–374, 2006.

[287] Carlos Palenzuela, Paolo Pani, Miguel Bezares, Vitor Cardoso, Luis Lehner, and Steven Liebling. Gravitational wave signatures of highly compact boson star binaries. *Physical Review D*, 96(10), Nov 2017.

[288] Vasileios Paschalidis and Nikolaos Stergioulas. Rotating Stars in Relativity. *Living Rev. Rel.*, 20(1):7, 2017.

[289] P. S. Pasquini and O. L. G. Peres. Bounds on Neutrino-Scalar Yukawa Coupling. *Phys. Rev. D*, 93(5):053007, 2016. [Erratum: Phys.Rev.D 93, 079902 (2016)].

[290] M. Pavon Valderrama and E. Ruiz Arriola. Renormalization of NN interaction with chiral two pion exchange potential: Non-central phases. *Phys. Rev. C*, 74:064004, 2006. [Erratum: Phys.Rev.C 75, 059905 (2007)].

[291] K. R. Pechenick, C. Ftaclas, and J. M. Cohen. Hot spots on neutron stars - the near-field gravitational lens. *The Astrophysical Journal*, 274:846, nov 1983.

[292] Kalliopi Petraki, Lauren Pearce, and Alexander Kusenko. Self-interacting asymmetric dark matter coupled to a light massive dark photon. *JCAP*, 1407:039, 2014.

[293] Daniel R. Phillips, Daris Samart, and Carlos Schat. Parity-Violating Nucleon-Nucleon Force in the $1/N_c$ Expansion. *Phys. Rev. Lett.*, 114(6):062301, 2015.

[294] A. Pichlmaier, V. Varlamov, K. Schreckenbach, and P. Geltenbort. Neutron lifetime measurement with the UCN trap-in-trap MAMBO II. *Phys. Lett.*, B693:221–226, 2010.

[295] H. David Politzer. Reliable Perturbative Results for Strong Interactions? *Phys. Rev. Lett.*, 30:1346–1349, 1973.

[296] J. A. Pons, S. Reddy, M. Prakash, J. M. Lattimer, and J. A. Miralles. Evolution of protoneutron stars. *Astrophys. J.*, 513:780, 1999.

[297] Sergey Postnikov, Madappa Prakash, and James M. Lattimer. Tidal Love Numbers of Neutron and Self-Bound Quark Stars. *Phys. Rev.*, D82:024016, 2010.

[298] M Punturo et al. The einstein telescope: a third-generation gravitational wave observatory. *Classical and Quantum Gravity*, 27(19):194002, 2010.

[299] M. Punturo et al. The Einstein Telescope: A third-generation gravitational wave observatory. *Class. Quant. Grav.*, 27:194002, 2010.

[300] G. G. Raffelt. *Stars as laboratories for fundamental physics: The astrophysics of neutrinos, axions, and other weakly interacting particles*. 5 1996.

[301] Georg Raffelt and David Seckel. Bounds on Exotic Particle Interactions from SN 1987a. *Phys. Rev. Lett.*, 60:1793, 1988.

[302] Scott W. Randall, Maxim Markevitch, Douglas Clowe, Anthony H. Gonzalez, and Marusa Bradac. Constraints on the Self-Interaction Cross-Section of Dark Matter from Numerical Simulations of the Merging Galaxy Cluster 1E 0657-56. *Astrophys. J.*, 679:1173–1180, 2008.

[303] D. G. Ravenhall, C. J. Pethick, and J. R. Wilson. Structure of Matter Below Nuclear Saturation Density. *Phys. Rev. Lett.*, 50(26):2066–2069, 1983.

[304] J. I. Read and G. Gilmore. Mass loss from dwarf spheroidal galaxies: the origins of shallow dark matter cores and exponential surface brightness profiles. *Monthly Notices of the Royal Astronomical Society*, 356(1):107–124, jan 2005.

[305] Jocelyn S. Read, Luca Baiotti, Jolien D. E. Creighton, John L. Friedman, Bruno Giacomazzo, Koutarou Kyutoku, Charalampos Markakis, Luciano Rezzolla, Masaru Shibata, and Keisuke Taniguchi. Matter effects on binary neutron star waveforms. *Phys. Rev. D*, 88:044042, 2013.

[306] Jocelyn S. Read, Benjamin D. Lackey, Benjamin J. Owen, and John L. Friedman. Constraints on a phenomenologically parametrized neutron-star equation of state. *Phys. Rev. D*, 79:124032, June 2009.

[307] Sanjay Reddy, Madappa Prakash, and James M Lattimer. Neutrino interactions in hot and dense matter. *Phys. Rev. D*, 58:013009, 1998.

[308] Sanjay Reddy and Dake Zhou. Dark Lepton Superfluid in Proto-Neutron Stars. 7 2021.

[309] Adam G. Riess, Stefano Casertano, D'Arcy Kenworthy, Dan Scolnic, and Lucas Macri. Seven Problems with the Claims Related to the Hubble Tension in arXiv:1810.02595. 10 2018.

[310] Adam G. Riess, Stefano Casertano, Wenlong Yuan, Lucas M. Macri, and Dan Scolnic. Large Magellanic Cloud Cepheid Standards Provide a 1% Foundation for the Determination of the Hubble Constant and Stronger Evidence for Physics beyond ΛCDM. *Astrophys. J.*, 876(1):85, 2019.

[311] Luke F. Roberts and Sanjay Reddy. Neutrino Signatures From Young Neutron Stars. 12 2016.

[312] Luke F. Roberts and Sanjay Reddy. Charged current neutrino interactions in hot and dense matter. *Phys. Rev. C*, 95(4):045807, 2017.

[313] M. S. Roberts and A. H. Rots. Comparison of Rotation Curves of Different Galaxy Types. **??***jnlA&A*, 26:483–485, August 1973.

[314] M. S. Roberts and R. N. Whitehurst. The rotation curve and geometry of m 31 at large galactocentric distances. *The Astrophysical Journal*, 201:327, oct 1975.

[315] Carl L. Rodriguez, Benjamin Farr, Will M. Farr, and Ilya Mandel. Inadequacies of the Fisher Information Matrix in gravitational-wave parameter estimation. *Phys. Rev.*, D88(8):084013, 2013.

[316] Carl L. Rodriguez, Benjamin Farr, Vivien Raymond, Will M. Farr, Tyson B. Littenberg, Diego Fazi, and Vicky Kalogera. Basic Parameter Estimation of Binary Neutron Star Systems by the Advanced LIGO/Virgo Network. *Astrophys. J.*, 784:119, 2014.

[317] Alessandro Roggero, Abhishek Mukherjee, and Francesco Pederiva. Quantum Monte Carlo calculations of neutron matter with non-local chiral interactions. *Phys. Rev. Lett.*, 112:221103, 2014.

[318] Roger W. Romani, Alexei V. Filippenko, and S. Bradley Cenko. A SPECTROSCOPIC STUDY OF THE EXTREME BLACK WIDOW PSR j1311-3430. *The Astrophysical Journal*, 804(2):115, may 2015.

[319] Roger W. Romani, Alexei V. Filippenko, Jeffrey M. Silverman, S. Bradley Cenko, Jochen Greiner, Arne Rau, Jonathan Elliott, and Holger J. Pletsch. PSR j1311-3430: A HEAVYWEIGHT NEUTRON STAR WITH a FLYWEIGHT HELIUM COMPANION. *The Astrophysical Journal*, 760(2):L36, nov 2012.

[320] Roger W. Romani, D. Kandel, Alexei V. Filippenko, Thomas G. Brink, and WeiKang Zheng. PSR J1810+1744: Companion Darkening and a Precise High Neutron Star Mass. *Astrophys. J. Lett.*, 908(2):L46, 2021.

[321] Ermal Rrapaj and Sanjay Reddy. Nucleon-nucleon bremsstrahlung of dark gauge bosons and revised supernova constraints. *Phys. Rev.*, C94(4):045805, 2016.

[322] Ermal Rrapaj, Alessandro Roggero, and Jeremy W. Holt. Microscopically constrained mean-field models from chiral nuclear thermodynamics. *prc*, 93:065801, Jun 2016.

[323] Ermal Rrapaj, Alessandro Roggero, and Jeremy W. Holt. Microscopically constrained mean field models from chiral nuclear thermodynamics. *Phys. Rev. C*, 93(6):065801, 2016.

[324] V. C. Rubin, N. Thonnard, and Jr. Ford W. K. Extended rotation curves of high-luminosity spiral galaxies. IV - systematic dynamical properties, SA through SC. *The Astrophysical Journal*, 225:L107, nov 1978.

[325] Vera C. Rubin and Jr. Ford W. Kent. Rotation of the andromeda nebula from a spectroscopic survey of emission regions. *The Astrophysical Journal*, 159:379, feb 1970.

[326] R. F. Sawyer. Condensed pi- phase in neutron star matter. *Phys. Rev. Lett.*, 29:382–385, 1972.

[327] D. J. Scalapino. Pi- condensate in dense nuclear matter. *Phys. Rev. Lett.*, 29:386–388, 1972.

[328] Thomas Schäfer and Frank Wilczek. Continuity of quark and hadron matter. *Phys. Rev. Lett.*, 82:3956–3959, 1999.

[329] A. Serebrov et al. Measurement of the neutron lifetime using a gravitational trap and a low-temperature Fomblin coating. *Phys. Lett.*, B605:72–78, 2005.

[330] A. P. Serebrov et al. Experimental search for neutron: Mirror neutron oscillations using storage of ultracold neutrons. *Phys. Lett.*, B663:181–185, 2008.

[331] Brian D. Serot and John Dirk Walecka. The Relativistic Nuclear Many Body Problem. *Adv. Nucl. Phys.*, 16:1–327, 1986.

[332] Brian D. Serot and John Dirk Walecka. Recent progress in quantum hadrodynamics. *Int. J. Mod. Phys. E*, 6:515–631, 1997.

[333] M. Servillat, C. O. Heinke, W. C. G. Ho, J. E. Grindlay, J. Hong, M. van den Berg, and S. Bogdanov. Neutron star atmosphere composition: the quiescent, low-mass x-ray binary in the globular cluster m28. *Monthly Notices of the Royal Astronomical Society*, 423(2):1556–1561, may 2012.

[334] Alberto Sesana, Francesco Haardt, Piero Madau, and Marta Volonteri. Low-frequency gravitational radiation from coalescing massive black hole binaries in hierarchical cosmologies. *The Astrophysical Journal*, 611(2):623–632, aug 2004.

[335] Irwin I. Shapiro. Fourth Test of General Relativity. *Phys. Rev. Lett.*, 13:789–791, 1964.

[336] B. K. Sharma, M. Centelles, X. Vinas, M. Baldo, and G. F. Burgio. Unified equation of state for neutron stars on a microscopic basis. *A&A*, 584:A103, 2015.

[337] Jessie Shelton and Kathryn M. Zurek. Darkogenesis: A baryon asymmetry from the dark matter sector. *Phys. Rev.*, D82:123512, 2010.

[338] David Shoemaker. Advanced LIGO anticipated sensitivity curves. Technical Report LIGO-T0900288-v3, LIGO Scientific Collaboration, https://dcc.ligo.org/LIGO-T0900288/public, 2010.

[339] Albert M Sirunyan et al. Measurement of angular parameters from the decay $B^0 \to K^{*0}\mu^+\mu^-$ in proton-proton collisions at $\sqrt{s} = 8$ TeV. *Phys. Lett. B*, 781:517–541, 2018.

[340] T. H. R. Skyrme. CVII. The nuclear surface. *Phil. Mag.*, 1:1043–1054, 1956.

[341] T.H.R. Skyrme. A unified field theory of mesons and baryons. *Nuclear Physics*, 31:556–569, 1962.

[342] M. Soares-Santos et al. First measurement of the Hubble constant from a dark standard siren using the Dark Energy Survey galaxies and the LIGO/Virgo binary-black-hole merger GW170814. *Submitted to: Astrophys. J.*, 2019.

[343] D. T. Son. Superconductivity by long range color magnetic interaction in high density quark matter. *Phys. Rev. D*, 59:094019, 1999.

[344] David N. Spergel and Paul J. Steinhardt. Observational evidence for self-interacting cold dark matter. *Physical Review Letters*, 84(17):3760–3763, apr 2000.

[345] David N. Spergel and Paul J. Steinhardt. Observational evidence for self-interacting cold dark matter. *Phys. Rev. Lett.*, 84:3760–3763, Apr 2000.

[346] David N. Spergel and Paul J. Steinhardt. Observational evidence for selfinteracting cold dark matter. *Phys. Rev. Lett.*, 84:3760–3763, 2000.

[347] A. W. Steiner and S. Gandolfi. Connecting neutron star observations to three-body forces in neutron matter and to the nuclear symmetry energy. *Phys. Rev. Lett.*, 108:081102, February 2012.

[348] Andrew W. Steiner. Deep crustal heating in a multicomponent accreted neutron star crust. *Phys. Rev. C*, 85:055804, May 2012.

[349] Andrew W. Steiner, James M. Lattimer, and Edward F. Brown. The neutron star mass-radius relation and the equation of state of dense matter. *Astrophys. J. Lett.*, 765(1):L5, 2013.

[350] Andrew W. Steiner, Madappa Prakash, James M. Lattimer, and Paul J. Ellis. Isospin asymmetry in nuclei and neutron stars. *Phys. Rept.*, 411:325–375, 2005.

[351] Nikolaos Stergioulas. Rotating Stars in Relativity. *Living Rev. Rel.*, 6:3, 2003.

[352] A. Steyerl, J. M. Pendlebury, C. Kaufman, S. S. Malik, and A. M. Desai. Quasielastic scattering in the interaction of ultracold neutrons with a liquid wall and application in a reanalysis of the Mambo I neutron-lifetime experiment. *Phys. Rev.*, C85:065503, 2012.

[353] K. Stovall et al. PALFA Discovery of a Highly Relativistic Double Neutron Star Binary. *Astrophys. J.*, 854(2):L22, 2018.

[354] M. Tanabashi et al. Review of Particle Physics. *Phys. Rev. D*, 98(3):030001, 2018.

[355] Z. Tang et al. Search for the Neutron Decay n$\rightarrow$ X+γ where X is a dark matter particle. 2018.

[356] J. H. Taylor, L. A. Fowler, and P. M. McCulloch. Measurements of general relativistic effects in the binary pulsar PSR1913+16. *Nature*, 277(5696):437–440, feb 1979.

[357] J. H. Taylor, R. N. Manchester, and A. G. Lyne. Catalog of 558 pulsars. *The Astrophysical Journal Supplement Series*, 88:529, oct 1993.

[358] J. H. Taylor and J. M. Weisberg. A new test of general relativity - gravitational radiation and the binary pulsar PSR 1913+16. *The Astrophysical Journal*, 253:908, feb 1982.

[359] I. Tews, J. Margueron, and S. Reddy. How well does GW170817 constrain the equation of state of dense matter? *Phys. Rev. C*, 98(045804), October 2018.

[360] Ingo Tews, Joseph Carlson, Stefano Gandolfi, and Sanjay Reddy. Constraining the speed of sound inside neutron stars with chiral effective field theory interactions and observations. 2018.

[361] K. S. Thorne and V. B. Braginskii. Gravitational-wave bursts from the nuclei of distant galaxies and quasars - proposal for detection using doppler tracking of interplanetary spacecraft. *The Astrophysical Journal*, 204:L1, feb 1976.

[362] Kip S. Thorne. Laws of motion and precession for black holes and other bodies. *Physical Review D*, 31(8):1815–1837, 1985.

[363] P. Tisserand et al. Limits on the Macho Content of the Galactic Halo from the EROS-2 Survey of the Magellanic Clouds. *Astron. Astrophys.*, 469:387–404, 2007.

[364] Richard C. Tolman. Static solutions of Einstein's field equations for spheres of fluid. *Phys. Rev.*, 55:364–373, 1939.

[365] Sean Tulin and Hai-Bo Yu. Dark Matter Self-interactions and Small Scale Structure. *Phys. Rept.*, 730:1–57, 2018.

[366] MICHAEL S. TURNER. Gravitational radiation from supernova neutrino bursts. *Nature*, 274(5671):565–566, aug 1978.

[367] Michele Vallisneri. Use and abuse of the Fisher information matrix in the assessment of gravitational-wave parameter-estimation prospects. *Phys. Rev. D*, 77:042001, 2008.

[368] M. H. van Kerkwijk, R. P. Breton, and S. R. Kulkarni. EVIDENCE FOR a MASSIVE NEUTRON STAR FROM a RADIAL-VELOCITY STUDY OF THE COMPANION TO THE BLACK-WIDOW PULSAR PSR b195+20. *The Astrophysical Journal*, 728(2):95, jan 2011.

[369] U. van Kolck. The Problem of Renormalization of Chiral Nuclear Forces. *Front. in Phys.*, 8:79, 2020.

[370] D. Vautherin. Hartree-Fock Calculations with Skyrme's Interaction. 2. Axially Deformed Nuclei. *Phys. Rev. C*, 7:296–316, 1973.

[371] D. Vautherin and D. M. Brink. Hartree-Fock calculations with Skyrme's interaction. 1. Spherical nuclei. *Phys. Rev. C*, 5:626–647, 1972.

[372] Justin Vines, Eanna E. Flanagan, and Tanja Hinderer. Post-1-Newtonian tidal effects in the gravitational waveform from binary inspirals. *Phys. Rev.*, D83:084051, 2011.

[373] J. D. Walecka. A Theory of highly condensed matter. *Annals Phys.*, 83:491–529, 1974.

[374] J. D. Walecka. Equation of State for Neutron Matter at Finite T in a Relativistic Mean-Field Theory. *Phys. Lett. B*, 59:109–112, 1975.

[375] Steven Weinberg. Nonlinear realizations of chiral symmetry. *Phys. Rev.*, 166:1568–1577, 1968.

[376] Steven Weinberg. Gauge and Global Symmetries at High Temperature. *Phys. Rev. D*, 9:3357–3378, 1974.

[377] Steven Weinberg. A New Light Boson? *Phys. Rev. Lett.*, 40:223–226, 1978.

[378] Steven Weinberg. Baryon and Lepton Nonconserving Processes. *Phys. Rev. Lett.*, 43:1566–1570, 1979.

[379] Steven Weinberg. Nuclear forces from chiral Lagrangians. *Phys. Lett. B*, 251:288–292, 1990.

[380] Steven Weinberg. Effective chiral Lagrangians for nucleon - pion interactions and nuclear forces. *Nucl. Phys. B*, 363:3–18, 1991.

[381] Steven Weinberg. Three body interactions among nucleons and pions. *Phys. Lett. B*, 295:114–121, 1992.

[382] Frank Wilczek. Problem of Strong P and T Invariance in the Presence of Instantons. *Phys. Rev. Lett.*, 40:279–282, 1978.

[383] Kenneth G. Wilson. Confinement of Quarks. *Phys. Rev. D*, 10:2445–2459, 1974.

[384] G. Wlazłowski, J. W. Holt, S. Moroz, A. Bulgac, and K. J. Roche. Auxiliary-field quantum Monte Carlo simulations of neutron matter in chiral effective field theory. *Phys. Rev. Lett.*, 113:182503, 2014.

[385] G. Wlazłowski, J. W. Holt, S. Moroz, A. Bulgac, and K. J. Roche. Auxiliary-Field Quantum Monte Carlo Simulations of Neutron Matter in Chiral Effective Field Theory. *Phys. Rev. Lett.*, 113(18):182503, 2014.

[386] S. E. Woosley and Robert D. Hoffman. The alpha-process and the r-process. *The Astrophysical Journal*, 395:202, aug 1992.

[387] S. E. Woosley and T. A. Weaver. The Physics of supernova explosions. *Ann. Rev. Astron. Astrophys.*, 24:205–253, 1986.

[388] Dmitrii G Yakovlev, Pawel Haensel, Gordon Baym, and Christopher Pethick. Lev landau and the concept of neutron stars. *Physics-Uspekhi*, 56(3):289–295, mar 2013.

[389] Chen-Ning Yang and Robert L. Mills. Conservation of Isotopic Spin and Isotopic Gauge Invariance. *Phys. Rev.*, 96:191–195, 1954.

[390] A. T. Yue, M. S. Dewey, D. M. Gilliam, G. L. Greene, A. B. Laptev, J. S. Nico, W. M. Snow, and F. E. Wietfeldt. Improved Determination of the Neutron Lifetime. *Phys. Rev. Lett.*, 111(22):222501, 2013.

[391] Jesús Zavala, Mark Vogelsberger, and Matthew G. Walker. Constraining self-interacting dark matter with the milky way's dwarf spheroidals. *Monthly Notices of the Royal Astronomical Society: Letters*, 431(1):L20–L24, Feb 2013.

[392] J. L. Zdunik, M. Fortin, and Pawel Haensel. Neutron star properties and the equation of state for its core, 2016.

[393] Ya. B. Zeldovich, J. Einasto, and S. F. Shandarin. Giant voids in the universe. *Nature*, 300(5891):407–413, dec 1982.

[394] Ya. B. ; Novikov Zel'dovich, I. D. The Hypothesis of Cores Retarded during Expansion and the Hot Cosmological Model. *Soviet Astron. AJ (Engl. Transl.)*,, 10:602, 1967.

[395] Kathryn M. Zurek. Asymmetric Dark Matter: Theories, Signatures, and Constraints. *Phys. Rept.*, 537:91–121, 2014.

[396] F. Zwicky. Die Rotverschiebung von extragalaktischen Nebeln. *Helv. Phys. Acta*, 6:110–127, 1933.

[397] F. Zwicky. On the masses of nebulae and of clusters of nebulae. *The Astrophysical Journal*, 86:217, oct 1937.